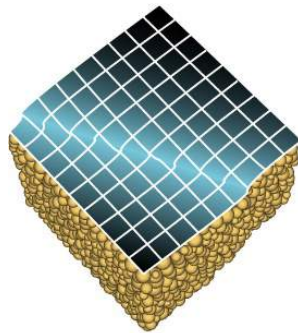


Book of Extended Abstracts

**4th International Symposium on
Computational Geomechanics**



ComGeo IV

2-4 May, 2018
Palazzo Bernabei, Assisi, Italy

Published by:

IC²E- International Centre for Computational Engineering
Rhodes, Greece & Swansea, UK

4th INTERNATIONAL SYMPOSIUM ON COMPUTATIONAL GEOMECHANICS (COMGEO IV),
Assisi, Italy, 2-4 May, 2018

Computational Geomechanics

BOOK OF EXTENDED ABSTRACTS

Published by:

IC²E - International Centre for Computational Engineering
Rhodes, Greece & Swansea, UK

Organizing Committee

Prof. G. N. Pande (Co-Chair)

*Swansea University, Swansea, UK
IC2E, Rhodes, Greece*

Prof. S. Pietruszczak (Co-Chair)

*McMaster University, Hamilton, Ontario, Canada
Cracow University of Technology, Poland*

Prof. C. Tamagnini (Co-Chair)

University of Perugia, Italy

Co-organizers

Prof. D. Salciarini

University of Perugia, Italy

Prof. W. Pula

Wroclaw University of Science & Technology, Poland

Dr. S. Drakos

IC2E, Rhodes, Greece

Scientific Committee

<i>E. Alonso (Spain)</i>	<i>G. Meschke (Germany)</i>
<i>J. Andrade (USA)</i>	<i>R. Michalowski (USA)</i>
<i>L. Andresen (Norway)</i>	<i>T. Nakai (Japan)</i>
<i>C. di Prisco (Italy)</i>	<i>H. Schweiger (Austria)</i>
<i>I. Einav (Australia)</i>	<i>A.P.S. Selvadurai (Canada)</i>
<i>L. Gambarotta (Italy)</i>	<i>J.F. Shao (France)</i>
<i>A. Gens (Spain)</i>	<i>H-S. Shin (S. Korea)</i>
<i>M. Hicks (Netherlands)</i>	<i>P. Simonini (Italy)</i>
<i>T. Hueckel (USA)</i>	<i>J. Tejchman (Poland)</i>
<i>C. Jommi (Italy)</i>	<i>H. Thomas (UK)</i>
<i>M. Karstunen (Sweden)</i>	<i>A. Truty (Poland)</i>
<i>L. Laloui (Switzerland)</i>	<i>C. Viggiani (France)</i>
<i>D. Lydzba (Poland)</i>	<i>R. Wan (Canada)</i>
<i>D. Masin (Czech Republic)</i>	

IC2E International Centre for Computational Engineering (IC2E) is a 'not for profit' organisation registered as an educational institution in the Aegean island of Rhodes, Greece.

The copyright of all works appearing here is retained by individual author or authors. No part of this publication or the information contained herein may be reproduced, stored in a retrieval system, or transmitted in any form or by any means, electronic, mechanical, or otherwise, without written prior permission from the IC2E, who act on behalf of authors.

Published by:

IC²E - International Centre for Computational Engineering

Rhodes, Greece & Swansea, UK

ISBN: 978-960-98750-3-5

Table of Contents

1. Constitutive relations for geomaterials

1.1 Macro/meso-scale approaches

Micromorphic modelling of periodic blocky materials with elastic joints: overall constitutive tensors and inertial terms.....	2
<i>A. Bacigalupo & L. Gambarotta</i>	
SANISAND model simulation under rotation of principal stress axes for granular media.....	4
<i>A.L. Petalas, Y.F. Dafalias & A.G. Papadimitriou</i>	
On specification of the conditions at failure in interbedded sedimentary rock mass.....	6
<i>P. Przecherski & S. Pietruszczak</i>	
Anisotropic undrained shear strength model for clays.....	8
<i>K. Krabbenhoft, S. Torres & X. Zhang</i>	
Cyclic behavior of water saturated dense sand.....	10
<i>H. P. Jostad, N. Sivasithamparam, P. Carotenuto, C. Madshus, H. Sturm, L. Andresen & K. H. Andersen</i>	
Particle/pore-size distribution and microstructure of saturation – key elements for rational description of mechanical behaviour of unsaturated soils.....	12
<i>G.N. Pande, S. Pietruszczak & M. Wang</i>	
Influence of grading on shear stiffness – the significance of accurate description of particle size distributions.....	14
<i>D. Barreto</i>	
A single hardening elastoplastic model for describing stress path dependency of plastic flow.....	16
<i>T. Nakai & H.M. Shahin</i>	
Approximation of Mohr envelope for the generalized Hoek-Brown criterion.....	18
<i>Y-K. Lee & S. Pietruszczak</i>	
Existence of unique fabric state surface for granular media at critical state.....	20
<i>P. Guo & J. Shi</i>	
Stress-dilatancy in barodesy.....	22
<i>G. Medicus & B. Schneider-Muntau</i>	
1.2 Micromechanical approaches	
Stress corrosion cracking, maturing of contacts, and creep in silica sand.....	24
<i>R.L. Michalowski, Z. Wang, D. Park & S.S. Nadukuru</i>	
The micromechanical nature of stresses in wet granular soils.....	26
<i>R. Wan, J. Duriez & F. Darve</i>	
Conformal discretization of heterogeneous geomaterial RVEs generated by excursion sets of random fields.....	28
<i>K. Ehab Moustafa Kamel, B. Sonon, J-B. Colliat, P. Gerard & T.J. Massart</i>	

Experimental and numerical investigation of dynamic fracture evolution in glass-bead chains under impact.....	30
<i>S. Jiang, L. Shen, F. Guillard & I. Einav</i>	
Contact topology during initial stages of particle breakage using x-ray tomography.....	32
<i>Z. Karatza, O. Okubadejo, E. Ando, S.A. Papanicolopoulos, G. Viggiani & J. Y. Ooi</i>	
Micromechanical modeling of time-dependent deformation and damage in claystone.....	34
<i>C. Bikong, Q.Z. Zhu & J.F. Shao</i>	
A dual porosity approach to model swelling of bentonite hydrated with brine.....	36
<i>Z. Li, T.S. Nguyen, G. Su & Q. Zheng</i>	

2. Modelling of instabilities and localized deformation

Computational modeling of fluid induced fracture propagation in deep geothermal reservoirs.....	39
<i>G. Meschke, I. Khisamitov, S. Beckhuis & J. Reinold</i>	
The level set discrete element method and its applicability to shear banding.....	41
<i>J. E. Andrade, R. Kawamoto, G. Viggiani & E. Andó</i>	
Borehole stability in brittle rock.....	43
<i>E. Gerolymatou</i>	
Modelling of hydraulic fracturing in rocks using coupled DEM/CFD approach.....	45
<i>M. Krzaczek, J. Kozicki & J. Tejchman</i>	
A strong discontinuity finite element model.....	47
<i>E. Sakellariadi</i>	
An isogeometric FE method for saturated and unsaturated soils with second gradient regularization.....	49
<i>C. Plúa, C. Tamagnini & P. Bésuelle</i>	
Micromechanical study of instability in granular materials using μ - GM constitutive model.....	51
<i>M. Pouragha & R. Wan</i>	
Modeling of localized damage in the presence of chemo-mechanical interaction.....	53
<i>S. Pietruszczak & S. Moallemi</i>	

3. Modelling of thermo-hydro-mechanical coupling and other transient problems

Thermo-poromechanics of a fluid inclusion.....	56
<i>A.P.S. Selvadurai</i>	
THCM analysis of shales.....	58
<i>L. Laloui, A. Ferrari & A. Minardi</i>	
Hydromechanical behavior of argillaceous rocks: constitutive law and applications.....	60
<i>M. Mánica, A. Gens, J. Vaunat & D. Ruiz</i>	
On the use of nitrogen to mitigate coal swelling during carbon sequestration.....	62
<i>L.J. Hosking & H.R. Thomas</i>	

Comparing FE and NURBS approximations for infiltration problems in unsaturated soils.....	64
<i>C. Jommi & E. Stopelli</i>	
Modelling tunnel response in highly expansive sulphated rock.....	66
<i>A. Ramon & E.E. Alonso</i>	
Coupled THM modeling of energy micro–pile behavior.....	68
<i>F. Ronchi, D. Salciarini & C. Tamagnini</i>	
A mathematical model for two-phase flow (gas and water) in a swelling geomaterials.....	70
<i>E.E. Dagher, T.S. Nguyen & J.A. Infante Sedano</i>	
Hazard and risk assessment of large seismic events owing to fluid injection.....	72
<i>B. Fryer, G. Siddiqi & L. Laloui</i>	
Mathematical modelling of a fault slip induced by water injection.....	74
<i>T.S. Nguyen, B. Graupner, Y. Gugliemi & J. Rutqvist</i>	
A discrete numerical model of the front region in piping erosion.....	76
<i>A.F. Rotunno, F. Froiio & C. Callari</i>	
A simplified, Newmark-like approach for the assessment of seismic performance of anchored diaphragm walls.....	78
<i>E. Cattoni, D. Salciarini & C. Tamagnini</i>	
Assessment of seismic vulnerability of large concrete dams by means of finite element modeling.....	80
<i>G. Buffi, P. Manciola, L. De Lorenzis, C. Tamagnini, A. Gambi & G. Montanari</i>	
4. Stochastic/probabilistic approaches	
Identification of the equivalent microstructure of porous materials: regularization and the stochastic optimization procedure.....	83
<i>D. Łydźba, Adrian Rózański & Damian Stefaniuk</i>	
General uncertainty in the reliability analysis of heterogeneous soil slopes at small failure probability.....	85
<i>A.P. van den Eijnden & M.A. Hicks</i>	
Random bearing capacity of square footing based on kinematical approach.....	87
<i>M. Chwala M. & W. Pula</i>	
Ultimate limit state assessment of dyke reliability using the Random Material Point Method.....	89
<i>G. Remmerswaal, M.A. Hicks & P.J. Vardon</i>	
Quantification of uncertainty in Geotechnical Engineering based on polynomial chaos.....	91
<i>S. Drakos & G.N. Pande</i>	
Reliability analysis of bearing capacity of square footing on spatially variable cohesive-frictional soil.....	93
<i>M. Kawa & W. Pula</i>	

5. Application of numerical techniques to practical problems

5.1 Slope stability

- 2D hydro-mechanical analyses of rainfall induced slope instability.....96
P. Sitarenios, F. Casini, A. Askarinejad & S.M. Springman
- Fluid-solid transition in unsteady shearing flows.....98
D. Vescovi, D. Berzi & C. di Prisco
- Comparison of limit state stability evaluation methods for geotechnical engineering.....100
H. Hernvall, J. Dijkstra & M. Karstunen
- Comparison of different strength reduction techniques on slope stability calculations.....102
B. Schneider-Muntau, F. Tschuchnigg, G. Medicus & W. Fellin

5.2 Offshore structures

- Suction caisson installation design from CPT, utilizing machine learning techniques.....104
R. T. Klinkvort, G. Sauvin & L. Andresen
- Macro-element modelling of suction buckets for the integrated analysis of jacket-supported offshore wind turbines.....106
B. Bienen, F. Pisanò, D. Moretti, D. Salciarini & C. Tamagnini
- Effect of installation history on the lateral response of monopiles in dry sand.....108
S. Fan, B. Bienen & M. Randolph
- Large deformation finite element analysis of spudcan penetration behaviour on uneven seabed.....110
H.D.V. Khoa, Y. Shin, H-J. Park, J-H. Kim, D-S. Kim, J. Han & S. Lee
- Implementation of a hypoplastic model with intergranular strain for the modelling of spudcan cyclic response in silty clay.....112
R. Ragni, B. Bienen, D. Masin, J. Jerman, D. Wang & M.J. Cassidy

5.3 Foundations

- 3D FEA of ultimate limit states: finite element limit analyses vs displacement based finite element analyses.....114
F. Tschuchnigg & H.F. Schweiger
- Estimation of pile capacities using Case Base Reasoning method.....116
H.K. Engin, F. Nadim, P. Carotenuto & K. Bach
- 3D spatial variability of mechanical properties of Emilia Romagna alluvial deposits and its implications in geotechnical design of foundations.....118
G. Vessia, A. Castrignano, D. Di Curzio & W. Pula
- Numerical implementation of a stress-saturation soil model with hydraulic hysteresis effects...120
Y. Zhang, A. Zhou, M. Nazem & J.P. Carter

5.4 Applications incorporating Material Point/Particle FE Method

- Numerical study of penetration problems in fine grained soils with the Particle Finite Element Method122

L. Monforte, M. Arroyo, A. Gens & J.M. Carbonell

Numerical simulation and verification of static liquefaction using the Material Point Method...124

L. Wobbes, J.R. Silva, V. Galavi, J.T. Eggenhuisen & C. Vuik

Modelling saturated soil column collapse with 2-Phase 2-Point Material Point Method.....126

V. Girardi, F. Ceccato & P. Simonini

Simulation of free water-fully saturated soil interaction using the Material Point Method.....128

F. Fatemizadeh, D.F. Stolle & C. Moormann

Simulation of vibratory driven piles with the axisymmetric Material Point Method.....130

V. Galavi, M. Martinelli, F.S. Tehrani, A. Elkadi & D. Luger

5.5 Underground structures

Isogeometric boundary element analysis of underground excavations considering effects of geology.....132

G. Beer & Ch. Duenser

Numerical anisotropic modelling of a deep drift at the Meuse/Haute-Marne URL.....134

E.D. Coarita-Tintaya, M. Souley, M.N. Vu & F. Golfier

A macroelement for coupled analysis of the mechanical response of deep tunnel fronts in cohesive soils.....136

C. di Prisco & L. Flessati

Eulerian analysis of tunnel excavation with an EPB shield.....138

N. Losacco, G.M.B. Viggiani & D. Branque

Development of a deep-learning based automatic tunnel incident detection system on CCTVs...140

K-B. Lee, H-S. Shin, & D-G. Kim

5.6 Other applications

Numerical analysis of soil penetration with advanced effective stress soil models.....142

Z.Y. Orazalin & A.J. Whittle

Numerical model of flat dilatometer test in normally and overconsolidated cohesionless soils...144

A. Truty & K. Podles

Numerical modelling of anchor load tests: influence of the grout.....146

C. Fabris, B. Pulko & H.F. Schweiger

Numerical analyses and model tests on countermeasure against damage of existing structure due to tunneling.....148

M. Suzuki, M. Kashiyama, T. Nakai & H.M. Shahin

Preface

Over the last few decades a rapid progress has been made in many areas of computational geomechanics and a broad spectrum of software is now readily available to the engineer. However, engineers are facing new challenges as demand for sustainable alternative means of energy production and solutions to environmental problems are being sought all over the world. Only computational methods can provide viable solutions of complex geotechnical and geo-environmental problems being faced by engineers of today. Need for co-operation and dialogue amongst all concerned at the highest technical level has never been greater than now.

The International Centre for Computational Engineering (IC²E) - a not for profit educational charity - is a unique independent organisation that is well placed to play an important role in promoting exchange of views, developing state-of-the art reports and giving unbiased advice to stake holders, private sector, governmental and non-governmental organisations.

Following the first three Symposia on “Computational Geomechanics” (ComGeo) held in Nice (France), Dubrovnik (Croatia) and Krakow (Poland), ComGeo IV is being organised in Assisi, Italy. ComGeo series of Symposia is a sequel to “Numerical Models in Geomechanics” NUMOG series which was launched in 1982 and included 10 international meetings that were organized over a period of 25 years. Each meeting had a limited number of participants and the focus was on preserving a high technical standard as well as an informal style. ComGeo series aims to maintain the same format, however, the scope of this series is much broader and will include new emerging research areas as and when needed.

This Book of Extended Abstracts of papers to be presented at ComGeo IV contains over 70 papers, which are organized in five major sections:

1. *Constitutive relations for geomaterials*
2. *Modelling of instabilities and localized deformation*
3. *Modelling of thermo-hydro-mechanical coupling and other transient problems*
4. *Stochastic/probabilistic approaches*
5. *Application of numerical techniques to practical problems*

All abstracts included here will be archived in a downloadable form in the e-Library of IC²E (<http://www.ic2e.org>), for wider dissemination.

We are grateful to the members of the Scientific Committee, for their co-operation and helpful suggestions.

S. Pietruszczak

G. N. Pande

C. Tamagnini

April 2018

1. Constitutive relations for geomaterials

MICROMORPHIC MODELLING OF PERIODIC BLOCKY MATERIALS WITH ELASTIC JOINTS: OVERALL CONSTITUTIVE TENSORS AND INERTIAL TERMS

A. Bacigalupo¹ and L. Gambarotta²

¹ IMT School for Advanced Studies, Lucca, Italy

² University of Genoa, Genoa, Italy

1. Introduction

It is well known that in continuum modelling of blocky structures, non-local constitutive models may be required to appreciate the size effects. In a simple two-dimensional approach, the granules or the blocks may be assumed to have polygonal or circular shape endowed with mass and gyroscopic inertia, connected with each other through homogeneous linear interfaces. Under this hypothesis, the deformability of the composite material is localized at the interfaces and a Lagrangian model can be assumed to simulate the structural behavior of the blocky structure.

The rotational degrees of freedom of the blocks suggests to consider the Cosserat model as equivalent continuum and accordingly homogenization techniques in the static field have been proposed for blocky rocks by Mühlhaus [1]. Dispersive propagation of harmonic waves in discrete blocky systems have been analysed by Sulem and Mühlhaus [2], who complemented their results with the identification of a Cosserat continuum in order to approximate the dispersive functions of the discrete model. A similar analysis was carried out for granular materials by Suiker and de Borst [3], where a second order micropolar continuum was also considered. On the other hand, it is worth noting that Merkel *et al.* have highlighted some limitations of the Cosserat model in simulating the optical band structure of hexagonally packed granular materials in the neighborhood of long waves [4]. In particular, these Authors criticized the inability of the Cosserat model to simulate the downward concavity of the optical branch in the Brillouin domain obtained in the Lagrangian model for long rotational wavelengths. It has been shown by the Authors [5] that this drawback may be overcome by assuming a continuum description of the discrete system based on a micropolar approach relying on a continualization of the dynamic governing equations in terms of translations and rotations that simulate with a good agreement both the acoustic and the optical branches in the frequency spectrum. Nevertheless, the resulting micropolar continuum model suffers some inconsistencies in the positive definiteness of the elastic potential density that affect the static elastic behavior and requires enhancements in the homogenization procedure. Here a simplified model of one dimensional blocky systems composed of rigid blocks connected by elastic joints is considered in order to explore a new homogenization technique capable of solving the problems that have emerged.

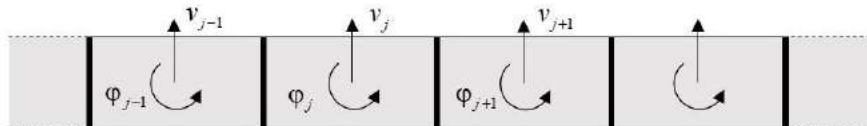


Figure 1. Simple 1D blocky system.

2. One dimensional blocky system

Let consider the block stack shown in Figure 1, where the rectangle rigid blocks of length ℓ and width b are connected through elastic interfaces having normal and tangential stiffness k_n and

k_t , respectively. The displacement of the i -th block consists of a transverse deflection $v_i = \psi_i \ell$ and a rotation φ_i . Each block has mass m and gyrotory inertia I . The equation of motion of the discrete model is

$$\begin{cases} (\psi_{i+1} - 2\psi_i + \psi_{i-1}) - \frac{1}{2}(\varphi_{i+1} - \varphi_{i-1}) + \bar{f}_i = I_\psi \ddot{\psi}_i \\ \frac{1}{2}(\psi_{i+1} - \psi_{i-1}) - \frac{1}{6}\alpha[\varphi_{i+1} + (4 + \delta)\varphi_i + \varphi_{i-1}] + \bar{c}_i = I_\varphi \ddot{\varphi}_i \end{cases} \quad (1)$$

with $\alpha = \frac{1}{2} \left[3 - \frac{k_n}{k_t} \left(\frac{b}{\ell} \right)^2 \right]$ and $\delta = \frac{6(1-\alpha)}{\alpha}$.

3. Micromorphic continuum model

To obtain a homogeneous equivalent model representing the Lagrangian system introduced in the previous Section, two macroscopic fields $\Psi(x, t)$ and $\Phi(x, t)$ are considered to represent the transversal deflection and rotation, respectively, of the blocks. By introducing the shift operator $E_\ell = \sum_{h=0}^{\infty} \frac{\ell^h}{h!} D^h = \exp(\ell D)$, with $D^h = \frac{\partial^h}{\partial x^h}$, to express $\psi_{i\pm 1}(t) = \exp[\pm \ell D] \psi_i$, $\varphi_{i\pm 1}(t) = \exp[\pm \ell D] \varphi_i$ (see [6]) and the up-scaling law $\frac{\partial \Psi}{\partial x} := \frac{\psi_{i+1} - \psi_{i-1}}{2\ell}$ and $\frac{\partial \Phi}{\partial x} := \frac{\varphi_{i+1} - \varphi_{i-1}}{2\ell}$, the equation of motion of the equivalent 1D continuum may be obtained within a given accuracy in terms of the block length ℓ . The simplest continuum model is obtained by truncating the equation of motion at order ℓ^3 and takes the form

$$\begin{cases} \ell^2 \frac{\partial^2 \Psi}{\partial x^2} - \ell \frac{\partial \Phi}{\partial x} + \bar{f} \ell = I_\psi \left[\ddot{\Psi} - \frac{\ell^2}{6} \frac{\partial^2 \ddot{\Psi}}{\partial x^2} \right] \\ \ell \frac{\partial \Psi}{\partial x} - \Phi + \frac{1}{36} \alpha \delta \ell^2 \frac{\partial^2 \Phi}{\partial x^2} + \bar{c} \ell = I_\varphi \left[\ddot{\Phi} - \frac{\ell^2}{6} \frac{\partial^2 \ddot{\Phi}}{\partial x^2} \right] \end{cases} \quad (2)$$

This model is characterized by overall constitutive parameters and inertial terms associated to a positive defined elastic potential density and kinetic energy density and is able to provide good approximations of the dispersive functions of the Lagrangian model.

5. References

- [1] Mühlhaus, H. B. (1993). Continuum models for layered and blocky rock, (Hudson I.A. Ed.) *Comprehensive Rock Engineering*, **2**, 209-231.
- [2] Sulem J., Mühlhaus H-B. (1997). A continuum model for periodic two-dimensional block structures, *Mechanics of Cohesive-Frictional Materials*, **2**, 31-46.
- [3] Suiker, A. S., de Borst, R. (2005). Enhanced continua and discrete lattices for modelling granular assemblies, *Phil. Trans. Royal Society of London A*, **363**, 2543-2580.
- [4] Merkel, A., Tournat, V., Gusev, V. (2011). Experimental Evidence of Rotational Elastic Waves in Granular Phononic Crystals, *Physical Review Letters*, **107**, 225502.
- [5] Bacigalupo, A., Gambarotta, L. (2017). Dispersive wave propagation in two-dimensional rigid periodic blocky materials with elastic interfaces, *J. Mech. Phys. Solids*, **102**, 165-186.
- [6] Rosenau, P. (2003). Hamiltonian dynamics of dense chains and lattices: or how to correct the continuum, *Physics Letter A*, **311**, 39-52.

SANISAND MODEL SIMULATION UNDER ROTATION OF STRESS PRINCIPAL AXES FOR GRANULAR MEDIA

*Alexandros L. Petalas*¹, *Yannis F. Dafalias*^{2,3} and *Achilleas G. Papadimitriou*³

¹ *Chalmers University of Technology, Sweden*

² *University of California at Davis, USA*

³ *National Technical University of Athens, Greece*

1. Introduction

A reformulation of the dilatancy expression used in the two surface, bounding surface model for sands by Dafalias & Manzari [1] within critical state theory, is presented in this work; the aim is to account for the effect of continuously rotating stress principal axes (PA). The reformulation is generic and can be used in conjunction with other similar constitutive models without introducing an additional plastic strain mechanism or double expression for the dilatancy, as is usually proposed in the literature.

2. Reformulation of dilatancy to account for stress PA rotation

In the multiaxial formulation presented in [1] the dilatancy is given by

$$\mathbf{D} = A_d (\boldsymbol{\alpha}_\theta^d - \boldsymbol{\alpha}) : \mathbf{n} \quad (1)$$

where A_d positive constant; $\boldsymbol{\alpha}$ the deviatoric back-stress ratio tensor; \mathbf{n} the unit-norm deviatoric component of the normal to the yield surface; $\boldsymbol{\alpha}_\theta^d = \sqrt{2/3} [g(\theta, c) M_c \exp(n^d \psi - m)] \mathbf{n} = \alpha_\theta^d \mathbf{n}$ is the deviatoric dilatancy back-stress ratio tensor that lies on the dilatancy surface and is function of the state parameter ψ ; M_c the critical state stress ratio in triaxial compression; $g(\theta)$ a Lode angle θ interpolation function as in [1]; m the half size of the small yield surface while the definition of the scalar-valued α_θ^d is self-evident. In this work the expression 1 is reformulated as:

$$\begin{aligned} \mathbf{D} &= A_d [B(k, N_\alpha) \boldsymbol{\alpha}_\theta^d - C(g(\theta), N_\alpha) \boldsymbol{\alpha}] : \mathbf{n} = \\ &= A_d [B(k, N_\alpha) \alpha_\theta^d - C(g(\theta), N_\alpha) \alpha N_\alpha] \end{aligned} \quad (2)$$

where $\boldsymbol{\alpha} = \alpha \mathbf{n}_\alpha$ with α the norm and \mathbf{n}_α the unit norm direction of $\boldsymbol{\alpha}$, and $N_\alpha = \mathbf{n}_\alpha : \mathbf{n}$ a measure of non-coaxiality (non-proportionality) of $\boldsymbol{\alpha}$ and \mathbf{n} tensors.

The $B(k, N_\alpha)$ densification function is introduced in Eq. (2) to account for the decreasing rate of the contractive volumetric strain per cycle of applied stress PA rotation and is given by

$$B(k, N_\alpha) = \exp[-k(1 - |N_\alpha|)] \quad (3)$$

where k is a scalar-valued term, which evolves from 0 towards its saturation value k_s . When many cycles of stress PA rotation are applied the B functions decreases the $B\alpha_\theta^d$ term in Eq. (2) and thus D is progressively decreasing until $B\alpha_\theta^d = C\alpha N_\alpha$ and $D=0$.

The contraction function $C(g(\theta), N_\alpha)$ ensures contractive response during stress PA rotation irrespective of the initial density and stress state of the soil as observed in experimental studies [2, 3] and is given by

$$C(g(\theta), N_\alpha) = [g(\theta) - [g(\theta) - 1] |N_\alpha|^{50}]^{h_N} \quad (4)$$

where h_N = a positive material constant. Its effect is stronger when θ or equivalently the intermediate stress parameter b is larger (TC: $\theta = 0^\circ, b = 0$; TE: $\theta = 60^\circ, b = 1$) that is consistent with experimental observations. Both functions are active when stress PA are rotated since $|N_\alpha| < 1$, and inactive for radial paths when $|N_\alpha| = 1$.

3. Simulations

Fig. 1.a shows the experimental data and Fig. 1.b the simulations of the accumulation of the volumetric strain within 27 cycles of stress PA rotation, for three cases with $b = 0.1, b = 0.5$ and $b = 1$. The simulations with the modified dilatancy (solid lines in Fig. 1.b) are very accurate for the cases of $b = 0.1$ and $b = 1$ and acceptable for the $b = 0.5$ case, apart from the observed dilation/contraction oscillations. For comparison the inaccurate simulations of the original dilatancy definition of Eq. 1 are shown by dashed lines in Fig. 1.b.

4. Acknowledgments

The research leading to these results has received funding from the European Research Council under the European Union's Seventh Framework Program (FP7/2007-2013) / ERC IDEAS Grant Agreement n° 290963 (SOMEF) and partial support by NSF project CMMI-1162096.

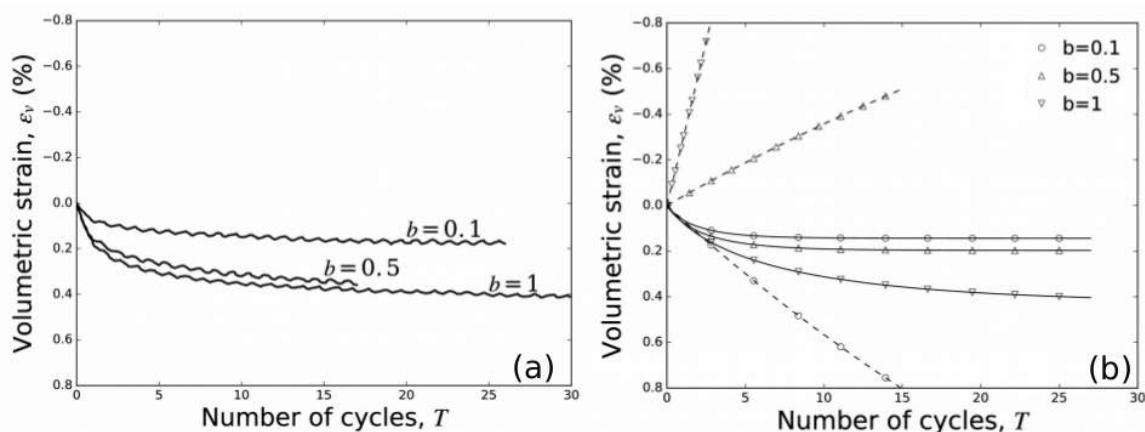


Figure 1. Volumetric strain evolution accumulation in drained stress PA rotation. Toyoura sand, $p = 100$ kPa, $D_r = 70\%$ ($e = 0.737$), $\eta = 0.866$. (a) Experimental data after Tong et al. [2]; (b) Simulations with the model in Dafalias & Manzari [1] (dashed lines) and with the modified dilatancy of Eq. (2) (solid lines)

References

- [1] Dafalias, Y. F. and Manzari, M. T. (2004). Simple plasticity sand model accounting for fabric change effects. *Journal of engineering mechanics*, **130**, 622–634.
- [2] Tong, Z.-X., Zhang, J.-M., Yu, Y.-L., and Zhang, G. (2010). Drained Deformation Behavior of Anisotropic Sands during Cyclic Rotation of Principal Stress Axes. *Journal of Geotechnical and Geoenvironmental Engineering*, **136**, 1509–1518.
- [3] Miura, K., Miura, S., and Toki, S. (1986). Deformation behavior of anisotropic dense sand under principal stress axes rotation. *Soils and Foundations*, **26**, 36–52.

ON SPECIFICATION OF CONDITIONS AT FAILURE IN INTERBEDDED SEDIMENTARY ROCK MASS

P. Przecherski¹ and S. Pietruszczak^{2,1}

¹*Cracow University of Technology, Cracow, Poland*

²*McMaster University, Hamilton, Ont., Canada*

1. Introduction

This presentation describes a methodology for assessing the conditions at failure in interbedded sedimentary rocks. The structure of the material examined in this work is typical of the Carpathian Flysch Belt and has an arrangement of alternating marine deposits of claystones and sandstones with varying thickness. The approach involves a numerical investigation at the mesoscale that allows the assessment of strength properties for different orientations of stratification. A comprehensive set of data generated through this investigation is then employed to identify material functions in a continuum framework that accounts for the effects of inherent anisotropy at the macroscale. The conditions at failure in both compression and tension regimes are addressed and the performance of the macroscopic criterion is verified for different stress trajectories.

2. Assessment of conditions at failure; meso- and macroscale approach

Laboratory testing of interbedded rock mass poses significant problems. Those include difficulties associated with testing of inclined samples as well as restrictions on the sample size, i.e. the largest dimension is typically much smaller than that associated with REV. In view of this, the approach advocated here involves a simple computational assessment of strength based on properties of constituents and their respective volume fractions. Given this set of ‘virtual data’, a macroscopic criterion can be formulated accounting for the effects of anisotropy, and the associated material functions can be identified.

Assume that the conditions at failure for both constituent materials can be approximated using the classical Mohr-Coulomb criterion with Rankine’s cut-off in the tensile regime. Thus,

$$F = \max(F_1, F_2) = 0; \quad F_1 = \sqrt{3}\bar{\sigma} - \eta_f g(\theta)(\sigma_m + C); \quad F_2 = \max_{n_i} (\sigma_{ij} n_i n_j - f_t(n_i)) \quad (1)$$

In the expressions above, $\bar{\sigma} = (s_{ij} s_{ij} / 2)^{1/2}$, $\sigma_m = -\sigma_{ii} / 3$, θ is the Lode’s angle and $C = c \cot \phi$. For the tension cut-off criterion, n_i defines the unit normal to the plane, while f_t is the corresponding tensile strength. Note that, for an isotropic material, $f_t = \text{const}$.

The assessment of strength at the macroscale is based now on standard FE analysis. The simulations employ an elastic – perfectly plastic idealization and involve a series of triaxial tests performed at different orientations of the sedimentary layers relative to the direction of loading. Typical results are given in Fig.1, which shows the evolution of axial *compressive* strength R_c with the inclination angle (β) for different confining pressures and volume fractions μ_1 of sandstone.

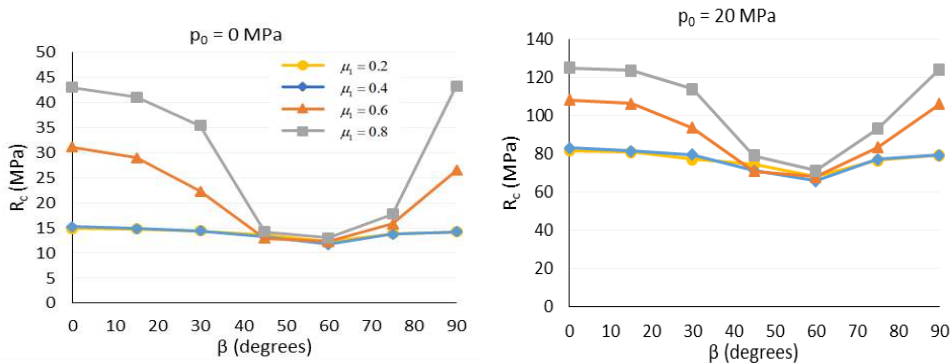


Fig.1

The macroscopic failure criterion is obtained by preserving the functional form consistent with representation (1) and postulating that the strength depends on orientation of the sample relative to the direction of loading. Following the methodology outlined in ref. [1], the anisotropy parameter is defined as

$$\eta_f = \hat{\eta}_f \left(1 + A_{ij} l_i l_j + a_1 (A_{ij} l_i l_j)^2 + a_2 (A_{ij} l_i l_j)^3 + \dots\right); \quad C = \text{const.} \quad (2)$$

Here, l_i represents a unit vector, referred to as a ‘loading direction’, whose components are the normalized magnitudes of tractions on planes normal to the principal material axes. The latter are defined by the eigenvectors of the operator A_{ij} , which is a traceless second-order tensor. The dependence of the strength properties on the volume fraction of constituents is accounted for by postulating that $\hat{\eta}_f, A_{ij}, a_1, a_2 \dots$ are functions of μ_1 .

For failure in tension regime, Rankine’s failure criterion, $F_2=0$, can be generalized to

$$F_2 = \max_{n_i} \left(\sigma_{ij} n_i n_j - f_i(n_i) \right) = 0; \quad f_i = \hat{f}_i \left(1 + \Omega_{ij} n_i n_j + b_1 (\Omega_{ij} n_i n_j)^2 + b_2 (\Omega_{ij} n_i n_j)^3 + \dots \right) \quad (3)$$

Here, Ω_{ij} is again a symmetric traceless tensor which describes the bias in the spatial distribution of tensile strength while $\hat{f}_i, b_1, b_2 \dots$ are the coefficients of approximation.

The identification process, in the compression regime, is based on the results of the numerical simulations of a series of axial compression tests described earlier. For a given volume fraction μ_1 , the parameter C has been estimated using the orientation average for all tests. Given this value, the material function $\eta_f = \eta_f(l_i)$ has been identified. In this case, for each specific orientation of the sample and the given confining pressure, the value of η_f satisfying $F_1 = 0$ was determined, together with the corresponding loading direction. The results generated a set of data in the affined plane $\eta_f - l_2$, which was then approximated using the best-fit (i.e. least-square) procedure. For assessment of strength in the tensile regime, a conceptually similar procedure was employed in which the approximation coefficients were determined from the results of simulations of axial tension tests performed at different values of inclination angle β .

The last part of this work is focused on the extension of this framework to account for variation in the volume fraction of constituent materials. A general identification scheme is discussed first, followed by a simplified approach that makes use of the results of *uniaxial* compression (i.e. at zero confinement). In the latter case, the relation between the strength parameter η_f and the volume fraction of sandstone μ_1 is established first for different orientations β , cf. Fig.2. The results allow for an explicit identification of the approximation coefficients defining the relation $\eta_f = \eta_f(l_i, \mu_1)$. Finally, the performance of the proposed criterion is verified for a number of different stress trajectories and the results are compared with ‘virtual data’, e.g. Fig.3.

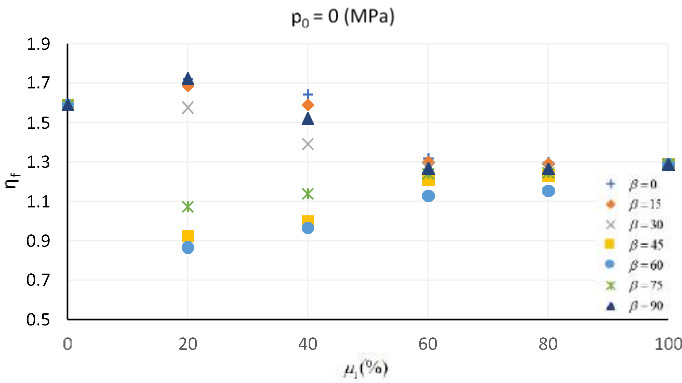


Fig.2

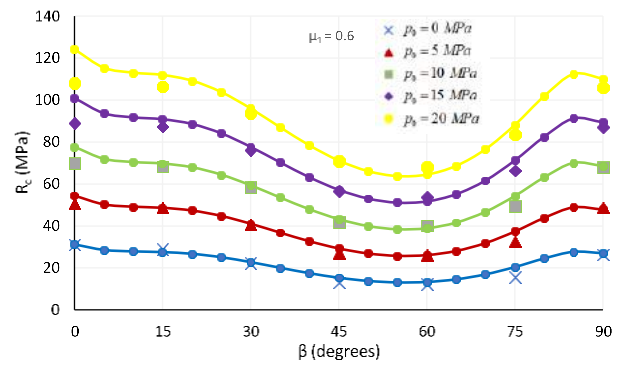


Fig.3

3. References

- [1] Pietruszczak, S. & Mróz, Z (2001). On failure criteria for anisotropic cohesive-frictional materials. *Int. J. Num. Meth. Eng.*, **25**, 509-524.

ANISOTROPIC UNDRAINED SHEAR STRENGTH MODEL FOR CLAYS

K. Krabbenhoft¹, S.G. Galindo-Torres¹ and X. Zhang¹

¹ *School of Engineering, University of Liverpool, UK*

Many geotechnical problems may be analyzed assuming undrained conditions. That is, under the assumption that the dissipation of the excess pore pressures generated in response to loading is negligible during the time period of interest, e.g. the period of construction or the period from load application to possible failure. For such problems, it is common practice to model the material behaviour with reference to total, rather than effective, stresses. The simplest possible elastoplasticity model within the total stress framework is the linear elastic-perfectly plastic Tresca model which involves two parameters: the undrained Young's modulus (or the shear modulus) and the undrained shear strength, both of which may be specified to vary with depth. While crude, this model does – with careful selection of the two parameters – offer a reasonable estimate of both the deformation characteristics under working conditions and the strength characteristics at the ultimate limit state.

Somewhat surprisingly, while there have been tremendous advances in the development of constitutive models for clays based on the more rigorous and arguably theoretically more satisfactory effective stress approach, total stress models have evolved little beyond the aforementioned linear elastic-perfectly plastic Tresca model. Considering that a number of salient features are not captured by this model, there appears to be scope for an extension of these types of linear elastic-perfectly plastic models, analogous in many ways to the extension of such models in the more general effective stress setting. This work is concerned with one such extension. Following the conventional constitutive modeling paradigm, the model, denoted AUS (Anisotropic Undrained Shear strength model), is based on elastoplasticity. Rather than the standard Tresca strength criterion, the so-called Generalized Tresca criterion is used. This strength criterion involves two parameters, namely the undrained shear strengths in triaxial compression and extension, and may be shown to be consistent with the effective stress Mohr-Coulomb model under undrained conditions [1]. This Generalized Tresca yield function (see Figure 1) is given by

$$F = \sigma_1 - \sigma_3 - \left(\frac{s_{uc}}{s_{ue}} - 1 \right) (\sigma_2 - \sigma_3) - 2s_{uc} = 0 \quad (1)$$

where $\sigma_1 \geq \sigma_2 \geq \sigma_3$ are the principal stresses (positive in compression) and s_{uc} and s_{ue} are the undrained shear strengths in triaxial compression and extension respectively.

The Generalized Tresca model pertains to isotropic materials, i.e. materials that have the same properties in all directions. The unequal strengths in compression and extension implied by the model is essentially a Lode angle effect and is not due to physical anisotropy, i.e. different properties in different directions. The AUS model extends the Generalized Tresca model to anisotropic materials, in particular to the case of cross anisotropy, stemming for example from a preferential direction of deposition. However, the two effects – Lode angle dependence and anisotropy – are clearly delineated and treated separately. Secondly, in contrast to the linear elastic Tresca models (standard as well as Generalized), the AUS model incorporates plasticity prior to failure. This is achieved by means of a hardening Generalized Tresca yield surface involving two parameters that can be related to the axial strain at half the failure stress in triaxial compression and extension. These parameters can, together with the undrained shear strengths, be inferred directly from experiments.

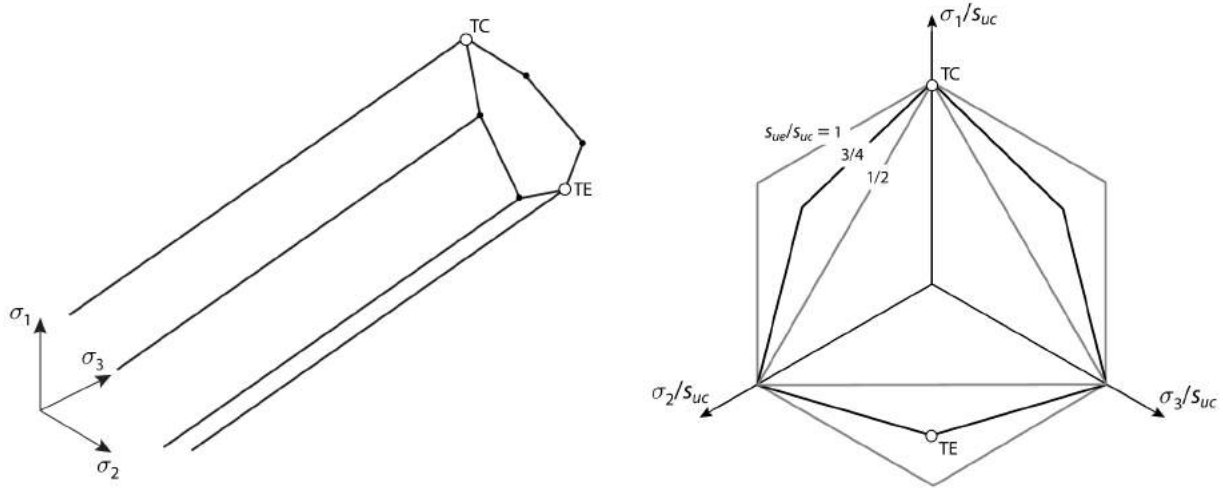


Figure 1. Generalized Tresca yield surface

As an example of the response of the model, consider the scenario where a sample has been taken out of the ground, trimmed appropriately and then subjected to a state of biaxial compression at an angle α relative to the normal to the plane of anisotropy. In other words, for $\alpha = 0^\circ$ the sample is loaded normal to the plane of anisotropy and the strength is $s_{uc,0} = s_{uc}$ while for $\alpha = 90^\circ$ the sample is loaded parallel to the plane of anisotropy and the measured strength is $s_{uc,90} = s_{ue}$. The results, which have been computed numerically, are shown in Figure 2. The strength dependence on the angle of inclination is here, qualitatively, similar to previously reported experimental results.

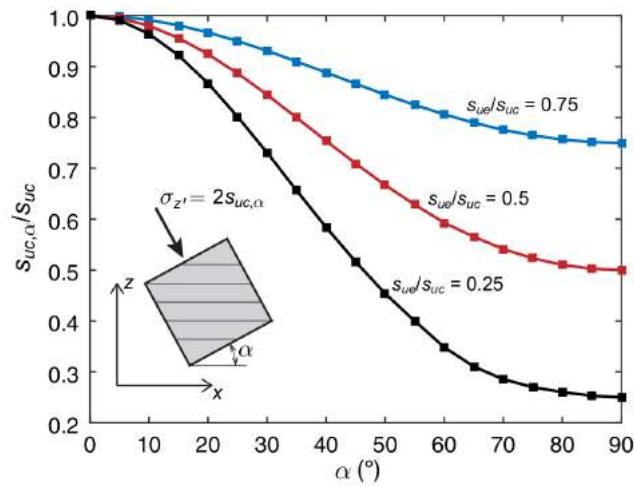


Figure 2. Undrained strength as function of load inclination relative to the plane of anisotropy for different s_{ue}/s_{uc} and $s_{us} = \frac{1}{2}(s_{uc} + s_{uc})$

In the presentation, application to various boundary value problems, including 3D analysis of monopiles subjected to combined loading, will be given.

References

- [1] Krabbenhoft, K. and Lyamin, A. V. (2015). Generalized Tresca criterion of undrained total stress analysis. *Geotechnique Letters*, **5**, 313–317.

CYCLIC BEHAVIOR OF WATER SATURATED DENSE SAND

*H.P. Jostad¹, N. Sivasithamparam¹, P. Carotenuto¹, C. Madshus¹,
H. Sturm¹, L. Andresen¹ and K.H. Andersen¹*
NGI, Oslo, Norway

1. Laboratory tests

The characteristic behavior of water saturated dense sand is presented and discussed based on results from a large number of different laboratory tests carried out at NGI during the last 50 years. This includes incremental and accumulated response under drained, undrained and partly drained monotonic and cyclic triaxial and DSS tests with different combinations of average and cyclic stress histories. The measured response, e.g. cyclic and accumulated shear strains and accumulated pore pressure versus the number of applied cycles, is at NGI for instance used to develop so-called cyclic contour diagrams [1]. Examples of cross sections of these (3D) diagrams are shown in Figure 1.

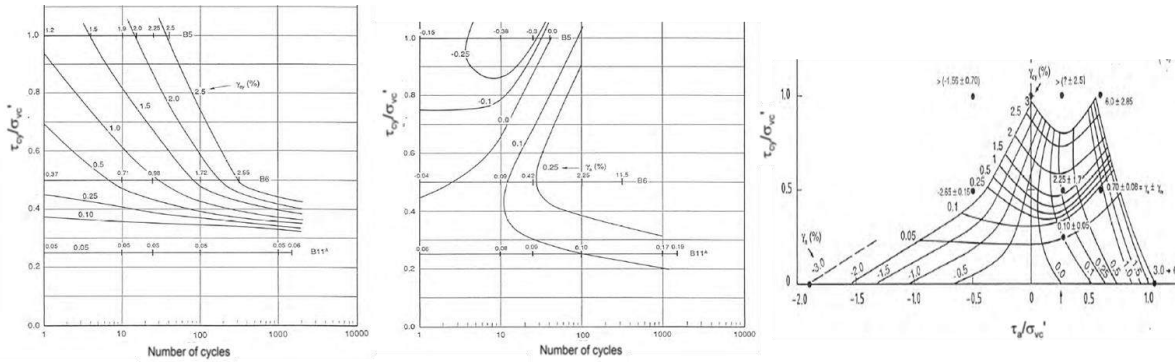


Figure 1. Cyclic undrained contour diagram in the 3D (τ_{cy}/σ_{vc}' , τ_a/σ_{vc}' , N -space) for a very dense North Sea sand. a) Cross section of the cyclic shear strain γ_{cy} , and b) accumulated shear strain γ_a for a constant normalized average shear stress τ_a/σ_{vc}' . c) Cross section for a given number of undrained cycles, $N = 100$.

Recently, some special undrained cyclic triaxial tests have been carried out at NGI where the effect of different degree of drainage of the accumulated pore pressure was considered. These tests give interesting results regarding the cyclic response at different stress states of a dense sand with almost the same void ratio but different strain histories before reaching the considered states.

In addition to the different tests carried at NGI, the large database of cyclic tests presented by Wichtmann and Triantafyllidis [2], improved models for design of offshore foundations subjected to cyclic loading from waves, wind and currents may be develop. Four different material models are evaluated, one elasto-plastic boundary surface model, one hypoplastic model and two explicit strain accumulation models.

2. Incremental (implicit) constitutive models

In incremental (implicit) models, the behaviour of the sand is defined by the current state (e.g. effective stresses, void ratio and fabric), the incremental stress or strain direction and the stress history together with a set of sand dependent material properties. The effect of cyclic loading (as for instance defined by an equivalent number of cycles [1]) is not directly incorporated in these incremental models. Figure 2 shows an example of the measured stress path in a $p'-q/2$ plot and the corresponding shear stress-strain curve for a given cycle in an undrained triaxial tests of a dense

North Sea sand ($Dr = 80\%$). These type of results are used to calculate the hardening modulus H and dilatancy D within the cycles. Some of these results will be presented at NUMGE 2018 [3].

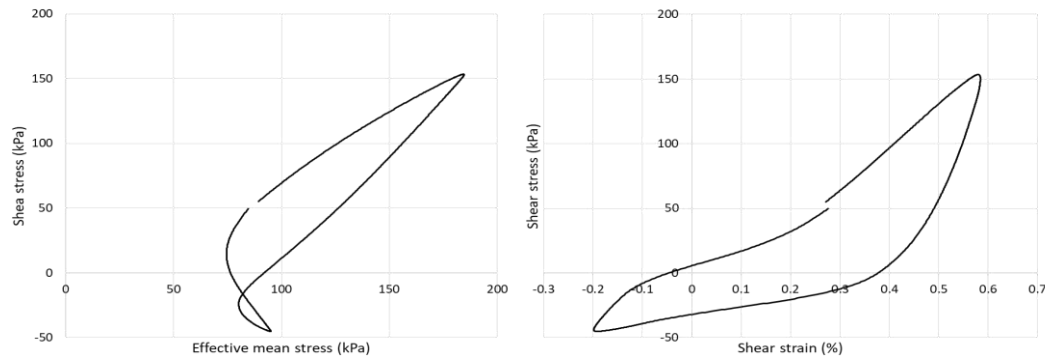


Figure 2. Measured effective stress path (or indirectly shear induced pore pressure) and shear strain during a single cycle ($N = 9$) in a undrained triaxial test of a dense North Sea sand.

Some potential improvements of the Sanisand model [4] are proposed including features as stress induced anisotropic (small strain) elastic stress-strain relationship, stress path dependent phase transformation line, cyclic degradation of the hardening function , etc.

3. Explicit strain accumulation models

One alternative to incremental (implicit) models is to use explicit models where the measured responses are described by data in cyclic contour diagrams (Figure 1) as the Partially Drained Accumulation Model (PDCAM) [5] or a set of predefined independent empirical equations as the High-Cycle Accumulation (HCA) model [6]. Advantages, limitations and potential improvements of these models are also presented in the paper.

4. Objective

The main purpose of the paper is to give input and motivations for further developments of more accurate soil models for the complex behaviour of water saturated dense sand subjected to cyclic loading that can be used in design of offshore foundations in dense sand.

5. References

- [1] Andersen, K.H. (2015). Cyclic soil parameters for offshore foundation design. *Proc., Int. Symp. on Frontiers in Offshore Geotechnics, ISFOG*, Oslo, Norway, June 2015.
- [2] Wichtmann, T. & Triantafyllidis, T. (2016). An experimental data base for the development, calibration and verification of constitutive models for sand with focus to cyclic loading. Part II: tests with strain cycles and combined cyclic and monotonic loading. *Acta Geotechnica*, **11**, 763-774.
- [3] Dahl, B.M., Løyland, M.S. & Jostad, H.P. (2018). Interpretation of cyclic behavior of a saturated dense sand within an elasto-plastic framework. *To be presented at NUMGE2018*, Porto, Portugal
- [4] Dafalias, Y. & Manzari, M. (2004). Simple plasticity sand model accounting for fabric change effects. *Journal of Engineering Mechanics*, **130** (6).
- [5] Jostad, H.P., Grimstad, G., Andersen K.H. & Sivasithamparam, N. (2015). A FE procedure for calculation of cyclic behaviour of offshore foundations under partly drained conditions. *Proc., Int. Symp. on Frontiers in Offshore Geotechnics, ISFOG*, Oslo, Norway, June 2015.
- [6] Niemunis, A., Wichtmann, T. & Triantafyllidis, T. 2005. A high-cycle accumulation model for sand. *Computers and Geotechnics*; **32**. No. 4, 245–263.

PARTICLE/PORE SIZE DISTRIBUTION & MICROSTRUCTURE OF SATURATION – KEY ELEMENTS FOR RATIONAL DESCRIPTION OF MECHANICAL BEHAVIOUR OF UNSATURATED SOILS

G.N. Pande¹, S. Pietruszczak² and Min Wang³

¹ *Swansea University, Swansea SA1 8EN*

² *McMaster University, Hamilton, Ont., Canada*

³ *Rockfield Software Ltd. Swansea SA1 8AS*

Modelling the mechanical response of unsaturated soils is much more complex and challenging than that of dry or saturated soils. In the past few decades, many researchers have attempted to modify and extend existing models, in a rather ad-hoc manner, by incorporating additional state parameters such as suction (S), its variation with degree of saturation (S_r) and volumetric strain (ϵ_v). These developments, however, ignore an important aspect of the behavior of unsaturated soils, viz. microstructure of saturation. This paper describes how the Particle Size Distribution (PSD) or Pore Size Distribution (POSD) and micro-structure of saturation play a crucial role in the determining deformation and failure of unsaturated soils. It is shown that mechanical response of two soils having the same initial conditions and S_r but different PSDs can be different. This difference, of course, disappears when soil is either dry or fully saturated.

Unsaturated soil as a composite material

From the point of view of mechanics, unsaturated soil is a composite material with soil skeleton, water, air as its constituents. In addition, there are three interfaces, viz. skeleton/water, skeleton/air and water/air. Whilst influence of surface energy at the skeleton/air interface can be neglected, influence of surface tension acting at the water/air interface and contact angle for water/skeleton interface cannot be ignored. Fig. 1 shows schematically how a load (isotropic stress) imposed on an unsaturated soil is shared by its constituents. The surface tension acting on the water menisci adhering to the soil particles induces an isotropic state of stress, i.e. suction (S), which can be given by:

$$S = \frac{A_{wa}T}{n(1-S_r)} \quad (1)$$

where, A_{wa} is area of water-air interface per unit volume of the soil (1/m), T is unit surface tension (kN/m) of water and n is the porosity of the soil. Here, contact angle of water with particles is taken as zero. A_{wa} plays a crucial role in the assessment of suction and it depends on the PSD and microstructure of saturation. Three idealized micro-structures of saturation can be visualised. For soils at high degree of saturation, the water phase is continuous but air phase is discontinuous (Type A). Here, air is in the form of isolated bubbles and this micro-structure is likely to occur at degrees of saturation within the range $0.90 < S_r < 1$, and that too only in the wetting phase. For soils at medium degree of saturation ($0.30 < S_r < 0.80$), water and air phases are both continuous (Type B). The range of applicability of this micro-structure is comparatively large and it takes place in wetting as well as drying phase. Finally, for soils at low degree of saturation ($0 < S_r < 0.30$), air phase is continuous, while water phase is discontinuous. This microstructure, known as ‘pendular’, can occur only during ‘drying’ stage. The limits of degree of saturation for the types of microstructure given above are indicative. Moreover, the transition from one microstructure to the other is unlikely to be smooth as hydraulic instabilities arise in change from one type to the other. Like all composite materials, unsaturated soils have initial stresses i.e. initial suction (eq. 1), which in turn depends on previous loading/unloading history as well as POSD, initial value of S_r and microstructure of saturation.

Interpretation of ‘constant suction’ tests

A large number of the so called ‘constant suction tests’ carried out at various degrees of saturation, have been reported in the literature [1]. A constant difference between air pressure ($p_a >$ atmospheric pressure) and pore water pressure ($p_w = 0$) is maintained in the sample. It is believed by many experimentalists that these tests are unique and are neither the so called ‘drained’ or ‘undrained’ tests. The authors of this paper are of the opinion [2] that most constant suction tests are ‘drained’ tests and their results can be interpreted based on established principles of soil mechanics, provided the influence of initial suction (S_0) and its evolution is accounted for. Moreover, in normal engineering problems, soil elements are subjected to strains not exceeding 20%. If initial micro-structure of saturation is of Type B, the sample tested at $0.30 < S_r < 0.80$ will not get fully saturated and will not experience any excess pore pressure. This implies that soil element is ‘drained’ and suction acts simply as an additional confining pressure. Moreover, water content within the sample is constant. Invoking phase relation, it can be shown [2] that S_r is simply a function of strain imposed by suction S . Some experimentalists claim that they observe water coming out of the samples in constant suction tests. In view of the authors, what they are observing is ‘end effect’ as the sample is not homogenous. Moreover, for water to flow, a hydraulic gradient is required which does/should not exist.

Influence of PSD/POSD on S_0

The most important factor influencing S_0 and subsequent evolution of suction is A_{wa} , which depends on PSD/ POSD and microstructure of saturation. SWRC can be computed for different packing of uniform sized grains [3]. Dividing PSD in various small intervals and adopting mean particle size within the interval, SWRC can be computed for any soil and is shown to match experiments. To demonstrate the influence of the gradation curve on S_0 , we choose two soils (A and B) with the same mechanical properties of soil skeleton, the same initial void ratios but different gradation curves. For soil A, the D_{10} , D_{30} and D_{60} are 0.003, 0.020 and 0.100 mm. For soil B, they are 0.006, 0.059 and 0.140 mm respectively. Computed SWRCs for the two soils are shown in Fig. 2 where wide difference in the values of S_0 is seen for $0.30 < S_r < 0.80$.

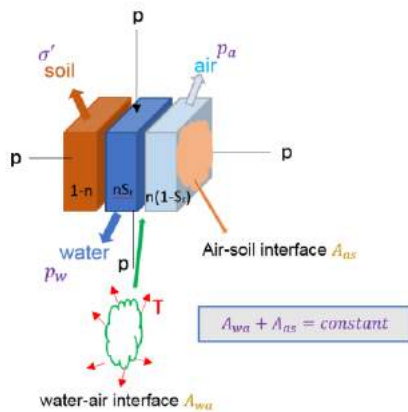


Fig. 1 Schematic of unsaturated soil (unit volume)

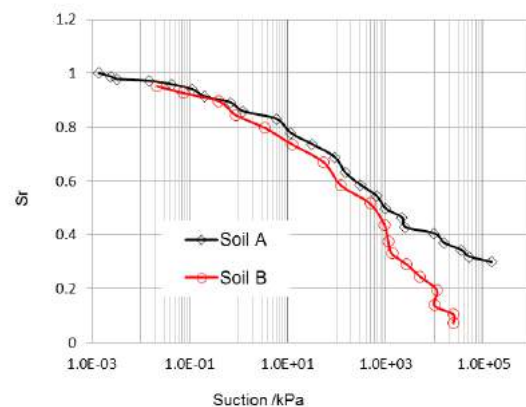


Fig. 2 Computed SWRC of the two soils

References

- [1] Sivakumar, V. (1993) A critical state framework for unsaturated soil, Ph.D. Thesis, University of Sheffield, UK.
- [2] Pande, G. & Pietruszczak, S. (2015). On Unsaturated Soil Mechanics – Personal Views on Current Research. *Studia Geotechnica et Mechanica*, 37(3), 73-84.
- [3] Pande, G.N., Pietruszczak, S., Wang M. Incorporation of gradation curve in the description of mechanical behaviour of unsaturated soils, (Submitted to *Intl. Jl. Geomechanics*).

INFLUENCE OF GRADING ON SHEAR STIFFNESS – THE SIGNIFICANCE OF ACCURATE DESCRIPTION OF PARTICLE SIZE DISTRIBUTIONS

*D. Barreto*¹

¹ *Edinburgh Napier University, Edinburgh, United Kingdom*

1. Introduction

Various relationships between grading parameters and shear stiffness have been proposed. For example, Wichtmann & Triantafyllidis [1] to relate the coefficient of uniformity ($c_u=d_{60}/d_{10}$), to the shear stiffness. Menq [2] also used the mean particle diameter (d_{50}) in addition to c_u to estimate the shear stiffness. Considering that parameters such as c_u and d_{50} only refer to specific fractions of the PSD, Sun et al [3] proposed a new (c_g) parameter that considers the entire shape of the PSD. They then used c_g to estimate shear stiffness values and argued that this parameter was better than other existing ones to predict shear stiffness values.

Although, the work by Sun et al [3] considers the entire PSD for the calculation of c_g , it shares a deficiency with the existing ones; they cannot easily consider variations in PSD with time. This is important because in geotechnical applications there are phenomena such as internal erosion, dissolution, degradation and crushing that produce changes in PSD and therefore changes in shear stiffness. Furthermore, c_u , d_{50} and c_g relate only to the shape of the PSD, but have no link with physical properties and therefore lack a definite physical meaning that can be used to interpret stiffness evolution.

2. Grading entropy coordinates (and inter-particle contact force entropy coordinates)

In the context of grading, the meaning of the term ‘entropy’ refers to a ‘multiplicity of the microstates of a system’ [5]. Statistical entropy allows the microscopic configuration of a system to be described, in this case the representation of a particle size distribution, as a coordinate pair, which then plots as a single point in a grading entropy diagram. A vectorial depiction of a change in grading, rather than a family of distribution curves, is then available. The grading entropy coordinates are the relative base entropy A, and the normalised entropy increment B. The parameter A is a measure of the skewness or symmetry of a particle size frequency distribution, while B is a measure of the kurtosis or peakiness of a particle size frequency distribution. Further details are discussed elsewhere [6-7].

As a mathematical concept, the coordinates A and B can also be used to evaluate the characteristics of the magnitude of normal contact forces which are obtained from DEM simulations. It can be postulated that these force entropy coordinates may be related to grading entropy, but this is out of scope for this study. The emphasis here is not on the processes that the methodology can represent (i.e. dissolution, erosion, breakage, etc.) but in the concept of entropy coordinates and their relationship with initial shear stiffness.

3. Initial shear stiffness and its relationship with grading entropy coordinates.

Following the ideas by [3] Figure 1 illustrates the evolution of the normalised initial shear stiffness obtained from resonant column tests on silica sands by [1]. The different symbols represent different mean particle diameters (d_{50}). There are two sets of data, one for tests at 100 kPa confining pressure (above) and the other one at 400 kPa (below). Note that a void ratio function $[(2.17-e)^2/(1+e)]$ has been used. Independently of stress level, there is a linear relationship between the relative base entropy (A) and initial shear stiffness. This is in contrast to the work in [1] and [3],

where non-linear relationships have been found using a similar approach. Physically however, Figure 1 illustrates that G is a function of the symmetry of the PSD.

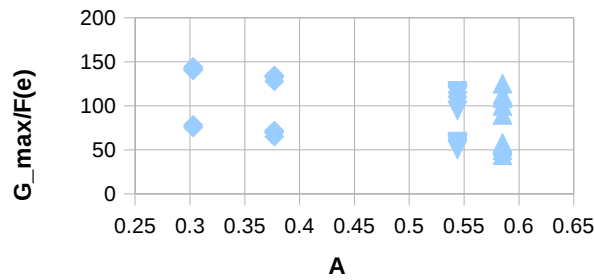


Figure 1. Relationship between relative base entropy and initial shear stiffness

4. Contact force entropy and stress-strain response.

The results of a set of DEM simulation of triaxial compression tests with different initial densities is presented in Figure 2. There is a significant amount of information of such a diagram, here it is highlighted that each test starts at different initial points (dependent on density); and that all tests converge into a single point at large strain. In other words, the magnitude of contact forces and entropy coordinates are suitable to understand the mechanics of critical states.

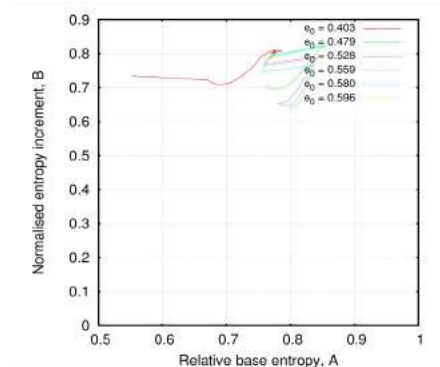


Figure 2. Entropy diagram for a set of DEM simulations of triaxial compression tests

5. References

- [1] Wichtmann, T. and Triantafyllidis, T. (2013). *Stiffness and damping of clean quartz sand with various grain-size distribution curves*. *Journal of Geotechnical and Geoenvironmental Engineering*, **140**(3), 293–320.
- [2] Menq, F. Y. (2003). *Dynamic properties of sandy and gravelly soils*. Doctoral dissertation. Austin, TX, USA: The University of Texas at Austin
- [3] Sun, Y., Shen, Y. and Chen, C. (2018), A grading parameter for evaluating the grading-dependence of the shear stiffness of granular aggregates. *Particuology*. <http://dx.doi.org/10.1016/j.partic.2017.05.006>
- [4] Lorincz, J., Imre, E., Galos, M., Trang, Q. P., Rajkai, K., Fityus, S. & Telekes, G. (2005). Grading entropy variation due to soil crushing. *Int. J. Geomech.* **5**(4), 311–320,
- [5] Warn, J. R. W. 1969. *Concise chemical thermodynamics*. London, UK: Van Nostrand Reinhold.
- [6] McDougall, J.R, Imre, E., Barreto, D. and Kelly, D. 2013b. *Volumetric consequences of particle loss by grading entropy*. *Géotechnique*, **63**(3): 262–266.
- [7] Lörincz, J. (1986). *Grading entropy of soils*. PhD thesis, Technical Sciences, Technical University of Budapest, Budapest, Hungary

A SINGLE HARDENING ELASTOPLASTIC MODEL FOR DESCRIBING STRESSES PATH DEPENDENCY OF PLASTIC FLOW

T. Nakai¹ and H.M. Shahin²

¹ Geo-Research Institute, Nagoya, Japan

² Islamic University of Technology, Gazipur, Bangladesh

According to the classic plasticity, the direction of plastic flow (direction of plastic strain increments) is independent of the direction of stress increments. This means that the stress-dilatancy relation (stress ratio-plastic strain increment ratio relation) is not influenced by the stress path. However, it was experimentally pointed out that the stress-dilatancy relation of soils depends on the stress path, except for the stress condition near or at failure. To describe such behavior, usually double hardening theory or tangential plasticity theory are employed. However, these theories need, plural sets of yield functions and hardening parameters and additional coefficients of tangential plastic modulus, which make constitutive model complex and needs more material parameters.

Fig. 1 shows the observed stress ratio- strain increment ratio relation of normally consolidated clay under various stress paths in diagram (a). Diagram (b) shows the results plotted as $\eta=q/p$ vs. $d\varepsilon_v^p/d\varepsilon_d^p$ using ordinary stress and strain increment invariants. Diagram (c) shows the same data using the stress and strain increment invariants based on the t_{ij} concept ($X=t_s/t_N$ vs. $d\varepsilon_N^*/d\varepsilon_S^*$) [1]. The results in diagram (b) depend on not only the magnitude of intermediate principal stress but also the stress paths. It is seen from diagram (c) that even using the t_{ij} concept, the results depend on stress path except near and at peak strength, though there is not much difference between the triaxial compression and extension conditions.

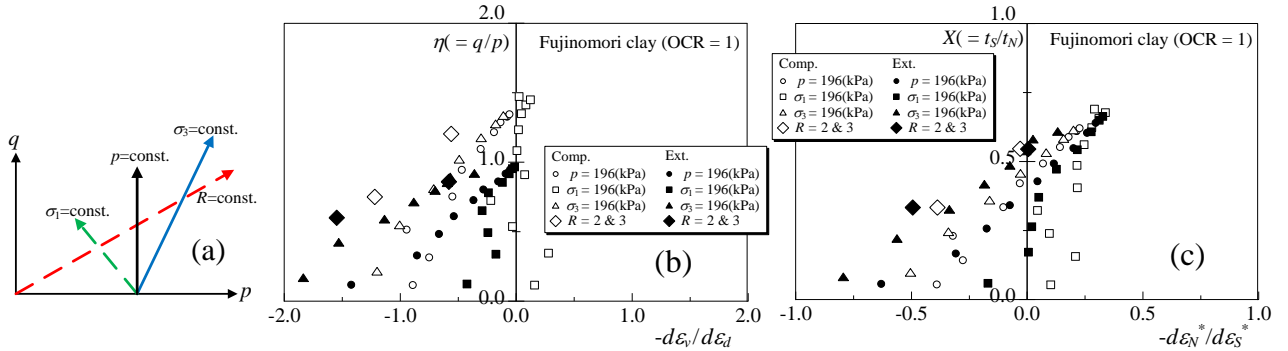


Fig. 1 Observed stress-dilatancy relations

The authors and others proposed a 3D elastoplastic model which is called the Subloading t_{ij} model [2, 3]. In this model, the influence of intermediate principal stress on the soil behavior is considered by the t_{ij} concept [1], the influence of density and confining pressure is considered by introducing the Subloading surface concept [4], In addition, to describe the behavior of naturally deposited soil, imaginal density is introduced as a state variable and its decay rule is assumed. However, the above-mentioned stress path dependency of plastic flow is not explained in a robust fashion. In the present research, to describe simply the stress path dependency on the direction of plastic flow, the authors present a rational formulation by splitting the plastic strain increment.

According to the Subloading t_{ij} model [2] obeying the associated flow (AF) rule in t_{ij} space, the plastic strain increment and the increment of plastic volumetric strain are calculated as

$$d\varepsilon_{ij}^p = \Lambda \frac{\partial F}{\partial t_{ij}} = \frac{dF}{h^p} \frac{\partial F}{\partial t_{ij}}, \quad d\varepsilon_v^p = d\varepsilon_{kk}^p = \frac{dF}{h^p} \frac{\partial F}{\partial t_{kk}} \quad (\text{where, } F : \text{yield function, } h^p : \text{plastic modulus}) \quad (1)$$

Now, the increment of volumetric strain in Eq. (1) can be expressed as follows, by adding two terms which are canceled each other:

$$d\varepsilon_v^p = \frac{dF}{h^p} \frac{\partial F}{\partial t_{kk}} = \frac{dF}{h^p} \frac{\partial F}{\partial t_{ij}} - \left\langle \frac{\partial F}{\partial t_{kk}} t_N \right\rangle^2 A \frac{dt_N}{t_N} \frac{\partial F / \partial t_{kk}}{\partial F / \partial t_{kk}} + \left\langle \frac{\partial F}{\partial t_{kk}} t_N \right\rangle^2 A \frac{dt_N}{t_N} \frac{\delta_{kk}}{3} \quad (dt_N : \text{increment of mean stress } t_N) \quad (2)$$

where $\langle (\partial F / \partial t_{kk}) t_N \rangle$ is a non-negative function which is unity at isotropic stress condition and decreases with the increase of stress ratio. A is a non-dimensional function which represents the inverse of the stiffness of the isotropic component. Referring to Eq. (2), the plastic strain increment can be given by the following form, where the plastic increment is expressed by the summation of two components – i.e., component (AF) which satisfies the associated flow rule in t_{ij} space and the component (IC) which is produced isotopically with the change of mean stress t_N , regardless that the increment of plastic volumetric strain increment is the same as that in Eq. (1).

$$d\varepsilon_{ij}^p = \left\{ \frac{dF}{h^p} - \left\langle \frac{\partial F}{\partial t_{kk}} t_N \right\rangle A dt_N \right\} \frac{\partial F}{\partial t_{ij}} + \left\langle \frac{\partial F}{\partial t_{kk}} t_N \right\rangle^2 A \frac{dt_N}{t_N} \frac{\delta_{ij}}{3} = d\varepsilon_{ij}^{p(AF)} + d\varepsilon_{ij}^{p(IC)} \quad (3)$$

Here, although the plastic strain increment is divided into two components, the combined plastic volumetric strain, which is the hardening parameter, is always the same as that of the model obeying associated flow rule. As the results, the loading condition is also the same as that of the model obeying associated flow rule, and no additional material parameter is necessary. Further, the loading condition of the present model is the same as that of model obeying associated flow rule. Fig. 2 shows the yield surface and the development of the plastic strain increments schematically. For example, when stress changes from current state A to states B or C which are on the same successive yield surface, total plastic strain increment are given by the summation of (AF) component and (IC) component. Blue arrows correspond to the case of AB ($dt_N < 0$), and red arrows correspond to the case of AC ($dt_N > 0$).

Fig.3 shows the analytical results corresponding to the observed arrangement in Fig. 1(c). The analytical results of Fig.3 in which the stress path dependency is properly taken into consideration describe well the observed results. The thick gray curve in Fig.3 shows the relation obtained from the yield surface and normality rule, which is satisfied by the plastic strain increment obeying the associated flow rule.

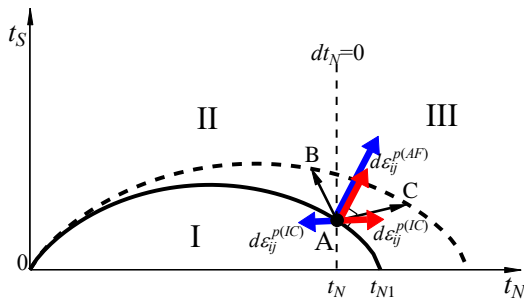


Fig. 2 Yield surface and plastic strain increment

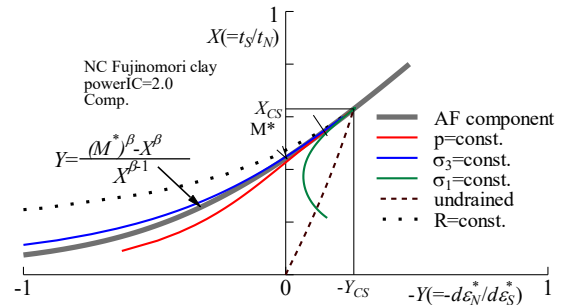


Fig. 3 Calculated stress-dilatancy relation

References:

- [1] Nakai, T. & Mihara, Y (1984). A new mechanical quantity for soils and its application to elastoplastic constitutive models, *Soils and Foundations*, **24**(2), 82-94.
- [2] Nakai, T., Shahin, H.M., Kikumoto, M., Kyokawa, H., Zhang, F. & Farias, M.M. (2011). A simple and unified three-dimensional model to describe various characteristics of soils, *Soils and Foundations*, **51**(6), 1149-1168.
- [3] Nakai, T. (2012). *Constitutive Modeling of Geomaterials: Principles and Applications*, CRC Press, Boca Raton/London/New York.
- [4] Hashiguchi, K. (1980), Constitutive equation of elastoplastic materials with elasto-plastic transition, *Jour. of Appli. Mech.*, ASME, **102**(2), 266-272.

APPROXIMATION OF MOHR ENVELOPE FOR THE GENERALIZED HOEK-BROWN CRITERION

Y.-K. Lee¹ and S. Pietruszczak²

¹ *Kunsan National University, Gunsan, Jeonbuk, South Korea*

² *McMaster University, Hamilton, Ont., Canada*

1. Introduction

The Hoek-Brown (H-B) criterion [1], which defines the maximum principal stress (σ_1) at failure for a given minor principal stress (σ_3), is an empirical failure condition that has been widely accepted in rock mechanics and used in many practical engineering projects, such as underground tunnel excavations, design of slopes in rock formations, etc. Its latest version, referred to as the generalized Hoek-Brown (GHB) criterion [2], incorporates the strength parameters m_b , s and a , which are determined from some empirical formulas in conjunction with the Geological Strength Index (GSI) and the disturbance factor (D), the latter reflecting the rock mass disturbance due to excavation or stress relaxation. Despite its popularity, the GHB criterion has a disadvantage in that it cannot provide the corresponding Mohr failure envelope, except for $a=0.5$, i.e. $GSI=100$. This limits its applicability in standard geotechnical analysis related to assessment of slope stability and/or bearing capacity of rock foundation. In general, these types of problems are solved by either the limit equilibrium method or the limit analysis employing the strength formula defined in terms of normal and shear stress acting on a potential fracture plane.

In view of this, in order to broaden the application of the GHB criterion, this work presents an analytical representation of an approximate Mohr envelope corresponding to the GHB criterion. The idea behind the formulation is to best-fit the quadratic or cubic polynomial to the function that defines the dependence of normal stress on the instantaneous friction angle. For the polynomial curve fitting, the principle of the orthogonal projection of a function onto a function subspace is invoked. Subsequently, by solving the approximate equation for the sine of friction angle, an explicit formula for the critical value of shear stress (τ) associated with a given normal stress (σ) acting on the failure plane can be established.

2. Specification of approximate Mohr failure envelope for the GHB criterion

By invoking the stress measures P and Q normalized with respect to the uniaxial strength of the intact rock material (σ_{ci}) [3],

$$P = \frac{\sigma}{m_b^{a/(1-a)} \sigma_{ci}} + \frac{s}{m_b^{1/(1-a)}}, \quad Q = \frac{\tau}{m_b^{a/(1-a)} \sigma_{ci}} \quad (1)$$

it can be shown that the following two equations hold for the Mohr envelope in P - Q space

$$\tilde{P} = \left(\frac{1}{x} - 1 \right) H(x) \quad \text{with} \quad \tilde{P} = \frac{2P^{1-a}}{a}, \quad H(x) = \left(1 + \frac{x}{a} \right)^{1-a} \quad (2)$$

$$Q = \left(\frac{a}{2} \right)^{a/(1-a)} \frac{\sqrt{1-x^2}}{2} \left(\frac{1}{x} - 1 \right)^{a/(1-a)} \quad (3)$$

where $x = \sin(\phi_i)$ and ϕ_i is the instantaneous friction angle.

If $H(x)$ in Eq. (2) is best-fitted by a linear or quadratic polynomial, Eq. (2) reduces to a quadratic or cubic equation, respectively. Solving the resulting equation for x and substituting the solution into Eq. (3) yields an approximate Mohr failure envelope of the GHB criterion. Fig. 1 shows the results corresponding to $GSI=80$, which indicate that the quadratic polynomial approximates the original curve $H(x)$ very well.

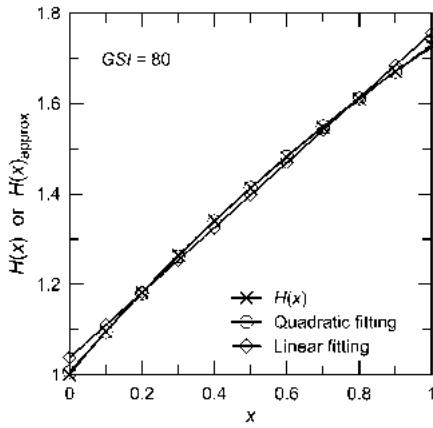


Fig. 1. Best-fit approximations of $H(x)$ with linear and quadratic polynomials

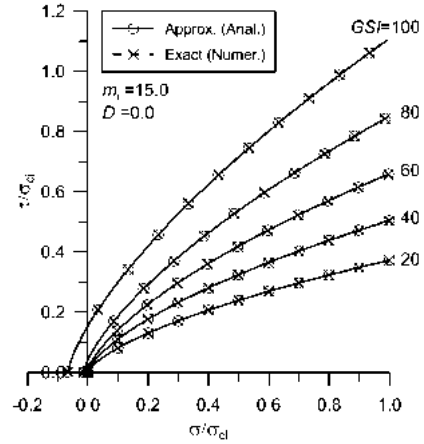


Fig. 2. Approximate Mohr envelopes vs. the exact envelopes (evaluated numerically)

3. On the accuracy of the approximate Mohr envelope

Fig. 2 shows the approximate Mohr envelopes (for $m_i=15$ and $D=0.0$) based on the quadratic fitting of $H(x)$, together with the exact ones for five different values of GSI , i.e. 20, 40, 60, 80 and 100. The results clearly show that the approximate Mohr envelopes are very accurate; i.e. the percentage prediction error is less than 0.2% in the entire range of considered GSI values.

4. Concluding remarks

In this work, an explicit analytical formula for Mohr failure envelope which closely approximates the GHB criterion is established. The approach is based on best-fitting the equation which relates the normal stress and the instantaneous friction angle, by the linear or quadratic polynomial. It is shown that the shear strength prediction by the approximate Mohr envelopes is very precise.

5. Acknowledgement

This research was supported by Basic Research Program through the National Research Foundation of Korea (NRF) funded by the Ministry of Education (NRF-2016R1D1A1A09917357).

6. References

- [1] Hoek, E. & Brown, E.T. (1980). *Underground Excavations in Rock*. Institution of Mining and Metallurgy, London.
- [2] Hoek, E., Carranza-Torres, C.T. & Corkum, B. (2002). Hoek-Brown failure criterion -2002 edition. In: Proc. 5th North American Rock Mechanics Sympo., Toronto, **1**, 267-273.
- [3] Rojat, F., Labiouse, V. & Mestat, P. (2015). Improved analytical solutions for the response of underground excavations in rock mass satisfying the generalized Hoek-Brown failure criterion. *Int. J. Rock Meth. Min. Sci.*, **79**, 193–204.

EXISTENCE OF UNIQUE FABRIC STATE SURFACE FOR GRANULAR MEDIA AT CRITICAL STATE

P. Guo¹, S. Zhou² and J. Shi¹

¹ *McMaster University, Hamilton, Ont., Canada*

² *Tongji University, Shanghai, P. R. China*

1. Introduction

The stress-strain behavior of a granular material is affected by its internal structure, which is related to the spatial connectivity of particles and the force chain network. Consequently, the concept of the critical state in granular soils needs to make proper reference to the fabric structure that develops at critical state. The results of DEM simulations for dense polydisperse system of elastic spheres reveal that a surface of the fabric state at the critical state can be uniquely defined. On the deviatoric plane, the critical state fabric surface can be expressed as an inverted Lade's surface (Thornton, 2000; Barreto and O'Sullivan, 2012, Zhao and Guo 2013 and Shi and Guo, 2017). Zhao and Guo (2013) further find that, at the critical state, the joint invariant between the deviatoric stress and the fabric tensor can be expressed as $s_{ij}F_{ij} = \alpha p^{0.894}$ in which $F_{ij} = (15/2)(\phi_{ij} - \delta_{ij}/3)$ and $\phi_{ij} = \langle n_i n_j \rangle$ with \mathbf{n} being the unit contact normal vector. It has also been known that the anisotropic behavior of granular materials may not uniquely depend on the entire contact network, since not all contacts play the same role in resisting material deformation. According to Radjai *et al.* (1996), the entire contact network can be partitioned into a sub-network of "strong contacts" and that of "weak contacts". In this study, we examine the fabric state in the strong and weak sub-networks of a granular material at the critical state, through both micromechanical analysis and DEM simulations.

2. Micromechanical analysis

The micromechanical description of the stress tensor within a REV with volume V of spherical particles can be related to the contact forces \mathbf{f} and branch vectors \mathbf{l} as

$$\sigma_{ij} = \frac{1}{V} \sum_{k=1}^{N_c} \mathbf{f} \otimes \mathbf{l} = \frac{N\hat{l}}{V} \int_{\Omega} E(\mathbf{n}) f_i n_j d\Omega \quad (1)$$

where \hat{l} is the average length of branch vector, $E(\mathbf{n})$ is the distribution probability density function (PDF) for the contact normal. In most cases it is sufficient to assume $E(\mathbf{n}) = (1/4\pi)(\delta_{ij} + F_{ij})n_i n_j$ with $F_{ii} = 0$. Different approaches have been proposed to obtain the local contact forces from the stress tensor (Emeriault and Cambou, 1996). Based on the representation theorem, the local contact force can be generally expressed as an isotropic function of \mathbf{n} and $\boldsymbol{\sigma}$:

$$f_i(\mathbf{n}) = A\sigma_{ij}n_j + B(\sigma_{kl}n_k n_l)n_i + C\sigma_{kk}n_i \quad (2)$$

with A, B and C being constants. Substitution of Eq. (2) into Eq. (1) yields

$$s_{kl}F_{kl} = 15K_{\phi}p/2 \quad \text{or} \quad s_{kl}\phi_{kl} = K_{\phi}p \quad (3)$$

in which $K_{\phi} = (A + B + 3C - 1)/(A + B)$. Obviously, Eq. (3) is applicable to the critical state.

2. Findings from DEM simulations

Discrete element simulations are carried out to investigate the evolution of fabric in different force chain networks in initially isotropic granular assemblies along various imposed stress paths.

DEM simulations were performed on cubic specimens consisting of approximately 20000 elastic spheres with the diameters ranging from 0.2mm to 0.6mm and the mean particle diameter of $d_{50} = 0.4\text{mm}$. A linear force-displacement contact law was employed where the contact behavior was governed by the normal stiffness k^n , tangential stiffness k^s and the inter-particle friction coefficient $\mu = 0.5$. The tangential and the normal contact stiffness at particle contacts were assumed as $k^n / d_{50} = k^s / d_{50} = 1000\text{MPa}$. Figure 1 presents the envelope of the stress states and fabric tensor of the entire contact network at the critical state. The stress envelope can be described as $I_1^3 / I_3 = 32.64$ and the fabric tensor satisfies Eq. (3) with $K_\phi = 0.040$ when $p' = 300\text{kPa}$. As p' was increase to 1000 kPa, $K_\phi = 0.048$. The critical fabric state can also be reasonably described by the iverted Lade's surface $I_{1\phi}^3 / (2I_{1\phi}I_{2\phi} - 2I_{3\phi}) = \eta^*$ (Thornton, 2000; Zhao and Guo, 2013) with $\eta^* = 1.8008 \pm 0.0001$. It should be noted that $\eta^* = 1.8$ corresponds to an isotropic state.

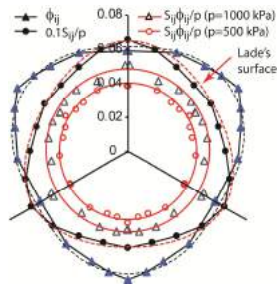


Figure 1: State surfaces of stress and fabric tensor in deviatoric plane

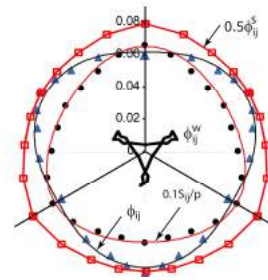


Figure 2: State surfaces of stress, fabric tensors in different contact networks

The fabric tensor, ϕ_{ij}^s , of the strong subnetwork, which is the bearing network toward loading, can be related to the applied stresses uniquely via $\phi_1^s : \phi_2^s : \phi_3^s = \sigma_1 : \sigma_2 : \sigma_3$, which implies that the principal directions of ϕ_{ij}^s coincide with the principal stress directions. At the critical stress state, the deviator of fabric tensor of the strong subnetwork is much larger than that of the whole contact network. When plotted in the deviatoric plane, the fabric state of the strong network can be approximately expressed as a Lade's surface, as shown in Figure 3. The weak contact sub-network does not have very strong internal structure and can be practically considered as nearly isotropic

References

- [1] Barreto, D. And O'Sullivan, C. (2012) The influence of inter-particle friction and the intermediate stress ratio on soil response under generalised stress conditions. *Granul Matter* 14(4): 505–521.
- [2] Emeriault, F. and Cambou, B. (1996). Micromechanical modelling of anisotropic non-linear elasticity of granular medium. *Int. J. Solids Structures* 33(18), 2591-2607.
- [3] Radjaï, F., Jean, M., Moreau, J.-J. and Roux, S. (1996). Force distributions in dense two-dimensional granular systems. *Phys Rev Lett* 77(2), 274–277.
- [4] Shi, J. And Guo, P. (2017). Fabric evolution of granular materials along imposed stress paths. Submitted to *Journal of Engineering Mechanics*.
- [5] Thornton, C. (2000). Numerical simulations of deviatoric shear deformation of granular media. *Geotechnique* 50(1), 43-53.
- [6] Zhao, J. and Guo, N. (2013). Unique critical state characteristics in granular media considering fabric anisotropy. *Geotechnique* 63(8), 695–704.

STRESS-DILATANCY IN BARODESXY

*G. Medicus*¹ and *B. Schneider-Muntau*¹

¹ *University of Innsbruck, Innsbruck, Austria*

Asymptotic behavior of soil deserves particular attention: If soil is deformed with a proportional strain path, the resulting stress path asymptotically approaches a proportional stress path [1, 2, 3]. In the constitutive model *barodesy* – introduced by Kolymbas [4] – the link between proportional strain paths and proportional stress paths is an equation, which acts as a *stress-dilatancy relation*:

$$\mathbf{R} = -\exp(\alpha \mathbf{D}^0) \quad (1)$$

where the scalar quantity α is a function of $\text{tr} \mathbf{D}^0$ (dilatancy), \mathbf{D}^0 is the normalized stretching [5, 6].

Stress-dilatancy relations link ratios of strain components with ratios of stress components. This implies that the mobilized friction angle is related to dilatancy: If soil is deformed with a proportional dilatant path, the maximum mobilized friction angle φ_m is larger than the critical friction angle φ_c . This fact is experimentally proven [1, 2, 3] and can be well described with the relation by Chu & Lo [2], which provides similar results as barodesy, see Figure 1.

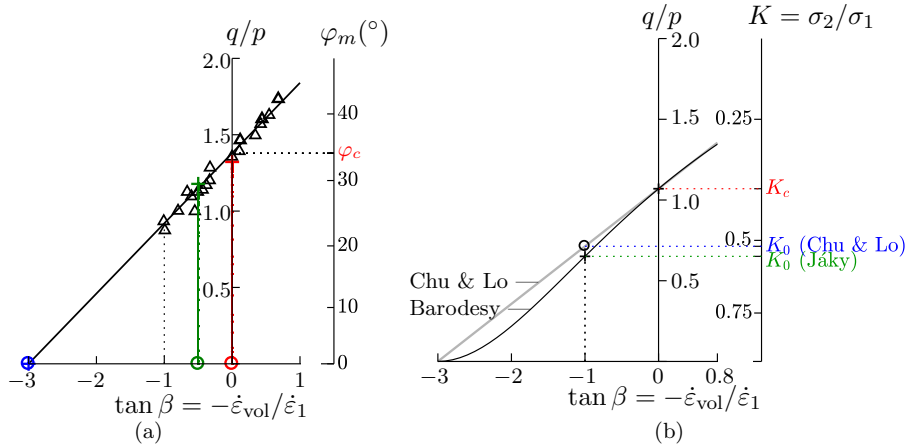


Figure 1. Asymptotic states of triaxial tests: Soil samples are deformed with proportional strain paths. In (a) experimental results of Sydney sand (\triangle , $\varphi_c \approx 34.1^\circ$) are approximated with the relation by Chu & Lo [2]. In (b) Chu & Lo's relation is compared with barodesy [6] for a soil with $\varphi_c = 27^\circ$.

To investigate soil behavior, experiments, e.g. triaxial tests, are carried out. When evaluating stress and strain, the sample is assumed as one single homogeneous element with rectilinear deformation. However, in experimental testing, it is impossible to obtain a perfectly homogeneous sample with a constant void ratio distribution. Tomographic surveys on experiments by Desrues et al. [7] show that shear bands develop from the very beginning of triaxial tests. Therefore a homogeneous deformation, i.e. an element test, is questionable well before the peak.

Finite element simulations on homogeneous samples only result in homogeneous deformations and not in the development shear bands. In order to obtain shear bands, at least one weak element has to be included in the simulation [8, 9]. In this work, we carry out finite element simulations of fine-meshed biaxial tests with barodesy [10, 11] with a normally distributed void ratio over all elements in a narrow range, cf. [12]. The randomly distributed void ratio results in a scatter of dilatancy and

therefore in a scatter of peak strength in the elements. Thus, patterns of shear bands develop from the very beginning of the biaxial test, see Figure 2. We evaluate stress and dilatancy and the pattern of the shear bands with ongoing shear strain.

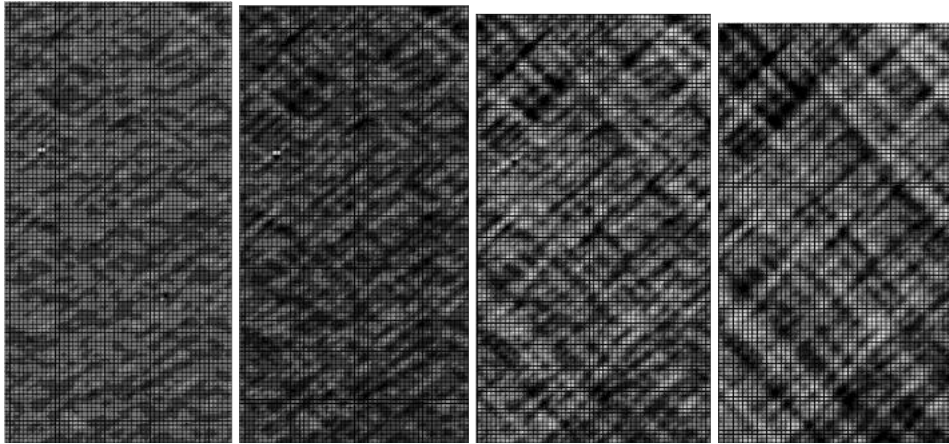


Figure 2. Finite element simulations with barodesy: Shear strain $\sqrt{2/3}(\boldsymbol{\varepsilon} : \boldsymbol{\varepsilon})$ distribution at $\varepsilon_{\text{axial}} \approx 1.7\%$, 2.9% , 4.7% , 6.7% (left to right) is shown, the peak is at $\varepsilon_{\text{axial}} \approx 7.4\%$. The initial void ratio $e_{\text{initial}} = [0.5495 \dots 0.5505]$ is normally distributed.

Acknowledgement The first author is grateful for the financial support by the Austrian Science Fund (FWF): P 28934-N32.

References

- [1] Goldscheider, M. (1967). Grenzbedingung und Fließregel von Sand. *Mechanical Research Communications*, **3**, 463–468.
- [2] Chu, J. and Lo, S.-C. R. (1994). Asymptotic behaviour of a granular soil in strain path testing. *Géotechnique*, **44**, 65–82.
- [3] Topolnicki, M., Gudehus, G., and Mazurkiewicz, B. (1990). Observed stress-strain behaviour of remoulded saturated clays under plane strain conditions. *Géotechnique*, **40**, 155–187.
- [4] Kolymbas, D. (2009). Sand as an archetypical natural solid. Kolymbas, D. and Viggiani, G. (eds.), *Mechanics of Natural Solids*, pp. 1–26, Springer: Berlin.
- [5] Medicus, G. (2014). *Barodesy and its application for clay*. Ph.D. thesis, University of Innsbruck.
- [6] Medicus, G., Kolymbas, D., and Fellin, W. (2016). Proportional stress and strain paths in barodesy. *Int. J. Num. Anal. Meth. Geomech.*, **40**, 509–522.
- [7] Desrues, J. J. M., Mevoli, F., Andò, E., Bésuelle, P., Viggiani, C., Debove, L., Charrier, P., and Toni, J. B. (2017). Localisation precursors in geomaterials? *11th IWBDG2017*, Cyprus, May.
- [8] Schneider-Muntau, B., Chen, C.-H., and Bathaeian, S. M. I. (2017). Simulation of shear bands with Soft PARTicle Code (SPARC) and FE. *Int. J. Geomath.*, **8**, 135–151.
- [9] Medicus, G., Schneider-Muntau, B., and Kolymbas, D. (2018). Second order work in barodesy. *submitted to: Acta Geotechnica*.
- [10] Medicus, G. and Fellin, W. (2017). An improved version of barodesy for clay. *Acta Geotechnica*, **12**, 365–376.
- [11] Gudehus, G., et al. (2008). The soilmodels.info project. *Int. J. Num. Anal. Meth. Geomech.*, **32**, 1571–1572.
- [12] Nübel, K. (2002). *Experimental and Numerical Investigation of Shear Localization in Granular Material*. Ph.D. thesis, Universität Karlsruhe.

STRESS CORROSION CRACKING, MATURING OF CONTACTS, AND TIME EFFECTS IN SILICA SAND

R.L. Michalowski¹, Z. Wang², D. Park¹ and S.S. Nadukuru³

¹ University of Michigan, Ann Arbor, U.S.A.

² Country Garden Holdings Co. Ltd., Guangdong, China

³ Geosyntec Consultants, Keenesaw, GA 30144, U.S.A.

1. Background

Silica sand is known to exhibit time-dependent properties when subjected to sustained loads. A hypothesis was suggested that the key cause of those changes is in the stress corrosion cracking of the textural features at grain surfaces at contacts [1]. Grain-scale experiments were carried out in a custom-designed apparatus [2] to collect evidence in support of the hypothesis. Atomic Force Microscopy was used to quantify the roughness of the grain surfaces (texture).

2. Measurements of grain deflection owed to contact maturing

An apparatus for measuring grain deflection under a sustained load is shown in Fig. 1(a) and an example of results is demonstrated in Fig. 1(b). The primary dependence of the deflection was found to be on the initial roughness of the grain surface. The process associated with stress corrosion cracking was prevalent in the first three weeks after application of the load, and it was termed *contact maturing*. Subsequent experiments on specimens of sand revealed the importance of the presence of moisture and chemistry of the pore fluid on the maturing of contacts.

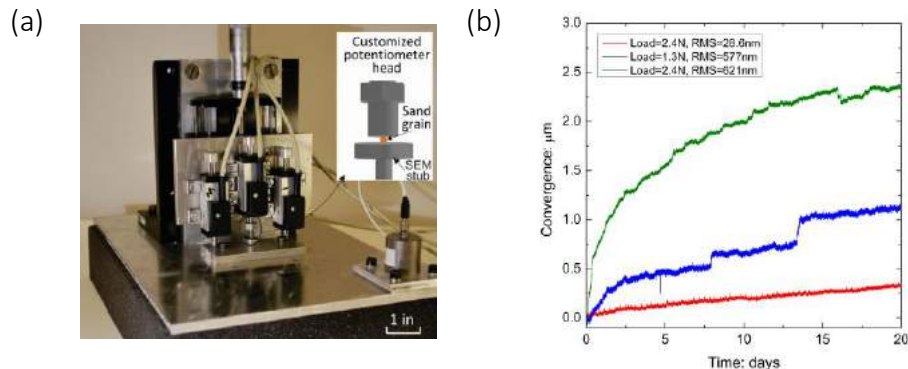


Figure 1. (a) Apparatus, and (b) time-dependent deflection of Ottawa sand grains

The results of grain deflection tests are consistent with the contact maturing hypothesis, but testing has been found challenging due to sensitivity of the process to temperature, moisture, and external vibrations.

3. Modeling

The contact maturing process was modelled using the distinct element method, with an individual grain simulated as an assembly of bonded sub-particles. The bonds are capable of transferring forces and moments, allowing simulations of continua. Once tension above a certain threshold occurs in the bond, stress corrosion cracking begins in the bond, modeled as a time-dependent reduction in the size of the bond [3]. Preliminary calculations indicate that the process of contact maturing may be associated with the evolution of contacts where the number of “micro

force chains” across a nominal contact increases as a result of stress corrosion cracking. This, in turn, leads to an increase in the stiffness of individual contacts, leading to an increase in small-strain stiffness at the macroscopic scale. The latter is a phenomenon observed at the scale of sand deposits, and is often interpreted as a manifestation of sand *ageing*.

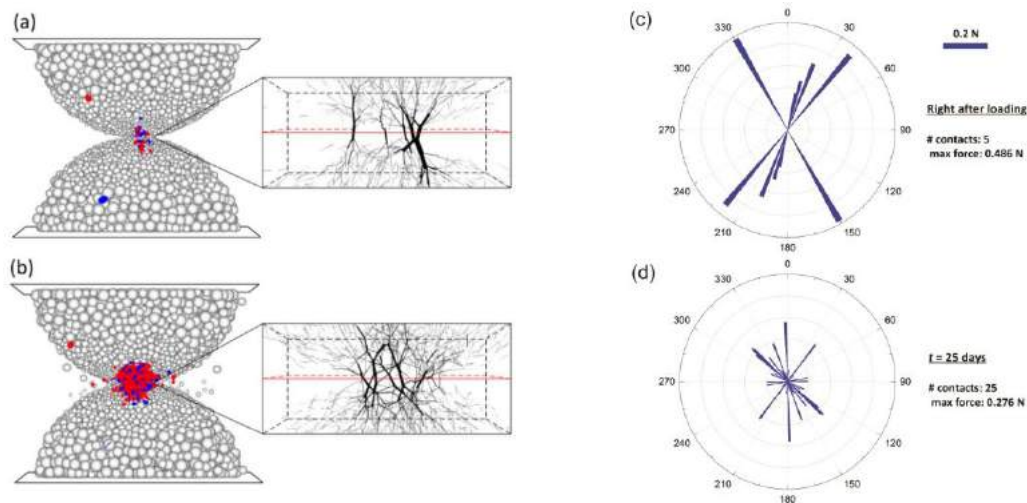


Figure 2. Simulation: (a) Grains in contact at $t = 0$, (b) after 25 days, (c) distribution of contact forces at $t = 0$, and (d) distribution of contact forces after 25 days

A model of two grains in contact is presented in Fig. 2. The micro force chains at the contact immediately after application of the load are shown in Fig. 2(a), and after 25 days of sustained load (2.4 N), in Fig. 2(b). The number of force chains across the interface between two grains increased in that time from 5 to 25, resulting in a more even distribution of forces across the nominal contact, Fig. 2(b,c).

4. Final comment

Results of testing individual contacts are consistent with the hypothesis of contact maturing, indicating static fatigue as the key cause of time-dependent effects in silica sand. The process is sensitive to environmental factors, such as temperature and moisture. Contact maturing is believed to be a key contributor to *ageing* of silica sands. The distinct element approach to modeling grains and contacts is promising; it predicts the evolution of contacts, leading to an increase in the contact stiffness, and the small-strain stiffness in sand. It is expected that this study will allow explaining such phenomena as a delayed increase in cone penetration resistance of sand after compaction by vibratory means, and the time-dependent increase in shaft resistance of displacement piles (*pile setup*).

Acknowledgement

The work presented was supported by the National Science Foundation through grant CMMI-1537222. This support is greatly appreciated.

References

1. Michalowski, R.L., Wang, Z. & Nadukuru, S.S. (2018). Maturing of contacts and ageing of silica sand. *Géotechnique*, **68**, 132-145 (doi:10.1680/jgeot.16.P.321).
2. Wang, Z. & Michalowski, R.L. (2018). An apparatus for testing static fatigue at sand grain contacts. *Geotech. Testing J.*, **41** (doi:10.1520/GTJ20170251).
3. Potyondy, D.O. (2007). Simulating stress corrosion with a bonded-particle model of rock. *Int. J. Rock Mech. Min. Sci.*, **44**, 677-691 (doi:10.1016/j.ijrmms.2006.10.002).

THE MICROMECHANICAL NATURE OF STRESSES IN WET GRANULAR SOILS

R. Wan¹, J. Duriez² and F. Darve³

¹ *University of Calgary, AB, Canada*

² *RECOVER, Irstea, France*

³ *Univ. Grenoble Alpes, 3SR, F-38000 Grenoble, France*

1. Introduction

The question of how wet granular soils as a three-phase (solid, water, air) material behave both mechanically and hydraulically is rather complex due to the presence of interfaces, see e.g. [1]. In essence, these interfaces do not allow us to apply classical mixture theory where only the volumes of the phases are taken into account. This is particularly true in the pendular regime, where surface tension forces within the various interfaces are often not negligible with respect to the other intergranular interactions. The total stress tensor as the average stress within a three-phase granular medium has been formally derived following a comprehensive microscopic formulation to reveal various detailed stress contributions associated with the solid phase, the two immiscible fluid phases and the three interfaces in terms of microstructural interconnects [2]. A capillary stress tensor emerges which is non-spherical in nature and generalizes the isotropic suction term in Bishop's equation, which is known to be unrealistic. Also the χ - parameter in Bishop's equation is elucidated.

2. μ -UNSAT Equation

The point of departure is the homogenization of stresses in partially saturated granular media, recognizing the various contributions of internal forces operating at the microscopic level, i.e.

1. the solid phase stress with the solid volume V_s arising from the various tractions acting on the surface of solid particles, such as fluid pressures, surface tension and contact forces,
2. the distinct air (u_a) and water (u_w) pressures within the corresponding volumes V_a and V_w , and
3. the surface stress [3], $\pi_{ij} = \gamma(n_i n_j - \delta_{ij})$ acting within the air-water interface, where γ as the air-water surface tension, n_i the oriented normal to the interface, and δ_{ij} the Kronecker delta tensor.

The above last item is sufficient to properly describe the surface tension internal forces existing within the air-water interface, including fluid-solid interfaces [2]. Expressing the total stress Σ_{ij} as a volume averaging of the individual stresses from each phase, including the air-water interface as a distinct phase, and following a rather comprehensive microscopic treatment, the μ -UNSAT equation emerges as [2]:

$$\Sigma_{ij} - u_a \delta_{ij} = \sigma_{ij}^{cont} + \sigma_{ij}^{cap}; \text{ with } \sigma_{ij}^{cont} = \frac{1}{V} \sum_{cont} f_i^c \ell_j, \text{ and} \quad (1a)$$

$$\sigma_{ij}^{cap} = -\frac{1}{V} \left[s \left((\mu_{Vw})_{ij} + (\mu_{Sw})_{ij} \right) + \gamma \left((\mu_{Saw})_{ij} + (\mu_{\gamma})_{ij} \right) \right] \quad (1b)$$

Equation (1a) describes, in tensorial form, a Terzaghi-like expression whereby total stress is partitioned into a contact stress σ_{ij}^{cont} arising from the contact forces f_i and a capillary stress σ_{ij}^{cap} due to the air-water mixture as given in Eq. (1b). The latter is microstructure dependent arising from the following microstructural tensors:

$$(\mu_{Vw})_{ij} = V_w \delta_{ij}; (\mu_{Sw})_{ij} = \int_{S_w} n_i x_j dS; (\mu_{Saw})_{ij} = \int_{S_{aw}} (\delta_{ij} - n_i n_j) dS; \text{ and } (\mu_{\gamma})_{ij} = \int_{\Gamma} \nu_i x_j d\ell \quad (2)$$

where x_i is the position of any point on a particle's surface with respect to its centroid, ν_i the tangent to the interface S_{aw} being orthogonal to the contact line contour Γ where air, water and solid meet, n_i the outward normal to the wetted surfaces S_w or the interface S_{aw} , and $s = u_a - u_w$ as suction.

As a tensorial quantity, the capillary stress in the proposed μ -UNSAT equation generalizes the isotropic suction term in Bishop's equation by highlighting various stress contributions proportional to the surface tension, the air-water interface, and the contact lines of length Γ . More importantly, the capillary stress is non-spherical in character, which is at variance with Bishop's equation. Also, the debate about whether $\chi = S_r$ in the original Bishop's equation can be resolved as its expression in terms of microscopic variables can be now readily identified in Eq. (1b).

3. Results and Conclusion

The computation of both stresses and deformations in a granular assembly of particles connected by distinct liquid bridges has been performed within the Discrete Element Modelling (DEM) framework which provides access to all pertinent microstructural information in Eqs. (1a,1b,2) needed to verify the developed analytical expression. Fig. 1 demonstrates clearly the non-spherical nature of the capillary stress as revealed by the various microstructure tensors introduced in Eq.(2). Indeed, due to the anisotropic distribution of the water menisci and particle contacts within the body, the suction component in Bishop's relation is no longer a spherical tensor.

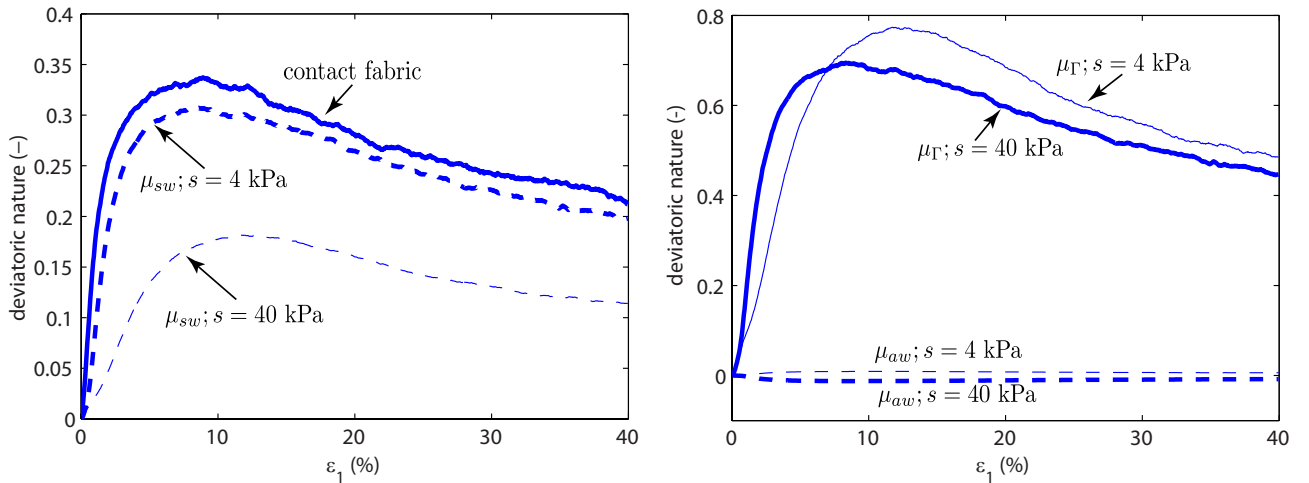


Figure 1. Non-spherical nature of microstructure tensors that enter the capillary stress expression

As a main conclusion, the general expression of total stress in unsaturated soils (coined as μ -UNSAT in this work) can formally explain why Bishop's equation could not be verified experimentally since several decades. The contact stress term has also been recently proven [4] to be a relevant stress variable that can describe both the failure and strain behaviours of three-phase materials with the same constitutive equations that apply to two-phase (dry or water-saturated) conditions.

References

- [1] Pietruszczak, S. and Pande, G. (1991). On the mechanics of partially saturated soils. *Comp. & Geotechnics*, **12:1**, 55–71.
- [2] Duriez, J., Eghbalian, M., Wan, R., and Darve, F. (2017). The micromechanical nature of stresses in triphasic granular media with interfaces. *Journal of the Mechanics and Physics of Solids*, **99**, 495–511.
- [3] Gurtin, M. E. and Murdoch, A. I. (1975). A continuum theory of elastic material surfaces. *Archive for Rational Mechanics and Analysis*, **57:4**, 291–323.
- [4] Duriez, J., Wan, R., Pouragha, M., and Darve, F. (2018). Revisiting the existence of an effective stress for wet granular soils with micromechanics. *Int. J. Num. Anal. Meth. Geomech.*, pp. 1–20 DOI: 10.1002/nag.2774.

CONFORMAL DISCRETIZATION OF HETEROGENEOUS GEOMATERIAL RVES GENERATED BY EXCURSION SETS OF RANDOM FIELDS

K. Ehab Moustafa Kamel¹, B. Sonon¹, J-B. Colliat², P. Gerard¹, and T.J. Massart¹

¹ *Université libre de Bruxelles (ULB), Belgium*

² *Université Sciences et Technologies Lille 1, Villeneuve d'Ascq Cedex, France*

Microscale features such as pore size and shape distributions and pore network connectivity strongly govern the coupled mechanical and transport macroscopic behaviour of porous/heterogeneous geomaterials. It is therefore of interest to develop multiscale computational tools to explore the links between microstructural features and the corresponding macroscopic properties by generating realistic Representative Volume Elements (RVEs). These can be obtained either experimentally (e.g. CT scan) since nowadays modern experimental techniques allow characterizing the properties of the various phases and pore space in porous/heterogeneous materials. They can also be made available virtually by generation algorithms reproducing the relevant morphological features [1, 2].

In both cases, the RVE geometry must be discretized in view of solving the formulation of the implied physics with a numerical technique such as the Finite Element method (FE). Non-conformal discretization approaches, such as extended finite elements, with level-sets coupling can avoid constraints related to the conformal meshing of complex geometries. However, such approaches can become complex to solve coupled problems. Therefore, this contribution presents a framework for the generation of conforming finite element meshes for complex RVEs to be able to conduct multi-scale FE simulations in regular codes and softwares. An implicit representation of the RVE geometry is used by means of level set functions during the mesh generation procedure, providing a natural link between the RVE geometry generation and the mesh generator. This also allows a systematic treatment of morphologies of arbitrary complexity as classically met in the micro-morphology of geomaterials.

Geomaterial microstructures present high degree of complexity due to the presence of heterogeneities and arbitrary morphological features. Here, the tool used to produce realistic microstructural geometries is based on the principle of excursion sets of correlated Gaussian random fields [2]. A morphological control of the porous space is thereby achieved on key parameters such as the volume fraction of the solid and pore phases, and the size distribution and connectivity in the pore space. Indeed, the pores contributing to the permeability of the medium are the critical pores, i.e. those ensuring the hydraulic conductivity on either side of the microstructure. Control in this case means the ability to analytically determine correlations between statistical quantities (mean, variance, threshold, correlation length) and morphological quantities (volume, surface, diameter, Euler characteristic) thanks to the Lipschitz-Killing curvatures.

The mesh generation procedure consists in an extension of the methodology proposed by Persson [3]. It is based on an optimization process that uses an input level set function expressed as a signed distance field and an ad-hoc truss analogy. This allows defining a tension/compression force-field on the elements of the truss to steer it to an equilibrated situation satisfying an element size function. The mesh conformity with material interfaces, meanwhile, is obtained by constraining their normal movement acting like boundary supports [4]. An efficient control is thereby achieved on the material interfaces, together with a local control of the element sizes to build optimized conforming meshes. This principle is incorporated after the extraction of the interfaces into a hierarchical 3D constrained Delaunay triangulation procedure successively meshing the internal material interfaces, the external boundaries and the bulk of the phases in the RVE to produce high quality periodic or not FEM meshes exploitable.

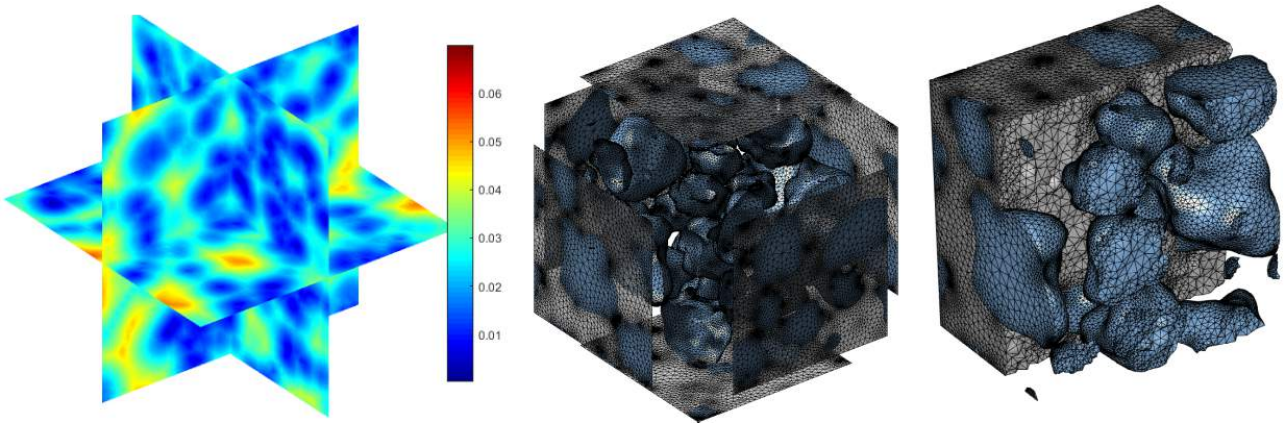


Figure 1. Meshing process of a RVE generated by [1] (Left) Cut view of elements size map, (Center) Interfaces and boundaries mesh, (Right) 3D optimized mesh – Inclusions and cut view of the matrix

The implementation is adapted and optimized for the RVEs generator developed in [3] focused on to complex multi-body RVEs (see Figure 1). A natural extension allows treating general implicit geometries such as CTX scans or RVEs generated by [2] (see Figure 2).

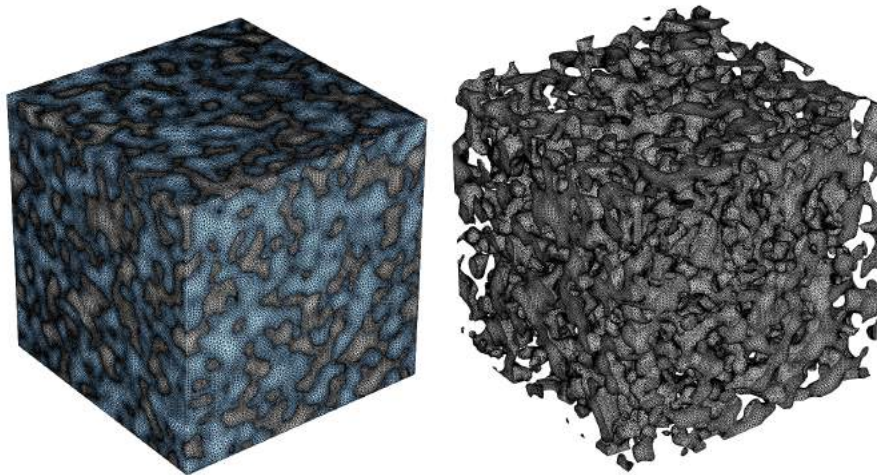


Figure 2. Mesh of a RVE generated by [2] methodology: (Left) Porous media, (Right) Pore space

References

- [1] Sonon, B., François, B., and Massart, T. J. (2012). A unified level set based methodology for fast generation of complex microstructural multi-phase rves. *Computer Methods in Applied Mechanics and Engineering*, **223**, 103 – 122.
- [2] Roubin, E., Colliat, J.-B., and Benkemoun, N. (2015). Meso-scale modeling of concrete: A morphological description based on excursion sets of random fields. *Computational Materials Science*, **102**, 183 – 195.
- [3] Ehab Moustafa Kamel, K., Sonon, B., Colliat, J.-B., Gerard, P., and Massart, T. J. An integrated approach for the conformal discretization of complex inclusion-based microstructures. *In Preparation*.
- [4] Persson, P.-O. and Strang, G. (2004). A simple mesh generator in matlab. *SIAM Review*, **46**, 2004.

EXPERIMENTAL AND NUMERICAL INVESTIGATION ON DYNAMIC FRACTURE EVOLUTION IN GLASS-BEAD CHAINS UNDER IMPACT

Sheng Jiang, Luming Shen, François Guillard and Itai Einav
School of Civil Engineering, University of Sydney, NSW 2006, Australia

1. Background

Fracture of brittle grains under impact plays an important role in controlling the compaction behaviour and the permeability of the granular materials. Fracturing is considered to be a process through which atomic bonds get broken, and new surfaces are formed through either the creation of new crack or the extension of existing crack. The initiation, propagation and coalescence of these cracks alter the effective material stiffness and can ultimately lead to failure. These processes have been largely studied through the application of energy-based methods, such as Griffith's fracture criterion [1], involving the determination of the stress threshold at which a crack initiates and begins to propagate. Experimental work has demonstrated that similar structures and morphology are developed in brittle homogenous solids during the high speed fracture process [2; 3]. Much of this fracture-induced morphology is dependent on the loading conditions and specific properties in brittle materials and can be used as a tool to identify and analyze the fracture dynamics [4]. However, in some specific granular materials (*e.g* cemented sand or sandstone), fractures propagate not only in the grains, but also through the inter-grain medium that has completely different microscopic geometrical and mechanical characteristics. Many previous studies focused on the fracture mechanisms derived from the intrinsic properties of grains and paid less attention to the effects of inter-grain medium. Hence, this paper conducts a systematic study of the dynamic fracture evolution through glass-bead chains with the inter-grain medium.

2. Methodology and Results

Split Hopkinson pressure bar experiments on chains of three 7 mm-diameter glass beads separated by two 0.1 mm-thickness copper shims (inter-grain medium here) are performed under different impact velocities, ranging from 5.3 m/s to 14.2 m/s. In the chain system, the front bead (close to incident bar) is more prone to fracture than the back bead (close to transmitted bar), while the middle bead (in the middle of the chain) is only damaged slightly regardless of the impact velocities applied. Two typical chain failure patterns are discovered throughout the impact velocity range (see Figure 1 (a)), namely, (A) crushing-damage-crushing, and (B) crushing-damage-damage. To some extent, the level of chain absorbed energy determines damage degree of the chain system. Severe damage pattern (A) is more likely to occur in the high absorbed energy section (above the red fitting line), while the damage pattern B is easier to appear in the low absorbed energy section (below the blue fitting line).

A corresponding numerical study is also conducted by implementing the '*Brittle Cracking*' damage model for the glass in Abaqus/Explicit, where elements are deleted after failure. The simulation results qualitatively reproduce the experimental results (see Figure 1 (b)). The front bead damages most severely, which is followed by the slightly damaged back bead and the totally intact middle bead. Comparisons between glass bead chains with and without inter-grain materials (two copper shims here) clearly show that these inter-grain materials significantly alter the fracture mechanisms (mainly happen on the middle bead) and decreases the total chain damage degree (less element deleted). The initiation of the cracks is predicted by calculating the maximum tensile stress near the contact point according to the Hertzian theory [5]. The middle bead contacted with two thin flat copper shims has the higher tensile stress near contact area than the other two beads, thereby it

is more difficult to break. Also, the elastic modulus of the chain system calculated based on analytical solution [6] increases after inserting comparatively stiffer inter-grain materials. Under the same impact level, less damage is detected in the chain system with inter-grain material.

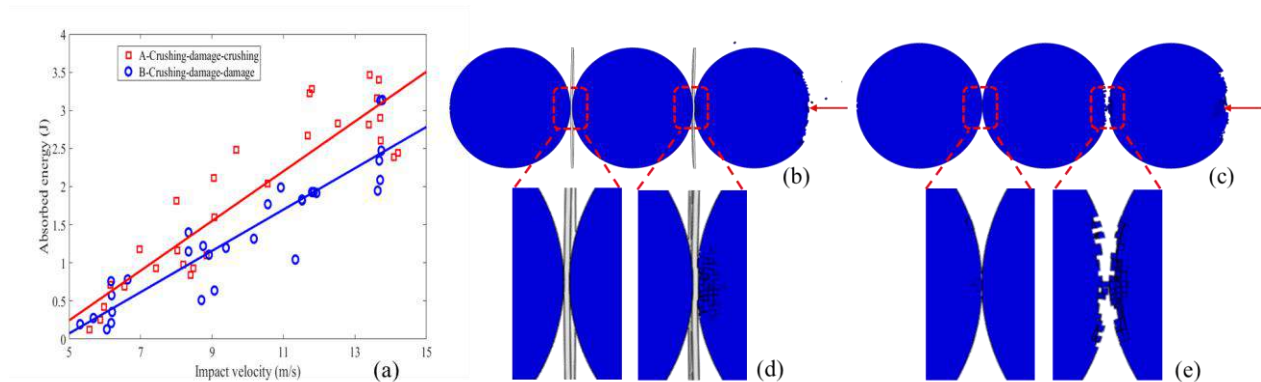


Figure 1. (a) The relation between the chain absorbed energy and the impact velocity from experiment; (b,c) Comparisons of the simulated damage pattern of chains between with and without inter-grain medium under impact velocity 13.5 m/s; (d,e) Zoom near the contacts, as indicated by red rectangles in (b,c)

3. Conclusions

Regardless of the impact velocity, two damage patterns are discovered in the three-glass-bead chain system from impact loading tests. Under the same impact velocity, the severe damage patterns are prone to occur in the high absorbed energy section, while the slight damage patterns dominate the low absorbed energy section. The corresponding numerical studies show that the stiff inter-grain materials can reduce the total chain damage degree and greatly affect chain damage patterns.

4. Acknowledgments

The work is supported in part by the Australian Research Council through Discovery Projects (DP170102886) and by the National Natural Science Foundation of China (Grant No. 11232003). The authors acknowledge the scientific and technical assistance of the Sydney Informatics Hub at the University of Sydney and, in particular, access to the high performance computing facility Artemis.

5. References

- [1] Griffith, A. A., & Eng, M. (1921). VI. The phenomena of rupture and flow in solids. *Phil. Trans. R. Soc. Lond. A*, 221(582-593), 163-198.
- [2] Sharon, E., Gross, S. P., & Fineberg, J. (1995). Local crack branching as a mechanism for instability in dynamic fracture. *Physical review letters*, 74(25), 5096.
- [3] Jiang, S., Shen, L., Guillard, F., & Einav, I. (2018). Energy dissipation from two-glass-bead chains under impact. *International Journal of Impact Engineering*.
- [4] Sharon, E., & Fineberg, J. (1996). Microbranching instability and the dynamic fracture of brittle materials. *Physical Review B*, 54(10), 7128.
- [5] Johnson, K. L. (1985). Contact mechanics. In: Cambridge university press, Cambridge.
- [6] Dvorkin, J., Mavko, G., & Nur, A. (1991). The effect of cementation on the elastic properties of granular material. *Mechanics of Materials*, 12(3-4), 207-217.

CONTACT TOPOLOGY DURING INITIAL STAGES OF PARTICLE BREAKAGE USING X-RAY TOMOGRAPHY

Z. Karatza¹, O. Okubadejo², E. Andò², S.-A. Papanicolopoulos¹, G. Viggiani², J. Y. Ooi¹

¹ School of Engineering, The University of Edinburgh, Edinburgh EH9 3JL, U.K.

² Univ. Grenoble Alpes, CNRS, Grenoble INP**, 3SR, F-38000 Grenoble, France

1. Introduction

Experimental studies of particle breakage have focused on how breakage is affected by the micro-scale and the boundary and loading conditions [1]. These experiments have been complemented by numerical studies, such as simulations using the discrete element method, focusing on particle kinematics and the internal topology of the particle assembly [2]. Additionally, in constitutive models the overall degree of particle breakage is taken into account by considering changes between the initial and final grain size distribution curves [3], aiming to capture the bulk response throughout the test or the unloaded, post-testing state of the specimen observed experimentally. Recent advances in XCT have enabled the full-field measurement of many processes in 3D, giving researchers a new tool with which to explore micro-mechanical behaviour [4].

The main aim of this research is to achieve a better understanding of the particle-scale mechanisms that lead to particle breakage during the initial stages of breakage, through the use of x-ray computed micro-tomography (XCT). Highly spherical zeolite granules (D_{50}^{intact} of 1.36 mm) were tested under strain-controlled oedometric compression (more details can be found in [5]). X-ray scanning was performed with a pixel size of 12.25 $\mu\text{m}/\text{px}$, meaning that individual particles are described by a large number of pixels ($> 100 \text{ px}/D_{50}^{\text{intact}}$). In this work we are investigating the effect of the coordination number on particle breakage, using the reconstructed 3D images.

2. Image processing

Grain breakage will produce fragments that are either big enough to be clearly identified as new particles, or too small with respect to the resolution and just considered as “powder” fragments (which will not be studied in this work). The tool we propose (discrete Digital Image Correlation – dDIC) takes an incremental approach from the beginning of the test, tracking intact particles into the next image. A particle is recognised as broken when the rigid registration fails and through a local segmentation process, individual fragments are identified and tracked. Once the tracking of the broken particles is successful, they are identified in the previous loading increment (pre-breakage) and the coordination number is investigated, by looking at the maximum gradient of the grey scale image. In the case where the gradient is low, this indicates the presence of a contact.

3. Results and Conclusions

From the inspection of the images it is found that the majority of breakage occurs within a height of $2D_{50}^{\text{intact}}$ from the bottom (loading) boundary. This indicates a strong boundary effect, caused by the friction at the loading platen and the initial filling process. A number of statistically significant broken particles is investigated and related to the coordination number of the particles while still intact; the results are presented in Table 1.

The particles broke with a small chipping close to a contact, with axial splitting, or with more complicated breakage patterns (multiple splitting). As shown in Table 1, the particles with the fewer

** Institute of Engineering Univ. Grenoble Alpes

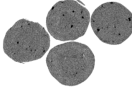
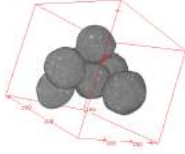
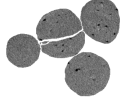
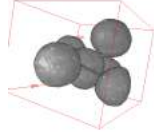
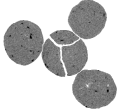
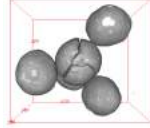
Breakage mode	Average coordination number	2D slice	3D image
Surface chipping	6.6		
Axial splitting	4.9		
Multiple splitting	4.7		

Table 1. Investigation of breakage mode with respect to coordination number.

contacts exhibit the most intricate breakage patterns. The correlation between number of contacts and breakage mode is not very strong, which indicates that breakage will be affected by the contact forces rather than the number of contacts. This means that a number of contacts will be passive, carrying weak forces, and it is the contacts carrying strong forces which determine the strength of the material contributing mainly to the bulk response [6]. This ongoing work requires a more detailed investigation into the coordination number and the fabric tensor (particle orientations, inter-particle contact normal direction and void space geometry), to enhance our understanding about the micro-mechanisms that lead to particle breakage.

References

- [1] Nakata, Y., Hyodo, M., Hyde, A. F. L., Kato, Y., and Murata, H. (2001). Microscopic particle crushing of sand subjected to high pressure one-dimensional compression. *Soils and Foundations*, **41(1)**, 69–82.
- [2] Cil, M. B. and Alshibli, K. A. (2014). 3D evolution of sand fracture under 1D compression. *Géotechnique*, **64(5)**, 351–364.
- [3] Einav, I. (2007). Breakage mechanics part I: theory. *Journal of the Mechanics and Physics of Solids*, **55(6)**, 1274–1297.
- [4] Karatza, Z., Andò, E., Papanicolopoulos, S.-A., Ooi, J. Y., and Viggiani, G. (2018). Evolution of deformation and breakage in sand studied using X-ray tomography. *Géotechnique*, **68**, 107–117.
- [5] Karatza, Z., Andò, E., Papanicolopoulos, S.-A., Viggiani, G., and Ooi, J. Y. (2017). Evolution of particle breakage studied using x-ray tomography and the discrete element method. *EPJ Web Conf.*, **140**, 07013.
- [6] Minh, N. H., Cheng, Y. P., and Thornton, C. (2014). Strong force networks in granular mixtures. *Granular Matter*, **16(1)**, 69–78.

MICRO-MECHANICAL MODELING OF TIME-DEPENDENT DEFORMATION AND DAMAGE IN CLAYSTONE

C. Bikong¹, Q.Z. Zhu² and J.F. Shao^{1,2}*

¹ University of Lille, LaMcube FRE2016 CNRS, Lille, France

² HOHAI University, College of Civil Engineering, Nanjing, China

**Corresponding author: jian-fu.shao@polytech-lille.fr*

1. Introduction

Clayey rocks such as claystone and shale are widely investigated in various engineering domains, in particular in oil industry for the production of shale gas and in the context of underground disposal of nuclear waste as a potential geological barrier. According to extensive laboratory investigations, clayey rocks exhibit time-dependent deformation in creep tests. So far, the classical viscoelastic or viscoplastic theories have been used for the description of creep deformation in clayey rocks. However, it has been observed that in some hard clayey rocks, such as the Callovo-Oxfordian (COx) claystone which is investigated in the French project of underground disposal of radioactive waste, the time-dependent deformation in such materials is mainly related to the time-dependent propagation of micro-cracks and frictional sliding along micro-cracks. Further, the macroscopic mechanical responses of clayey rocks are inherently dependent on their mineralogical compositions and porosity. Classical phenomenological models are not able to explicitly take into account such effects of micro-structures. Therefore, it is needed to develop constitutive models considering the time-dependent micro-crack propagation and influences of micro-structures.

2. Methodology and results

In this study, we have proposed a micromechanical approach for modeling time-dependent deformation and damage due to microcrack growth and frictional sliding. The COx claystone is considered as a reference material. The micro-mechanical model is formulated using an Eshelby solution based homogenization method. To this end and based on micro-structural investigations in previous studies, the COx claystone is represented as a composite material with two separated scales. At the mesoscopic scale, the claystone is seen as a three-phase composite. Quartz and calcite grains are embedded inside a continuous clay matrix. At the microscopic scale, the clay matrix is considered as a porous material with a family of pores embedded in a solid phase (clay aggregate). It is assumed that micro-cracks initiate and propagate at the mesoscopic scale. The time-dependent deformation is assumed to be induced by the time-dependent propagation of oriented microcracks inside the clay matrix. A three-step homogenization procedure is proposed. The effective elastic properties of the porous clay matrix (clay aggregate and pores) are first determined from a Mori-Tanaka scheme in the first step. In the second step, the elastic behavior of the cracked porous clay matrix (homogenized porous clay matrix + induced micro-cracks) is then determined using an Eshelby solution based homogenization method by considering micro-cracks as spheroidal inclusions. Effects due to cracks interactions are taken into account with different homogenization schemes. An anisotropic distribution of induced cracks is considered. Depending on loading path, cracks are propagating in some preferential orientations so that the claystone exhibits an induced anisotropy. Furthermore, in closed cracks, the frictional sliding is described by a local friction criterion and coupled with the crack propagation. The frictional sliding is at the origin of macroscopic time-dependent plastic deformation while macroscopic damage is related to the crack propagation. Finally, in the third step of homogenization, the macroscopic mechanical properties of

the claystone (homogenized cracked clay matrix + mineral inclusions) are determined again by a homogenization procedure by taking into account effects of calcite and quartz grains. A sensitivity study is performed in order to evaluate macroscopic influences of some micro-structural parameters. Finally, comparisons between numerical results and experimental data from creep tests are presented.

In Figure 1, we show the influence of confining pressure on the macroscopic creep strain. The creep strain is reduced when the confining stress is higher. In Figure 2, numerical results are compared with experimental data for uniaxial compression creep tests in the sample with 56% clay, 20% calcite and 24% quartz. The proposed micro-mechanical model can explicitly predict influences of mineralogical compositions on the macroscopic creep deformation.

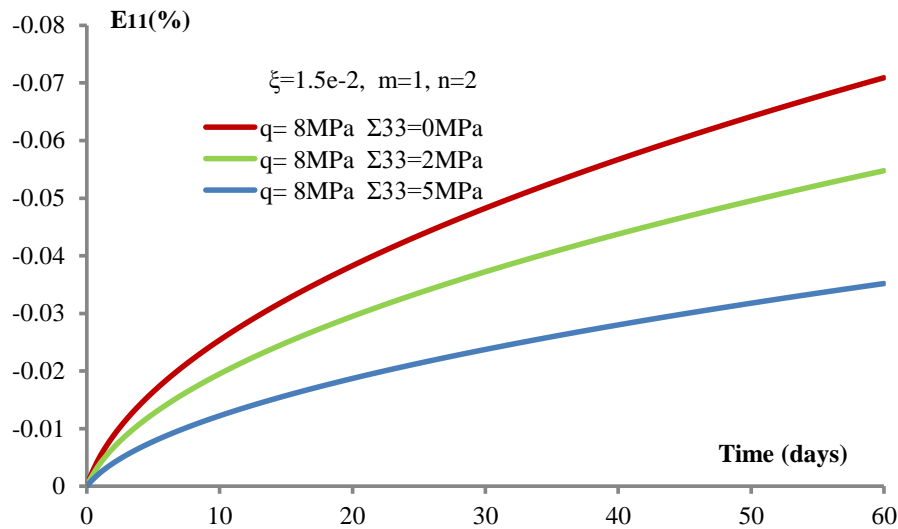


Figure 1: Influence of confining stress on creep deformation of Claystone

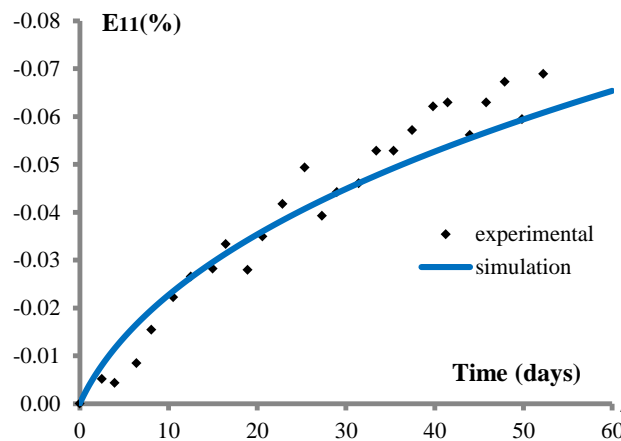


Figure 2: Comparison between numerical modeling and experimental data for creep deformation $\Sigma_{11} = -8MPa, f_0 = 56\%, f_1 = 20\%, f_2 = 24\%$

References:

- Robinet, J.C., 2008. Mineralogie, porosité et diffusion des solutes dans l'argilite du callovo-oxfordien de bure (meuse/haute-marne, France) de l'échelle centimétrique à micrométrique. University of Poitiers, France.
- Zhu, Q.Z., Shao, J.F., 2015. A refined micromechanical damage–friction model with strength prediction for rock-like materials under compression. *Int. J. Solids Structures* 60-61, 75-83.

A DUAL POROSITY APPROACH TO MODEL SWELLING OF BENTONITE HYDRATED WITH BRINE

Z. Li¹, T.S. Nguyen², G. Su², Q. Zheng²

¹ Consultant, Geoenvironmental Consulting, Ottawa, Canada

² Canadian Nuclear Safety Commission, Ottawa, Canada

1. Introduction

The Canadian Nuclear Safety Commission (CNSC), Canada's nuclear regulator, conducts regulatory research in order to build independent knowledge on safety aspects related to the deep geological disposal of radioactive wastes. A major component of the repository system consists of engineered seal materials that contain highly expansive clay minerals, such as MX-80 bentonite. In Canadian sedimentary rock formations that are currently considered as one of the candidate host rock types for deep geologic repositories, highly concentrated brine has been found. This concentrated brine affects the hydraulic-mechanical properties of the bentonite seal by reducing the swelling potential of the bentonite clay mineral. Therefore, the CNSC is conducting research in order to further understand how the concentrated brine influences the performance of bentonite-based seals as a barrier to radionuclide migration. In this study, a model based on the dual porosity approach and coupling amongst hydraulic-chemical-mechanical factors was developed and calibrated with laboratory swelling experiments on MX-80 bentonite, where the samples were hydrated with brine and the evolution of the swelling pressure was monitored for approximately a year.

2. Experimental method

Queen's University in collaboration with the CNSC performed swelling tests on sealing materials. A bentonite- sand (B/S) mixture and pure MX-80 bentonite (B) with initial moisture content of 11% was compacted to target dry densities and then loaded into a stainless steel test cell. Constant volume swelling test was carried out by hydrating from the bottom with synthetic model brine water. The hydraulic head is maintained at 1.5 m. The swelling-pressure was continually monitored by a load cell at the top for approximately one year.

3. A model for bentonite swelling based on double porosity

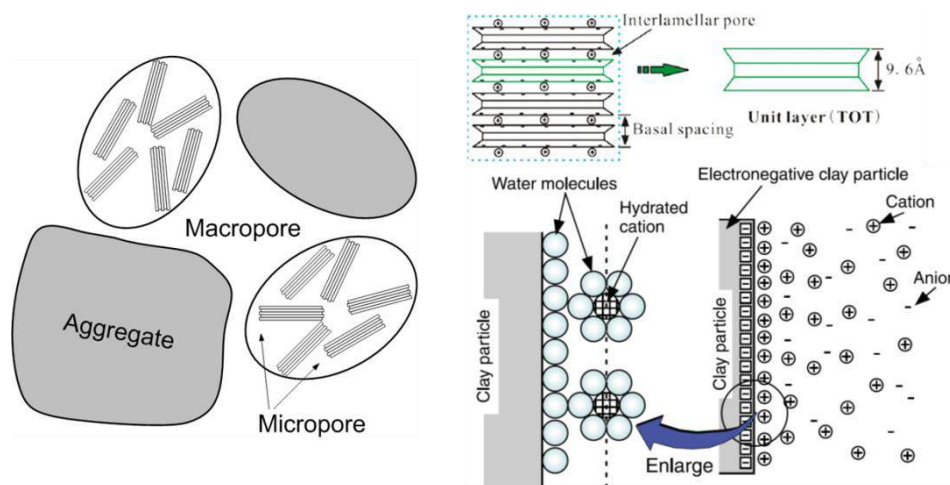


Figure 1. Illustration of multiple pore scales in bentonite

The multiple scales of porosity of bentonite are illustrated in Figure 1. The nanopores or interlamellar pores are the ones that exist between the unit clay layer (TOT) within a clay stack. The clay stacks are in turn flocculated into aggregates. The space between the clay stacks constitutes what we call micropores in this work. The expansion of the diffuse double layer (DDL) in the micropores due to electro-chemical forces is assumed to be responsible for most of the swelling of bentonite, although the molecular forces at the nanopore scale may also play a significant role. Considerations of mass balance of water and total dissolved solids in the macropore and micropore spaces, together with mass exchange between the two pore types, result in a set of governing equations that represent: i) porewater flow in the macropores and micropores and water exchange between the two types of pores; ii) solute transport in micropores and macropores and exchange of solutes between them; and, iii) a phenomenological equation for the swelling pressure which depends on the shrinkage or expansion of the DDL in the micropores.

4. Modelling results and discussion

The modelling results are in good agreement with the experimental data as shown in Figure 2. It is shown that the high salinity of brine substantially reduces the swelling potential when compared to the case for de-ionized water hydration. Samples with higher initial dry density have higher swelling potential for both types of water. Samples with pure bentonite also have higher swelling potential than samples made of bentonite-sand mixture. In the case of brine, there is an early increase in the swelling pressure, followed by a decrease to much smaller values with time. The above finding is interpreted as follows: water from the macropores first infiltrates into the micropores resulting in an early increase of the swelling pressure with chemical transport into the micropores lagging behind the water infiltration due to the known semi-permeable membrane effect. Therefore the salt concentration takes more time to increase in the micropores, resulting in a gradual decrease in the swelling pressure due to the shrinkage of the DDL.

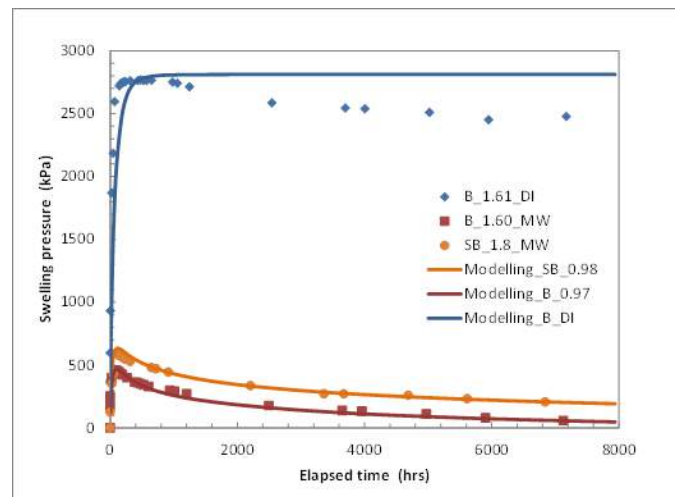


Figure 2. Swelling pressure of bentonite seals. The symbols (e.g. B_1.61_DI) indicate B (bentonite) or SB (sand-bentonite mixture) at the initial dry density (e.g. 1.61 Mg/m³) followed by the type of infiltrating water (MW for model water or brine, DI for de-ionized water).

5. Reference

[1] Queen's University, 2018. Laboratory determination of sealing material performance. Report submitted to Canadian Nuclear Safety Commission.

2. Modelling of instabilities and localized deformation

COMPUTATIONAL MODELING OF FLUID INDUCED FRACTURE PROPAGATION IN DEEP GEOTHERMAL RESERVOIRS

G. Meschke¹, I. Khisamitov¹, S. Beckhuis¹ and J. Reinold¹

¹ *Institute for Structural Mechanics, Ruhr University Bochum, Germany*

1. General

The hydraulic stimulation of deep geothermal reservoirs is characterized by the creation of hydraulically driven fractures, which eventually interact with pre-existing fractures and natural faults. In the presentation, two computational modelling strategies formulated in a coupled poromechanics framework are discussed: IGFEM-XFEM and Variational-interface models.

2. IGFEM-XFEM Model

In the interface-enriched generalized finite element method (IGFEM)-XFEM model cracks and borehole geometries are directly incorporate in the underlying mesh and no costly re-meshing is needed [1, 2, 3]. In contrast to the classical approach the fluid flow inside the crack is modelled explicitly and coupled with the pressure field of the porous media flow, which is approximated by the IGFEM using linear shape functions for the pressure field across the crack. The advantage of the IGFEM is the straightforward definition of Dirichlet boundary conditions on non-matching meshes, like crack interfaces. The explicit fluid flow in the crack is coupled with the flow in the porous bulk medium by means of Lagrange multipliers by prescribing the pressure of the explicit fluid flow to the pressure of the porous media flow. A gradient jump in the porous media pressure field is described using the IGFEM as

$$p(x) = \underbrace{\sum_{i=1}^n N_i(x) p_{pi}}_{\text{standard part}} + \underbrace{\sum_{i=1}^{n_{en}} \psi_i(x) \alpha_i}_{\text{enriched part}} \quad (1)$$

where $\psi_i(x)$ are the enriched shape functions, α_i are the enriched degrees of freedom that lie on the intersection points of the fracture with the elements. Figure 1 shows how the enriched shape functions are generated by the standard shape functions of the children elements (1) and (2) in an intersected parent element. With regard to the nodal numbering of the children elements, for the situation shown in Figure 1, the enriched shape functions are given as

$$\psi_1(x) = N_1^{(2)}(x) + N_2^{(1)}(x), \quad \psi_2(x) = N_1^{(1)}(x) + N_2^{(2)}(x).$$

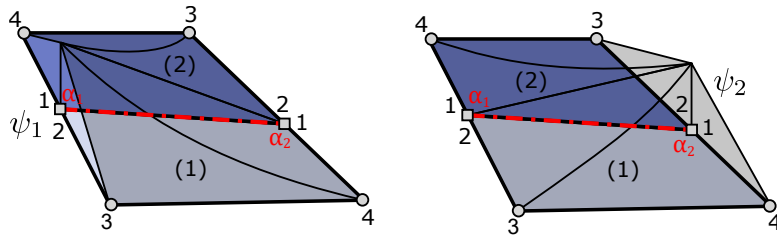


Figure 1. IGFEM - enrichment functions and element partitioning

3. Variational-interface model

The variational-interface model, based on an energetic competition between the elastic and fracture energies, is formulated with help of the zero-thickness interface elements embedded into a discretized system and inserted between the bulk finite elements over the entire domain [4]. Assuming the brittle behavior of rocks, the proposed model is formulated on the basis of GRIFFITH's criterion of crack equilibrium. The total energy of a mechanical system is decomposed into the bulk, interface and fracture surface energies. Minimization of the total functional is a solution of the fracture propagation problem. For the sake of smoothness and convergent behavior of the Newton-Raphson scheme, the fracture state in the interfaces is regularized with a new degree of freedom c approximated only along the interface zones. The equilibrium point for each loading step is achieved by the staggered-scheme proposed in [5] where, first, the mechanical problem is solved and, subsequently, the damage variable is obtained. The staggered iterations continue until a convergence criterion is met. The variational-interface approach is easily extendable for 3D-settings without considerable effort. Furthermore, the proposed model is formulated for the theory of poroelasticity. The interface elements are adapted to the Biot's theory using the effective stress concept. Additionally, a mass balance equation for the interface element is constructed with help of the damage variable distribution and cubic law. The hydraulic fracturing problem is solved by the backward-Euler scheme with the internal nonlinear Newton-Raphson iterations.

4. Benchmarks

The proposed models are validated with the analytical solutions provided in [6] for both fracturing regimes: toughness and viscosity. Additionally, the influence of the leak-off and the back-stress phenomena is analyzed using an one-dimensional fracture problem. Furthermore, a number of numerical benchmarks are performed for an analysis of the interaction of existing cracks and influence of the confining stresses on the hydraulic fracturing.

References

- [1] Moës, N., Dolbow, J., and Belytschko, T. (1999). A finite element method for crack growth without remeshing. *International journal for numerical methods in engineering*, **46**, 131–150.
- [2] Soghrati, S., Aragón, A. M., Armando Duarte, C., and Geubelle, P. H. (2012). An interface-enriched generalized fem for problems with discontinuous gradient fields. *International Journal for Numerical Methods in Engineering*, **89**, 991–1008.
- [3] Salimzadeh, S. and Khalili, N. (2015). Fully coupled xfem model for flow and deformation in fractured porous media with explicit fracture flow. *International Journal of Geomechanics*, **16**, 04015091.
- [4] Khisamitov, I. and Meschke, G. (2018). Variational approach to interface element modeling of brittle fracture propagation. *Computer Methods in Applied Mechanics and Engineering*, **328**, 452–476.
- [5] Miehe, C., Hofacker, M., and Welschinger, F. (2010). A phase field model for rate-independent crack propagation: Robust algorithmic implementation based on operator splits. *Computer Methods in Applied Mechanics and Engineering*, **199**, 2765–2778.
- [6] Detournay, E. (2004). Propagation regimes of fluid-driven fractures in impermeable rocks. *International Journal of Geomechanics*, **4**, 35–45.

THE LEVEL SET DISCRETE ELEMENT METHOD AND ITS APPLICABILITY TO SHEAR BANDING

*J.E. Andrade*¹, *R. Kawamoto*², *G. Viggiani*³, and *E. Andò*³

¹ *California Institute of Technology, CA, USA*

² *University of Tsukuba, Tsukuba, Japan*

³ *Universite Grenoble Alps, Grenoble, France*

1. Extended abstract

The discrete element method (DEM) [1] is widely used in geomechanics to simulate the behavior of granular materials. Although this model, and variants thereof [2, 3], have been successful in replicating experimental results at the bulk scale [4], they have not been compared to experimental results at lower length scales, such as that of strain localization. Here, we use another variant of DEM called the level set discrete element method (LS-DEM) [5], which represents arbitrary particle geometries via level set functions, to simulate a specimen of more than 53,000 particles in triaxial compression, capturing not only its macroscopic stress-strain and volume-strain behavior, but also its localized behavior, in this case, the shear band that forms [6].

Because LS-DEM can capture arbitrary particle geometries, we choose to simulate a specimen of a natural granular material, Hostun sand. This has two advantages: one, we show that LS-DEM is capable of simulating natural granular materials with complex particle shapes, and two, we glean these particle shapes from an X-ray computed tomographic (XRCT) image of an experimental specimen through a process called LS-imaging [7], which allows direct comparison with experimental results. LS-imaging, from an XRCT image, constructs a virtual specimen where every particle has the same geometry as its corresponding particle in the experimental specimen.

After the imaging process, which provides initial conditions to the LS-DEM simulation, the computational specimen is compressed triaxially under the same loading conditions as the experiment. Figure 1a-b shows the LS-DEM specimen before and after triaxial compression, respectively, and Figure 2 shows the stress-strain and volume-strain responses of both the experimental and LS-DEM specimens.

In addition to similar stress-strain and volume-strain responses, in the LS-DEM simulation, a shear band, of similar thickness and inclination as that in the experiment, forms. Furthermore, inside the shear band, local deviatoric strains and particle rotations are similar to those in the experiment: Figure 1c shows the local incremental deviatoric strains in a slice of the LS-DEM specimen at the end of loading, and Figure 1d shows that quantity in the same slice of the experimental specimen. This gives us reason to believe that additional quantities in the simulation are also accurate; one such quantity we can compute in the simulation but cannot compute experimentally is the measurement of interparticle forces. In our LS-DEM simulation, we can see the evolution of these interparticle forces and their effect on stress. In particular, the stress state inside the shear band rotates as loading proceeds, but the stress state outside the shear band remains oriented toward the direction of loading. Continued development of LS-DEM to simulate additional stress paths, in particular, those that are difficult to perform experimentally, could have implications on plasticity modeling.

References

- [1] Cundall, P. A. and Strack, O. D. L. (1979). A discrete numerical model for granular assemblies. *Géotechnique*, **29**, 47–65.
- [2] Garcia, X., Latham, J.-P., Xiang, J., and Harrison, J. (2009). A clustered overlapping sphere algorithm to represent real particles in discrete element modelling. *Geotechnique*, **59**, 779–784.

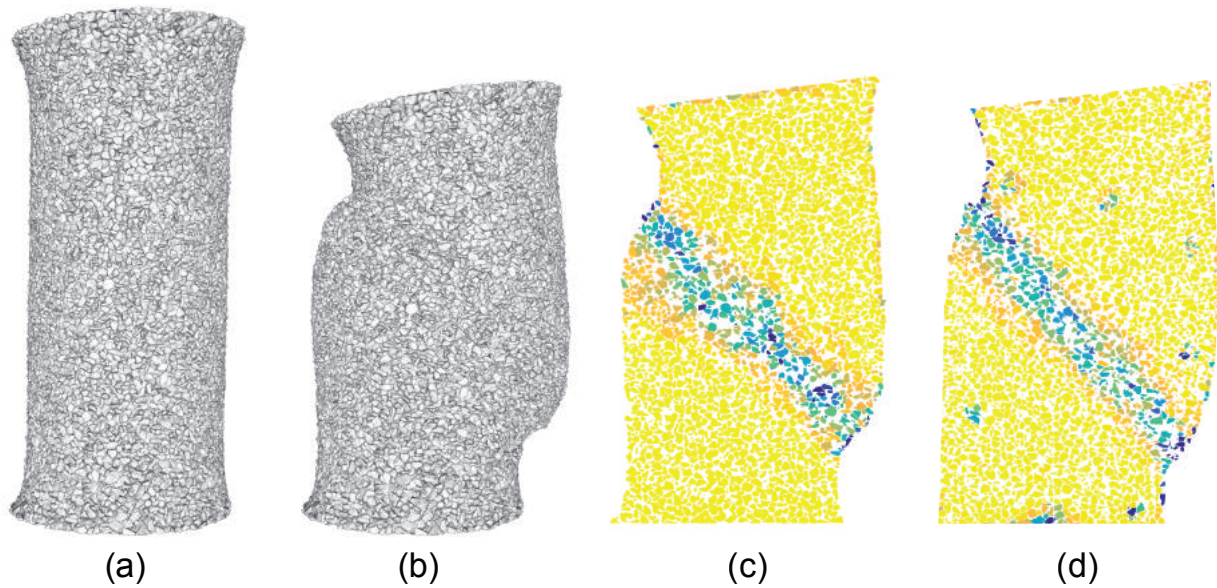


Figure 1. LS-DEM specimen at the (a) beginning and (b) end of triaxial compression. Local incremental deviatoric strains in a slice of the (c) LS-DEM and (d) experimental specimens.

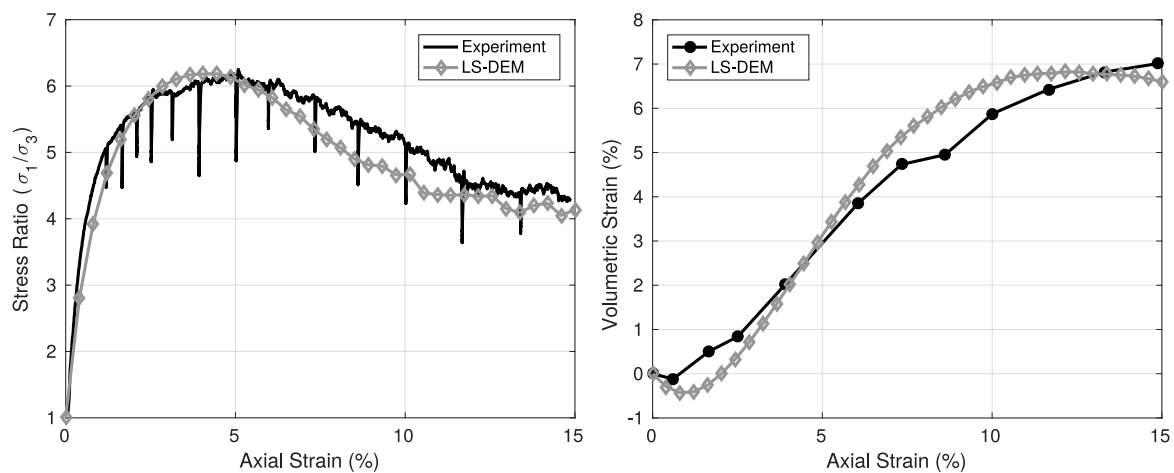


Figure 2. Macroscopic stress-strain and volume-strain graphs of experiment and LS-DEM simulation.

- [3] Hart, R., Cundall, P. A., and Lemos, J. (1988). Formulation of a three-dimensional distinct element model - part ii: Mechanical calculations for motion and interaction of a system composed of many polyhedral blocks. *International Journal of Rock Mechanics and Mining Sciences*, **25**, 117–125.
- [4] Lee, S. J., Hashash, Y. M., and Nezami, E. G. (2012). Simulation of triaxial compression tests with polyhedral discrete elements. *Computers and Geotechnics*, **43**, 92 – 100.
- [5] Kawamoto, R., Andò, E., Viggiani, G., and Andrade, J. E. (2016). Level set discrete element method for three-dimensional computations with triaxial case study. *Journal of the Mechanics and Physics of Solids*, **91**, 1 – 13.
- [6] Kawamoto, R., And, E., Viggiani, G., and Andrade, J. E. (2018). All you need is shape: Predicting shear banding in sand with ls-dem. *Journal of the Mechanics and Physics of Solids*, **111**, 375 – 392.
- [7] Vlahinic, I., Ando, E., Viggiani, G., and Andrade, J. E. (2013). Towards a more accurate characterization of granular media: extracting quantitative descriptors from tomographic images. *Granular Matter*, pp. 1–13, doi:10.1007/s10035-013-0460-6.

BOREHOLE STABILITY IN BRITTLE ROCK

*E. Gerolymatou*¹

¹ *Chalmers University of Technology, Gothenburg, Sweden*

1. Introduction

Borehole stability and its prediction is an important part of the production from reservoirs. The failure takes place in the form of breakouts, whose geometry depends on the properties of the rock and the stress state. Due to the softening behavior of the rock, simulating the procedure poses significant challenges. This is especially the case, when the failure of the rock around the borehole is brittle, as continuity is lost. In the present work, a semi-analytical method based on conformal mapping is presented for the simulation of borehole breakouts in the brittle regime. In what follows, the method is described briefly and some results are presented. Possible extensions to general stress states are discussed. Finally, conclusions are drawn.

2. Method

For the sake of brevity, the basics of conformal mapping will not be repeated here. The interested reader may find their details in [1]. In the specific case, the mapping to the exterior of an arbitrarily shaped opening in the w domain from the exterior of the unit circle in the z domain will be considered. The goal is to find an approximate mapping of the form

$$w = \sum_{n=0}^k q_n z^{1-n} \quad (1)$$

where q_n , $n = 0, \dots, k$ are complex constants, that will map the unit circle $|z| = 1$ on the desired

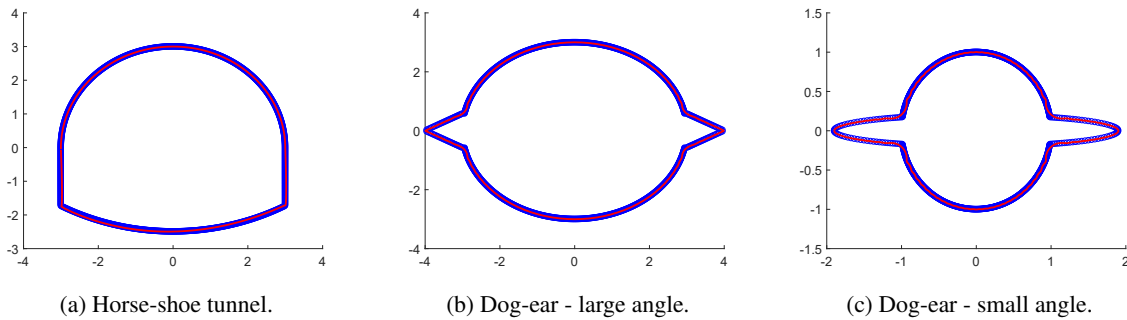


Figure 1. Shape fitting.

boundary in the w -space. It is noted that the arguments of z and w do not necessarily coincide. A variation of the method of simultaneous equations is used here, introduced by Kantorovich [2]. The actual boundary can theoretically be expressed as a real function of the angle θ and the same holds for its square. Expressing the curve of the boundary as a complex equality and equating the terms with the same exponents provides the solution. This method can be applied when the function of the boundary in the z space is known, which is generally not the case. To circumvent the problem, a procedure similar to the one suggested by Fornberg [3] is used here. The k -roots of unity in the z -space are used

for the series expansion. For the first iteration, it is assumed that the arguments correspond with the ones of the corresponding points in the w -space. Then, the method suggested above is used and an approximate mapping is evaluated. The arguments of the points in the w -space are assessed again and the values of the function $f(\theta)$ are evaluated again. The procedure is repeated, until a satisfactory fit is achieved. Examples are shown in figure 1 for 100 terms.

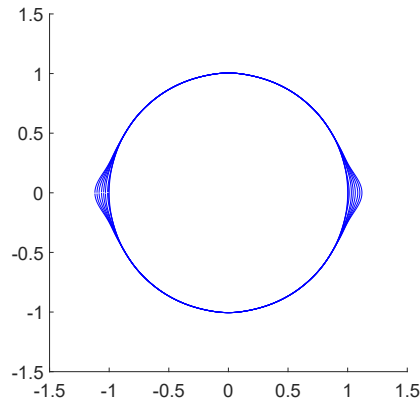


Figure 2. Progressive failure in a round borehole.

A similar method of equating the coefficients of exponents of the same order is used to approximate the coefficients of the analytical functions for the evaluation of the stress field. The areas that fail are removed and the procedure is repeated. An example is shown in figure 2 using 20 terms.

3. Extensions

Though the example presented here was evaluated using a two-dimensional stress field, the underlying assumption of plane strain conditions can be used to solve the problem for any initial stress state, even if that is not coaxial to the borehole. As out of plane strains are equal to zero and in-plane strains are known, the out of plane stress components can be easily evaluated, if their initial values are known. This means that arbitrarily oriented stress fields can be considered, in conjunction with failure criteria taking into account all three stress invariants.

4. Conclusions

As may be observed from the examples presented above, the use of numerical conformal mapping, as suggested in the present work, provides suitable solutions to the problem of brittle borehole breakouts. In spite of its formulation in two dimensions, the method is not restricted to two dimensional stress states or failure criteria. It is characterized by a rather low numerical cost, given that the results shown in figure 1 required a total of 12 sec, while the result in figure 2 a total of 68 sec on a personal computer.

References

- [1] Muskhelishvili, N. (1977). *Some basic problems of the mathematical theory of elasticity*. Noordhoff International Publishing.
- [2] Kantorovich, L. (1933). On some methods of constructing a function effecting a conformal transformation. *Bulletin of the Academy of Sciences of the USSR*, **7**, 229–235.
- [3] Fornberg, B. (1980). A numerical method for conformal mapping. *SIAM Journal on Scientific and Statistical Computing*, **1**, 386–400.

MODELLING OF HYDRAULIC FRACTURING IN ROCKS USING COUPLED DEM/CFD APPROACH

M. Krzaczek¹, J. Kozicki¹ and J. Tejchman¹

Gdansk University of Technology, Gdansk, Poland

mkrzacze@pg.gda.pl, jkozicki@pg.gda.pl, tejchmk@pg.gda.pl

1. Introduction

Hydraulic fracturing is a well stimulation technique to increase the productivity of petroleum reservoirs in which rocks are fractured by a pressurized liquid. The process involves the high-pressure injection of fluid (primarily water, containing sand or other proppants suspended with the aid of thickening agents) into a wellbore to create cracks in the deep-rock formations through which natural gas and petroleum will flow more freely. When the hydraulic pressure is removed from the well, small grains of hydraulic fracturing proppants hold the fractures open. The modelling of the fluid-driven fracture propagation into rocks comprises the coupling of different physical mechanisms, including deformation of the solid skeleton induced by the fluid pressure on fracture surfaces, flow of the pore fluid along new fractures and through the region of surrounding existing fractures and pronounced heat changes. There are two main approaches for modelling the propagation of hydraulically driven complex fracture patterns: continuum-based models and discontinuous meso-scale models at the grain level. The continuum-based meso-scale models are obviously unable to fully render meso-scale coupled thermal-hydraulic-mechanical effects. As compared with conventional continuum mechanics methodologies used in most of existing numerical studies, discontinuous meso-scale models at the grain level (such as the discrete element method (DEM)) are more realistic since they allow for a direct simulation of meso-structure and are very useful for studies of the mechanism of the initiation, growth and formation of fractures [1], [2]. Various methods were developed to model fluid flow in pores and fractures at the grain level when using DEM. The commonly used approach to describe fluid flow and predict interaction mechanisms between flowing fluid and particles was the pore-network modelling that assumed that fluid flows through channels connecting pores that accumulate pressure. In this approach, a simplified laminar viscous Poiseuille flow [3] or Stokes flow [4] are usually assumed. The pore network model is built through a weighted Delaunay triangulation over the discrete element packing. The finite volume method is usually applied to solve the governing equations of motion. [3]. The model may describe incompressible [5] or compressible fluids [6]. Most of DEM/CFD models meet the following simplified assumptions [3]: isothermal conditions, single phase flow, laminar fluid flow in pores and fractures and small grains displacements in rocks. In the paper, a significant extension of the pore-network model is proposed (called virtual pore network (VPN)).

2. Fluid flow model

The VPN model accurately reproduces grains and voids geometry (pores and fractures). The voids and fractures (fluid domain) are discretized with the aid of triangular (in 2D) or tetrahedral (in 3D) control volumes (called the virtual pores). Similarly to the pore-network method, the virtual pores are connected by channels that connect their gravity centres. Fluid flows in channels while virtual pores accumulate pressure and volume fraction of phases. The Poiseuille flow model is assumed in channels. To model multiphase flow of compressible fluid, the fluid volume (VOF) model [7] is implemented. VOF is a surface-tracking technique applied to a fixed Eulerian mesh and can simulate two or more immiscible fluids by solving a single set of equations. Hence, the Poiseuille flow equation can be expressed for 3D problems and secondary-phase fluids as:

$$\frac{\partial}{\partial t} (\alpha_q \rho_q h) = \frac{\partial}{\partial x} \left(\frac{\alpha_q \rho_q h^3}{12\mu_q} \frac{\partial P}{\partial x} \right) + \frac{\partial}{\partial z} \left(\frac{\alpha_q \rho_q h^3}{12\mu_q} \frac{\partial P}{\partial z} \right), \quad (1)$$

where index q denotes the liquid phase, α_q is the volume fraction, ρ_q is the density, h is the hydraulic channel aperture, μ_q is the dynamic viscosity and P denotes the pressure. Equation 1 is not solved for the gas phase that is computed based on the following constraint $\sum_{q=1}^2 \alpha_q = 1$. In order to capture large grain displacements in rocks, a special transformation algorithm is applied, based on the assumption that mass is a topological invariant. This algorithm transforms simulation results computed at time step 'n' in the old grid to the new grid that may be significantly geometrically deformed. It enables to investigate fluid flow in topologically variable pores and fractures (i.e. some pores and fractures may vanish and new ones may appear).

3. Coupled DEM/CFD simulation results

The microscopic mechanical constants for rocks were calibrated with preliminary DEM simulations of uniaxial compression and splitting tension [2]. The rock material was described as 3-4-phase material. VPN was calibrated by simulating permeability tests.

The series of numerical coupled DEM/CFD simulations were performed to study the process of filling pores and fractures with the fracturing fluid in rock specimens. The influence of the fluid pressure, fluid velocity, initial rock porosity, location and number of existing discontinuities (faults, joints, bedding layers) on the initiation and propagation of hydraulic fractures was carefully investigated. The numerical results were qualitatively in agreement with the experiments with respect to the fracture pattern.

4. Conclusions

In contrast to commonly used pore-network approaches, VPN reproduces more realistically fluid flow in pores and fractures in rocks and enables also to investigate multi-phase fluid flow. A strong relationship between the initial fraction of the liquid phase in pores and fractures and the propagation speed of the hydro-fracking process was observed in coupled DEM/CFD analyzes. The impact of initial discontinuities in rocks on the hydraulic fracture geometry was also pronounced.

5. References

- [1] Nitka, M. & Tejchman, J. (2018). A three-dimensional meso scale approach to concrete fracture based on combined DEM with X-ray μ CT images. *Cement and Concrete Research*, **107**, 11-29.
- [2] Suchorzewski, J., Tejchman, J. & Nitka, M. (2017). Experimental and numerical investigations of concrete behaviour at meso-level during quasi-static splitting tension. *Theoretical and Applied Fracture Mechanics*, doi: 10.1016/j.tafmec.2017.10.011, 2017.
- [3] Yoon, J. S., Zang, A. & Stephansson, O. (2014). Numerical investigation on optimized stimulation of intact and naturally fractured deep geothermal reservoirs using hydro-mechanical coupled discrete particles joints model. *Geothermics*, **52**, 165–184.
- [4] Tong, A-T., Catalano, E. & Chareyre, B. (2012). Pore-Scale Flow Simulations: Model Predictions Compared with Experiments on Bi-Dispersed Granular Assemblies. *Oil & Gas Science and Technology – Rev. IFP Energies Nouvelles*, **67**(5), 743-752.
- [5] Chareyre, B., Cortis, A., Catalano, E. & Barthélémy, E. (2012). Pore-scale modeling of viscous flow and induced forces in dense sphere packings. *Transport in Porous Media*, **94**(2), 595-615.
- [6] Scholtès, L. & Donzé, F. (2012). Modelling progressive failure in fractured rock masses using a 3D discrete element method. *I. Journal of Rock Mechanics and Mining Sciences* **52**, 18-30.
- [7] Hirt, C.W. & Nichols, B.D. (1981). Volume of fluid (VOF) method for the dynamics of free boundaries. *Journal of Computational Physics*, **39**(1), 201–225.

A STRONG DISCONTINUITY FINITE ELEMENT MODEL

E. Sakellariadi

Università Politecnica delle Marche, Ancona, Italy

1. Basic strong discontinuity model

In strong discontinuity finite element models a standard FEM formulation is enriched by considering an opening crack or sliding shear surface embedded within the finite element mesh. The discontinuity in the displacement field is directly taken into account, hence the “strong” designation, rather than “weak” discontinuity models in which the displacement field is continuous and there is a jump in the strain field. In [1] a systematic study and classification of embedded discontinuity models within a unified framework was presented, with the conclusion that optimal performance is achieved when using what is named a “SKON” (statically and kinematically optimal nonsymmetric) formulation. The main characteristics of this approach are here briefly summarized.

In standard FEM formulation, the nodal displacement vector \mathbf{d} is linked to the strain vector $\boldsymbol{\varepsilon}$ through the kinematic condition $\boldsymbol{\varepsilon} = \mathbf{B}\mathbf{d}$, \mathbf{B} being the strain interpolation matrix containing the derivatives of the shape functions, and this strain vector is in turn linked to the stress vector $\boldsymbol{\sigma}$ by means of some assumed constitutive law $\boldsymbol{\sigma} = \mathbf{D}\boldsymbol{\varepsilon}$, of which the simpler form would be linear elasticity ($\mathbf{D} = \mathbf{D}_e$). An equilibrium equation can be written, arriving at the well-known expression:

$$f_{int} = \int_A \mathbf{B}^T \boldsymbol{\sigma} \, dA = \int_A \mathbf{B}^T \mathbf{D}_e \mathbf{B} \mathbf{d} \, dA \quad . \quad (1)$$

In the “SKON” approach, the displacement field is decomposed into a continuous part linked to the stress-deformation behaviour of the medium, and a discontinuous part deriving from the opening and sliding of the discontinuity. Within a single element, the displacement jump is approximated by a piecewise constant function, on the grounds that elements with linear displacement interpolation functions are being used throughout [2]. The kinematic condition is hence written in the form $\boldsymbol{\varepsilon} = \mathbf{B}(\mathbf{d} - \mathbf{H}\mathbf{e})$, in which the discontinuity has been represented by a column vector $\mathbf{e} = [e_n, e_s]^T$, containing the two additional degrees of freedom e_n and e_s which correspond to the jump in the displacement field in directions normal and parallel to the discontinuity, and \mathbf{H} is a matrix reflecting the effect of the displacement jump on the nodal displacements. The idea is to subtract the contribution of the displacement jump from the nodal displacement vector \mathbf{d} , thus linking the strains in the bulk material only to the displacements produced by the continuous deformation.

The tractions transmitted by the crack, represented by a column vector \mathbf{t} , must be linked to the discontinuity displacement vector \mathbf{e} by some appropriate constitutive law. Various possibilities are available; for example, a law in damage format is proposed in [2]. A final static condition needed to complete the model is formulated as a natural stress continuity condition, requesting that the traction vector across the discontinuity \mathbf{t} must be equal to the stress vector components in the direction normal and parallel to the discontinuity, similar to static boundary conditions.

2. Combination with original constitutive law

In the model here presented, which was first conceived in [3], and subsequently used for the modelling of hydraulic fracturing in [4], a discontinuity surface embedded in a medium is described as a continuous distribution of edge dislocations, thus quantifying the relative displacements across the discontinuity surface. In particular, the relative opening or sliding displacement at a point \mathbf{x}' of the discontinuity is expressed as the elementary dislocation strength $d\mathbf{b}(\mathbf{x}')$ column vector; this in

turn is expressed in terms of dislocation density $\delta(\mathbf{x}')$, which is better suited for the mathematical solution of the resulting equations, by writing $d\mathbf{b}(\mathbf{x}') = \delta(\mathbf{x}')d\Gamma$ where $d\Gamma$ is a portion of the discontinuity surface. Through the use of existing standard fundamental solutions $\Psi(\mathbf{x}, \mathbf{x}')$ from the theory of linear elasticity, which quantify the stress and displacement fields due to a point dislocation in an elastic medium, it is possible to write integral equations which express the effect produced by the discontinuity in any point of the medium:

$$\boldsymbol{\sigma}(\mathbf{x}) = \int_{\Gamma} \Psi(\mathbf{x}, \mathbf{x}') \delta(\mathbf{x}') d\Gamma \quad . \quad (2)$$

These equations, using appropriate discretization techniques, can be transformed into a relationship between tractions and the discontinuity displacements, and can therefore be used as an internal constitutive material law linking the \mathbf{t} and \mathbf{e} column vectors of the “SKON” formulation.

Furthermore, in this case there is no need to make any assumption or simplification regarding the displacement jump values. The nodal displacement vector \mathbf{d} is still decomposed into a continuous part deriving from the stress-deformation behaviour of the medium and a discontinuous part arising from the discontinuity, but in this case the displacements linked to the discontinuity are expressed by means of appropriate displacement influence functions existing in the literature for an edge dislocation embedded in a continuous linear elastic medium.

3. The resulting formulation

The combination of these two models leads to an original finite element formulation for a medium containing embedded discontinuities. The bulk material equations are the standard FEM expressions (Eq.1), while the discontinuity is separately discretized and a number of nodes is defined, for which expressions deriving from Eq.2 are written. Appropriate coupling equations are added, constructing a resolving system which will of course be non-symmetric.

The initial geometry of the discontinuities must be known; this is not a limitation to the model, since the major interest is not to predict crack propagation, but to investigate and calculate global stress-deformation behaviour of a material containing discontinuities. The main advantage is that linear elasticity is applicable. This mathematical approach is justified by actual observed behaviour: in fact, it is often the case in soil mechanics that the whole stress-deformation behaviour of a large soil mass is determined by the presence of discontinuities in its interior, rather than by some complex constitutive law pertaining to the entire soil volume. Progressive failure of slopes due to shear band propagation is a significant example.

The model has been validated in the case of a well-documented excavation in which the position of two shear bands can be inferred from experimental data. The results obtained from the model in terms of ground surface settlements match the measured values very closely.

4. Acknowledgements

This ongoing research is currently financed and supported within the research project: “PRIN 2017-2020 – Innovative monitoring and design strategies for sustainable landslide risk mitigation”.

5. References

- [1] Jirasek, M. (2000). Comparative study of finite elements with embedded cracks. *Comp. Meth. Appl. Mech. and Eng.*, **188**, 307–330.
- [2] Jirasek, M. (2002). Numerical modeling of strong discontinuities. *Revue française de génie civil*, **6**, 1133–1146.
- [3] Cleary, M.P. (1976). Continuously distributed dislocation model for shear bands in geological materials. *Int. J. Num. Meth. Eng.*, **10**, 679–702.
- [4] Narendran, V.M. & Cleary, M.P. (1984). Elastostatic interaction of multiple arbitrarily shaped cracks in plane inhomogeneous regions. *Eng. Fracture Mechanics*, **19**, 481–506.

A ISOGEOMETRIC FE METHOD FOR SATURATED AND UNSATURATED SOILS WITH SECOND GRADIENT REGULARIZATION

C. Plua¹, C. Tamagnini² and P. Besuelle¹

¹ *Université Grenoble Alpes, CNRS, Laboratoire 3SR, France*

² *University of Perugia, Perugia, Italy*

1. Motivation

It is well known that, upon failure of geotechnical structures, the displacement and strain fields are usually characterized by the presence of localized shear zones where high strain gradients occur, also called shear bands. This work aims at modeling the phenomenon of strain localization by means of a local second gradient regularization technique belonging to the family of generalized continua with microstructure [1]. This technique allows to obtain objective solutions free of the pathological mesh dependency which is observed in classical finite element solutions obtained with local constitutive models. In the numerical implementation of the theory, an Isogeometric Finite Element formulation has been adopted. The higher order of continuity guaranteed by the basis functions employed in IsoGeometric Analysis (IGA) [2] allows a straightforward implementation of the second gradient continuum approach, which requires C1–continuous approximations of the displacement field.

2. Coupled HM formulation

A fully coupled formulation for hydromechanical problems in unsaturated porous soils is considered in this work. Let \mathcal{S}_u and \mathcal{S}_w be the spaces of solutions for the fields (\mathbf{u}, p_w) , and \mathcal{V}_u and \mathcal{V}_w the corresponding space of variations. The variational formulation of the coupled flow and deformation problem in a unsaturated, 2nd gradient soil is given as follows: find $\mathbf{u} \in \mathcal{S}_u$ and $p_w \in \mathcal{S}_w$ so that, for any $\boldsymbol{\eta} \in \mathcal{V}_u$ and $\psi_w \in \mathcal{V}_w$, we have:

$$G(\mathbf{u}, p_w, \boldsymbol{\eta}) = \int_{\mathcal{B}} (\boldsymbol{\sigma}'' \cdot \nabla^s \boldsymbol{\eta} + \boldsymbol{\Sigma} \cdot \nabla \nabla \boldsymbol{\eta}) \, dv - \int_{\mathcal{B}} S_w p_w \nabla \cdot \boldsymbol{\eta} \, dv - \int_{\mathcal{B}} \rho \mathbf{b} \cdot \boldsymbol{\eta} \, dv + \int_{\partial_t \mathcal{B}} (\bar{\mathbf{t}} \cdot \boldsymbol{\eta} + \bar{\mathbf{T}} \cdot D\boldsymbol{\eta}) \, da = 0 \quad (1)$$

$$H(\mathbf{u}, p_w, \psi_w) = \int_{\mathcal{B}} \psi_w (C_w + C_s) \dot{p}_w \, dv + \int_{\mathcal{B}} \psi_w S_w \nabla \cdot \mathbf{v}^s \, dv - \int_{\mathcal{B}} \nabla \psi_w \cdot \mathbf{w}^w \, dv + \int_{\partial_q \mathcal{B}} \psi_w \bar{q}_w \, da = 0 \quad (2)$$

where, for what concerns the 2nd gradient contribution, $\boldsymbol{\Sigma}$ is the double stress tensor and $\bar{\mathbf{T}}$ the double traction vector on the boundary $\partial_t \mathcal{B}$, doing work on the normal derivative of the virtual displacement $D\boldsymbol{\eta} := (\nabla \boldsymbol{\eta}) \mathbf{n}$.

After numerical time integration of eq. (2) and the spatial discretization with NURBS–based shape functions, the solution of the discrete evolution problem at time station t_{n+1} , over the time step $\Delta t_{n+1} = t_{n+1} - t_n$, is provided by the following system of non–linear algebraic equations:

$$\mathbf{f}^{\text{int}}(\mathbf{d}_{n+1}) + \mathbf{f}_{\text{sg}}^{\text{int}}(\mathbf{d}_{n+1}) - \mathbf{g}_s(\mathbf{p}_{n+1}) - \mathbf{f}_{b,n+1}^{\text{ext}} - \mathbf{f}_{t,n+1}^{\text{ext}} - \mathbf{f}_{T,n+1}^{\text{ext}} = \mathbf{0} \quad (3)$$

$$s_w(\mathbf{p}_{n+1}) + \mathbf{g}_w(\mathbf{d}_{n+1}) - \Delta t_{n+1} \mathbf{h}^{\text{int}}(\mathbf{d}_{n+1}, \mathbf{p}_{n+1}) - \Delta t_{n+1} \mathbf{h}_{n+1}^{\text{ext}} = \mathbf{0} \quad (4)$$

where $\mathbf{f}_{\text{sg}}^{\text{int}}(\mathbf{d}_{n+1})$ and $\mathbf{f}_{T,n+1}^{\text{ext}}$ are the 2nd gradient contributions to the internal and external force vectors, respectively.

In order to capture the coupling effects between the solid and fluid phases induced by the irreversible dilation or contraction experienced by the solid skeleton upon loading, an advanced three-invariant isotropic hardening elastoplastic model for bonded soils [3] is adopted to describe the standard part of the constitutive model for the solid skeleton. An isotropic linear elastic relationship between the hyperstress tensor and second displacement gradient has been adopted for the second gradient part of the constitutive model, uncoupled from the standard part.

3. Selected results

The capabilities of the proposed approach are demonstrated by means of some representative IBVPs. Fig. 1 shows some results from the simulation of rainfall-induced failure of a partially saturated slope upon water infiltration from the ground surface.

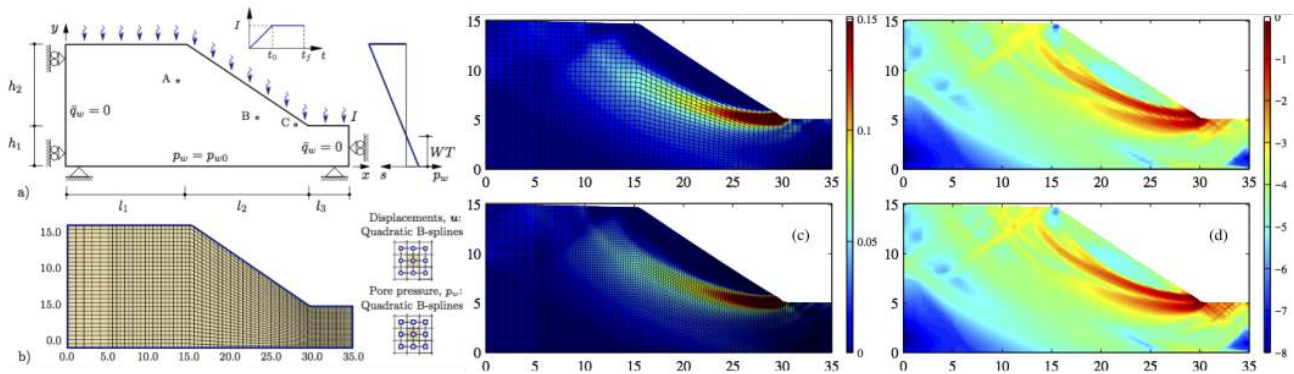


Figure 1. Rainfall-induced failure of a slope: a) problem geometry; b) domain discretization; c) contours of the second invariant of strain for two different discretizations; d) contours of the magnitude of $\nabla\nabla u$, in log-scale, for two different discretizations.

The results show that the proposed approach is capable of capturing the localized failure mechanism developed after about 70 h from the beginning of the rainfall, and provides a smooth resolution of the high pore pressure gradients observed close to the downward propagating wetting front. The solution obtained is independent from the discretization adopted. This proves that the second gradient regularization ensures objective results, effectively removing the mesh dependency of classical FE implementations in presence of strain localization.

References

- [1] Chambon, R., Caillerie, D., and Matsushima, T. (2001). Plastic continuum with microstructure, local second gradient theories for geomaterials: localization studies. *International Journal of Solids and Structures*, **38**, 8503–8527.
- [2] Cottrell, J. A., Hughes, T. J., and Bazilevs, Y. (2009). *Isogeometric analysis: toward integration of CAD and FEA*. John Wiley & Sons.
- [3] Tamagnini, C., Castellanza, R., and Nova, R. (2002). A generalized backward euler algorithm for the numerical integration of an isotropic hardening elastoplastic model for mechanical and chemical degradation of bonded geomaterials. *Int. J. Num. Anal. Meth. Geomech.*, **26**, 963–1004.

MICROMECHANICAL STUDY OF INSTABILITY IN GRANULAR MATERIALS USING μ -GM CONSTITUTIVE MODEL

M. Pouragha¹ and R. Wan¹

¹ *University of Calgary, Calgary, AB, Canada*

1. Introduction

Previous studies on the micromechanics of granular materials have succeeded in relating macroscopic variables such as stress and strain to their microscopic origins in relation to contact forces and displacements [1, 2]. Whereas such micro-macro relations have often been implemented into continuum based constitutive models, a coherent constitutive framework which properly relates stresses to strains through their respective multiscale expressions is still missing in the literature.

Following a decomposition of particle-scale mechanisms [3], the current study presents a novel micromechanical framework, named μ -GM, from which a rate-independent, incrementally nonlinear constitutive model naturally emerges based on multiscale expressions for stress and strain [4, 5]. The developed model is next implemented into a Finite Element Modelling (FEM) solver to investigate the strain localization and instability characteristics of granular materials. The results indeed show that the microstructure within the shear band matches that at critical state in diffuse failure. Further investigations into the spatial variation of microvariables inside, outside, and near the shear band shed new lights into the micromechanical origins of instabilities in granular materials.

2. μ -GM Model

The modelling procedure starts from the basic assumption that increments of stress and strain in granular materials can be expressed in terms of a common statistical descriptors:

$$\dot{\boldsymbol{\sigma}} = \mathbf{K} \dot{\mathbf{S}}, \quad \dot{\boldsymbol{\varepsilon}} = \mathbf{L} \dot{\mathbf{S}} \quad (1)$$

where $\{\boldsymbol{\sigma}, \boldsymbol{\varepsilon} \in \mathbb{R}^m\}$ are stress and strain vectors, and $\{\mathbf{S} \in \mathbb{R}^l\}$ is a vector that contains prominent statistical microvariables, such as anisotropy parameters, coordination number and the likes, with $l \geq m$. The static and kinematic transfer matrices, \mathbf{K} and \mathbf{L} , denote $\mathbb{R}^l \rightarrow \mathbb{R}^m$ transformations that are not invertible. Thus, for a constitutive model to emerge, $l - m$ additional relations between elements of $\{\mathbf{S} \in \mathbb{R}^l\}$ should exist to render the system of equations deterministic. These additional ‘‘consistency relations’’ describe the interdependencies among the microvariables.

Based on the observations in [3], the microvariables are assumed to evolve due to non-dissipative (nd) and dissipative (d) mechanisms whose effects are assumed to be additive with reference to two different kinematical transformations, \mathbf{L}_{nd} , and \mathbf{L}_d . Thus,

$$\dot{\mathbf{S}} = \dot{\mathbf{S}}_{nd} + \dot{\mathbf{S}}_d, \quad \dot{\boldsymbol{\varepsilon}}_{nd} = \mathbf{L}_{nd} \dot{\mathbf{S}}_{nd}, \quad \dot{\boldsymbol{\varepsilon}}_d = \mathbf{L}_d \dot{\mathbf{S}}_d \quad (2)$$

with total strain increment being $\dot{\boldsymbol{\varepsilon}} = \dot{\boldsymbol{\varepsilon}}_{nd} + \dot{\boldsymbol{\varepsilon}}_d$. The static transformation matrix, \mathbf{K} , is the same for both mechanisms. The consistency relations are also assumed to be expressed for each mechanism separately, i.e.

$$G_{nd}^i(\mathbf{S}_{nd}) = 0 \rightarrow \frac{\partial G_{nd}^i}{\partial \mathbf{S}_{nd}} \dot{\mathbf{S}}_{nd} = 0, \quad G_d^i(\mathbf{S}_d) = 0 \rightarrow \frac{\partial G_d^i}{\partial \mathbf{S}_d} \dot{\mathbf{S}}_d = 0 \quad (3)$$

With enough consistency relations, and a variable β to describe the evolution of the two mechanisms [4], the system of equations can be closed and a constitutive model emerges in the following form:

$$\dot{\boldsymbol{\sigma}} = \mathbf{D} \dot{\boldsymbol{\varepsilon}}, \quad \mathbf{D} = \beta \mathbf{D}_{nd} + (1 - \beta) \mathbf{D}_d \quad (4)$$

The system of equations in its general form also predicts the evolution of microvariables in \mathbf{S} which can be used to incrementally update the state of material.

3. FEM Simulations and Discussion

The developed model has been implemented into FEM to simulate the response of an initially dense sample to biaxial loading condition. With direct access to microvariables, the constitutive model enables us to visualize the evolution of the microstructure in different failure modes, see Fig. 1.

Figures 1-(a), (b), (c), and (d) present the distribution of deviatoric strain and void ratio, as well as coordination number and fabric anisotropy. As expected, the void ratio within the shear band is larger than the one outside it. While not presented here, the stress-strain response of the Gauss points within the shear band approached the critical state, indicating a locally diffuse failure mode. The larger void ratio within the shear band is accompanied by smaller values of coordination number. Intriguingly, Fig. 1-(d) shows that the fabric anisotropy is maximum at the boundary of shear band. This has been further investigated in Figs. 1-(e), (f), and (g) where the evolution of deviatoric stress (q), volumetric strain, and the fabric response are presented. The trends in these figures indicate that the fabric anisotropy inside and outside the shear band decreases as the former approaches the critical state, and the latter undergoes unloading. However, a point on the boundary of shear band follows a path with more pronounced volume change that does not approach the critical state.

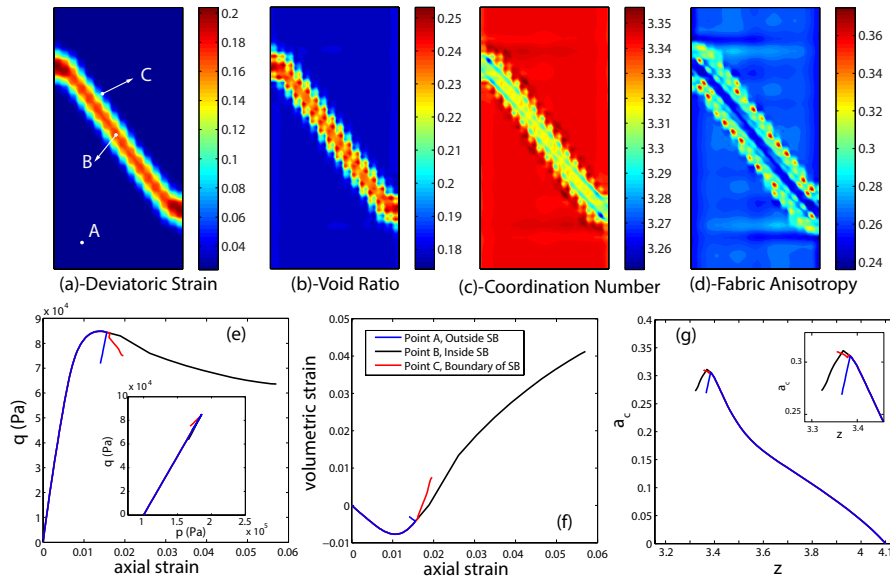


Figure 1. Spatial distribution of (a) deviatoric strain, (b) void ratio, (c) coordination number, and (d) fabric anisotropy. Sub-figure (e), (f), and (g) present the variation of deviatoric stress, volumetric strain and the fabric response during the loading for three selected points inside, outside and on the boundary of shear band.

References

- [1] Rothenburg, L. and Bathurst, R. (1989). Analytical study of induced anisotropy in idealized granular materials. *Géotechnique*, **39**, 601–614.
- [2] Pouragha, M. and Wan, R. (2016). Strain in granular media—a probabilistic approach to Dirichlet tessellation. *J. Eng. Mech.*, p. C4016002.
- [3] Pouragha, M. and Wan, R. (2017). Non-dissipative structural evolutions in granular materials within the small strain range. *Int. J. Solids Struct.*, **110**, 94–105.
- [4] Pouragha, M. and Wan, R. μ -GM: A purely micromechanical constitutive model for granular materials. *in preparation*.
- [5] Pouragha, M., Wan, R., and Gong, X. (2017). Instability analysis of granular media via a purely micromechanical constitutive model. *IWBDG2017*, pp. 507–513, Springer, Cham.

MODELING OF LOCALIZED DAMAGE IN THE PRESENCE OF CHEMO-MECHANICAL INTERACTION

S. Pietruszczak¹ and S. Moallemi²

¹*McMaster University, Hamilton, Ont., Canada*

²*Rocscience Inc., Toronto, Ont.*

1. Introduction

This presentation gives an overview of the research conducted by the authors in relation to description of the onset and propagation of localized damage in cohesive-frictional materials. The first part provides a brief outline of the formulation of the problem. The propagation of damage is described in terms of an embedded discontinuity approach, which employs volume averaging [1-3]. The approach incorporates the notion of a ‘characteristic dimension’, which is explicitly defined as the ratio of the area of macrocrack to the selected reference volume, the latter identified with that of a finite element containing the discontinuity. Some numerical examples are provided, which include a mixed-mode fracture test as well as a three-point bending of a specimen with an inclined notch (3D case). The next part of this work deals with description of chemo-mechanical interaction in geomaterials and its coupling with the onset and propagation of localized damage. First, a general formulation of the problem is reviewed, which incorporates the framework of chemo-plasticity. The areas of applications of this approach include description of the intergranular pressure solution in chalk as well as the alkali-aggregate reaction in concrete. The focus in the presentation is on the latter topic. In particular, the issue of the size effect in concrete structures, subjected to a broad range of loading conditions that include a chemo-mechanical coupling, is addressed. Numerical examples deal with a series of three-point bending tests as well as compression tests. For continuing alkali-silica reaction, it is demonstrated that by increasing the size of the structure, a spontaneous failure may occur under a sustained load. It is clearly shown that the size effect is associated with propagation of localized damage whose description requires an explicit definition of a characteristic length.

2. Modeling of fracture propagation via a constitutive relation with embedded discontinuity

The onset of localized deformation and the orientation of the localization plane can be defined based on the bifurcation criterion. The damage propagation process is modelled through an enhanced discrete representation of the constitutive law with embedded discontinuity [3]. For a discontinuous motion, the symmetric part of the velocity gradient is defined as

$$\nabla^S \mathbf{v}(\mathbf{x}, t) = \nabla^S \hat{\mathbf{v}}(\mathbf{x}, t) + \mathcal{H}(\phi) \nabla^S \tilde{\mathbf{v}}(\mathbf{x}, t) + \delta(\phi) (\mathbf{n} \otimes \tilde{\mathbf{v}})^S$$

Here, $\hat{\mathbf{v}}$ and $\tilde{\mathbf{v}}$ are two continuous functions, $\mathcal{H}(\phi)$ is the Heaviside step function and $\phi = \phi(\mathbf{x}, t)$ is the level-set function that represents the geometry of the crack. Note that $\nabla^S \mathcal{H}(\phi) = \delta(\phi) \nabla \phi$, where δ is the Dirac delta function and the gradient of a level-set function represents the normal to the surface, i.e. $\nabla \phi = \mathbf{n}$. Taking the volume average of the last term in the equation above, which is associated with localized deformation along the macrocrack, leads to a resolution of the total strain rate into two elementary parts. The first one, denoted as $\dot{\hat{\boldsymbol{\epsilon}}}$, is associated with the intact part of the reference volume, while the other one, referred to as $\dot{\tilde{\boldsymbol{\epsilon}}}$, represents the discontinuous motion along the crack averaged over this volume, i.e.

$$\dot{\boldsymbol{\epsilon}} = \dot{\hat{\boldsymbol{\epsilon}}} + \dot{\tilde{\boldsymbol{\epsilon}}} \quad \text{where} \quad \dot{\tilde{\boldsymbol{\epsilon}}} = \chi (\mathbf{n} \otimes \dot{\mathbf{g}})^S$$

In the expression above, $\dot{\mathbf{g}}$ is the velocity discontinuity along the interface, i.e. $\dot{\mathbf{g}} = \llbracket \mathbf{v} \rrbracket = \llbracket \mathcal{H} \rrbracket \tilde{\mathbf{v}}$ and

$\chi = \Delta a / \Delta v$ where Δa represents the surface area of the crack within the considered referential volume Δv . By imposing now the continuity of traction along the interface, the constitutive law is obtained, viz.

$$\dot{\boldsymbol{\sigma}} = \tilde{\mathbb{D}} : \dot{\boldsymbol{\varepsilon}} ; \quad \tilde{\mathbb{D}} = \mathbb{D} - \mathbb{D} : \mathbb{E} : \mathbb{D}, \quad \mathbb{E} = \chi \mathbf{n} \otimes (\mathbf{K} + \chi \mathbf{n} \cdot \mathbb{D} \cdot \mathbf{n})^{-1} \otimes \mathbf{n}$$

where \mathbf{K} is the tangential operator which defines the interfacial properties. The latter can be identified by invoking, for example, a plasticity framework that incorporates strain-softening and relates the velocity discontinuity to the rate of traction. In the numerical implementation, the volume of the finite element is perceived as a reference volume and the macrocrack is traced in a discrete manner by using the level-set method. Within this scheme, the failure/bifurcation criterion is checked in the candidate elements adjacent to the crack tip and, if met, the average direction of propagation is established. In 3D case, in order to avoid numerical difficulties associated with an abrupt change in the crack surface orientation, a crack smoothing algorithm has been implemented.

In order to illustrate the framework some numerical examples are provided. The first one deals with simulation of a mixed-mode cracking test and the results based on embedded discontinuity approach are directly compared with XFEM simulations. The predictions from both these methodologies are virtually identical and are consistent with the experimental data; this gives the advantage to the former scheme in view of its simplicity in the numerical implementation. The follow up example involves numerical analysis of fracture propagation in 3D conditions. In particular, a three-point bending test is simulated in which the fracture pattern involves a progressive twisting of the crack surface and its propagation in the direction aligned with that of the prescribed displacements.

The next part involves modeling of the mechanical response associated with a chemo-mechanical interaction and the evolution of localized damage resulting from this coupling. First, a chemo-plasticity framework is outlined for which the kinetics of the reaction is examined in the context of the alkali-silica reaction in concrete/reinforced concrete. The numerical examples are focused on the assessment of deterministic size effect in concrete structures experiencing different fracture modes that include tensile failure, formation of macrocracks in compression regime as well as damage due to chemical interaction (cf. [4]). It is clearly shown that the size effect is triggered by the onset and propagation of localized damage; the latter associated with strain-softening, whose rate is controlled by a ‘characteristic length’ that needs to be uniquely defined. For continuing alkali-silica reaction, it is demonstrated that, by increasing the size of the structure, a spontaneous failure may occur under a sustained load.

5. References

- [1] Pietruszczak, S. & Mróz, Z. (1981). Finite element analysis of deformation of strain softening materials. *Int. J. Num. Meth. Eng.*, **17**, 327-334.
- [2] Pietruszczak, S. (1999). On homogeneous and localized deformation in water-infiltrated soils. *Int. J. Damage Mech.*, **8**, 233-253.
- [3] Haghghat, E. & Pietruszczak, S. (2015). On modeling of discrete propagation of localized damage in cohesive-frictional materials. *Int. J. Num. Anal. Meth. Geomech.*, **39**, 1774-1790.
- [4] Moalemmi, S., Pietruszczak, S. & Mroz, Z. (2017). Deterministic size effect in concrete structures with account for chemo-mechanical loading, *Int. J. Comp. Struct.*, **182**, 74-86.

3. Modelling of thermo-hydro-mechanical coupling and other transient problems

THERMO-POROMECHANICS OF A FLUID INCLUSION

A.P.S. Selvadurai

McGill University, Montréal, Canada

1. Introduction

The development environmentally effective engineering strategies for the long-term disposal and storage of heat-emitting nuclear fuel waste continues to be a challenge to many countries that rely on nuclear power for energy production. Deep geologic disposal concepts for the heat-emitting nuclear waste are favored by many countries. Even though several fabricated metallic and geologic barriers are used to retard radionuclides migration, the rock formations in which a deep geologic repository is located is expected to provide the greatest retardation potential for the release of radionuclides to the environment. The candidate geologic formations tend to vary from country to country and these include the argillaceous boom clays in Belgium, the granitic rock formations in Canada, Finland, Switzerland and Sweden, the Callovo-Oxfordian clay-rock formations in France, the Opalinus clays in Switzerland and the argillaceous rocks in Canada. These rocks present unique research challenges in terms of the characterization of the thermo-hydro-mechanical behaviour of the formations so that the performance of a deep geologic repository can be assessed for the validation of the proof of concept. A recent research activity of the Canadian proposals for the siting of a deep geologic repository for the storage of non-heat emitting low and intermediate level nuclear waste focuses on the argillaceous rock formations of southern Ontario and more specifically the argillaceous Cobourg limestone. This rock formation is characterized by its extremely low permeability (10^{-23} m² to 10^{-20} m²) and heterogeneity that contributes to a rock fabric with lighter nodular regions of calcite and dolomite separated by darker argillaceous partings with a composition of calcite, dolomite, quartz and a clay fraction. From a visual perspective, the Cobourg limestone is heterogeneous with influences of scale (Figure 1).

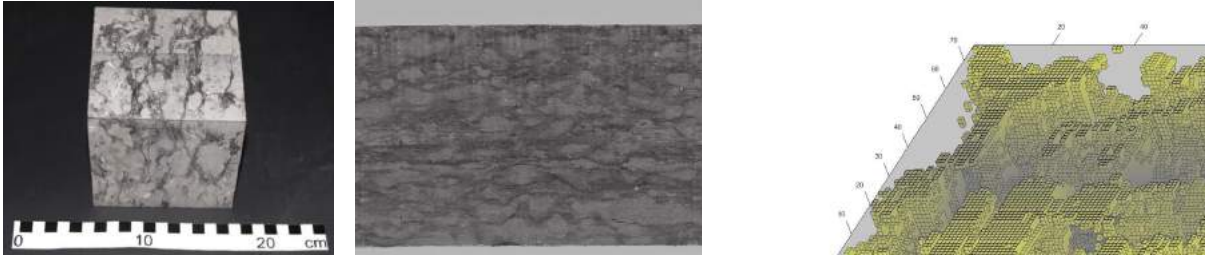


Figure 1. The fabric of the Cobourg limestone

2. Theoretical Developments

The theory of thermo-poroelasticity is the simplest extension of Biot's classical theory of poroelasticity [1] to include influences of heat. The classical theory thermo-poroelasticity has a wide range of applications with relevance to geological disposal of heat emitting nuclear fuel waste [2], geothermal heat extraction, energy resources extraction and in geologic sequestration of greenhouse gases in supercritical form [3]. In instances where geologic disposal of heat emitting waste is contemplated, the geologic medium is expected to be relatively free of fractures so that the mode of heat transfer is primarily through conduction. Further simplifications can be introduced by developing a theory of thermo-poroelasticity where the heat conduction process is uncoupled from the elastic deformations and the fluid transport processes. The governing equations take the forms

$$(K_D + \frac{G_D}{3})\nabla(\nabla \cdot \mathbf{u}) + G_D \nabla^2 \mathbf{u} - \alpha \nabla p - K_D \beta_s \nabla T = \mathbf{0} \quad (1)$$

$$S \frac{\partial p}{\partial t} + \nabla \cdot \left[-\frac{\mathbf{K}}{\mu(T)} \nabla p \right] + \alpha \frac{\partial(\nabla \cdot \mathbf{u})}{\partial t} - [n\beta_f(T) + (\alpha - n)\beta_s] \frac{\partial T}{\partial t} = 0 \quad (2)$$

$$c_p^*(T) \frac{\partial T}{\partial t} - k_c^* \nabla^2 T = 0 \quad (3)$$

where the dependent variables are the displacement components, \mathbf{u} the pore fluid pressure p and the temperature T . The application of continuum theories represented by (1) to (3), must recognize the heterogeneous character of the a rock similar to the Cobourg when testing laboratory samples of the rock and the development of effective properties of the heterogeneous rock that can be used in analytical and computational modelling. For example, the *Voigt-Reuss-Hill* estimates for the skeletal bulk and shear moduli of the lighter and darker rock fractions can be used in conjunction with *Hashin-Shtrikman* bounds to develop the deformability characteristics of the heterogeneous rock. Similar concepts can be applied to generate other material parameters encountered in (1) to (3). The suitability of the approach needs to be investigated through laboratory-scale investigations. In this research, we focus attention on the modelling of a thermo-poro-elastic behaviour of fluid inclusion that is located within the sample of the Cobourg limestone. The direct measurement of thermally-induced pore fluid pressure generation in very low permeability rock is a difficult task because of the anomaly that can be created by a pore fluid pressure measuring device. The approach requires the thermo-poromechanical characterization of the rock as well as the study of a bench-scale heater experiment [4] to observe the cavity pressure rise and decay following the boundary heating of the specimen. The approach also requires the development of micrographic images of the Cobourg Limestone fabric that is used to establish the volume fractions of the mineralogical composition of the rock that is used to estimate, among others, the Biot coefficient used in the THM modelling.

3. Concluding remarks

The weakly coupled form of thermo-hydro-mechanical behaviour of rocks is a suitable approximation for intact rocks where the heat transfer is a conductive process. With heterogeneous rocks such as the Cobourg limestone, theories of effective material behaviour can be used to develop estimates for the mechanical, physical and transport parameters. The paper discusses the development of innovative experimental configurations and techniques that can be used to examine the applicability of the reduced thermo-poroelastic modelling to heterogeneous poroelastic media. Combined approaches involving conceptual model development, computational implementations and innovative experimental simulations that are well-formulated initial boundary value problems are essential for validating the multiphase phenomena, which will ultimately be used in establishing reliable strategies for deep geologic disposal of heat-emitting nuclear waste.

5. References

- [1] Biot, M.A. (1941). General theory of three-dimensional consolidation, *J. Appl. Phys.*, **12**, 155-164.
- [2] Selvadurai, A.P.S. & Nguyen, T.S. (1995) Computational modelling of isothermal consolidation of fractured porous media, *Comp. Geotech.*, **17**, 39-73.
- [3] Selvadurai, A.P.S. & Suvorov, A.P. (2016) *Thermo-Poroelasticity and Geomechanics*, Cambridge University Press, Cambridge.
- [4] Selvadurai, A.P.S. & Najari, M. (2017). Thermo-hydro-mechanical behaviour of the argillaceous Cobourg limestone, *J. Geophysical Research. Solid Earth*, **122**, doi:10.1002/2016JB013744.

THCM ANALYSIS OF SHALES

L. Laloui¹, A. Ferrari¹, A. Minardi¹

¹ *Laboratory for Soil Mechanics – Swiss Federal Institute of Technology in Lausanne (EPFL),
Lausanne, Switzerland*

A constant growing interest in the geomechanical behavior of shales has risen in the last decades due their involvement in new energy-related fields such as the hydrocarbon extraction from unconventional reservoirs, the deep geothermal energy, the sequestration of CO₂, and the geological storage of nuclear waste. In this context, fundamental issues are related to the involved complex multiphysical conditions where temperature, chemistry, and hydraulics are expected to play a major in controlling the mechanical response of these geomaterials. This lecture introduces the most recent advances for the laboratory testing and modelling of the THCM behaviour of shales, highlighting the effects of temperature, partial saturation (suction), and chemistry (pore fluid composition) on the mechanical behaviour of shales.

The hydro-mechanical interaction is a primary aspect to analyze the behavior of shales. Due to the low permeability and high stiffness, the coupling effect of mechanical stress and pore water pressure changes is a challenging feature to be assessed. Experimental procedure and testing equipment are developed to face these challenges and quantify the key hydro-mechanical parameters controlling the response of shales. A high-pressure oedometric cell allows for the analysis of the transition from the pre-yield behavior to the normally consolidated state, and the evaluation of the shales' compressibility. The analysis of the settlement versus time curves yields information on the consolidation, the permeability and the creep of the material as a function of the void ratio [1]. An advance thermo-hydro-mechanical triaxial device allows the analysis of stiffness and strength properties of shales. A reliable experimental procedure to test shales in drained conditions is presented in [2]. Main results highlight the anisotropic elastic behavior of the tested shale and the stress dependence of the Young's modulus. The observed mechanical response before the failure is highly nonlinear, with irreversible deformation exhibited upon unloading. These features clearly support the need of an elasto-plastic theoretical framework.

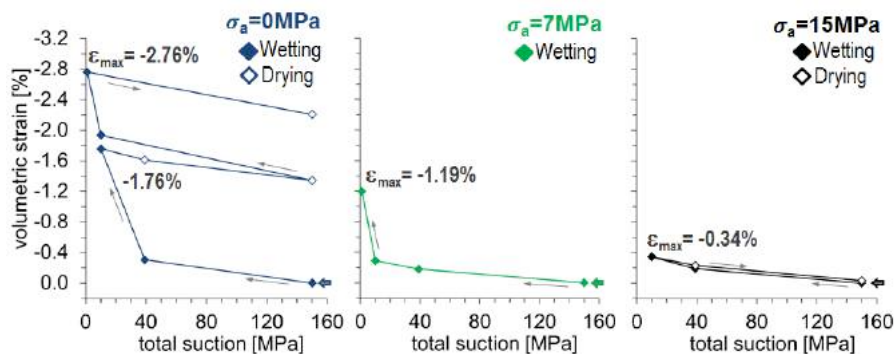


Figure 1. Volumetric response of a gas shale to total suction changes [5].

The behavior of shales is expected to change significantly when they move to partially saturated conditions. A workflow established for the analysis of the water retention behavior of shales in non-isochoric conditions has been developed in [3]; the method allows for the determination of the main drying and wetting paths of the water retention curves of shale. Further experimental evidence presented in [4] and [5] demonstrate also the impact of wetting and drying

processes on the anisotropic volumetric response shales. Figure 1 shows the volumetric response of a gas shale undergoing wetting-drying cycles performed at different mechanical stress; the graphs highlight the irreversible response and the impact of the stress on the swelling behavior.

The impact of temperature and chemical composition of pore fluid on the mechanical behavior of shales is analyzed by ad-hoc testing layouts based on the high-pressure oedometric cell previously introduced. Figure 2 shows the response of a shale to thermal loadings [6]; the graph highlight the dependency of the material's behavior on its overconsolidated state. Further results demonstrate the impact of temperature on the yield stress of the material.

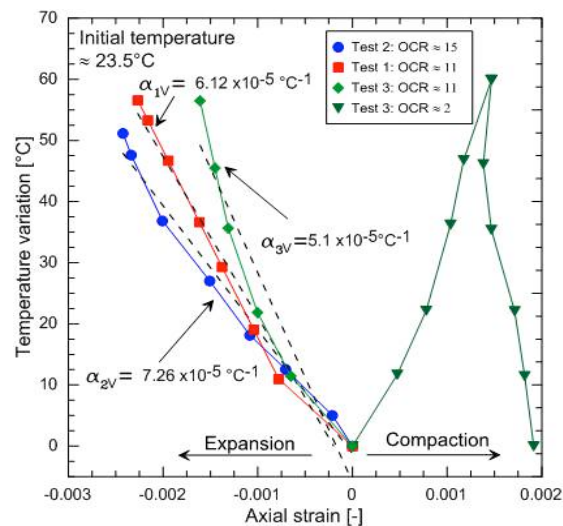


Figure 2. Volumetric response of a shale induced by thermal loadings [6].

In conclusion, the advanced experimental characterization of shales represents a key ingredient for a comprehensive analysis of their behavior and the development of constitutive models capable to reproduce their response in multiphysical conditions. The observed behavior highlights the need of an elasto-plastic theoretical framework to properly predict the response of shales when subjected to multiphysical loadings.

References

- [1] Ferrari A., Favero V., Laloui L. (2016). One-dimensional compression and consolidation of shales. *International Journal of Rock Mechanics and Mining Sciences* 88:286-300.
- [2] Favero, V., Ferrari, A. and Laloui, L. (2017). Anisotropic behaviour of Opalinus Clay through consolidated and drained triaxial testing in saturated conditions. *Rock Mechanics and Rock Engineering*, pp.1-15.
- [3] Ferrari A, Favero V, Marschall P, Laloui L, (2014). Experimental analysis of the water retention behaviour of shales. *International Journal of Rock Mechanics and Mining Sciences*. 72, pp. 61–70.
- [4] Minardi A., Crisci E., Ferrari A., Laloui L. (2016). Anisotropic volumetric behaviour of Opalinus Clay shale upon suction variation. *Géotechnique Letters* 6(2):144-148.
- [5] Minardi A., Ferrari A., Ewy R., Laloui L. (2018). The impact of the volumetric swelling behavior on the water uptake of gas shale. *Journal of Natural Gas Science and Engineering* 49(1):132-44.
- [6] Favero, V., Ferrari, A. and Laloui, L. (2016). Thermo-mechanical volume change behaviour of Opalinus Clay. *International Journal of Rock Mechanics and Mining Sciences*, 90, pp.15-25.

HYDROMECHANICAL BEHAVIOUR OF ARGILLACEOUS ROCKS: CONSTITUTIVE LAW AND APPLICATIONS

M. Mánica¹, A. Gens¹, J. Vaunat¹ and D. Ruiz¹
¹Universitat Politècnica de Catalunya, BarcelonaTech

1. General

The hydromechanical behaviour of argillaceous rocks exhibits a series of characteristics such as plastic strains before peak, softening, anisotropy, time-dependency (creep) and variation of permeability with damage [1]. Those features must be taken into account in the development of constitutive laws if realistic results are to be obtained. Once an appropriate constitutive model is in place, it is possible to tackle, by numerical methods, boundary value problems representing engineering problems.

2. Constitutive model

The constitutive model has been developed in the framework of elasto-plasticity using corner-smoothed Mohr-Coulomb yield surfaces that account for hardening before peak strength and softening afterwards (see Figure 1). The corresponding increase and reduction of friction angle and cohesion are controlled by the accumulated shear plastic strain that acts as the hardening parameter.

To this basic scheme other important features have been added:

- Non-associated plasticity to prevent excessive dilatancy.
- Plastic anisotropy following the stress-scaling procedure described in Manica et al. [2].
- Time-dependent visco-plastic response to account for creep, adopting a modified form of Lemaitre's law

In addition, a successful representation of the coupled hydromechanical behaviour of the rock requires the incorporation of permeability enhancement due to rock damage. Although the real situation involves the generation of cracks and other discontinuities, here a continuum approach, based on the variation of permeability on the magnitude of plastic strains (represented by the value of the plastic multiplier), has been adopted. The constitutive model is fully described in [3].

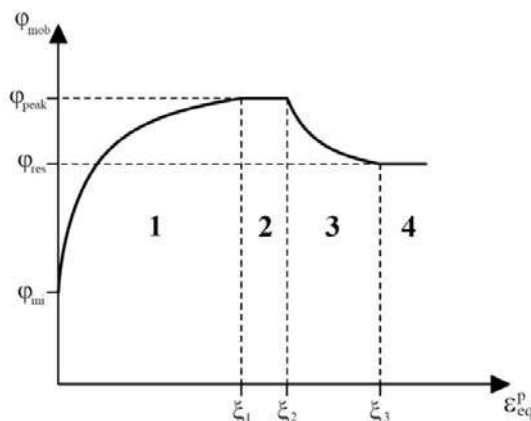


Figure 1: Evolution of friction angle in hardening and softening.

3. Analysis of an excavation

A coupled hydromechanical analysis has been performed to simulate in an approximate manner the excavation of a drift in the Meuse/Haute Marne Underground Research laboratory in Eastern France [4]. The rock is a Callovo-Oxfordian claystone (COx). The drift has a 2.6 m

diameter circular section and has been excavated with a road header at 490 m depth. The drift alignment was parallel to the major horizontal principal stress. As a result, the state of stress perpendicular to the axis of the drift was practically isotropic with $\sigma_v = 12.7$ and $\sigma_h = 12.4$ MPa. The in-situ pore water pressure in zones not affected by excavations is 4.7 MPa. The excavation was simulated in plane strain using a deconfinement curve. The parameters for the constitutive model have been mainly obtained from laboratory tests on COx specimens.

As Figure 2 shows, a quite reasonable reproduction of tunnel convergences and pore pressures is achieved. It can be observed that, in spite of a practically isotropic stress state (in cross-section), horizontal movements are significantly higher than vertical ones, a clear indication of the anisotropy of the rock. The results from the simulation exhibit also anisotropy but the actual degree of anisotropy is underestimated. The time-dependent displacements observed at long times are well reproduced by the creep component of the constitutive model. The model also successfully accounts for the pore pressure increase in PRE_04 when excavation approaches as well as for the observed evolution of the PRE_05 pressure. This good agreement has been achieved in spite of the fact that the 2D plane-strain representation of the real excavation can only be approximate. It should also be noted that the rapid reduction of the water pressures in PRE_02 and PRE_03 can only be obtained only if the increase of permeability due to damage is considered

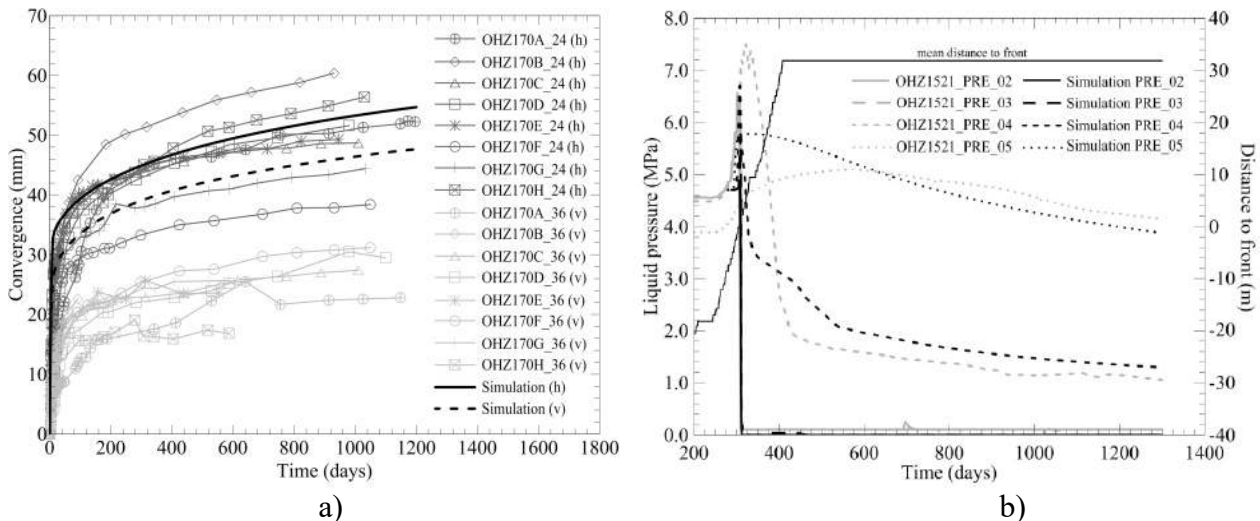


Figure 2. Analysis of a tunnel excavation. a) Observed and computed horizontal and vertical convergences, b) Observed and computed pore pressures in borehole OHZ1521

5. References

- [1] Gens, A. (2013) On the hydromechanical behaviour of argillaceous hard soils-weak rocks. In: Anagnostopoulos A et al., editors. *Proc. 15th European Conference on Soil Mechanics and Geotechnical Engineering*, Athens, Greece. Part 4, IOS Press, Amsterdam, 2013, 71–118.
- [2] Manica, M., Gens, A., Vaunat J., & Ruiz, D.F.. (2016). A cross-anisotropic formulation for elasto-plastic models. *Geotechnique Letters*, **6**, 156–162.
- [3] Manica, M., Gens, A., Vaunat J., & Ruiz, D.F.. (2017). A time-dependent anisotropic model for argillaceous rocks. Application to an underground excavation in Callovo-Oxfordian claystone. *Computers and Geotechnics*, **85**, 341-350.
- [4] Seyed, D., G. Armand, G. & A. Noiret, A. (2017). “Transverse Action”. A model benchmark exercise for numerical analysis of the Callovo-Oxfordian claystone hydromechanical response to excavation operations. *Computers and Geotechnics*, **85**, 287-305.

ON THE USE OF NITROGEN TO MITIGATE COAL SWELLING DURING CARBON SEQUESTRATION

L.J. Hosking¹ and H.R. Thomas¹

¹Geoenvironmental Research Centre, Cardiff School of Engineering, Cardiff University, Queen's Buildings, Newport Road, Cardiff, CF24 3AA, UK

1. Introduction

Carbon sequestration in coal has in principle some very well-established benefits and drawbacks. Coal can store large amounts of carbon dioxide (CO₂) in the adsorbed phase, even at relatively low pressures, leading to reduced compression and injection costs [1]. Moreover, the adsorption of CO₂ reduces the risk of its migration, providing a more secure store compared to other candidate reservoirs. Another important benefit is the opportunity to offset capital and operational costs by using the injected CO₂ for enhanced coalbed methane (ECBM) recovery.

Whilst field trials of carbon sequestration in coalbeds around the world have to varying levels reflected the benefits described above, the main technical challenge faced has been a low initial CO₂ injectivity followed by a further permeability loss as the coal swells in response to CO₂ adsorption [2]. Overcoming the challenge posed by coal swelling is critical for the future prospects of carbon sequestration in coal. The present work addresses this issue by examining the potential role of nitrogen (N₂) in mitigating coal swelling, the premise being results from the Yubari field trial in Japan. A series of numerical simulations have been performed to study carbon sequestration and coal permeability changes for both the injection of pure CO₂ and CO₂-rich binary gas with N₂.

2. Background of the theoretical formulation and numerical model

A coupled THCM model developed by Thomas and co-workers, e.g. [3][4], forms the basis for the numerical simulations presented in this work. The model employs a mechanistic approach to solve for heat transfer, moisture and chemical/gas transport, and mechanical behaviour. The model has been extensively verified and applied to simulate the reactive transport of multicomponent chemicals and gas in a range of geological media, e.g. [4][5]. The numerical simulations presented in this work have been performed using the reactive gas transport module of the model assuming the isothermal flow of a single phase, multicomponent gas in a coalbed described as a single porosity equivalent continuum with homogenous, isotropic and elastic properties.

3. Description of the numerical simulations performed

Three simulations have been performed for carbon sequestration in a hypothetically isolated, axisymmetric coalbed with 1 m thickness and 200.1 m radius (0.1 m radius injection well). Test A dealt with the injection of 6 tCO₂ over the 30 day simulation period. Test B again considered the injection of 6 tCO₂, this time mixed with N₂ added at 10% mole fraction. Test C considered the injection of 6 t of mixed gas comprising 90% CO₂ and 10% N₂ by mass fraction. The physical and chemical properties of coal were based on the Bowen Basin coal tested by Connell et al. [6].

The decision to deal with fixed quantities of CO₂ injection was made in preference to fixing the injection pressure to better reflect the practical reality of a carbon sequestration project, where operators would be more concerned with maintaining a certain injection rate at the most economical (i.e. lowest) injection pressure. Hence, the results of the numerical simulations are presented in terms of the predicted evolution of the gas pressure and coalbed permeability at the injection point. Analysis of the gas injection pressure required to maintain the specified rate of sequestration is then used as a simple proxy to economic cost. The permeability is presented to show the different responses of the coalbed for the injection scenarios considered.

4. Conclusions based on the analysis of injection pressures and coal permeability changes

Figure 1 shows, in all cases, the expected trend of decreasing permeability consequent increases in the injection pressure required to maintain the prescribed sequestration rates. It can be seen that N₂ had a negligible impact on the extent of coal swelling compared to the benchmark case (Test A), whether added to the 6 tCO₂ by 10% mole fraction (Test B) or as a substitute for 0.6 t of the CO₂ (Test C). Furthermore, both cases resulted in a higher injection pressure and hence an implied weaker economic case. In conclusion, mixing N₂ into the injected gas stream was not effective in mitigating coal swelling under the conditions considered, and was actually detrimental to the viability of the sequestration options explored. Based on the results of the Yubari project in Japan, further work is recommended to examine whether the cyclic injection of CO₂ and N₂ can yield improved results.

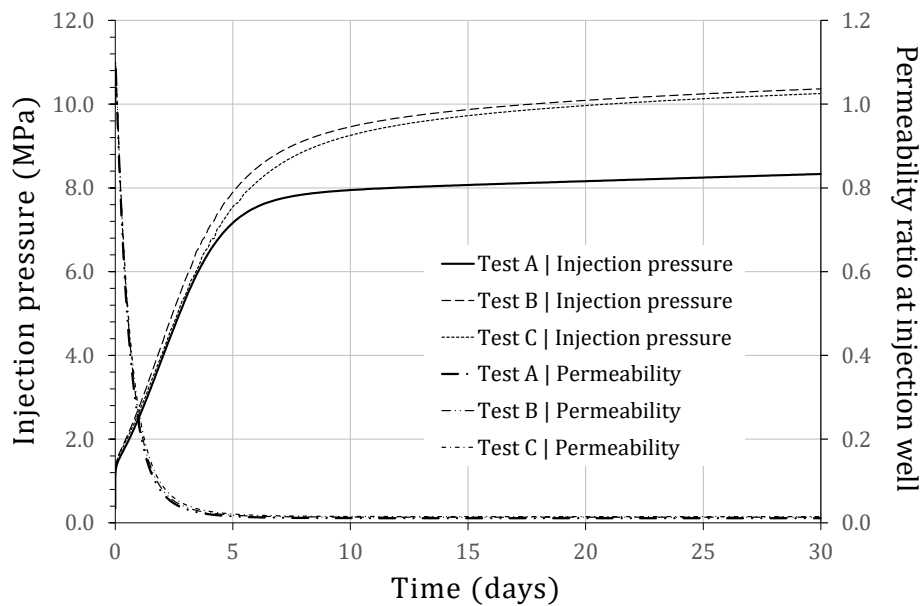


Figure 1. Evolution of injection pressure and coal permeability at the injection well for each Test.

5. References

- [1] Pan, Z., et al., CO₂ storage in coal to enhance coalbed methane recovery: a review of field experiments in China. *International Geology Review*, 2017: p. 1-23.
- [2] Reeves, S.R., An overview of CO₂-ECBM and sequestration in coal seams, in Carbon dioxide sequestration in geological media - State of the science: AAPG studies in geology. 2009. p. 17-32.
- [3] Thomas, H.R. and Y. He, Modelling the behaviour of unsaturated soil using an elasto-plastic constitutive relationship. *Géotechnique*, 1998. 48(5): p. 589-603.
- [4] Sedighi, M., H.R. Thomas, and P.J. Vardon, Reactive Transport of Chemicals in Unsaturated Soils: Numerical Model Development and Verification. *Canadian Geotechnical Journal*, 2016. 53(1): p. 162-172.
- [5] Hosking, L.J., H.R. Thomas, and M. Sedighi, A dual porosity model of high pressure gas flow for geoenery applications. *Canadian Geotechnical Journal*, 2018 (In Press).
- [6] Connell, L.D., et al., Laboratory characterisation of coal matrix shrinkage, cleat compressibility and the geomechanical properties determining reservoir permeability. *Fuel*, 2016. 165: p. 499-512.

COMPARING FE TO B-SPLINES APPROXIMATION FOR INFILTRATION PROBLEMS IN UNSATURATED SOILS

C. Jommi^{1,2} and E. Stopelli¹

¹ *Politecnico di Milano, Milano, Italy*

² *Delft University of Technology, Delft, The Netherlands*

1. Background and motivation

In the field of hydrology and geotechnical engineering, flow in unsaturated soils is typically modelled adopting a one-phase approach, based on Richards' equation, which combines the water mass conservation principle with an extended Darcy's law and a simplified description of the soil water retention properties. Although the resulting mathematical formulation is a standard parabolic equation, it has non-linear characteristics, which has been tackled in the past by means of various discretisation techniques, e.g. [1-4].

Richards' equation is based on the assumption that the presence of air in the soil pores has no effect on water movement. This simplifying assumption may result in underestimating the plug effect of air, with some potentially relevant geotechnical implications. The true nature of the physical process suggests recasting Richards' equation as a coupled two-phase problem, adding the mass balance law for gas, together with the relevant constitutive relationships among the governing equations. The latter choice allows for a physically accurate description of the flow characteristics, including the sharp fronts occurring during water or air infiltration. However, it also complicates the numerical treatment of the conservation equations, which may become degenerate parabolic equations, characterised by perturbations moving with finite speed. In this case, finite element numerical schemes may suffer from serious divergence and oscillation problems, especially when interpolating polynomials of increasing order are used.

2. B-spline interpolation

A B-spline based numerical formulation is proposed, which provides clear advantages in terms of numerical and physical accuracy compared to the more common Lagrange polynomial interpolation. B-spline based elements are particularly suited for non-linear geometrical and physical problems, thanks to their regular mathematical properties.

Increasing order B-spline interpolation functions have been implemented in a numerical code for the analysis of flow problems in unsaturated soils and their performance has been analysed with reference to a benchmark problem from Liakopoulos, frequently used test this kind of numerical algorithms [5].

3. Results

Figure 1 reports the numerical solution of Liakopoulos problem obtained with FE and B-splines discretisation. Progressive desaturation of an initially saturated sand column is analysed, by allowing water flow from the bottom of the model. The reference FE solution (Fig. 1a) for air pressure needs 500 linear elements in order to avoid oscillations around the sharp desaturation front. The solution coincides with that obtained with B-splines formulation with linear interpolation order.

Contrarily to FE discretisation, increasing the order of B-splines interpolation allows a stable and non-oscillating solution to be obtained at dramatically decreasing computational time. The B-spline solution in Fig. 1b requires 1/10 of the CPU time needed for the corresponding Results in Fig. 1a, using 20 elements with 4th order interpolation scheme.

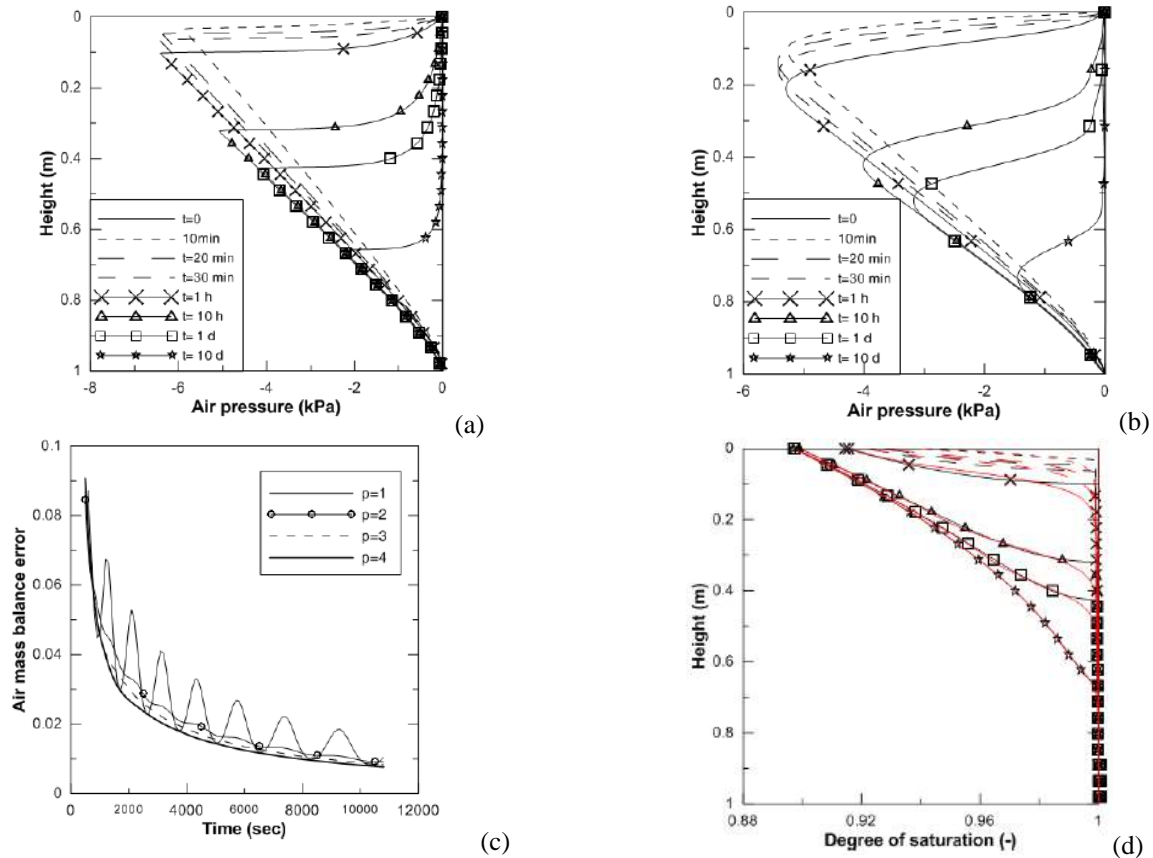


Figure 1. Paradigmatic numerical results on Liakopolous problem: (a) reference 500 FE linear elements; (b) 20–4th order B-spline interpolation; (c) mass balance error over time (d) comparison between p=1 and p=4 interpolation schemes.

Also, advantages in terms of stability of the time-stepping scheme and accurateness of the discretised solution can be appreciated on the mass balance error over time, which can be demonstrated to decrease monotonically if at least a 3rd order scheme is chosen (Fig. 1c). Increasing regularity properties of B-splines interpolation smoothen the sharp front, although the error in the approximation is confined in a small depth around the front, and does not affect the accuracy of the solution elsewhere (Fig. 1d).

4. References

- [1] Celia, M.A., Bouloutas, E.T. & Zarba, R.L. (1990). A general mass-conservative numerical solution for the unsaturated flow equation. *Water Resources Research*, **26**, 1483–1496.
- [2] Rathfelder, K. & Abriola, L.M. (1994). Mass conservative numerical solution of the head-based Richards equation. *Water Resources Research*, **30**, 2579–2586.
- [3] Wood, W.L. (1996). A note on how to avoid spurious oscillation in the finite-element solution of the unsaturated flow equation. *Journal of Hydrology*, **176**, 205–218.
- [4] Kavetski, D., Binning, P. & Sloan, S.W. (2001). Adaptive time stepping and error control in a mass conservative numerical solution of the mixed form of Richards equation. *Advances in Water Resources*, **24**, 595–605.
- [5] Jommi, C., Vaunat, J., Gens, A., Gawin, D. & Schrefler, D. (1997). *Multiphase flow in porous media: a numerical benchmark*. Proceedings of NAFEMS World Congress '97, Stuttgart, **2**, 1338–1349.

MODELLING TUNNEL RESPONSE IN HIGHLY EXPANSIVE SULPHATED ROCK

Anna Ramon^{1,2}, Eduardo E. Alonso¹

¹ *Division of Geotechnical Engineering and Geosciences, Department of Civil and Environmental Engineering, Universitat Politècnica de Catalunya, Barcelona, Spain*

² *International Centre for Numerical Methods in Engineering, Barcelona, Spain*

1. Introduction

Expansions in Triassic and Tertiary calcium sulphate formations generates important damage and failures in tunnels [1], [2], [3] and may also result in the heave of infrastructures and buildings [4], [5]. The development of precipitation of gypsum in discontinuities of the rock explains the severe expansions observed in these formations. Gypsum precipitation results from calcium sulphate supersaturated groundwater. The dissolution of anhydrite, present in the rock, provides supersaturation conditions in calcium sulphate with respect to gypsum. The coexistence of a certain content of anhydrite, water and also the presence of some damage or discontinuities in the rock, triggers and maintain the development of expansions in the rock.

Lilla tunnel, built through an Eocene anhydritic claystone in Spain, is a singular case affected by intense expansions. The original flat slab experienced a sustained heave at a maximum rate of 2 mm/day during more than a year. Pressure cells installed at rock-invert interface recorded high swelling pressures up to 5 MPa in test sections with invert arch. The development of swelling strains in a 4 – 5 meters thick layer located below the tunnel floor was recorded by continuous extensometers installed in boreholes. The severe expansions suffered by the tunnel motivated the reconstruction of the tunnel into a highly reinforced circular cross section. The records of instrumentation during operation show that the expansive mechanisms evolved after tunnel reconstruction. The maximum recorded swelling pressure reaches 7 MPa at one pressure cell in one instrumented section. However the maximum pressures measured along the tunnel stay in the range of 5 - 6 MPa in the majority of the instrumented sections.

2. Model description

A hydro-chemo-mechanical model has been developed to simulate expansions in anhydritic rock. The formulation includes an embedded fracture model and describes precipitation of gypsum in discontinuities. The calculation of rock permeability considers the aperture of the fractures and the separation between fractures. The model defines the opening of discontinuities from the current tensile strains. The aperture of fractures increases the permeability of rock mass and also determines the occurrence of precipitation. The formulation of the model takes into account the presence of soluble minerals (anhydrite and gypsum) that may precipitate or dissolve and non-soluble clay minerals in the rock mass and describes the chemical reactions of dissolution and precipitation of soluble minerals and the transport of solutes. The precipitation and dissolution of crystals follow kinetic equations based on the degree of supersaturation of groundwater in sulphates. The amount of precipitated mass of gypsum and the current applied stresses determine the calculated deformations induced by crystal precipitation. Paper [6] describes in more detail the characteristics of the model.

3. Modelling analysis

The excavation and performance of Lilla tunnel with flat slab has been modelled. The simulation reproduces the generation of fracture opening induced by the excavation of the tunnel and also due to the development of expansions associated with the occurrence of gypsum

precipitation below tunnel floor. Figure 1 shows the variation with depth of calculated permeability after tunnel excavation. The model reproduces the confining effect of the abutments in the calculated heave across the width of the tunnel floor in accordance with field observations. The model is capable of reproducing the general trend of heave recorded at tunnel floor level despite the heterogeneity of vertical displacements measured along Lilla tunnel.

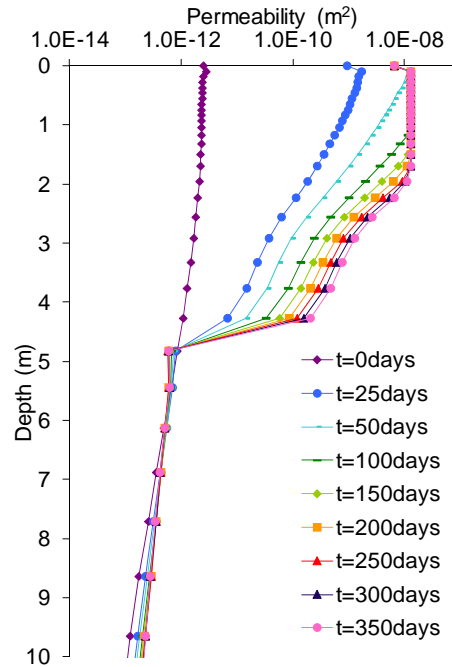


Figure 1. Variation with depth of calculated permeability (Logarithmic scale) below de flat slab at the axis of the tunnel after the excavation of the tunnel ([6]).

5. References

- [1] Wittke, M. (2006). Design, construction, supervision and long-term behaviour of tunnels in swelling rocks. *Proc EUROCK 2006: Multiphysics Coupling and Long Term Behaviour in Rock Mechanics*, Liège, 211-216.
- [2] Anagnostou, G., Serafeimidis, K., and Vrakas, A. (2015). On the occurrence of anhydrite in the sulphatic claystones of the gypsum Keuper. *Rock Mech Rock Eng* (2015) 48:1–13. DOI 10.1007/s00603-014-0568-y
- [3] Alonso, E.E., Berdugo, I.R. and Ramon, A. (2013). Extreme expansive phenomena in anhydritic-gypsiferous claystone: the case of Lilla tunnel. *Géotechnique* 63 No. 7, 584 –612, [<http://dx.doi.org/10.1680/geot.12.P.143>].
- [4] Ramon, A. and Alonso, E.E. 2013. Heave of a railway bridge: modelling gypsum crystal growth. *Géotechnique*, 63(9): 720–732. doi:10.1680/geot.12.P.035.
- [5] Ramon, A. and Alonso, E.E. 2018. Heave of a building induced by swelling of an anhydritic Triassic claystone. *Rock Mechanics and Rock Engineering*, sent for publication.
- [6] Ramon, A., Alonso, E. E. & Olivella, S. (2017). Hydro-chemo-mechanical modelling of tunnels in sulfated rocks. *Géotechnique* 67, No. 11, 968–982 [<http://dx.doi.org/10.1680/jgeot.SiP17.P.252>].

COUPLED THM MODELING OF ENERGY MICRO-PILE BEHAVIOR

F. Ronchi¹, D. Salciarini¹ and C. Tamagnini¹

¹ *University of Perugia, Perugia, Italy*

1. Introduction

The work presents the results of fully coupled, 3D thermo–hydro–mechanical (THM) FE analyses carried out to investigate the coupling effects of the heating/cooling cycles on a single energy pile of small diameter, installed in a saturated, fine grained soil. This study has been performed as a part of the development stage of an innovative geotechnology – the energy micro–pile (EmP) – currently under investigation at the University of Perugia for the exploitation of low–enthalpy geothermal energy in the retrofitting of existing buildings [1].

A prototype of the EmP under development has been installed in a test site at the Engineering Campus of the University of Perugia. The prototype is a bored and cast in place micro–pile, with a length of 12 m and a diameter of 0.18 m (slenderness ratio equal to 67). High–density polyethylene pipes (with an inner diameter of 12.5 mm and a thickness of 1.7 mm) have been inserted into the grout in a U-shaped loop to allow the circulation of the heat–carrier fluid along the prototype and to make it work as a heat–exchanger. Full details about the EmP design are given in [1].

The FE simulation program has been focused mainly on the evaluation of such crucial aspects of the EmP design as the assessment of mechanical effects induced in the pile and the soil during thermal loading conditions and the effect of varying thermal properties of the soil on the thermal input/output of the pile.

2. Governing equations of the coupled THM processes

Under the assumption of linear kinematics (‘small deformations’) and full saturation of the soils, the balance of mass, momentum and energy equations for the porous medium can be defined as reported in [2].

$$\nabla \boldsymbol{\sigma}' - \nabla u + \rho \mathbf{b} = \mathbf{0} \quad (1)$$

$$\frac{1}{Q} \dot{u} - \beta_{\text{eff}} \dot{T} + \nabla \cdot \mathbf{v}^s + \nabla \cdot \left\{ \frac{1}{\mu_w} \boldsymbol{\kappa} (-\nabla u + \rho_w \mathbf{b}) \right\} = 0 \quad (2)$$

$$\rho C_{p,\text{eff}} \dot{T} + \nabla \cdot \{-\lambda_{\text{eff}} \nabla T\} + \rho_w C_{p,w} \left\{ \frac{1}{\mu_w} \boldsymbol{\kappa} (-\nabla u + \rho_w \mathbf{b}) \right\} \cdot \nabla T = 0 \quad (3)$$

where: $\boldsymbol{\sigma}' = \boldsymbol{\sigma} + u \mathbf{1}$ is the effective stress tensor; u is the pore water pressure; T is the absolute temperature; \mathbf{b} is the body force vector (gravity) per unit mass; ρ is the soil density; μ_w is the water viscosity; $\boldsymbol{\kappa}$ is the hydraulic permeability and $\lambda_{\text{eff}} = (1 - n)\lambda_s + n\lambda_w$, $C_{p,\text{eff}} = (1 - n)C_{p,s} + nC_{p,w}$ and $\beta_{\text{eff}} = (1 - n)\beta_s + n\beta_w$ are the effective thermal conductivity, heat capacity and volumetric expansion coefficients of the soil, respectively.

As for the mechanical properties of the solids, the pile has been considered as a linear thermoelastic material. Two different isotropic hardening elasto–plastic models have been considered for the fine–grained soil: the classical Modified Cam–Clay (MCC) model and a similar critical state model incorporating a thermal hardening/softening mechanism for the critical friction angle, assumed as an internal variable [3]. A linear thermoelastic model for the soil has also been considered for comparison.

3. FE modeling

A FE model of the prototype EmP has been built using the FE code ABAQUS, as shown in Fig. 1. By considering the symmetry of the problem in terms of geometry and loading conditions, only a quarter of the entire domain has been discretized. The bottom of the model has been placed at a depth of 20 m from the ground surface. Preliminary simulations have shown that the effects of the cylindrical lateral boundary on the deformation and conduction processes in the soil are minimal by assuming an outer diameter of 4 m ($D/D_p = 22$).

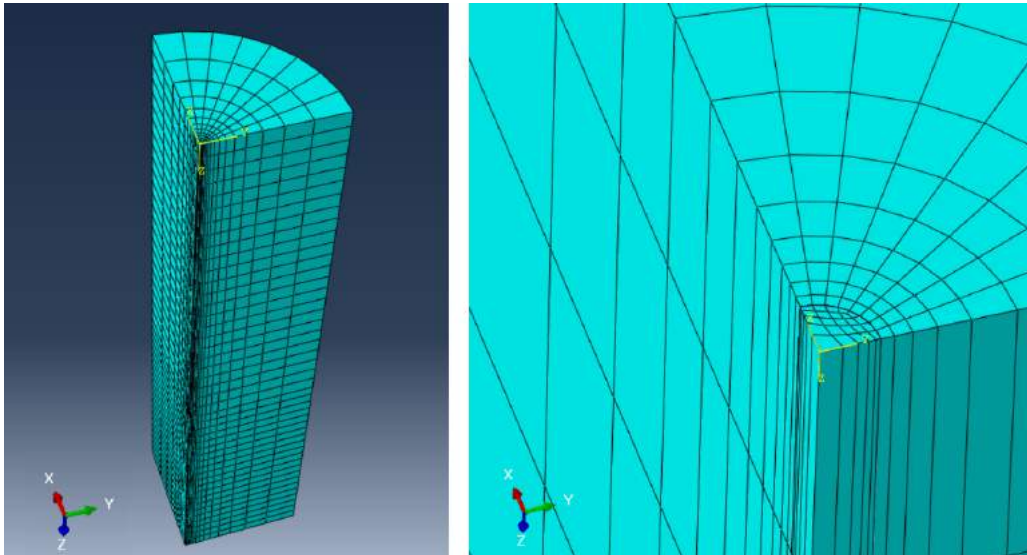


Figure 1. FE model of the prototype with the details of the adopted structured spatial discretization.

The simulations have been carried out considering the following loading stages: 1) initialization of material state and application of gravity loading; 2) hydro–mechanical loading stage, with a load of 500 kN applied at the pile head over a period of 1 day; 3) consolidation stage for a period of 30 days at constant temperature; 4) activation of the EmP with an harmonic (half–sine) heating cycle of 60 days.

The results highlight the importance of a suitable modeling of the inelastic behavior of the soil for the accurate prediction of the pile–soil interaction effects and of the pore pressure evolution within the soil during the heating process. These results will be compared with experimental data from the in–situ testing campaign, when they become available.

References

- [1] Ronchi, F., Salciarini, D., and Tamagnini, C. (2018). Thermal response prediction of a prototype energy micro-pile. *Geomechanics for Energy and the Environment*. (in print).
- [2] Lewis, R. W. and Schrefler, B. A. (1998). *The finite element method in the deformation and consolidation of porous media (2nd edition)*. John Wiley and Sons Inc., New Jersey, NY, USA.
- [3] Tamagnini, C. and Ciantia, M. O. (2016). Plasticity with generalized hardening: constitutive modeling and computational aspects. *Acta Geotechnica*, **11**, 595–623.

A MATHEMATICAL MODEL FOR TWO-PHASE FLOW (GAS AND WATER) IN A SWELLING GEOMATERIAL

E. E. Dagher^{1,2}, T.S. Nguyen^{1,2} and J.A. Infante Sedano²
¹ *Canadian Nuclear Safety Commission, Ottawa, Ont., Canada*
² *University of Ottawa, Ottawa, Ont. Canada*

1. Introduction

The Canadian Nuclear Safety Commission (CNSC), Canada's nuclear regulator, conducts regulatory research to build independent knowledge on safety aspects related to the deep geological disposal of radioactive wastes. In a deep geological repository (DGR) for the long-term containment of radioactive waste, gas could be generated through a number of processes including the degradation of organic matter, radioactive decay of the waste, corrosion of metals producing hydrogen gas (H₂), and the radiolysis of water producing H₂. If gas production exceeds the containment capacity of the engineered barriers or host rock, these gases could migrate through the engineered barriers and/or the host rock. The preferential migration pathway of these radioactive gases, to potentially expose people and the environment to radioactivity, might be through the access and ventilation shafts as these components are typically part of the repository design. Swelling soils (e.g., bentonite mixtures) are currently the preferred choice of seal materials used for those shafts. Understanding the long-term performance of these seals as barriers against gas migration is an important component in the design and long-term safety assessment of a DGR. This study proposes a mathematical hydro-mechanical (HM) model for migration of gas (two-phase flow) through a low-permeable swelling geomaterial.

2. Modelling Approach

An HM model to describe the migration of gas (two-phase flow) through a low-permeable swelling soil was developed using the theoretical framework of poromechanics. The model is an extension of the linear elastic advective-diffusive visco-capillary (ADVC) two-phase flow model proposed by Dagher et al. [1], which considered the following features:

- i. a Bishop's effective stress, with a χ parameter generalized from the work of [2];
- ii. gas dissolution into the liquid phase and subsequent gas migration from a) the advection of water, and b) diffusion of gas through the liquid phase;
- iii. a relation for the Air-Entry Value (AEV), and corresponding soil-water characteristic curves (SWCC), as a function of the porosity, n ;
- iv. a relation of the intrinsic permeability, k_{ij} , as a function of the porosity; and
- v. consideration of a damage model and its effect on the Young's Modulus, E , and k_{ij} .

This model expands upon the previous work by considering the effect of damage on the AEV and corresponding SWCCs. It also takes into account the swelling behavior of the geomaterial by considering a swelling strain (i.e., moisture shrinkage).

3. Experimental Set-up

Using the Finite Element Method, the model was used to numerically simulate 1D and 3D spherical flow through a low-permeable swelling soil. The results were verified against experimental results found in the current literature [3][4] for a confined cylindrical sample of near-saturated bentonite under a constant volume boundary stress condition. Figure 1 depicts an illustration of the experimental set-up for the 1D flow case [3] and the 3D spherical flow case [4].

For the 1D flow test, gas was injected from one end of the bentonite sample at increasing pressures over time, while maintaining a water backpressure at the other end. For the 3D spherical

flow test, gas was injected at the center of the bentonite sample, through an injection rod, while maintaining a specified water pressure at the radial porewater arrays. During the experiment, a number of key features were measured including the gas inflow and outflow, the pore-pressure at the pore-fluid arrays, and the total axial and radial stresses, and were compared to numerical results.

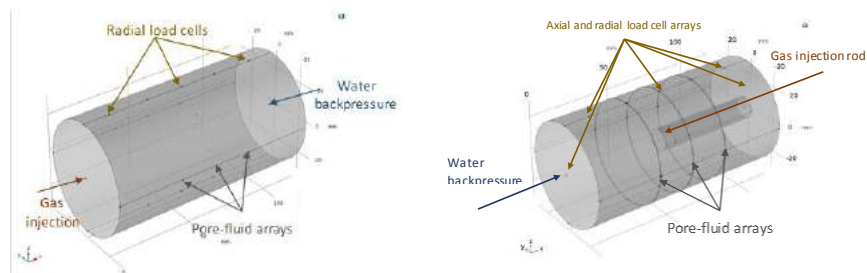


Figure 1. Experimental set-up for the 1D flow (left) and 3D spherical flow (right) tests

4. Results

Results of the 1D case are presented in figure 2. The consideration of the effect of damage on the AEV, and the inclusion of a swelling strain improved the existing model. For the 1D flow case, the modelling results provided better representation of the experimental gas inflow and pore-fluid pressure profiles. For the 3D spherical flow case, the modelling results provide good representation of the experimental inflow, porefluid pressure, and stress evolution profiles of the experimental results. The results provide a preliminary model to simulate multi-phase flow in swelling geomaterials and provide further understanding of the mechanisms associated with such phenomena. The model could not simulate gas outflow and future work will look at localization and the development of preferential flow pathways.

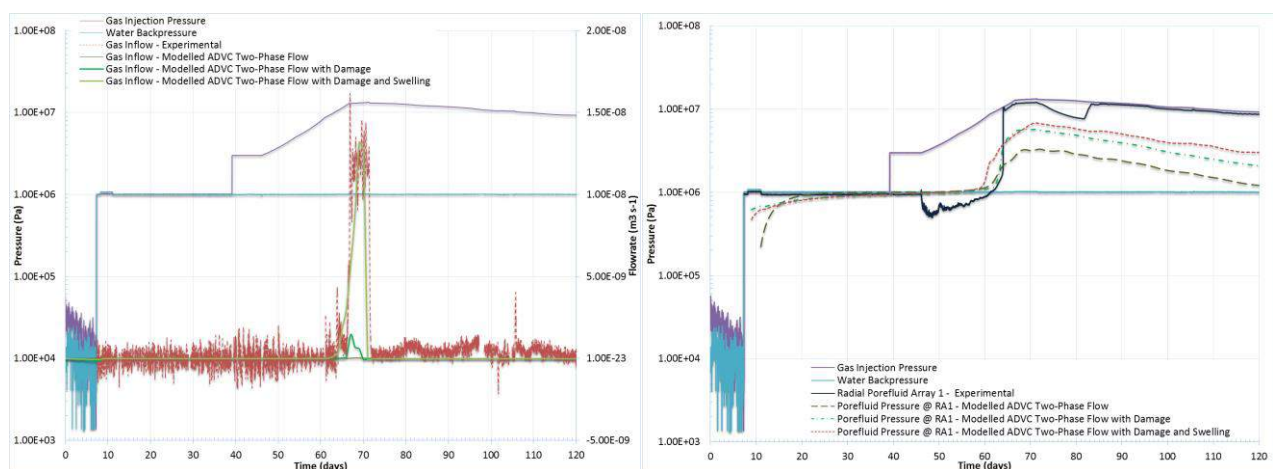


Figure 2. 1D flow results for (a) gas inflow profiles (b) porefluid pressure profiles

6. References

- [1] Dagher, E. E., Nguyen, T. S. & Infante Sedano, J. A., 2017 submitted. Development of a Mathematical Model for Gas Migration (Two-phase flow) in Natural and Engineered Barriers for Radioactive Waste Disposal. Geological Society of London
- [2] Khalili, N. & Khabbaz, M. H., 1998. A unique relationship for χ for the determination of the shear strength of unsaturated soils. *Géotechnique*, 48(5), pp. 681-687.
- [3] Harrington, J. F., Graham, C. C., Cuss, R. J. & Norris, S., 2017. Gas network development in a precompacted bentonite experiment: Evidence of generation and evolution. *Applied Clay Science*, Volume 147, pp. 80-89.
- [4] Daniels, K. A. & Harrington, J. F., 2017. The response of compact bentonite during a 1D gas flow test, British Geological Survey Open Report, OR/17/067, s.l.: British Geological Survey.

HAZARD AND RISK ASSESSMENT OF LARGE SEISMIC EVENTS OWING TO FLUID INJECTION

B. Fryer¹, G. Siddiqi² and L. Laloui¹

¹ Swiss Federal Institute of Technology in Lausanne, Lausanne, Switzerland

² Swiss Federal Office of Energy, Bern, Switzerland

1. Introduction

In the last few years, earthquakes which have been attributed to waste-water injection have been felt at the surface in the continental United States. These earthquakes have been primarily occurring in the crystalline basement rock located below the injection interval and not in the injection interval itself, generally on previously unrecognised faults (ex: [1]).

Previous studies have modelled fluid injection above crystalline basement rock and shown that seismicity can occur in the basement, at times even without fluid pressurization [2]. This study, however, quantifies the relative chance of large events specifically, which occur in the basement rock.

2. Methodology

A two phase FVM flow model based on the continuity equation for mass balance is sequentially coupled to a FEM mechanics model based on the conservation of momentum with no external forces and the linear theory of poroelasticity.

The resultant pressures and stresses are then used as input to a stochastic seismicity model based on the model first proposed by [3], which performs seismicity forecasting using Mohr-Coulomb failure criteria in a Monte Carlo fashion without having to explicitly model faults. The model used here is very similar except that it is able to do this semi-analytically, allowing the analysis to be performed more quickly and with less computer memory usage at the cost of assuming a fixed and known minimum principal stress, something that can reasonably well constrained using a mini-frac test.

This seismicity model assumes that the lithologies present in the model are all critically stressed [4] and could have an optimally oriented, critically stressed fault anywhere within them (representing a worst-case scenario in terms of seismic hazard prediction). This means that it will be the frictional strength of pre-existing faults within each lithology that will limit the differential stress (the difference between the maximum and minimum principal stresses) of each lithology [5], meaning that faults with larger coefficients of friction, such as those in basement rocks [6], are able to support larger differential stresses. This model also connects the differential stress to the Gutenberg-Richter b-value [7], meaning that these layers supporting larger differential stresses are also more likely to be able to host a large earthquake.

3. Results

This model is then implemented for a three-layer system where injection is occurring a sandstone reservoir which is overlain by a shale caprock and a granitic basement rock in a normal faulting stress regime. This results in a quantitative prediction of a high number of large events in the basement because the basement rock is experiencing a reduction of horizontal stress (which is the minimum principal stress in this case), bringing it closer to failure. Additionally, as granite tends to contain faults of a high coefficient of friction, this layer initially had a large differential stress. This results in a prediction of a low Gutenberg-Richter b-Value for that layer which ultimately means that it is likely that that layer will experience a large event.

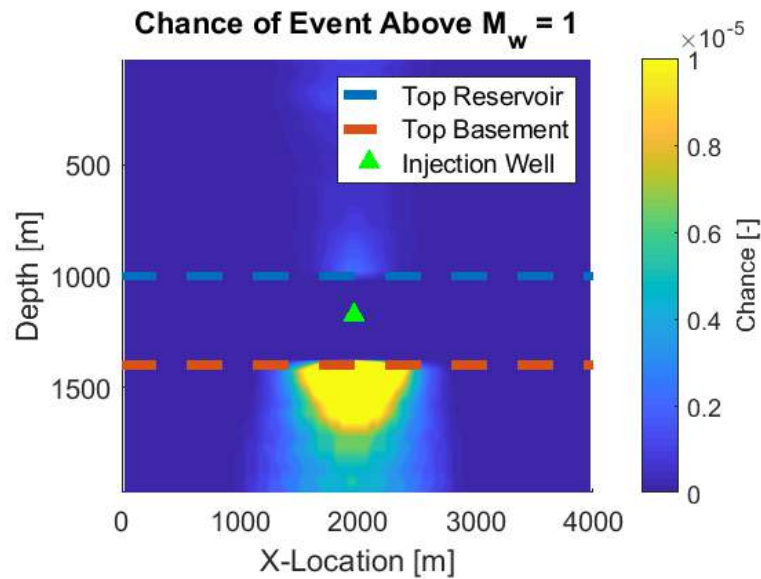


Figure 1. An example result from a three-layer (shale cap rock, sandstone reservoir, granitic basement) system in a normal faulting regime. The simulation is plane strain with injection occurring via a horizontal well.

4. Conclusion

A workflow for forecasting the chance of a large seismic event occurring within a three-layer system using a semi-analytical version of a previously existing seismicity model has been introduced. Using this model, various potential injection sites will be able to be compared in a quantitative manner for their risk of inducing large seismic events.

This work has been supported by a research grant (SI/500963-01) of the Swiss Federal Office of Energy.

References

- [1] Horton, S. (2012). Disposal of hydrofracking waste fluid by injection into subsurface aquifers triggers earthquake swarm in Central Arkansas with potential for damaging earthquake. *Seismological Research Letters*, **83**, 250–260, doi: 10.1785/gssrl.83.2.250.
- [2] Chang, K. and Segall, P. (2016). Injection-induced seismicity on basement faults including poroelastic stressing. *Journal of Geophysical Research*, **121**, 2708–2726, doi: 10.1002/2015JB012561.
- [3] Layland-Bachmann, C., Wiemer, S., Goertz-Allmann, B., and Woessner, J. (2012). Influence of pore-pressure on the event-size distribution of induced earthquakes. *Geophysical Research Letters*, **39**, doi:10.1029/2012GL051480.
- [4] Townend, J. and Zoback, M. (2000). How faulting keeps the crust strong. *Geology*, pp. 399–402.
- [5] Zoback, M. and Harjes, H. (1997). Injection-induced earthquakes and crustal stress at 9 km depth at the KTB deep drilling site, Germany. *Journal of Geophysical Research*, **102**, 18477–18491, doi:10.1029/96JB02814.
- [6] Zhang, Y., et al. (2013). Hydrogeologic controls on induced seismicity in crystalline basement rocks due to fluid injection into basal reservoirs. *Groundwater*, **51**, 525–538, doi: 10.1111/gwat.12071.
- [7] Schorlemmer, D., Wiemer, S., and Wyss, M. (2005). Variations in earthquake-size distribution across different stress regimes. *Nature*, **437**, 539–542, doi:10.1038/nature04094.

MATHEMATICAL MODELLING OF A FAULT SLIP INDUCED BY WATER INJECTION

T.S. Nguyen¹, B. Graupner², Y. Gugliemi³, J. Rutqvist³

¹Canadian Nuclear Safety Commission, Ottawa, ON, K1P 5S9, Canada

²Swiss Federal Nuclear Inspectorate, ENSI, Switzerland

³Lawrence Berkeley National Laboratory, Berkeley, California, USA

1. Introduction

The Canadian Nuclear Safety Commission (CNSC), Canada's nuclear regulator, conducts regulatory research in order to build independent knowledge on safety aspects related to the deep geological disposal of radioactive wastes. Faults located in the vicinity of deep geological repositories (DGR) for radioactive waste may constitute preferential pathways for radionuclides potentially released from the waste. Therefore, they must be considered in the design and safety assessment of the repositories. In the case of argillaceous rocks being considered as host formations, the faults in their undisturbed state are often hydraulically undistinguishable from the rock matrix. However, increase in porewater pressure due to various processes such as heat generated from the waste, can result in a reduction in the fault effective normal stress that might lead to fault slip, increase in permeability, and the generation of seismic events. In this research we developed a hydromechanical model for fault slip due to pressurization, and calibrated it to an injection test at the Mont Terri underground research laboratory in Switzerland.

2. Experimental setup

The experiment considered in this presentation consists of injection tests, at stepwise increases in the injection pressure, in a straddle packer set across a secondary fault zone in the Main fault hanging wall (Figure 1). The fault zone contains 12 striated fractures, most of them oriented N030° to N060°, dipping 50° to 70° SE. The injection flow rate was continuously recorded. A High-Pressure Pulse Probe borehole deformation tool measures the relative displacement of the two anchors attached to the injection chamber, one within the upper wall of the main fracture, and one within the lower wall. Pressure at a point 1.5 m down-dip from the fault was also recorded.

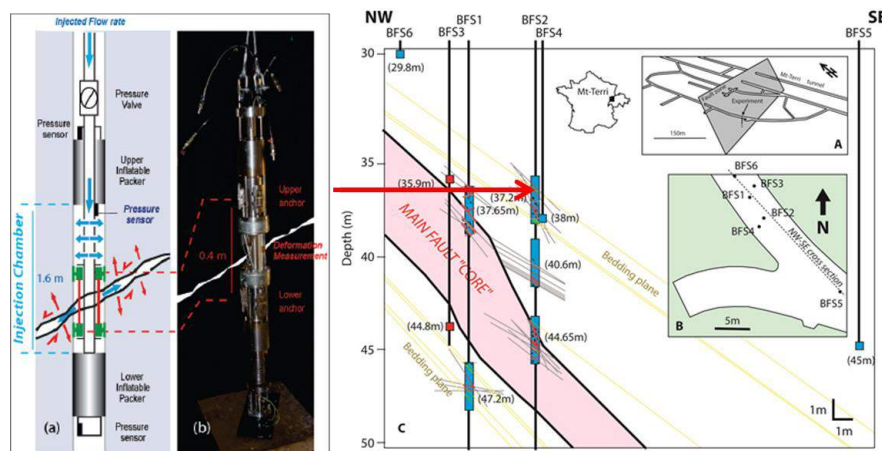


Figure 1. Water injection in a secondary fault

3. Mathematical model and results

The fault and the rock matrix were conceptualized as porous media, and the governing equations of the model were derived from the poromechanics framework. The rock matrix was modelled as an isotropic poro-elastic medium, while the fault is modelled as a transversely isotropic, poro-elastoplastic medium with principal directions coincident with the triad associated with the fault orientation. The Mohr-Coulomb criterion was adopted as a yield criterion with a non-associated flow rule. The permeability of the fault in the initial state was assumed to be equal to the one of the rock matrix. However it was made to increase when the fault opens due to a combination of normal and shear dilation induced by the pressure of the injected water.

The modelling results are compared to the experimental data for fault displacement and injected water flow rate in Figure 2. The injection pressure is also shown (in bars) for reference. The modelling results are consistent with the experimental evidence. They indicate that fault displacement is low, until a threshold injection pressure of approximately 5 MPa (50 bar) is exceeded. At this stage, the fault fails by shear, resulting in substantial slip and dilation and increases in permeability by many orders of magnitude leading to a substantial increase in the flow rate. After the pressure is reduced, permanent deformations still remain.

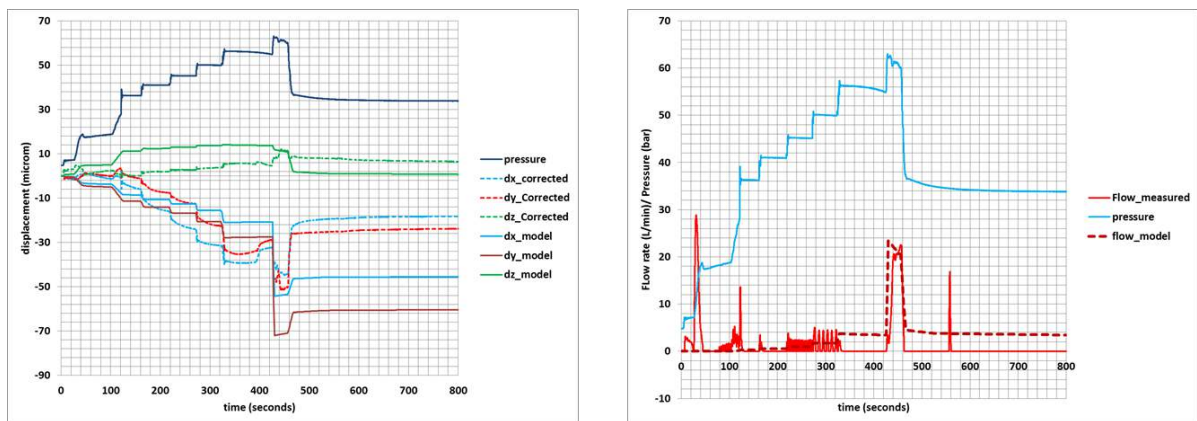


Figure 2. Fault displacement and injected flow rate

4. Acknowledgement

This work was performed as part of the DECOVALEX-2019 international collaborative project (decovallex.org) for the development and validation of mathematical models of coupled thermo-hydro-mechanical-chemical processes in geological disposal of radioactive waste. The authors sincerely thank the DECOVALEX-2019 participants in facilitating and providing peer review of the work.

A DISCRETE NUMERICAL MODEL OF THE FRONT REGION IN PIPING EROSION

A.F. Rotunno^{1,2}, F. Froiio² and C. Callari³

¹ *University of Rome “Tor Vergata”, DICII, Rome, Italy*

² *University of Lyon, École Centrale of Lyon, LTDS, Lyon, France*

³ *University of Molise, DiBT, Campobasso, Italy*

1. Introduction

Backward piping is amongst the most dangerous erosion processes affecting earth dams and levees [1]. After the erosion is triggered at the downstream side, the pipe propagates upstream while increasing in diameter (due to tangential erosion at its walls), and can lead to serious damage or cause failure of the embankment. At least three modeling scales are involved in the description of such phenomenon, namely the scale of the hydraulic work (*macro-scale*), the scale of the erosion conduits (*meso-scale*) and the scale of the saturated earthfill constituent (*micro-scale*). In this work we analyze, at the micro-scale, the backward erosion process driving the pipe propagation mechanism.

2. Numerical formulation and representative test

The numerical formulation is based on the coupling of the Discrete Element Method (DEM) with the Lattice Boltzmann Method (LBM) for the modeling of the solid- (granular) and the fluid phase, respectively [2]. The implementation of DEM follows a molecular dynamics approach and the interactions between grains are regulated by unilateral contacts and breakable bonds [3]. The coupling with the LBM is based on the implementation of non-slip conditions for moving boundaries (the grain boundaries) [4]. Both the numerical formulations and their coupling, are implemented in the in-house numerical code DEM’OCRITUS, developed at the LTDS.

After introducing the main features of the DEM–LBM model, as well as the coupling and parallelization schemes, we present and analyze a numerical test on a granular soil REV located on the erosion pipe front [5]. Figure 1 illustrates some results from the numerical test, in which the granular specimen is subjected to an hydraulic gradient between the inlet and outlet sections (left- and right side, resp.). The outlet region is confined by a layer of fixed (black-colored) grains, with the exception of a central opening as large as approximately 1/4 of the height of the specimen in the figure. The configuration is designed to reproduce as close as possible the conditions by which backward erosion triggers at the pipe front region and causes its upstream progression. In this plot we represent the norm of the macroscopic fluid velocity and the corresponding hydraulic configuration of the specimen, at an early stage of the backward erosion process. It can be observed that the flow concentrates in regions of increasing porosity, e.g. at the erosion front on the right of the specimen as well as in other regions where “tears” appear.

The formation of a main erosion pipe can be clearly inferred from Figure 2, in which we depict the fluid velocity along with the hydraulic configuration of the specimen for an advanced stage of piping process.

Acknowledgements: Research supported by GIS VOR 2012, LTDS 2012, GDRI–CNRS 2018 and PRIN 2010–2011 (2010BFXRHS 004) projects as well as by one PhD fellowship (UniRoma2) and a VINCI mobility programme (Università italo–francese).

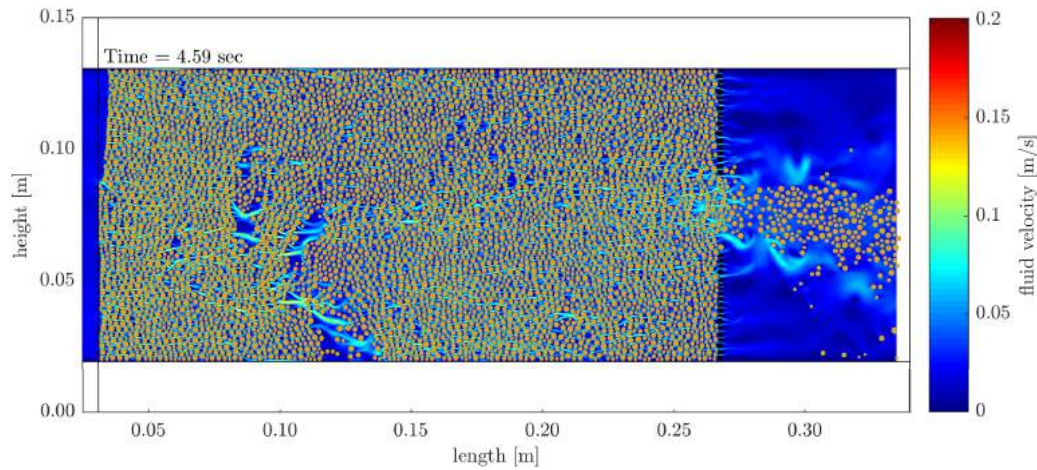


Figure 1. Representative test [5]: norm of the macroscopic fluid velocity and hydraulic configuration of the specimen at an early stage of erosion process.

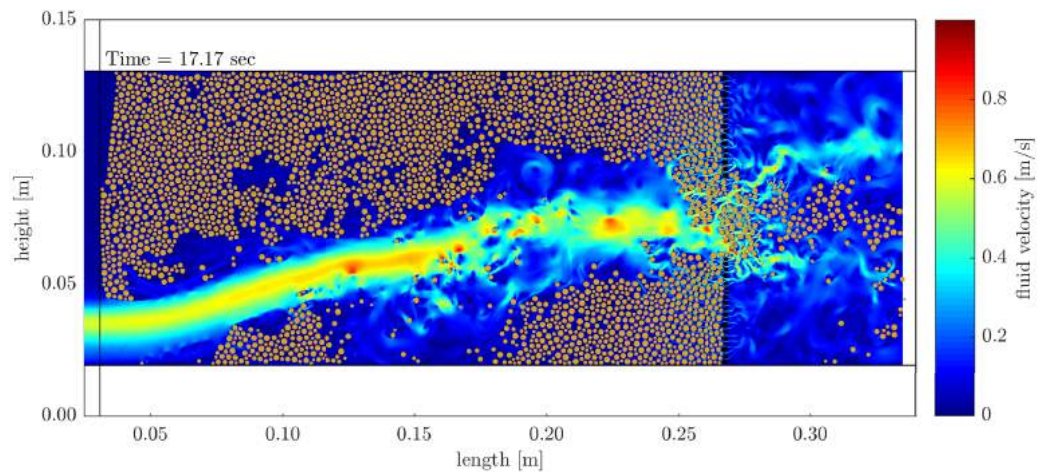


Figure 2. Representative test [5]: norm of the macroscopic fluid velocity and hydraulic configuration of the specimen at an advanced stage of erosion process.

References

- [1] Foster, M., Fell, R., and Spannagle, M. (2000). The statistics of embankment dam failures and accidents. *Canadian Geotechnical Journal*, **37**, 1000–1024.
- [2] Tran, D. K., Prime, N., Froiio, F., Callari, C., and Vincens, E. (2017). Numerical modelling of backward front propagation in piping erosion by DEM–LBM coupling. *European Journal of Environmental and Civil Engineering*, **21**, 960–987.
- [3] Cundall, P. A. and Strack, O. D. (1979). A discrete numerical model for granular assemblies. *Géotechnique*, **29**, 47–65.
- [4] Bouzidi, M., Firdaouss, M., and Lallemand, P. (2001). Momentum transfer of a boltzmann-lattice fluid with boundaries. *Physics of Fluids*, **13**, 3452–3459.
- [5] Rotunno, A. F., Froiio, F., and Callari, C. Discrete numerical modeling and micromechanical inspection of the front region in piping erosion, *In preparation*.

A SIMPLIFIED, NEWMARK–LIKE APPROACH FOR THE ASSESSMENT OF SEISMIC PERFORMANCE OF ANCHORED DIAPHRAGM WALLS

E. Cattoni¹, D. Salciarini² and C. Tamagnini²

¹ *eCampus University, Novedrate, Italy*

² *University of Perugia, Perugia, Italy*

1. Introduction

In recent years, much attention has been paid to the assessment of the performance–based design of flexible retaining structures, focusing on the evaluation of the deformation response of the soil–structure system under a given seismic load. While only a few examples of fully coupled, dynamic numerical simulations of flexible retaining structures with advanced models for soils can be found in literature – see, e.g., [1] – simple modifications of the classical Newmark method have recently been proposed to assess the permanent displacements of the structure at the end of the seismic excitation [2, 3]. All the aforementioned works refer to cantilevered diaphragm walls, for which the failure mechanisms at limit equilibrium are relatively simple to describe. However, this is not the case for anchored or propped flexible structures, where the velocity field at failure under a pseudo-static seismic load is quite complex and can be affected by the plastic yielding of the wall upon bending (see, e.g., [4]), who have investigated the failure mechanisms of propped diaphragm walls by means of lower- and upper-bound limit analysis finite element (FE) simulations.

2. Methodology and selected results

In this work, upper– and lower–bound limit analysis FE solutions are used: a) to investigate the two failure mechanisms which may occur during the seismic excitation of excavations in dry sand supported by parallel diaphragm walls propped at the crest, for the two possible directions of the horizontal acceleration; b) to evaluate the critical accelerations associated to each of them; c) to determine the accumulated permanent displacement field at the end of the earthquake, as the superposition of the collapse mechanisms associated to each horizontal directions of the earthquake action, by means of two distinct Newmark integration procedures over the input accelerogram. This last point is based on the following two main assumptions:

Assumption 1 *When the collapsing soil mass \mathcal{B}_f is in motion under inertia forces larger than the critical ones, the relative velocity field $\mathbf{v}_r^{(i)}$ is proportional to the normalized velocity field $\boldsymbol{\eta}^{(i)}$ according to $\mathbf{v}_r^{(i)}(\mathbf{x}, t) = V^{(i)}(t)\boldsymbol{\eta}^{(i)}(\mathbf{x})$.*

Assumption 2 *Under dynamic equilibrium conditions, the stress vector field \mathbf{t} acting on $\partial\mathcal{B}_f$ remains equal to $\mathbf{t}_f^{(i)}$ since the boundary between the failing soil body and the remaining stable soil mass is a slip line.*

Based on those assumptions, it is possible to show that the dynamic equilibrium equation of the soil mass mobilized in the i –th collapse mechanism ($i = 1, 2$) reduces to the following Newmark–like ODE:

$$\dot{V}^{(i)} = \frac{Mg}{Q_x} \langle k_x(t) - k_c^{(i)} \rangle \quad M := \int_{\mathcal{B}_f} \rho \, dv \quad Q_x := \int_{\mathcal{B}_f} \rho \boldsymbol{\eta}^{(i)} \cdot \mathbf{e}_e^{(i)} \, dv \quad (1)$$

where M and Q_x are the mass of \mathcal{B}_f and its normalized momentum in direction x , respectively, and $\boldsymbol{\eta}^{(i)}$ is the normalized velocity field computed from the Upper–Bound solution of LA.

The permanent (relative) displacement field associated to both collapse mechanisms is finally computed by vectorially composing the two fields $\mathbf{u}_r^{(+)}(\mathbf{x}, t)$ and $\mathbf{u}_r^{(-)}(\mathbf{x}, t)$ at the generic time $t \in [0, T_d]$:

$$\mathbf{u}_r(\mathbf{x}, t) = U^{(+)}(t)\boldsymbol{\eta}^{(+)}(\mathbf{x}) + U^{(-)}(t)\boldsymbol{\eta}^{(-)}(\mathbf{x}) = \mathbf{u}_r^{(+)}(\mathbf{x}, t) + \mathbf{u}_r^{(-)}(\mathbf{x}, t) \quad (2)$$

It is worth noting that this procedure allows the reconstruction of the full permanent displacement field around the excavation, not just the evaluation of horizontal soil movements at selected points. The

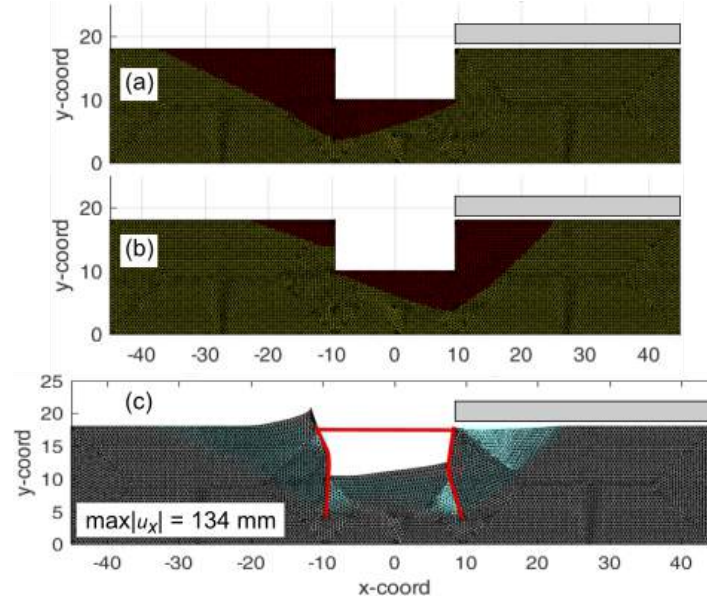


Figure 1. Deep excavation: plastic zones for (+) and (-) mechanisms and resulting \mathbf{u}_r field.

application of the method to a number of selected prototype excavations demonstrates the potentiality of the proposed approach, which can be extended easily to other complex geotechnical structures. As an example of application, Fig. 1 shows the results obtained on a excavation 8 m deep, supported by 14 m long walls, with a surcharge load $q = 50$ kPa applied on the right side of the excavation, subject to a earthquake with a PGA of $0.6 g$ and an Arias intensity of 3.84 m/s. The proposed method is capable of accounting for the differences in the critical accelerations in the positive and negative horizontal directions and easily captures the complex collapse mechanisms involving soil as well as wall yielding. The permanent displacement fields of the two collapse mechanisms interact with each other and one of them is associated to yielding on both sides of the excavation. In such conditions, studying the collapse mechanism of the single walls separately would result in inaccurate predictions of the seismic performance of the retaining structure.

References

- [1] Miriano, C., Cattoni, E., and Tamagnini, C. (2016). Advanced numerical modeling of seismic response of a propped rc diaphragm wall. *Acta Geotechnica*, **11**, 161–175.
- [2] Conti, R. and Viggiani, G. M. B. (2013). A new limit equilibrium method for the pseudostatic design of embedded cantilevered retaining walls. *Soil Dyn. and Earthquake Engng.*, **50**, 143–150.
- [3] Conti, R., Viggiani, G. M. B., and Burali d'Arezzo, F. (2014). Some remarks on the seismic behaviour of embedded cantilevered retaining walls. *Géotechnique*, **64**, 40–50.
- [4] Cattoni, E. and Tamagnini, C. (In print, 2018). Critical accelerations for propped diaphragm walls in sand by finite element limit analysis. *Journal of Earthquake Engineering*.

ASSESSMENT OF SEISMIC VULNERABILITY OF LARGE CONCRETE DAMS BY MEANS OF FINITE ELEMENT MODELLING

G. Buffi¹, P. Manciola¹, L. De Lorenzis², C. Tamagnini¹, A. Gambi³, G. Montanari³

¹ Department of Civil and Environmental Engineering, University of Perugia, Perugia, Italy

² Institute of Applied Mechanics, Technische Universität Braunschweig, Braunschweig, Germany

³ Romagna Acque Società delle Fonti S.p.A., Forlì, Italy

1. Introduction

For many years now, FEM – Finite Element Method – simulations have been recognized as essential tools in the analysis of the behaviour of dam systems [1]. A key point in the vulnerability evaluation of arch-gravity dams is the study of the behaviour under dynamic actions of the vertical construction joints. The mortar injections restore the monolithic behaviour between the blocks and, at the same time, ensure the correct deformation. However, the joints are also planes of weakness of the structure, in particular when dynamic forces such as seismic events occur [2]. In literature several models are available to simulate the opening, closing and/or shear sliding of joints under seismic events, also including non-linear effects [3,4,5,6]. However, rarely or never are different modelling procedures tested on the same structure. Therefore, the present study proposes and analyses three vertical joint modelling procedures, progressively closer to reality, building as many FE models of the same dam structure: monolithic, surface-to-surface and solid element joint representations. The latter model, including the vertical joints as slices with their own thickness and material, allows us to investigate the damage evolution throughout such discontinuities under a severe seismic event. Case of study is the Ridracoli dam, an arch-gravity dam located in central Italy (103.5m high, with a crest 432m long), which geometry has been rebuilt by technical drawings and by a UAV – Unmanned Aerial Vehicle – survey.

2. Dam body modelling

The monolithic model ensures the continuity between adjacent blocks, by means of surface-based *tie* constraint, which makes the translational degrees of freedom equal for the pair of surfaces. The surface-to-surface joint model simulates the discontinuity between blocks along the contact surfaces: a very large coefficient of friction is adopted to avoid the slipping of a pair of surfaces in the radial direction; subsequently, along the normal direction, a pressure-overclosure relationship is adopted: the surfaces transmit contact pressure and the slope of the relationship is assumed to be equal to the stiffness of the joint mortar. Finally, the solid element joint model simulates the joints between the blocks as independent solid elements, splitting the discontinuity surface and spacing the two resulting surfaces at 10cm. This distance is adopted intentionally larger than the mortar joint because it is also intended to represent, by simulating a heavier discontinuity, the interfaces with the adjacent blocks. These thin slices between blocks are characterized by their own mechanical properties, equal to the mortar properties.

3. Influence of joint modelling and elasto-plastic damage time-history analysis

The comparison analyses are carried out including the same hydrostatic level of the experimental tests (vibrodyne test, seismic event). The three FE representations provide natural frequencies very close to the experimental result ones. An accurate joints representation, such as that provided by the solid element joints model, reproduces reality better than more simplified procedures. However, the differences in terms of natural frequencies between the models are minimal; the average percentiles of the gap in terms of natural frequencies are: 0.75% between the monolithic m. and the surface-to-surface joint m., 0.82% between the monolithic m. and the solid element joint m., 0.31% between the surface-to-surface joint m. and the solid element joint m.. This

gap could be crucial if the study deals with the monitoring of the state of conservation of a structure. Moreover, if the aim of the analyses is the inspection of damage in the joints, independent elements with their own mechanical properties and degradation models allow us to detect the evolution of damage under severe seismic events. On the other hand, if the goal is to analyse the general response of the structure under seismic events, joint modelling does not substantially influence global behaviour and simplified models such as the monolithic one can be employed. Indeed, the mode shapes of the three FEM models are equal, fitting also with the ones provided by the vibrodyne test. The solid element joint model allows us to investigate the damage evolution throughout such discontinuities. Indeed, the CDP – Concrete Damage Plasticity – model is adopted for the concrete of the vertical joints while the other materials have linear elastic constitutive behaviour. The tensile damage T parameter, included in the CDP model, assumes value close to zero for undamaged material and close to the unity for totally damaged material. A SLC – Collapse Limit State – seismic event for the site of Ridracoli is applied to the FEM model: the Accumoli (RI) event, which occurred on 30/10/2016. The analysis is performed taking into account the normal reservoir level, the full condition. The decrease of the stiffness of the hydraulic mortar is concentrated close to the central part of the dam crowing and it assumes maximum value of 50%, Fig. 1, showing the overall functionality of the structure also under severe seismic events.



Figure 1. Tensile damage parameter T [-], under Accumoli (RI) seismic event, with the normal reservoir level condition.

4. Conclusions

The joint modelling procedure does not influence the global dynamic behaviour of the structure, the mode shapes do not change, and simplified model, such as the monolithic one, can be employed for the study of the general behaviour of the structure under seismic event. On the other hand, the inclusion of construction joints in FEM model like solid elements allows for the verification also of these discontinuities in case of severe seismic events ensuring the overall seismic vulnerability assessment of the structure.

References

- [1] ICOLD (2013). Bulletin 155 - Guidelines for use of numerical models in dam engineering.
- [2] Azmi M. and Paultre P. (2002). Three-dimensional analysis of concrete dams including contraction joint non-linearity. *Engineering Structures*. 24, 6.
- [3] David T. Lau, B. Noruziaan, and A. G. Razaqpur (1998). Modelling of contraction joint and shear sliding effects on earthquake response of arch dams. *Earthquake Engineering & Structural Dynamics*, 27, 10.
- [4] Bachmann H., Ahmadi M. T., Izadinaa M. (2001). A discrete crack joint model for nonlinear dynamic analysis of concrete arch dam. *Computers & Structures*. 79, 4.
- [5] Bfer G. (1985). An isoparametric joint/interface element for finite element analysis. *International Journal for Numerical Methods in Engineering*. 21, 4.
- [6] Fenves G. L., Mojtahedi S. and Reimer R. B. (1992). Effect of Contraction Joints on Earthquake Response of an Arch Dam. *Journal of Structural Engineering*. 118, 4.

4. Stochastic/probabilistic approaches

IDENTIFICATION OF THE EQUIVALENT MICROSTRUCTURE OF POROUS MATERIALS: REGULARIZATION AND THE STOCHASTIC OPTIMIZATION PROCEDURE

D. Łydźba¹, A. Różański¹ and D. Stefaniuk¹

¹ *Wrocław University of Science and Technology, Faculty of Civil Engineering, Poland*

1. Introduction

The aim of the homogenization is up-scaling of mathematical description of the process under consideration, from the scale of heterogeneities to the scale of engineering applications. For the linear problems, the micro- and the macro- descriptions are analogous in the mathematical form, except material properties involved in both descriptions. The material properties of the micro-description are space dependent whereas that of the macro-description, called as overall ones, are constant since they characterize macroscopically homogeneous medium. The evaluation of the overall properties in terms of the phase properties and the microstructure morphology can be interpreted as a direct problem of homogenization since it consists of projections from the known microstructure morphology. Conversely, the inverse problem asks to recover the microstructure morphology from the overall properties.

Analytical homogenization schemes based on the solution of single inclusion problem, e.g., the Mori-Tanaka (M-T) or the Self-Consistent approach, are computationally attractive tools for estimating the homogenized properties of porous media. The main disadvantage of these methods is the choice of proper microstructure.

The aim of this work is to formulate the methodology of the identification of microstructure for real porous materials within the framework of the Mori-Tanaka and the Self-Consistent schemes.

2. Methodology

The inverse problem, in general, has no unique solution, i.e. one can simply imagine that there exist an infinite number of microstructures leading to the same homogenized property. Therefore the inverse problem has to be additionally constrained to ensure a unique solution, i.e. we assume the morphology of the porous medium of the matrix/inclusion type. In particular, oblate spheroids (pore space) are embedded in a continuous matrix (solid phase). Moreover, the problem is “relaxed” by introducing the probability density function (PDF) describing the frequency of oblate spheroids. So, the solution of the inverse problem is the evaluation of the PDF of oblate spheroids as a function of aspect ratio. This microstructure is called as the equivalent one. The equivalent microstructure has to preserve the overall responses of the original porous material, and at the same time, it has to be invariant of components’ mechanical properties. Therefore, the concept of overall microstructure response function is introduced which represents projections of micro-properties of composite components onto the space of admissible values of overall properties, for prescribed morphology. The analysis is limited to the case of overall thermal conductivity of porous medium.

Using the definition of an equivalent microstructure the primary integral definition of effective thermal conductivity is transformed to the Fredholm integral equation of the first kind, i.e.

$$\int_0^1 P_m(\lambda_r^{\text{hom}}, \theta) M^{\text{eq}}(\theta) d\theta = \frac{(1-\phi)}{\phi} \frac{\lambda_s - \lambda^{\text{hom}}}{\lambda^{\text{hom}} - \lambda_r^{\text{hom}}}, \quad (1)$$

where P_m is the so called localization operator (for more details see, e.g., [1]) and λ^{hom} is the measured value of the porous medium thermal conductivity. Hence, the inverse problem that is to

be solved is as follows: given the kernel function P_m as well as the right side of Eq. (1), identify the probability density function, $M^{eq}(\theta)$.

By solving an inverse problem, an original and complex microstructure of the porous material is replaced by the virtual/equivalent microstructure of ellipsoidal morphology type. For the solution of the inverse problem, the optimization algorithm based on the simulated annealing approach is proposed. The correctness and effectiveness of the methodology proposed is illustrated by a sequence of numerical examples. The paper is the extension of the approach introduced in the earlier Authors work [2].

3. Equivalent microstructure approach for unsaturated soil

The approach can also be adopted for partially saturated soil. The unsaturated soil is now treated as a 3-phase medium, so in the M-T approach all phases are included and Eq. (1) is properly reformulated. We assume that the pore space (in general, being filled by water and air at the same time) is still described by one, common PDF, M^{eq} . However, the novel in this approach is that for a given saturation degree (S_r) the corresponding ellipsoid aspect ratio θ_{Sr} is identified according to the relation below:

$$S_r = \int_0^{\theta_{Sr}} M^{eq}(\theta) d\theta. \quad (2)$$

Therefore, for a given S_r a portion of M^{eq} function (corresponding to the interval 0 to θ_{Sr}) is prescribed to the water phase while the remaining part represents the air phase.

The solution of the inverse problem provides the equivalent microstructure for unsaturated soil under consideration. Once again, the identified M^{eq} is substituted into the M-T scheme. Obtained predictions together with laboratory measurements are presented in Fig. 1.

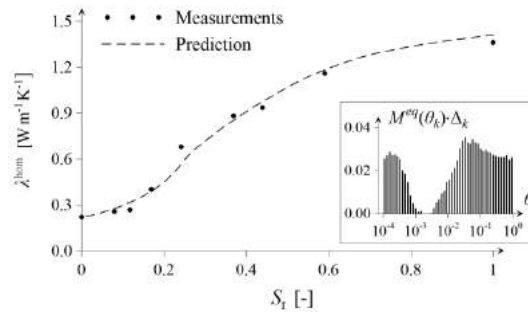


Fig.1. Prediction of soil thermal conductivity as a function of saturation degree.

4. References

- [1] Torquato, S. (2002). Motivation and Overview. In *Random Heterogeneous Materials* (pp. 1-19). Springer, New York, NY.
- [2] Łydźba, D., Róžański, A., & Stefaniuk, D. (2018). Equivalent microstructure problem: Mathematical formulation and numerical solution. *International Journal of Engineering Science*, 123, 20-35.

GENERAL UNCERTAINTY IN THE RELIABILITY ANALYSIS OF HETEROGENEOUS SOIL SLOPES AT SMALL FAILURE PROBABILITY

A. P. van den Eijnden¹ and M. A. Hicks¹

¹ *Delft University of Technology, Delft, The Netherlands*

Slope reliability analysis aims at identifying the reliability of a slope under different types of uncertainty. These include inherent uncertainty in the spatial variability, uncertainty in the (statistical) parameters, and uncertainty in the representativeness of the numerical models employed to predict the soil response in the boundary value problem capturing the slope under consideration. Semi-probabilistic methods (e.g. first order reliability method) have been used extensively for reliability analysis accounting for parametric uncertainty, whereas more rigorous approaches such as the random finite element method (RFEM) have been used to model the influence of uncertainty in the spatial variability of material parameters. Based on a combination of Monte Carlo simulation, finite element modelling and random field theory, the latter approach is able to address the reliability analysis of slopes in heterogeneous soils with fewer assumptions. To simulate events with small probabilities (i.e. at the weak tail of the distribution of the performance function), RFEM has recently been combined with subset simulation to address small-probability slope failure events in heterogeneous cohesive soils [1].

In this work, the combination of subset simulation with RFEM has been extended to account for cross-correlated random fields as well as uncertainty in the statistics of the material parameters. Starting from a homogeneous slope with known material strength parameters, the analysis of slope reliability is built up by adding the different types of uncertainty. This approach is used to demonstrate the need to correctly account for all material uncertainties in the evaluation of the slope reliability and mode of failure. An example of the slope model is given in Figure 1.

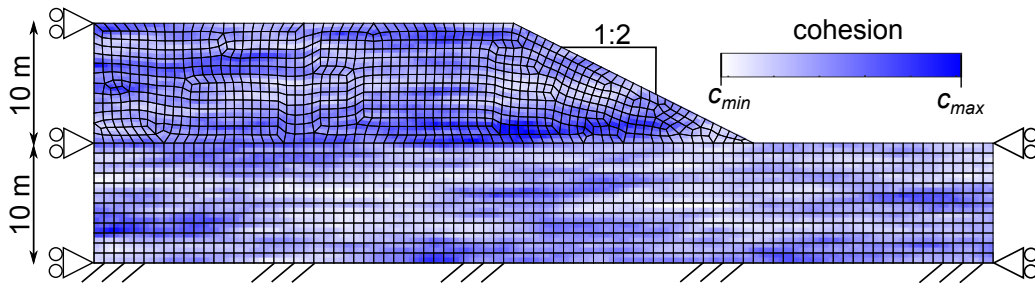


Figure 1. Geometry and boundary conditions of the slope with spatially variable material parameters. A typical spatial distribution of cohesion c with scales of fluctuation $\theta_h = 16$ m and $\theta_v = 2$ m is given as an example.

1. Homogeneous slopes based on mean strength parameters

Considering a homogeneous slope with mean cohesion μ_c and mean friction angle μ_ϕ , Figure 2 shows the limit state surface in the μ_c - μ_ϕ plane. Starting from an initial estimate of $\mu_c = 20$ kPa and $\mu_\phi = 20^\circ$, the uncertainty in this estimate has a leading influence on the encountered mode of failure. When only uncertainty in the cohesion exists, the failure mechanism is different from the case where only the friction angle is uncertain (see the failure mechanisms corresponding to points A and C). In addition, these mechanisms can be compared with the result of c - ϕ reduction (point B), in which the point of slope failure is searched along a line towards the origin. In general, the actual failure mechanism can relate to any point on the limit state surface, depending on the joint distribution of both μ_c and μ_ϕ .

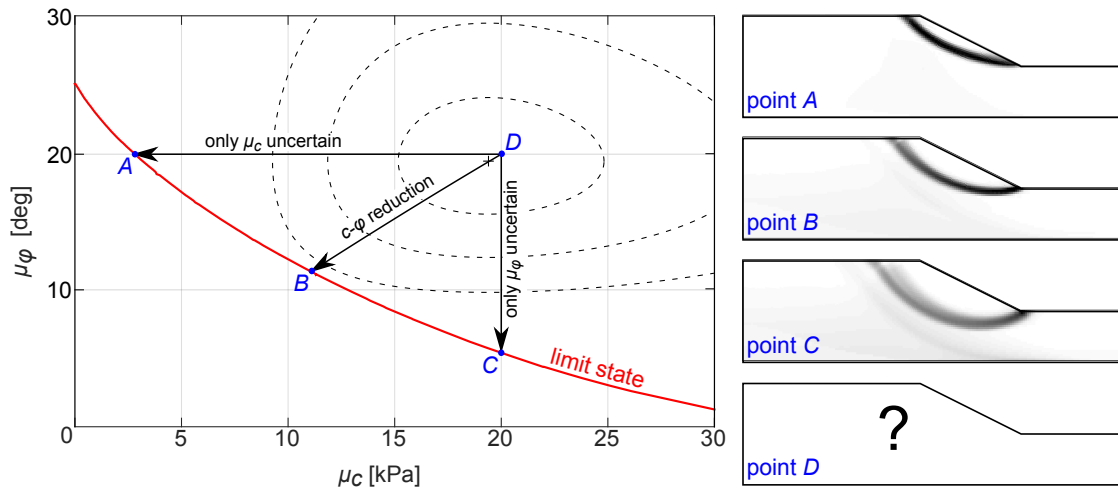


Figure 2. Left: Limit state surface of a homogeneous slope based on mean strength parameters μ_c and μ_ϕ . Right: Failure mechanisms for the points on the limit state surface, characterised by ε_q^p contours.

2. Heterogeneous slopes and general uncertainty

When introducing spatially variable material properties (see Figure 1), more forms of uncertainty are introduced due to the distribution of weak and strong zones in the domain. As a result, an unfavorable distribution of weak and strong zones could lead to slope failure, even while maintaining the first estimate of the mean strength parameters (i.e. slope failure at point D). This implies that, due to spatial variability, point D lies on the limit state surface in a high-dimensional variable space. Indeed, the introduction of spatial variability introduces many additional variables, each of which has a specific distribution, and slope failure events have to be searched for in the complete variable domain.

The final step is the combination of uncertainty in both the point statistics and spatial variability in the subset simulation framework. Based on the relative distribution of parameters, the behaviour of slopes with uncertainty in both the spatial variability and point statistics is studied. Depending on the relative degree of uncertainty between the point statistics and spatial variability, the importance of correctly accounting for all system variables is demonstrated. Results show clear differences in failure mode between slopes dominated by point statistics uncertainty and slopes dominated by uncertainty in spatial variability. These differences become more important with decreasing probability of failure.

3. Conclusions

For homogeneous slopes, with only c and ϕ as uncertain parameters, a range of possible failure modes exists. The occurrence of these modes depends on the specific parameter distributions, and a single evaluation (e.g. c - ϕ reduction) can mis-represent the relevant mode of failure. Extended to the general case of spatially variable soils, with many more variables in addition to the point statistics, this effect is more pronounced. Correctly analysing the failure modes in spatially variable soils requires treating all parameters consistently, especially when looking at small probability failure events.

Acknowledgments

This work is part of the research programme Reliable Dykes with project number 13864, which is partly financed by the Netherlands Organisation for Scientific Research (NWO). This work was carried out on the Dutch national e-infrastructure with the support of SURF Cooperative.

References

- [1] van den Eijnden, A. P. and Hicks, M. A. (2017). Efficient subset simulation for evaluating the modes of improbable slope failure. *Comp. & Geotechnics*, **88**, 267–280.

RANDOM BEARING CAPACITY OF SQUARE FOOTING BASED ON KINEMATICAL APPROACH

Chwała M.¹, Puła W.¹

¹ *Wroclaw University of Science and Technology, Wroclaw, Poland*

1. Introduction

The recent increase in the interest of researchers in probabilistic methods in geotechnics is a response to the need of the proper consideration of the spatial variability of soil. The authors examine the spatial soil strength parameters variability within one soil layer. As a deterministic background, three dimensional failure mechanism proposed by Michałowski [1] was adopted by the authors and utilized in numerical analyses. The failure mechanism originates from the kinematical approach of limit analysis; therefore, the resulting bearing capacity is an upper bound of the limit load. To describe the spatial variability of soil strength properties the random field theory was applied. The adoption of Vanmarcke's spatial averaging [2] to the slip surfaces in the failure mechanism, allows to derivate the integrals which describe the averaged values of the new variance on each slip surface and new covariances between them (components of the covariance matrix). As a result of the averaging procedure, the individual values of soil strength parameters were obtained for each of the slip surface in the failure mechanism. Based on the new set of soil parameters the optimal geometry is found by a created algorithm which uses the simulated annealing optimization scheme [3].

The numerical analyses were performed for square footing, for self-weighted cohesive-frictional soil. The angle of internal friction and cohesion were modelled by lognormal random fields; three values of vertical fluctuation scale are assumed to describe correlation strength in a random field, namely: $\theta_v = 0.25 m$, $\theta_v = 0.50 m$ and $\theta_v = 0.75 m$. For particular value of θ_v the four values of horizontal fluctuation scale θ_h are assumed: $\theta_h = \theta_v$, $\theta_h = 5\theta_v$, $\theta_h = 10\theta_v$ and $\theta_h = 30\theta_v$. A Monte Carlo simulation is used to obtain numerous bearing capacity values for each considered issue. The obtained results allowed to fit the probability density function and to determine the reliability indices.

2. Numerical algorithm

The three-dimensional failure mechanism was adopted for the random bearing capacity analysis by the implementation of the possibility of subjecting different values of friction angle and cohesion on the each slip surface. The failure mechanism consists of rigid blocks which are narrowed by triangles, a part of an ellipse with trapeze and conical surfaces. The simulated annealing optimization scheme was used in creating the optimization procedure. For the numerical analysis, the reasonable compromise between computation time and accuracy has to be established, thus the number of rigid blocks equal to 5 is chosen for further investigations.

According to Vanmarcke's spatial averaging theory, integrals for the covariance matrix components are derived for the Gaussian covariance function, due to the three-dimensional issue the covariance function is defined as in Eq. (1), where the parameters ω_1 , ω_2 , ω_3 are expressed by $\theta_x/\sqrt{\pi}$, $\theta_y/\sqrt{\pi}$, $\theta_z/\sqrt{\pi}$, respectively. While, θ_x , θ_y , θ_z denote the fluctuation scales in the specified directions (horizontal fluctuation scales are assumed to be equal $\theta_x = \theta_z$, and denoted as θ_h).

$$R(\Delta x, \Delta y, \Delta z) = \sigma_x^2 \exp \left\{ - \left[\left(\frac{\Delta x}{\omega_1} \right)^2 + \left(\frac{\Delta y}{\omega_2} \right)^2 + \left(\frac{\Delta z}{\omega_3} \right)^2 \right] \right\} \quad (1)$$

Spatial averaging transformed the initial random field into single variables actual for particular domains. In the case of the three-dimensional failure mechanism these are slip surfaces. Due to the averaging process, the point variance of the random field is subjected to reduction; the level of

reduction depends on the shape of the area of averaging and its relative size to the fluctuation scale. The covariance between two random variables obtained in agreement with the aforementioned method can be determined by Eq. (2).

$$\text{Cov}(X_{V_1}, X_{V_2}) = \frac{1}{|V_1||V_2|} \int_{V_1} \int_{V_2} R(x_1, y_1, z_1, x_2, y_2, z_2) dV_1(x_1, y_1, z_1) dV_2(x_2, y_2, z_2) \quad (2)$$

In a particular case, when $V_1 = V_2$ Eq.(2) expressed the formula for variance. For $n = 5$ rigid blocks there are 16 slip surfaces, thus the covariance matrix is 16x16 in size.

The created numerical algorithm starts at generating 16 independent values of friction angle and cohesion based on initial probability characteristics. The optimal failure geometry for the generated soil parameters is found through the optimization procedure. Next, the covariance matrix is determined and by using a modification of the algorithm given in [4], the new set of soil strength parameters is determined. The optimization procedure is called again for the new soil parameters; as a result the final value of bearing capacity is obtained. All procedure is repeated N times in the Monte Carlo framework to assure the reasonable accuracy in mean value estimation.

3. Numerical analysis and results

Numerical analyses were performed for square footing for multiple combinations of fluctuation scales. Cohesive-frictional soil was considered, the soil properties were characterized by: lognormal random fields with expected value $\mu_\phi = 20^\circ$ and standard deviation $\sigma_\phi = 3^\circ$ for friction angle, and $\mu_c = 20$ kPa, $\sigma_c = 4$ kPa for cohesion; random variable with $\mu_\gamma = 18.2$ kN/m³, $\sigma_\gamma = 1.092$ kN/m³ for unit weight; overburden pressure was equal to 14.4 kPa. In Fig. 1 the obtained results are shown as a function of θ_h/b ratio, where b is the width of the foundation. The rise in mean values and standard deviations with an increase in θ_h/b is observed; however, both values stabilized for $\theta_h/b > 5$ (this results from the relatively large horizontal fluctuation scale with respect to the failure mechanism). The strong influence of θ_v and θ_h on standard deviation causes the substantial dependence of reliability indices from fluctuation scales, and emphasizes the importance of reasonable estimation of fluctuation scales form field testing.

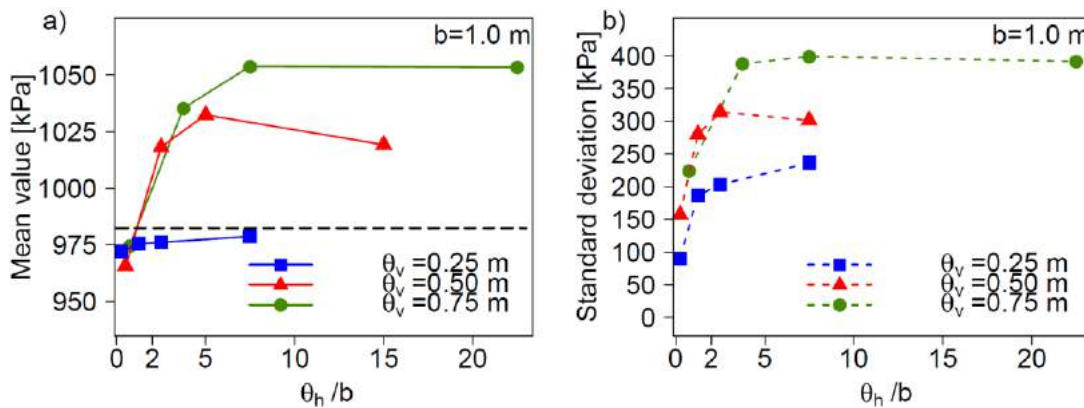


Fig. 1. Mean values (a) and standard deviations (b) obtained for three dimensional failure mechanism. Note that dashed horizontal line is the bearing capacity obtained for the expected value of soil parameters.

4. References

- [1] Michalowski R. L., An estimate of the influence of soil weight on bearing capacity using limit analysis. *Soils and Foundations*; 1997; 37; No. 4; 57-64.
- [2] Vanmarcke E.H. *Random fields – analysis and synthesis*. Cambridge: MIT Press;1983.
- [3] Kirkpatrick S., Gelatt C. D., Vecchi M. P. Optimization by Simulated Annealing, *Science*; 1983; 220:671-680.
- [4] Puła W., Chwała M., On spatial averaging along random slip lines in the reliability computations of shallow strip foundations. *Computers and Geotechnics*; 2015; 68; 128-136.

ULTIMATE LIMIT STATE ASSESSMENT OF DYKE RELIABILITY USING THE RANDOM MATERIAL POINT METHOD

G. Remmerswaal¹, M.A. Hicks¹ and P.J. Vardon¹

¹ *Geo-Engineering Section, Delft University of Technology, Delft, Netherlands*

1. Introduction

This paper investigates embankment reliability based on the ultimate limit state (ULS). The ULS is generally not clearly defined and, especially for flood defences, the ULS is currently under discussion. According to Dutch law [1], flooding which leads to either casualties or substantial financial damage is considered as the ultimate limit state of a flood defence structure. However, initial slope instability is regarded as flood defence failure according to guidelines for the assessment of macro-instability of dykes [2]. Allowing initial failure, but preventing a dyke breach, is not prohibited by the current Dutch regulations and can lead to more efficient design. Analysis of both large deformations as well as the influence of spatial variability of soil properties is important to assess the reliability of a dyke against breaching. This paper uses a new technique called the random material point method (RMPM) [3], which combines MPM [4] for modelling large deformations, with random fields [5] for modelling soil variability, in a Monte Carlo simulation.

2. Problem description

The influence of soil heterogeneity on slope stability has been evaluated for an idealised boundary value problem. A 5 m high clay dyke, see Figure 1, is modelled with 8850 material points (i.e. four per 4-node element), using implicit RMPM with a time step of 0.01 s. The clay has been modelled using a cohesion-softening constitutive model and the soil parameters given in Table 1. Random fields of peak and residual undrained shear strength have been generated using the mean values of c_p and c_r given in Table 1, a coefficient of variation of 0.2 and a vertical scale of fluctuation (θ_v) of 1 m, and then mapped onto the material points. A parametric study has been performed to investigate the influence of the horizontal scale of fluctuation (θ_h).

3. Influence of anisotropy of the heterogeneity on the reliability against a dyke breach

Six Monte Carlo simulations, each comprising over 200 realizations, have been performed, with each simulation using a different horizontal scale of fluctuation. Each realization is loaded under gravity to generate the in-situ stresses, with most slopes being unstable under their own weight. In Figure 2, the reliability against failure has been plotted against time. Initial slope failure generally occurs within a couple of seconds. The results correspond to the findings of Hicks and Samy [5], who showed that a larger degree of anisotropy results in a higher reliability against initial failure for a slope with a factor of safety, based on the mean property value, below one.

Figure 2b depicts the reliability against dyke breach, which has been defined as the height of the dyke falling below the external free water level, which is defined to be at 4.5 m. A clear increase

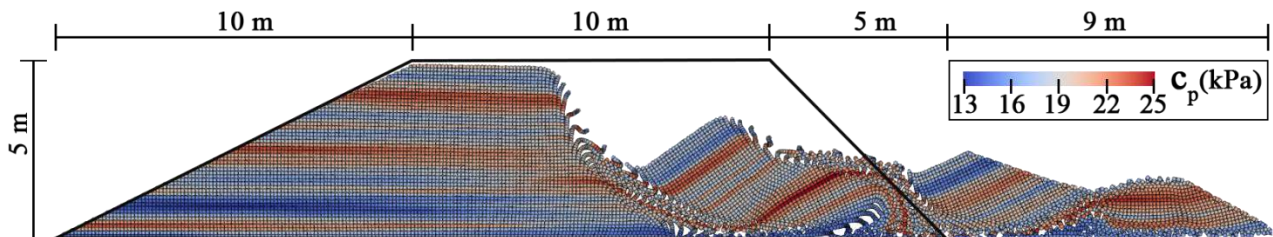


Figure 1. An example of a retrogressive failure mechanism for one realization of the spatial variability ($\theta_v = 1$ m, $\theta_h = 48$ m). Initial problem geometry shown in black.

Young's modulus E (kPa)	Poisson's ratio ν (-)	Mean peak cohesion c_p (kPa)	Mean residual cohesion c_r (kPa)	Softening modulus (kPa)	Unit weight γ (kN/m ³)
1000	0.45	18	4	-50	17

Table 1. Soil properties.

in reliability between initial failure and a dyke breach, from 0-20% up to 55-85%, is observed. Counter-intuitively, the reliability against a dyke breach decreases with a larger degree of anisotropy of the heterogeneity. As shown by Wang et al. [3], a larger degree of anisotropy increases the standard deviation of the sliding distance, which reduces the reliability.

4. Conclusions

As expected, the consideration of ULS failure results in a gain in reliability, and thereby to a more efficient design. The reliability gain decreases with an increase in the degree of anisotropy. Further investigation is necessary on the effect of 3D failure surfaces and pore pressures.

5. Acknowledgements

This work is part of the research programme AllRisk which is financed by the Netherlands Organisation for Scientific Research (NWO), project number P15-21 Project 4.

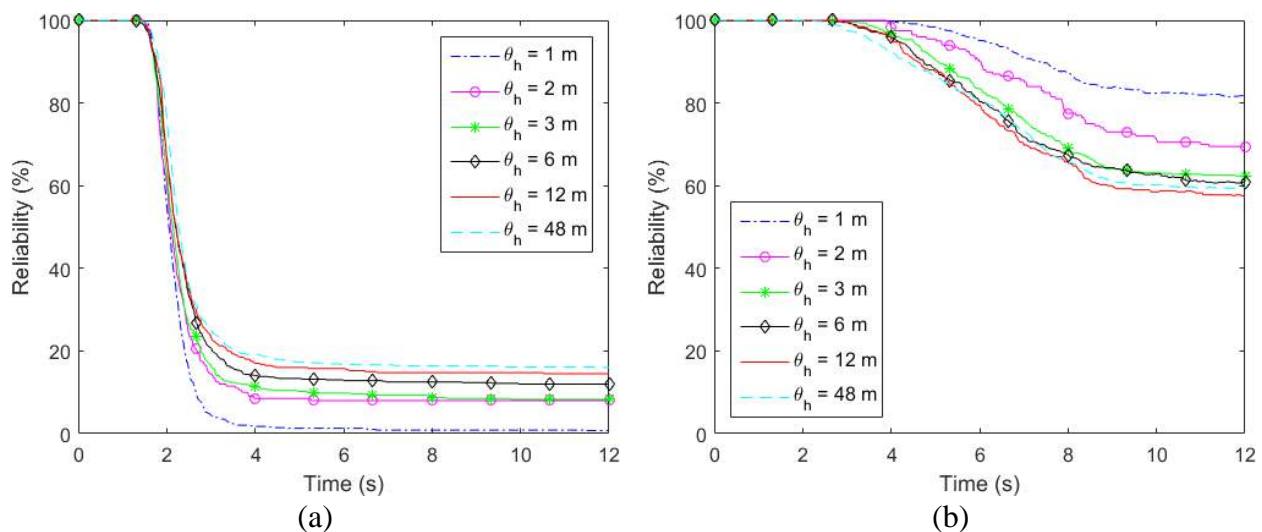


Figure 2. Reliability of Monte Carlo simulations with varying anisotropy. (a) Reliability against initial failure. (b) Reliability against a dyke breach.

6. References

- [1] Waterwet (2009). *Waterlaw: BWBR0025458*, Article 1.1, Accessed on 13th February 2018, from: <http://wetten.overheid.nl/BWBR0025458/2018-01-01#>
- [2] Ministerie van Infrastructuur en Milieu Netherlands (2016). *Schematiseringshandleiding macrostabiliteit: WBI 2017*. Helpdesk Water, Utrecht.
- [3] Wang, B., Hicks, M.A. & Vardon, P.J. (2016). Slope failure analysis using the random material point method. *Geotech. Lett.*, **6**(2), 113-118.
- [4] Sulsky, D., Chen, Z. & Schreyer, H.L. (1994). A particle method for history-dependent materials. *Comput. Methods in Appl. Mech. Eng.*, **118**(1-2), 179-196.
- [5] Hicks, M.A. & Samy, K. (2002). Influence of heterogeneity on undrained clay slope stability. *Q. J. Eng. Geol. Hydrogeol.*, **35**(1), 41-49.

QUANTIFICATION OF UNCERTAINTY IN GEOTECHNICAL ENGINEERING BASED ON POLYNOMIAL CHAOS

St. Drakos¹, GN. Pande^{1,2}

¹ *International Center for Computational Engineering, Rhodes/Swansea, Greece/UK*

² *ZCCE Swansea University, Swansea SA1 8EN, UK*

1. General

In recent years, advances in computing power has led to scientists and engineers being able to solve complex physical and mathematical problems in the field of geotechnical engineering. Large problems having complex geometries in three-dimensional space can now be solved in with materials with highly nonlinear behavior. However, the spatial variability of mechanical characteristics of geo-materials and the uncertainty of determining them restricts the usefulness of complex models in real life problems. This gap between theory and practice can be bridged by quantifying uncertainty of input parameters and this line of research is gaining attention of researchers in the scientific world, especially geotechnical engineers. The purpose of quantifying uncertainty knowing the probability distribution of input data is to be able to calculate the statistical variation in in the outcomes such as settlement, failure load etc. and design safer and more economical geotechnical structures. This stage of the calculations is complex and various methods have been developed such as Monte Carlo and the Random Finite Element Method [1], [2] or more sophisticated stochastic spectral Galerkin approaches [3], [4], [5]. This paper analyses the process of uncertainty propagation using polynomial chaos expansion for a shallow footing and compares the results with those obtained by the Monte Carlo Method and the Stochastic Galerkin Method. Computational efficiency is the main advantage of the approach over other methods.

3. Probabilistic Uncertainty Propagation

Given the distribution of soil parameters the aim is to calculate the Probability Distribution Function (*PDF*) of the outcome of the problem. Consider for example a geotechnical problem where the soil characterized by a yield criterion $f(\sigma, w)$ where σ is stress level at each time, $w = [w_1, w_2 \dots w_M]$ is the vector of yield function parameters and $y = [w, E, v]$ is a vector of the input parameters of the problem. Here E and v are the Young's Modulus and Poisson's ratio respectively. In that case the problem can be described by the following equations:

$$\left\{ \begin{array}{l} \sigma_{ij,j}(\mathbf{x}) = f(\mathbf{x}) \text{ in } D \\ \sigma_{ij}(\mathbf{x}) = C_{ijkl}(\mathbf{x})\varepsilon_{kl}(\mathbf{x}) \text{ in } D \\ \mathbf{u}(\mathbf{x}) = \mathbf{g}_D \text{ in } B_D \\ \sigma_{ij}(\mathbf{x})n_j = \mathbf{g}_N \text{ in } B_D \\ f(\sigma_{ij}, w) \leq 0 \end{array} \right. \quad (1)$$

Drakos & Pande (2015) developed an algorithm of Stochastic Finite method using the Generalized Polynomial Chaos and proved that the problem formulation (1) has the final form:

$$Q_m \otimes K_m = q_0 \otimes (f_0 + t_{gN}) - Q_m \otimes K_{Bm} \cdot g_d \quad (2)$$

In order to propagate the uncertainties from input parameters to the results for an elastoplastic

problem through the constitutive equation the strains must be calculated first. In an elasto-plastic problem of homogeneous isotropic body one of the field equations that must be satisfied at all interior points of the body is the Strain-Displacement relations: Using the displacement polynomial chaos expansion the Strain-Displacement relations is given by:

$$\varepsilon_{ij}(x, y) = \frac{1}{2} \left(\sum_{k=0}^Q u_{i,j}^{(k)}(x) \psi_k(y) + \sum_{k=0}^Q u_{j,i}^{(k)}(x) \psi_k(y) \right) = \sum_{k=0}^Q \varepsilon_{ij}^{(k)} \psi_k(y) \quad (3)$$

In an elastoplastic geotechnical problem the non linear behaviour of soil needs integrations algorithms for the exact stress value prediction at each point. Solving for each load increment, the boundary value problem the strain PCE can be calculated as before (eq. 2). At each increment $n+1$ they are also known the stress from the previous state σ^n the plastic strain $d\varepsilon_{kl}^{p,n}$ and the probability of yielding p_f^n . The basic steps in computing the new state of stress are as follows:

The mean value of elastic predictor and of the trial stress are given:

$$\langle d\sigma_{ij}^{n+1} \rangle = \langle C_{ijkl} d\varepsilon_{kl}^{n+1} - p_f^n d\varepsilon_{kl}^{p,n} \rangle \quad (4)$$

$$\langle \sigma_{ij}^{tr,n+1} \rangle = \langle \sigma_{ij}^n \rangle + \langle d\sigma_{ij}^{n+1} \rangle \quad (5)$$

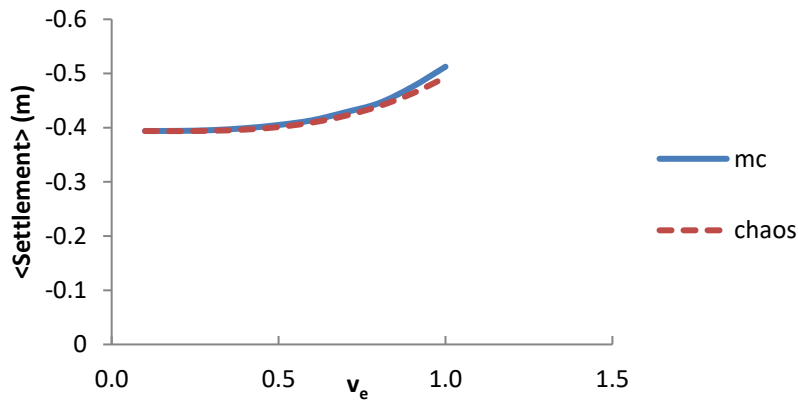


Fig. 1 Variation of settlement with coefficient of variation

Finally, a numerical experiment of a shallow foundation subjected to uniform vertical load is carried out in order to compare the accuracy and the computational cost of the proposed method with those of Monte Carlo Stochastic Galerkin Methods. Fig 1 shows variation of settlement of the foundation with a constant mean value of elastic modulus but varying coefficient of variation (v_e) for Monte Carlo (mc) and PC expansion (chaos) approaches. Polynomial Chaos method gives results close to that of Monte Carlo but is computationally vastly more efficient.

5. References

- Fenton, G. A., and Griffiths, D. V. (2002), "Probabilistic foundation settlement on spatially random soil." *J. Geotech. Geoenviron. Eng.*, 128(5), 381–390.
- Fenton, G. A., and Griffiths, D. V. (2005), "Three-dimensional probabilistic foundation settlement." *J. Geotech. Geoenviron. Eng.*, 131(2), 232–239.
- Drakos I. S. (2015). "Elastic Stress Predictor for Stochastic Finite Element Problems". *World Journal of Mechanics*, Vol.5 No.11, pp. 222-233.
- Drakos I. S (2015) "Quantitative of Uncertainty in unconfined flow problems", *International Journal of Geotechnical Engineering*, Taylor & Francis pp 213-22.
- Drakos St. I (2015). "Constitutive Relations of Stress and Strain in Stochastic Finite Element Method" *American Journal of Computational and Applied Mathematics*, Vol. 5, No. 6, pp. 164-173

RELIABILITY ANALYSIS OF SQUARE FOOTING BEARING CAPACITY ON SPATIALLY VARIABLE COHESIVE-FRICTIONAL SOIL

Kawa M.¹, Pula W.¹

¹ *Wroclaw University of Science and Technology, Wroclaw, Poland*

1. Introduction

The methods that combine the Random Field Theory with Monte-Carlo Simulations such as Random Finite Element Method (RFEM) or Random Finite Difference Method (RFDM) have been successfully used for reliability analysis of bearing capacity of strip foundations in many studies [1-3]. It seems, however, that so far these methods were not employed to the 3D problem of bearing capacity of square footing, probably due to high computational cost of such analysis. Performing such a calculations is the main focus of the present study.

The problem of critical load of square footing on spatially variable Mohr-Coulomb substrate is considered. Two separate cases of substrate are tested, i.e. purely cohesive and cohesive-frictional soil. In the first series of calculations surface smooth footing on weightless soil is assumed. Cohesion is assumed as the only spatially variable property (modeled with random field). The second series of calculations consider smooth footing on self-weight soil. Cohesion and friction angle are assumed as two independent specialty variable properties. The dimensions of the footing in all cases are assumed as 1x1m.

2. Random Field

3-dimensional random fields of cohesion and friction is generated using Fourier Series Method [4]. The method is slower than popular LAS [5] method but allows to reduce computation cost by using cuboid but non-uniform grid which can be adjusted to the problem. For all generated random fields anisotropic exponential correlation model is used (two horizontal scales of fluctuation, namely θ_x and θ_y are assumed to be equal):

$$\rho(\tau) = \exp\left\{\frac{-2|\tau|}{\theta_x} + \frac{-2|\tau|}{\theta_y} + \frac{-2|\tau|}{\theta_z}\right\} \quad (1)$$

For the first series of calculation cohesion has been assumed being normally distributed with mean value of 30kPa and coefficient of variation 0.1. Three different values of vertical fluctuation scale are considered i.e. 0.5, 1 and 2m. Also different values of the horizontal fluctuation scale in range from 1m to infinity have been assumed. The boundary value problem domain with single realization of random field for $\theta_x = \theta_y = 5\text{m}$ and is presented in Fig. 1. For the second series the random fields of friction and cohesion have been assumed as following lognormal and bounded distributions, respectively. Mean values and coefficient of variation has been assumed identical as in the paper [1] ($\mu_c = 36\text{kPa}$, $\sigma_c = 20\text{kPa}$, $\mu_\phi = 20^\circ$, $\mu_\phi = 4.8^\circ$) reflecting the data obtained for Taranto clay. In the present study the vertical scale of fluctuation for that case was constant and equal 0.5m, and horizontal scale of fluctuation was changed in the range from 1m to infinity.

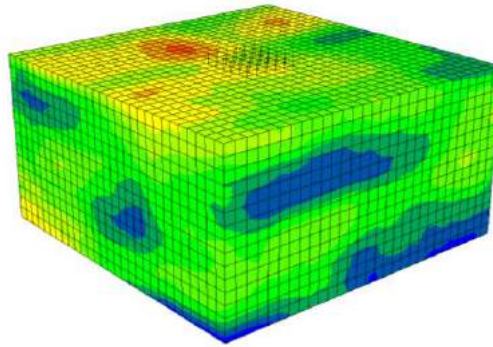


Fig. 1. The individual realization of random field generated with FSM. $\theta_x=\theta_y=5m$ $\theta_z=0.5m$

3. Results of numerical analysis

The individual realization of the boundary problem were modeled and solved in FLAC3D code. Every considered case of has been simulated at least 1000 times. Both mean values as well as coefficients of variation of obtained values of critical load has been computed. Results obtained in the first series of computations for 1000 of realizations are presented in Fig. 2. The obtained mean values of bearing capacity are very close to each other. The general trend is visible but the values can be slightly disturbed with numerical errors. The diagrams of coefficient of variation are numerically stable and show clear dependence on the values of both fluctuation scales.

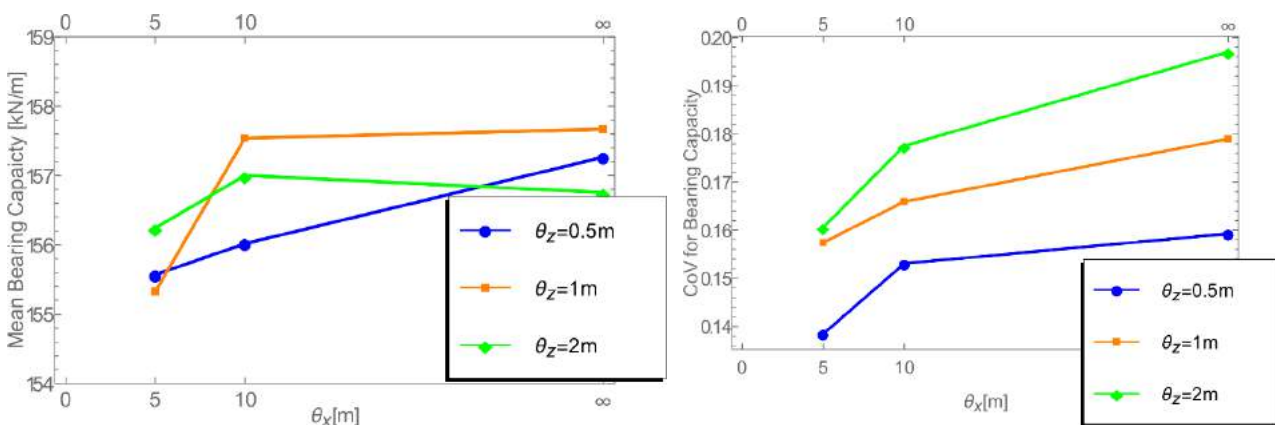


Fig 2. Mean values (right hand side) and coefficients of variation (left hand side) for bearing capacity of square footing on purely cohesive soil

4. References

- [1] Vessia, G., Cherubini, C., Pieczyńska, J., & Puła, W. (2009). Application of random finite element method to bearing capacity design of strip footing. *Journal of GeoEngineering*, 4(3), 103-112.
- [2] Pieczyńska-Kozłowska, J. M., Puła, W., Griffiths, D. V., & Fenton, G. A. (2015). Influence of embedment, self-weight and anisotropy on bearing capacity reliability using the random finite element method. *Computers and Geotechnics*, 67, 229-238.
- [3] Puła, W., Pieczyńska-Kozłowska, J. M., & Chwała, M. (2017). Search for the worst-case correlation length in the bearing capacity probability of failure analyses. *Geo-Risk 2017* (pp. 534-544).
- [4] Jha, S. K., & Ching, J. (2013). Simplified reliability method for spatially variable undrained engineered slopes. *Soils and Foundations*, 53(5), 708-719.
- [5] Fenton, G. A., & Vanmarcke, E. H. (1990). Simulation of random fields via local average subdivision. *Journal of Engineering Mechanics*, 116(8), 1733-1749.

5. Application of numerical techniques to practical problems

2D HYDRO-MECHANICAL ANALYSES OF RAINFALL INDUCED SLOPE INSTABILITY

P. Sitarenios^{1,2}, F. Casini¹, A. Askarinejad³ & S.M. Springman²

¹ *Department of Civil Engineering and Computer Science, University of Rome “Tor Vergata”, Italy*

² *Institute for Geotechnical Engineering, ETH Zurich, Switzerland*

³ *Geo-Engineering section, TU Delft, Netherlands*

1. Introduction

A full scale field experiment was conducted in 2009, in Ruedlingen, Switzerland, where a steep forested slope was subjected to artificial rainfall, resulting in slope failure 15 hours later [1,2]. The experimental campaign included laboratory and in-situ soil characterisation, as well as extensive slope instrumentation and monitoring over a period of nearly 1 year. The hydro-mechanical behaviour of the Ruedlingen slope is studied numerically and reported in this contribution, in order to investigate the failure mechanism and reveal the main triggering agent.

2. Numerical Analyses

The numerical investigation is carried out using the Code Bright Finite Element Method

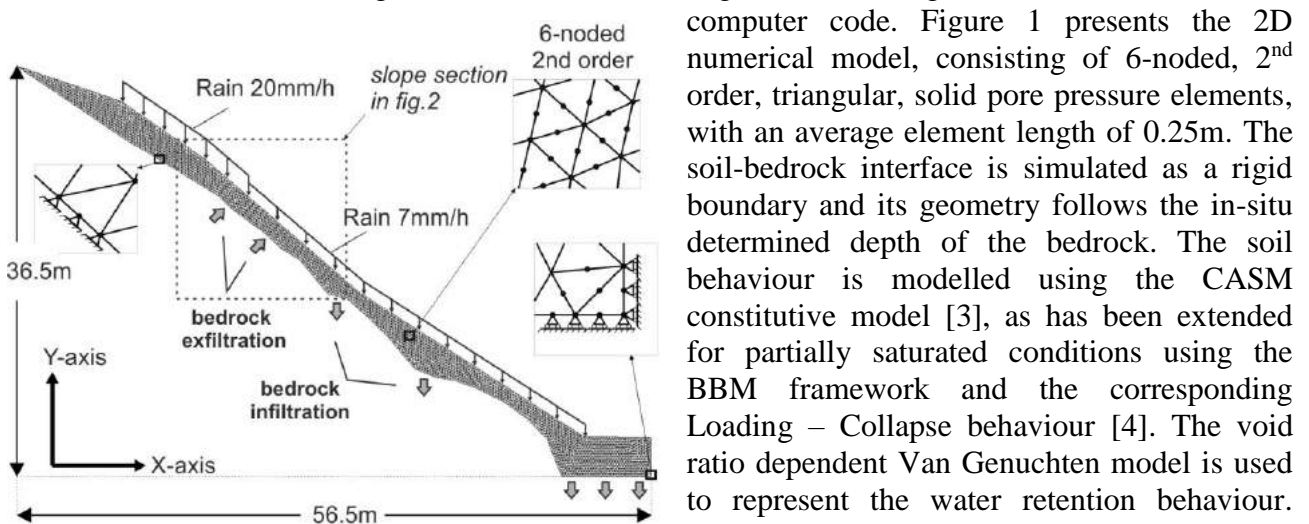


Figure 1. The 2D numerical model in Code Bright

computer code. Figure 1 presents the 2D numerical model, consisting of 6-noded, 2nd order, triangular, solid pore pressure elements, with an average element length of 0.25m. The soil-bedrock interface is simulated as a rigid boundary and its geometry follows the in-situ determined depth of the bedrock. The soil behaviour is modelled using the CASM constitutive model [3], as has been extended for partially saturated conditions using the BBM framework and the corresponding Loading – Collapse behaviour [4]. The void ratio dependent Van Genuchten model is used to represent the water retention behaviour. Table 1 summarizes the mechanical and hydraulic properties, which have been selected based on an extensive calibration exercise on

available experimental results for Ruedlingen soil behaviour (*e.g.*, [5]).

Mechanical Parameters (CASM)				BBM Framework	
κ	0.01	M	1.3 ($\phi_c=32^\circ$)	Pc (kPa)	10
λ	0.13	n	1.4	β (MPa-1)	1000
N_{iso}	2.21	r	2.5	r^*	0.75
Hydraulic permeability		Water Retention Behaviour (Van Genuchten model)			
k_{sat}	10^{-5} m/s	P_0 (kPa)	0.065	α	21.0
k_{rel}	S_r^3	λ	0.4	ϕ_0	0.40

Table 1. Soil parameters used in the analyses (symbols defined in [Code Bright Users Guide](#)).

3. Results

Following an initial consolidation step, rainfall was simulated as water inflow at the surface of the slope. Based on the field data, two zones were discretized with different rain intensities. The analyses also account for the hydraulic interaction between the soil and the bedrock, through suitable exfiltration and infiltration boundaries, also portrayed in figure 1. Their application follows field observations and results from existing seepage analyses [1].

The analyses managed to capture the experimental behaviour very well. Accurate prediction of the failure time required back-calculation of the saturated permeability, which was found equal to 10^{-5} m/s, one order of magnitude higher compared to its laboratory counterpart. Figure 2 presents the distribution of pore pressure, saturation degree, deviatoric deformation and displacements at failure. The results suggest that water exfiltration in the upper part of the slope is the main triggering agent. It is attributed to interconnected bedrock fissures, which re-direct rainfall water from the top of the slope towards lower altitudes [6, 7]. This causes an increase in pore pressure, which increases the mobilised soil strength and thus accelerates plastic straining, which finally leads to the formation of a failure surface at the soil–bedrock interface. Parametric analyses highlight the dominant role of hydraulic permeability in the predicted failure time, while soil strength parameters were also found to play a significant role.

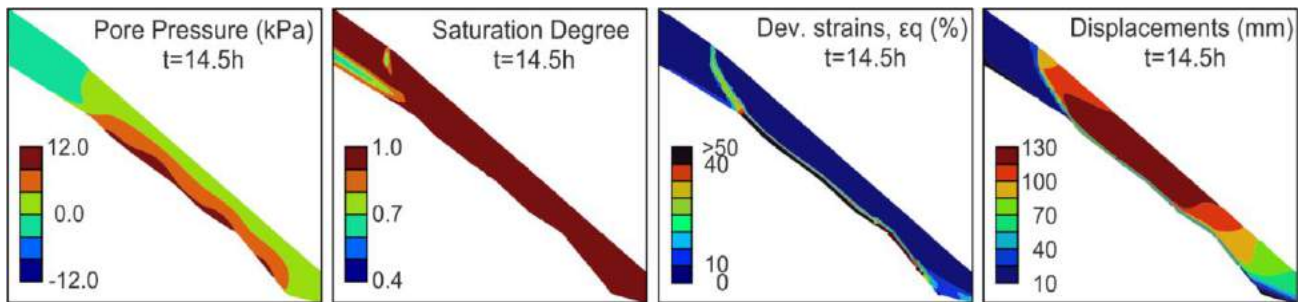


Figure 2. Distribution of main variables (see fig.1 for the portrayed slope section).

4. References

- [1] Askarinejad, A., Casini, F., Bischof, P., Beck, A., & Springman, S. M. (2012). Rainfall induced instabilities: a field experiment on a silty sand slope in northern Switzerland. *Italian Geotechnical Journal*, 3(12), 50-71.
- [2] Springman, S. M., Askarinejad, A., Casini, F., Friedel, S., Kienzler, P., Teyssiere, P., & Thielen, A. (2012). Lesson learnt from field tests in some potentially unstable slopes in Switzerland. *Acta Geotechnica Slovenica*, 1, 5-29.
- [3] Yu, H. S. (1998). CASM: A unified state parameter model for clay and sand. *International Journal for Numerical and Analytical Methods in Geomechanics*, 22(8), 621-653.
- [4] González, N.A. (2011). Development of a family of constitutive models for geotechnical applications. PhD Thesis, Technical University of Catalunya, Barcelona (Spain).
- [5] Casini, F., Serri, V., & Springman, S. M. (2013). Hydromechanical behaviour of a silty sand from a steep slope triggered by artificial rainfall: from unsaturated to saturated conditions. *Canadian Geotechnical Journal*, 50(1), 28-40.
- [6] Askarinejad, A., Laue, J. & Springman, S. M. (2014). Effect of bedrock shape and drainage properties on the stability of slopes. *International Conference on Physical Modelling in Geotechnics*. Perth, Australia, ICPMG 2014, 2014, Vol. 2, p. 1211-1217.
- [7] Elia, G., Cotecchia, F., Pedone, G., Vaunat, J., Vardon, P. J., Pereira, C., Springman, S. M., Rouainia, M., Van Esch, J., Koda, E., Josifovski, J., Nocilla, A., Askarinejad, A., Stirling, R., Helm, P., Lollino, P. & Osinski, P. 2017. Numerical modelling of slope–vegetation–atmosphere interaction: an overview. *Quarterly Journal of Engineering Geology and Hydrogeology*, 50, 249-270.

FLUID-SOLID TRANSITION IN UNSTEADY SHEARING FLOWS

D. Vescovi, D. Berzi and C. di Prisco
Politecnico di Milano, Milano, Italy

1. Introduction

The discontinuous and inhomogeneous nature of granular materials leads to complex mechanical behaviours, even in case of simple flow conditions. In particular, granular systems can behave like either fluids, meaning that they yield under shear stress, or like solids able to resist applied stresses without deforming. If grains are widely spaced and free to move in any direction, the medium behaves like a fluid and the stresses are proportional to the square of the strain rate under simple shearing. On the other hand, when particles are densely packed, a network of persistent contacts develops within the medium, and the granular material shows a solid-like, rate-independent behaviour. The mechanical response of the system during the solid-fluid transition, is still an open question.

Whereas several numerical results have been obtained in the literature concerning steady, shearing granular flows, unsteady conditions have been less investigated. In this work, we investigate the fluid-solid transition in unsteady, homogeneous, shear flows of a collection of identical, frictional spheres, by particle simulations.

2. Numerical simulations

The authors have performed DEM numerical simulations of unsteady simple shear flows of frictional spheres. The simulations have been carried out under constant volume in a cubic box of dimension L (figure 1a). 2000 particles of diameter d , density ρ_p , stiffness k_n and inter-particle friction coefficient $\mu = 0.3$ were used. The system of particles, initially at rest, is sheared by moving the boundaries in opposite directions at constant horizontal velocity V and setting the global shear rate $\dot{\gamma} = 2V/L$.

For steady, shearing flows, solid volume fraction ν larger (lower) than a critical, ν_c , indicates that a granular system is solid-like (fluid-like), i.e., rate-independent components of the stresses are present (absent). ν_c is the largest volume fraction at which a randomly collisional granular material can be sheared without force chains spanning the entire domain, and for the granular material here considered is 0.596 [1]. Simulations have been performed considering three volume fractions corresponding to fluid ($\nu = 0.59$), solid ($\nu = 0.62$) and near-to-critical ($\nu = 0.60$) conditions at steady state. At the steady state, there is a one-to-one relation between the critical volume fraction and the critical coordination number Z_c , independent of the shear rate [2, 3]. The coordination number Z , defined as the average number of contacts per particle, represents an important parameter to describe the granular interaction at large volume fractions, when force chains develop. In this work, we assume the system to experience a transition from fluid to solid states, under unsteady conditions, independently of the volume fraction, when the coordination number reaches its critical value Z_c . For the material here considered, $Z_c \approx 4$ [2, 4].

3. Results

The evolution of the dimensionless pressure pd/k_n and coordination number Z with the accumulated shear strain $\gamma = \dot{\gamma}t$ are illustrated in figure 1(b) and (c), respectively. Starting from fluid conditions, that is in absence of force chains, systems at less than critical volume fraction ($\nu = 0.59$) do not require a long transient regime to reach the steady state, since no persistent chains of contacts among particles form during shear. The continuous destruction and re-building of clusters, together

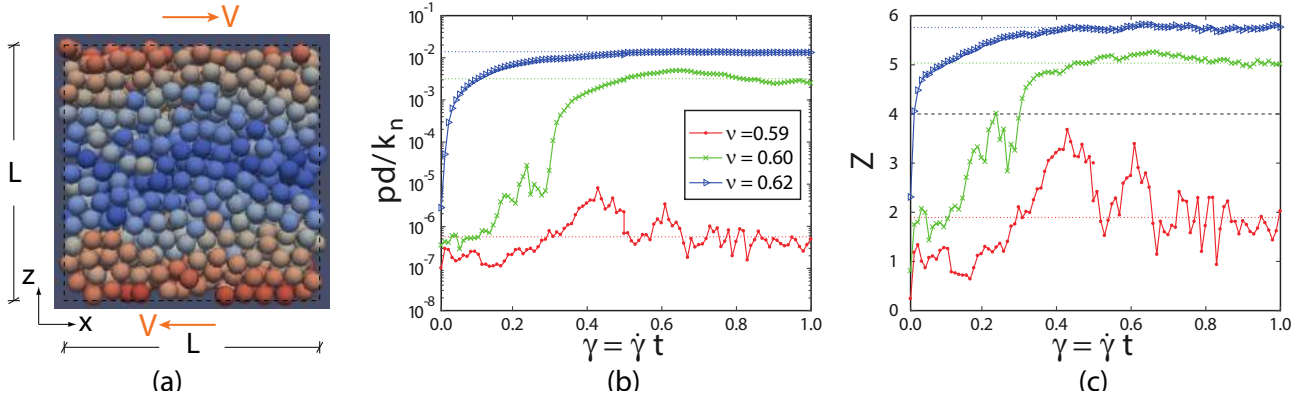


Figure 1. (a) Sketch of the flow configuration. Colours indicate speed, from blue (zero velocity of the particles in the core of the domain) to red (maximum velocity of the particles at the boundaries). Evolution of (b) scaled pressure and (c) coordination number for different values of the volume fraction. Steady state values are denoted with dotted lines; the dashed line represents the critical coordination number

with the free motion of single particles, gives rise to large fluctuations in both coordination number and pressure. At volume fraction much larger than the critical ($\nu = 0.62$), the system quickly solidifies during shear. The chains of contacts that span the entire domain require time to develop within the sample and, as a consequence, a clear transient regime is shown in terms of both p and Z . Once a contact network has been developed, the very small fluctuations of p and Z are due to micro-structural rearrangements during shear. Finally, in the case $\nu = 0.60$ the behaviour of p and Z is initially very similar to the fluid case with large oscillations and significant increase in the coordination number. Then, the granular material experiences a fluid-solid transition, and the fluctuations dramatically decrease. In this second stage, the pressure increases of almost 4 orders of magnitude. The critical value $Z = 4$ distinguishes the fluid-like (large fluctuations) from the solid-like (small fluctuations) behaviour (figure 1c).

4. Conclusions

The fluid-like behaviour is characterized by large fluctuations in pressure and coordination number, due to the continuous destruction/re-building of multi-particles aggregations, which, even if not spanning the entire domain, contribute to the structure of the system. Conversely, the fluctuations are much smaller when a contact network spanning the entire domain develops in the granular material (solid-like behaviour). The fluid-solid transition is characterized by a critical value of the coordination number, independent of the volume fraction.

Acknowledgments This work is funded by Fondazione Cariplo 2016-0769.

References

- [1] Chialvo, S., Sun, J., and Sundaresan, S. (2012). Bridging the rheology of granular flows in three regimes. *Phys. Rev. E*, **85**, 021305.
- [2] Sun, J. and Sundaresan, S. (2011). A constitutive model with microstructure evolution for flow of rate-independent granular materials. *J. Fluid Mech.*, **682**, 590–616.
- [3] Vescovi, D. and Luding, S. (2016). Merging fluid and solid granular behavior. *Soft Matter*, **12**, 8616–8628.
- [4] Vescovi, D., Berzi, D., and di Prisco, C. (2017). Fluid-solid transition in unsteady shearing flows. *EPJ Web of Conferences*, **140**, 03058.

COMPARISON OF LIMIT STATE STABILITY EVALUATION METHODS FOR GEOTECHNICAL ENGINEERING

H. Hernvall¹, J. Dijkstra¹ and M. Karstunen¹

¹ *Chalmers University of Technology, Gothenburg, Sweden*

1. Introduction

The limit equilibrium method (LEM) has for a long time been the industry's choice for the evaluation of slope stability, despite of the inherent limitations of LEM [1] and the development of more accurate methods based on finite element or finite difference discretisation. Reliable and fast methods to assess Ultimate Limit State (ULS) in a wide range of problems, with no need for advanced numerical analyses, remains attractive for industry. Two methods that have recently been developed to assess, among other things, slope stability are the Discontinuity Layout Optimisation (DLO) method [2] and the Finite Element Limit Analysis (FELA) method [3]. DLO gives an upper bound solution, whilst FELA has the capability to approximate both an upper and lower bound solution. In this work these two contemporary methods will be compared against a standard LEM considering both force and moment equilibrium. The software used for the analyses are Slope/W for LEM, Limistate:GEO for DLO and OptumG2 for the FELA.

2. Methodology

Two problems with closed-form solutions, a Prandtl footing [4, e.g.] and a Tresca vertical cut [5], were initially used to evaluate which method (LEM, DLO or FELA) yields the most accurate results. After the initial evaluation, the method with results closest to the closed-form solutions, i.e. in this case FELA, was chosen to be used as a reference for further evaluation. Subsequently, a ten meter high slope was analysed, considering four cases with an increasing number of variables, and three different slope inclinations, namely 1:1, 1:2 and 1:3, respectively. The different cases and the model parameters used are summarised in Table 1, and the cross-section of the slope in Case 4 is shown in Figure 1. The analyses were conducted for the short term (undrained) conditions.

Table 1. Overview of the different variables in the four cases and the soil parameters used in the models.

Case	Inclination	Two layers	Water table	Dry crust
1	Yes	-	-	-
2	Yes	Yes	-	-
3	Yes	Yes	Yes	-
4	Yes	Yes	Yes	Yes
Soil	γ_{dry} (kN/m^3)	γ_{sat} (kN/m^3)	s_u (kPa)	ϕ ($^\circ$)
Soil A	16	17	16.8 +1.3/m	-
Soil B	16	17	10	-
Dry Crust	19	19	50	30 $^\circ$

3. Results & Discussion

As the initial comparisons with the closed-form solutions showed that the average of the FELA upper and lower bounds were most accurate, FELA was used as the reference. The results of the

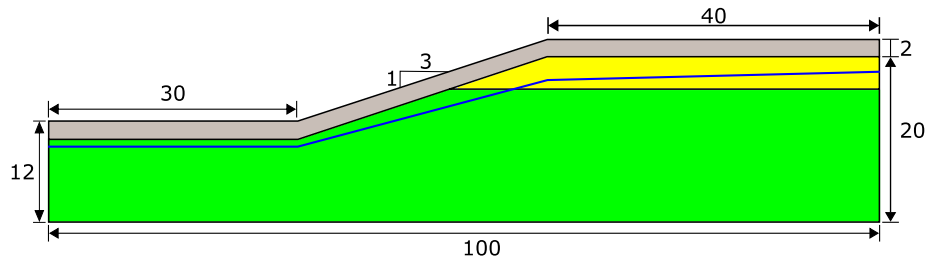


Figure 1. Side view of the slope in Case 4 with inclination 1:3. Green part is Soil A, Yellow part is Soil B and Grey part is dry crust. Thickness of the layer with soil B is 4 meters.

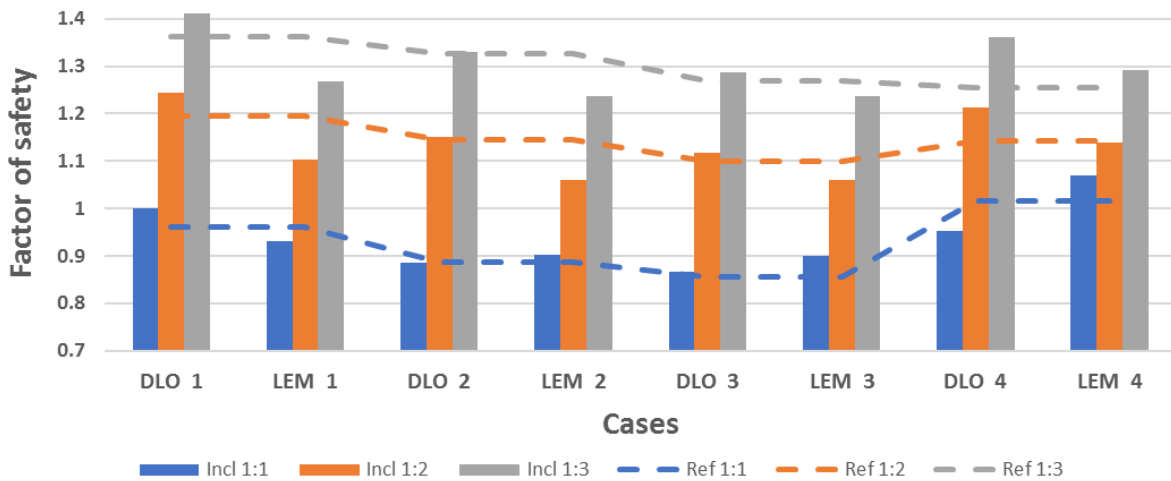


Figure 2. Results for all four cases for DLO and LEM, the dashed Ref lines are the average of the upper and lower bound from the FELA analyses.

simulations of the various cases are plotted in Figure 2. LEM had a disparity between -7.8 to 5.0% for cases 1, 2 & 3 compared to the reference FOS predicted by FELA. The disparity for DLO was somewhat smaller, between -0.3 and 4.1% for the same cases. In case 4, FELA had some problems, as the FOS did not increase with the addition of a dry crust, for slopes with inclination 1:2 and 1:3. FELA was also unable to form a stable lower bound mesh for the slope with 1:1 inclination (which is also theoretically unstable) in undrained conditions. As expected, however, these problems disappeared in drained analysis of case 4 for all three inclinations.

In conclusion the DLO and FELA methods are capable of matching the performance of LEM when it comes to slope stability problems. Since FELA has additional options to include more realism, such as strength anisotropy and seepage, it promises more realistic geotechnical stability analyses than LEM.

References

- [1] Krahn, J. (2003). The 2001 R.M. Hardy Lecture: The limits of limit equilibrium analyses. *Can. Geotech. J.*, **40**, 643–660.
- [2] Smith, C. and Gilbert, M. (2007). Application of discontinuity layout optimization to plane plasticity problems. *Proc. R. Soc. A*, **463**, 2461–2484.
- [3] Sloan, S. (2013). Geotechnical stability analysis. *Géotechnique*, **63**, 531–571.
- [4] Verruijt, A. (2001). *Soil Mechanics*.
- [5] Pastor, J., Thai, T. H., and Francescato, P. (2003). Interior point optimization and limit analysis: an application. *Communications In Numerical Methods In Engineering*, **19**, 779–785.

COMPARISON OF DIFFERENT STRENGTH REDUCTION TECHNIQUES ON SLOPE STABILITY CALCULATIONS

B. Schneider-Muntau¹, F. Tschuchnigg², G. Medicus¹ and W.Fellin¹

¹ *University of Innsbruck, Innsbruck, Austria*

² *Graz University of Technology, Graz, Austria*

1. Introduction

Limit equilibrium methods are commonly used in practical geotechnical engineering to determine the factor of safety. Powerful numerical techniques like the finite element limit analyses (FELA) and displacement based finite element method are utilized with increased regularity, where for the latter method a strength reduction analysis (SRFEA) is commonly used to compute the factor of safety. For strength reduction methods, usually, the Mohr-Coulomb strength parameters friction angle ϕ' and cohesion c' are reduced until limit equilibrium is reached. However, this method is only applicable to material models which utilize a Mohr-Coulomb or similar (e.g. Drucker-Prager) failure criterion. A new strength reduction method for models considering the critical state soil parameters N (ordinate intercept of the normal compression line (NCL)) and the critical friction angle ϕ'_c is presented and applied on the material model barodesy. Finally a slope stability problem is considered, where the results of SRFEA with different material models (Mohr-Coulomb and barodesy) are compared with factors of safety obtained with FELA.

2. Methods used for comparison of factors of safety

When performing a standard strength reduction finite element analysis (using Mohr-Coulomb strength parameters) the safety factor resulting from such an analysis can be obtained by reducing the strength parameters incrementally, starting from unfactored values ϕ'_{avail} and c'_{avail} , until no equilibrium can be found in the calculations. The corresponding strength parameters can be denoted as $\phi'_{failure}$ and $c'_{failure}$ and the safety factor FoS_{fe} is defined as:

$$FoS_{fe} = \frac{\tan \phi'_{avail}}{\tan \phi'_{failure}} = \frac{c'_{avail}}{c'_{failure}} \quad (1)$$

When performing a strength reduction finite element analysis in barodesy, the reduction procedure is comparable, but instead of reducing friction angle ϕ' and cohesion c' , the overconsolidation ratio (reduction of the ordinate intercept of the NCL N) and friction angle ϕ'_c are reduced. This concept is based on the fact, that peak strength envelopes are dependent on density (i.e. the initial void ratios), the lower the initial void ratio, the higher the peak strength. As long as the soil is highly overconsolidated, peak strength is higher than critical strength. In Mohr-Coulomb models high overconsolidation ratios are considered with the soil parameter c' , in barodesy the void ratio is directly included as state variable to consider density. The reduction of N corresponds to a shift of the normal compression line and with this to a reduction of the overconsolidation ratio. This can be seen as a reduction of the cohesion c' . As second parameter also the critical friction angle ϕ'_c is reduced. This reduction procedure is applicable for all models using parameters of critical soil theory like N and ϕ'_c and has been implemented for barodesy for clay [1] in the finite element software Abaqus as user subroutine [2]. Like in all strength reduction techniques, the strength parameters are dependent on a field variable, i.e. the reduction factor, and reduced incrementally until failure.

The concept of limit analysis is based on the theorems of plasticity developed by Drucker et al. [3, 4], namely the lower and upper bound theorem. Both limit theorems assume a perfectly

plastic material with an associated flow rule, and ignore the effect of geometry changes. The approach considers the stress equilibrium equations, the stress-strain relationship and the kinematical compatibility throughout the whole soil body. Hence, limit analysis calculates true collapse loads. The lower bound analysis uses equilibrium and the yield criterion and the upper bound analysis on the other hand, uses velocities and energy dissipation. By maximizing the lower bound and minimizing the upper bound the collapse load can be bracketed in between the lower and upper bound [5]. A detailed description of the formulation of the finite element limit analysis methods (FELA) as used in this paper is given in Sloan [6]. The displacement based finite element analyses were performed using associated and non-associated flow-rules and two different material models (Mohr-Coulomb and barodesy) and according strength reduction techniques. The factors of safety obtained with SRFEA are compared with results from FELA employing different approaches to consider non-associated plasticity [7]. The different approaches for slope stability analyses mentioned above lead to similar results in FoS, cf. Table 1.

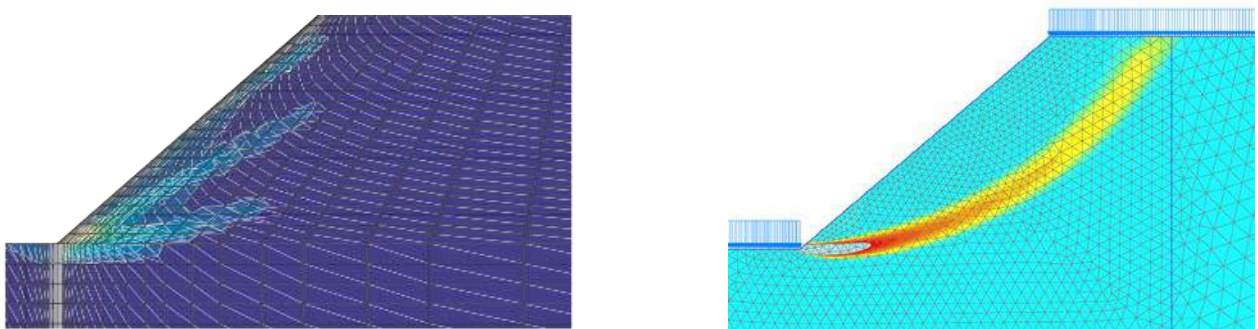


Figure 1: Shear band development in FE calculations with barodesy (left) and SRFEA (right)

	SRFEA _{Barodesy}	SRFEA _{MC}	FELA
FoS	1.49	1.45	1.45

Table 1: Results of slope stability analyses performed with different material models applying the different strength reduction techniques

5. References

- [1] Medicus, G. & Fellin, W. (2017). An improved version of barodesy for clay. 12:365, 365–376, *Acta Geotechnica* **2**:173–180.
- [2] Schneider-Muntau, B., Medicus, G. & Fellin, W. (2017). Strength reduction method in Barodesy. *Computers and Geotechnics*, online first.
- [3] Drucker, D.C., Greenberg, W. & Prager, W. (1951). The safety factor of an elastic plastic body in plane strain. *Trans. ASME J. Appl. Mech.* **73**, 371–378.
- [4] Drucker, D.C., Prager, W. & Greenberg, H. J. (1952). Extended limit design theorems for continuous media. *Q. J. Appl. Math.* **9** (4) 381–389.
- [5] Chen W.F. (2008). *Limit Analysis and Soil Plasticity*. Fort Lauderdale: J.Ross Publishing.
- [6] Sloan S.W. (2013). Geotechnical stability analysis. *Geotechnique* **63** (7), 531–572. 51st Rankine Lecture.
- [7] Tschuchnigg, F., Schweiger, H.F. and Sloan, S.W. (2015). Slope stability analysis by means of finite element limit analysis and finite element strength reduction techniques. Part I: Numerical studies considering non-associated plasticity. *Computers and Geotechnics* **70**: 169-177

SUCTION CAISSON INSTALLATION DESIGN FROM CPT, UTILIZING MACHINE-LEARNING

R. T. Klinkvort¹, G. Sauvin¹ and L. Andresen¹

¹ *NGI (Norwegian Geotechnical Institute), Oslo, Norway*

1. Introduction

The installation of suction caissons consists of lowering a cylindrical steel caisson to seabed; first, it will penetrate into the soil by self-weight and secondly it will penetrate further, to the installation depth, by applying suction within the caisson. The suction (pressure difference) is applied by pumping water out from the inside of the caisson through the top lid. The key design aspect during installation is the assessment of the penetration resistance and hence the necessary differential pressure. The total penetration resistance (Q_{tot}) of a suction caisson consist of both resistance along the skirt wall (F_{side}) and resistance at skirt tip (F_{tip}), this can be written as:

$$Q_{tot} = \Delta u \cdot A_{in} + W' = F_{side} + F_{tip} = \sum A_{side} \cdot \tau_{side} + A_{tip} \cdot q_{tip} \quad (1)$$

where, Δu is the differential pressure, A_{in} the inside caisson lid area, W' the submerge caisson weight, A_{side} the inside and outside skirt area, τ_{side} the soil skin resistance, A_{tip} the area of skirt tip, and q_{tip} the soil resistance at skirt tip.

Even though suction caissons have been used in many different soil conditions, there still exists today uncertainties related to the penetration resistance predictions. This paper presents an attempt to use a database of installation records to optimize a Cone Penetration Testing (CPT) based installation model. We establish a database, consisting of both measured installation data, caisson geometries and corresponding CPT data, from real field installations. We then calibrate a Deep Neural Network using this database.

2. The database

The database consists of data from 97 different field installations from 9 different locations. A total of 953m of penetration data are currently stored in the database. The database mainly consist of installation in clay but also have some layered and pure sand sites (~15% of the dataset). The database consist of the following; Caisson diameter (D), skirt thickness (t), Skirt length (L) and submerge weight of caisson corrected for any crane load (W') together with installation depth (z) versus differential pressure profiles (Δu). For each installation, data from one CPT located in the proximity of the installation is also stored. From the CPT tests, the following data were collected; Tip resistance (q_c), sleeve resistance (f_s) and pore pressure at tip (u).

	D [m]	t [m]	L [m]	z [m]	W' [kN]	Δu [kPa]	q_c [MPa]	f_s [MPa]	u [MPa]
Minimum	3	0.03	5	0	119	0	0	-0.3	-3.1
Maximum	9	0.08	15	15	1518	1023	42	0.7	0.8

Table 1. Range of collected data.

Table 1 gives an illustration of the diversity of the database. We divide the database into two datasets; and use approximately 90% of the data set to calibrate our model (train set) and the remaining set to test our model against (test set). The test set corresponds to one caisson installation from each site. The train set is further split into two parts; a part for training and a part for validation (20% of train set). The validation set is used to validate the model when the neural network is trained.

2. Artificial Neural Network

We use KERAS [1] running on top of TensorFlow in Python to perform a supervised regression analysis. The Artificial Neural Network (ANN) is a Multilayer Perceptron (MLP) model and consists of three layers with a width of 100 neurons each. We use the rectifier ('relu') activation function on all the layers and a least square loss function together with the Adam first-order gradient-based optimization. We calibrate the model with a batch size equal to the full size of the training part of the train set. To avoid over-fitting, we use an early stopping criterion so training of the network stops when no further improvements is seen on the validation set.

The input parameters to this model are the following: $z, q_c, f_s, u, \sum (f_s A_{side}), \sum (q_c A_{tip}), \sum (q_c A_{side})$. Because this ANN model does not include the "memory" of previous layers, we use the summation of the side and tip area multiplied with q_c , and f_s , respectively.

Following training, the accuracy of the ANN is evaluated as the difference between the predicted value and measured value divide by the measured value. This can be written as:

$$accuracy = \frac{X_{test} - Y_{test}}{Y_{test}} \quad (2)$$

where: X_{test} is the predicted total resistance (Q_{tot}), with the test data input. Y_{test} is the measured total resistance (Q_{tot}) for the test data. Figure 1 shows the accuracy of the model when compared with the never seen measured data in the test set.

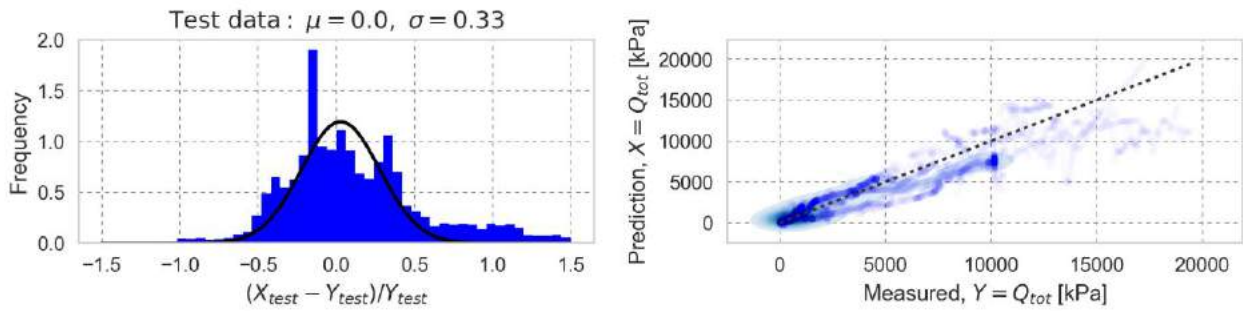


Figure 1. Evaluation of model accuracy on the never seen test set

The accuracy of the model shows a standard deviations of $\sigma= 0.33$ and a mean value of $\mu=0.0$. As a comparison the standard deviation of the train set data is slightly smaller, $\sigma= 0.27$, as expected.

4. Discussion and conclusion

We have established a database with suction caisson installation data and corresponding CPT data. The database will be updated when new data becomes available. The current database is used to calibrate an ANN suction caisson penetration model and to evaluate the accuracy of the model. We can see that the accuracy of the ANN model shows a standard deviation of 33%, which we regards as satisfactory for a model that only takes CPT and caisson geometry as input parameters. The disadvantages of the ANN model is that we do not know how the model is working and the ANN model should therefore only be used within its calibration range, for both caisson geometries and soil conditions. The current ANN does not include memory of any previous soil layers and an update of the model is currently ongoing. As all artificial neural networks, the model will only improve when the data set increases.

5. References

[1] Chollet, F et al. (2015). Keras. <https://github.com/fchollet/keras>.

MACRO-ELEMENT MODELLING OF SUCTION BUCKETS FOR THE INTEGRATED ANALYSIS OF JACKET-SUPPORTED OFFSHORE WIND TURBINES

B. Bienen¹, F. Pisanò², D. Moretti², D. Salciarini³ and C. Tamagnini³

¹ *The University of Western Australia, Perth, Australia*

² *Delft University of Technology, Delft, The Netherlands*

³ *University of Perugia, Perugia, Italy*

1. Introduction

As the water depth for offshore wind farms increases, jacket substructures represent an effective solution as they offer appropriate structural stiffness combined with reduced wave-induced loading. Jacket substructures can be supported by suction buckets, a foundation concept that offers silent installation and that is faster compared to standard piles. The influence of the foundation on the overall performance of the system (with respect to ultimate capacity, but also in terms of the natural frequency and accumulation of displacements under environmental cyclic loading) is well recognised, yet foundation performance is typically either evaluated separate to the structural response or the geotechnical behaviour is simplified considerably. This contribution explores an integrated approach to modelling the response of offshore wind turbines, using a hypoplastic macro-element model for each of the suction buckets supporting the jacket and assuming these are sufficiently spaced to neglect direct foundation interaction.

2. Macro-element model

The hypoplastic macro-element model adopted for this purpose builds upon an existing formulation [1], originally developed for flat circular foundations, but has been modified to allow for compressive (V_{0c}) as well as tensile (V_{0t}) bearing capacities, and calibrated to capture the behaviour of suction buckets in sand on the basis of centrifuge model tests.

The constitutive equation of the macro-element, incorporating the concept of *internal displacement* [2] reads:

$$\dot{\mathbf{t}}^* = \mathcal{K}_t(\mathbf{t}, \boldsymbol{\delta}, \boldsymbol{\eta}) \dot{\mathbf{u}} \quad (1)$$

in which:

$$\mathbf{t}^* := \frac{1}{V_0^*} \{V^*, H_x, M_y/\ell, H_y, M_x/\ell, Q/\ell\}^T \quad \mathbf{u} := \frac{1}{\ell} \{U_z, U_x, \Theta_y \ell, U_y, \Theta_x \ell, \Omega \ell\}^T \quad (2)$$

are the normalized force and displacement vectors; $\boldsymbol{\eta} = \text{dir}(\dot{\mathbf{u}})$; ℓ is a characteristic length of the footing and \mathcal{K}_t the macro-element tangent stiffness matrix, given by:

$$\mathcal{K}_t(\mathbf{t}^*, \boldsymbol{\delta}) := A_1(\rho) \mathcal{L}(\mathbf{t}^*) + \mathcal{N}(\mathbf{t}^*, \boldsymbol{\delta}) \quad (3)$$

$$\mathcal{N}(\mathbf{t}^*, \boldsymbol{\delta}) := \begin{cases} A_2(\rho) \mathcal{L}(\mathbf{t}^*) \boldsymbol{\eta}_\delta \boldsymbol{\eta}_\delta^T + A_3(\rho) Y(\mathbf{t}^*) \mathbf{m}(\mathbf{t}^*) \boldsymbol{\eta}_\delta^T & (\boldsymbol{\eta}_\delta \cdot \boldsymbol{\eta} > 0) \\ A_4(\rho) \mathcal{L}(\mathbf{t}^*) \boldsymbol{\eta}_\delta \boldsymbol{\eta}_\delta^T & (\boldsymbol{\eta}_\delta \cdot \boldsymbol{\eta} \leq 0) \end{cases} \quad (4)$$

In eqs. (3) and (4), ρ denotes a scaled norm of the internal displacement vector $\boldsymbol{\delta}$ and $\boldsymbol{\eta}_\delta = \text{dir}(\boldsymbol{\delta})$.

The key modification introduced in the model is the definition of the constitutive functions in terms of the modified vertical load and bearing capacity:

$$V^* := V + V_{0t} \quad V_0^* := V_{0c} + V_{0t}$$

This amounts to a translation of the origin of the loading space in the V direction of an amount equal to the tensile bearing capacity V_{0t} , as shown in Fig. 1. This technique can be applied to any failure locus developed for footings in unilateral contact with the soil, to incorporate uplift strength.

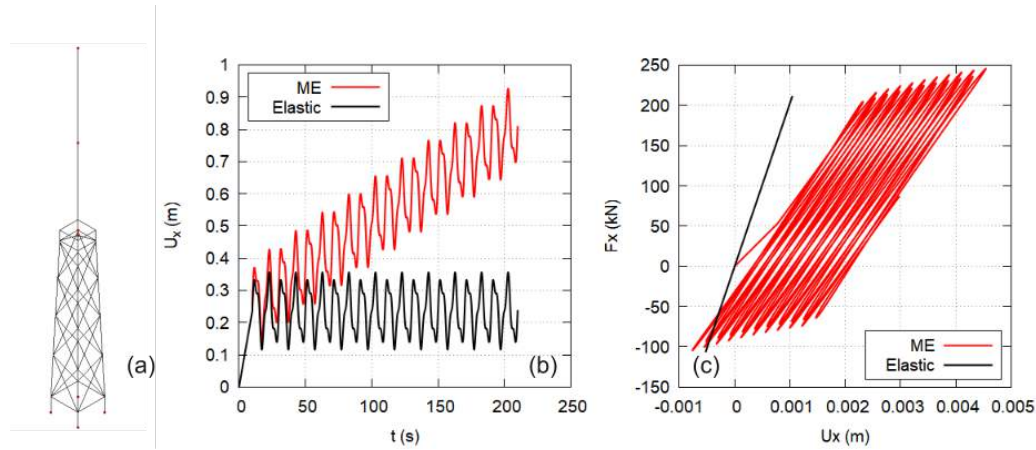


Figure 1. a) Integrated FE model; b) nacelle displacement u_x vs. time; c) upwind bucket: F_x vs. u_x .

3. Integrated approach: results of numerical simulations

The performance of a jacket-supported offshore wind turbines under cyclic loading has been assessed by means of the FE model shown in Fig. 1. To this end, the macro-element model has been incorporated in two different commercial FE codes (DIANA FEA and ABAQUS) via suitable user element routines, which integrate the constitutive equation (1) by means of an adaptive explicit 3rd-order Runge–Kutta scheme with error control. For comparison, a second FE model has been constructed in which the soil–foundation response has been modeled with linear, uncoupled springs. The macro-element model has been calibrated and validated against physical evidence of foundation performance obtained under natural and artificial gravity. Evidence of the response of suction bucket foundations under vertical cyclic loading into tension can be found in [3]. However, in the simulation presented, the tensile capacity of the buckets has not been considered.

A simplified set of environment loading conditions, with wind and wave loading acting in the same direction, has been used for the simulation. The magnitudes of wind and wave loads have been determined with the commercial software BLADED. The wave load is modelled with a triangular distribution applied to each leg of the structure, with a harmonic variation in time, with period $T = 10$ s, similar to the peak wave period in the JONSWAP spectrum. Wind load has been modeled as a concentrated force at the hub, composed of two parts: a constant force and an harmonic variation in time, with period $T' = 4$ s and amplitude equal to twice the standard deviation of the thrust force distribution. Figs. 1b and 1c show the time history of the nacelle displacement u_x and the horizontal load–displacement curve for one of the upwind buckets, respectively. Both figures show that the ME model predicts a progressive accumulation of horizontal displacements both at the foundation and at the top of the tower. However, nacelle displacements are two order of magnitude larger. This is a consequence of the permanent differential settlements of the upwind and downwind buckets, which results from the coupling effects between horizontal and vertical degrees of freedom. This effect cannot be captured by uncoupled springs, even if non-linear and capable of hysteretic behavior.

References

- [1] Salciarini, D., Bienen, B., and Tamagnini, C. (2011). A hypoplastic macroelement for shallow foundations subject to six-dimensional loading paths. *Proc. International Symposium on Computational Geomechanics (ComGeo II), Cavtat-Dubrovnik, Croatia*.
- [2] Salciarini, D. and Tamagnini, C. (2009). A hypoplastic macroelement model for shallow foundations under monotonic and cyclic loads. *Acta Geotechnica*, **4**, 163–176.
- [3] Bienen, B., Klinkvort, R., O’Loughlin, C., Zhu, F., and Byrne, B. (2018). Suction caissons in dense sand, part ii: vertical cyclic loading into tension. *Géotechnique*, pp. 1–15.

EFFECT OF INSTALLATION HISTORY ON THE LATERAL RESPONSE OF MONOPILES IN DRY SAND

Shengsheng Fan, Britta Bienen and Mark F. Randolph
Centre for Offshore Foundation Systems
The University of Western Australia, Perth, Australia

1. Background

Piles are extensively used as offshore foundations. Large diameter monopiles remain the most prevalent foundation option for offshore wind turbines. Significant research effort has been dedicated to the characterisation of the pile/soil interaction under lateral loading in service, mainly using p-y curves. These were originally developed for small diameter piles undergoing a very limited number of load cycles. In contrast, monopiles for offshore wind turbines can be of the order of 8 m in diameter and be subjected to millions of load cycles over their design life (Byrne et al. 2015). Little attention, however, has been given to date to the effect of pile installation on the subsequent response of monopiles under lateral loading. This paper investigates the effect of different installation methods, including quasi-static jacking, vibratory pile driving and impact driving on the accumulated monopile head displacements under subsequent lateral loading.

2. Methodology and assumptions

The pile installation was modelled using the Coupled-Eulerian Lagrangian (CEL) technique available within Abaqus/Explicit to appropriately model this large deformation process. However, it was not feasible to simulate the whole penetration process considering the extremely high computation cost. Hence, the pile was modelled 24.7 m pre-embedded into the soil using the wished-in-place technique and only the last 0.3 m penetration was modelled.

The pile was modelled as a rigid Lagrangian part. The tubular pile has a diameter of 5 m and a wall thickness of 0.1 m. The target embedment length was 25 m (5D). Only a quarter of the actual geometry was simulated (Fig 1). The soil domain, modelled as a Eulerian part, has a radius of 30 m (6D) and a depth of 40 m (8D). A void region with a depth of 5 m was defined on top of the soil to capture any soil heave during pile driving.

General contact was used to model the pile-soil interface with a penalty algorithm. The pile tip and inner surface were modelled as frictionless, while a roughness of $\tan\delta/\tan\phi = 0.5$ (where δ is the interface friction angle) was assumed for the pile external surface. Hard contact was used to describe the normal behaviour.

The lateral loading phase was modelled with implicit method within Abaqus/Standard. Only half of the real geometry was modelled. The radius and depth of the soil domain are exactly the same as the CEL model. The mesh for the lateral loading stage was similar to the CEL model (without the void). The pile was modelled as a linear elastic material. In order to consider the effect of installation history on the subsequent response of pile subjected to lateral loading, the soil state following the installation phase need to be used as an initial state. Therefore, the stress components and state-dependent variables, such as the void ratio, were mapped from the CEL model to the lateral loading model. A surface-to-surface contact was used to model the interaction between the pile and soil with a kinematic algorithm in the model for lateral loading. The normal behaviour was described using hard contact. The interaction properties were the same as in the CEL model. Monotonic lateral

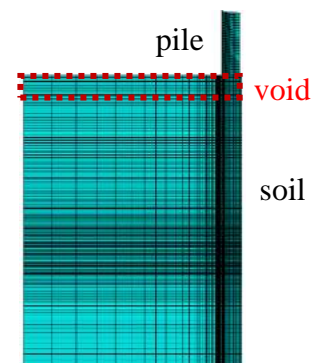


Figure 1. Installation model

loading was applied at an eccentricity of 3D until the lateral displacement of the pile at the mudline reached 10% of pile diameter.

The sand behaviour was modelled using a hypoplastic constitutive law by Kolymbas (1985, 1991) in the version of von Wolffersdorff (1996), with the enhancement of intergranular strains by Niemunis and Herle (1997), which is capable of capturing the stress- and state-dependent response of sand. The umat implementation of Gudehus et al. (2008) was used in the implicit analysis, while a vumat obtained using the umat and an interface code by Bienen et al. (2014) was used in the explicit analysis.

3. Preliminary results

The numerical analysis results show that the initial stiffness and ultimate capacity of the laterally loaded pile are significantly influenced by the installation method used. In particular, vibro driving causes a significant reduction of both initial stiffness and ultimate capacity (Fig 2). The soil surrounding the pile is significantly densified due to the continuous vibration. The horizontal stress is significantly reduced. In contrast, the degree of disturbance on the surrounding soil is relatively small for impact driving and jacking. The initial stiffness and ultimate capacity are slightly different compared with the wished-in-placed pile. The results reported are based on a soil sample with a relative density of 37% and a driving distance of 0.3 m, such that the effects of the large deformation process of installation may not be fully captured. Validation against centrifuge experimental data is underway. Further research is also required regarding the effects of driving distance, driving energy, driving frequency, pile/soil interaction properties and sand to enhance the understanding and quantification of the influence of installation history on the performance of monopiles under lateral loading from the ocean environment.

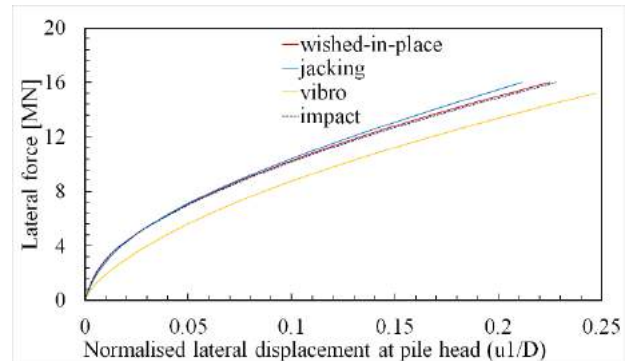


Figure 2. Load displacement curve

4. References

- [1] Bienen, B., Stanier, S., Vulpe, C. & Mašin, D. (2014). *Interface enabling constitutive models coded as user materials to be employed in explicit analysis*. The University of Western Australia, Centre for Offshore Foundation Systems, GEO: 14756, 20 p. Available, along with the interface code, for free download from www.soilmodels.info.
- [2] Byrne, B. W., R. McAdam, H. Burd, G. Houlsby, C. Martin, L. Zdravković, D. Taborda, D. Potts, R. Jardine, and M. Sideri. (2015). New design methods for large diameter piles under lateral loading for offshore wind applications. *3rd International Symposium on Frontiers in Offshore Geotechnics (ISFOG 2015), Oslo, Norway, June*, pp. 10-12.
- [3] Gudehus, G., Amorosi, A., Gens, A., Herle, I., Kolymbas, D., Mašin, D., Muir Wood, D., Niemunis, A., Nova, R. & Pastor, M. (2008). The soilmodels.info project. *International Journal for Numerical and Analytical Methods in Geomechanics*, Vol. 32, No. 12, pp. 1571-1572.
- [4] Kolymbas, D. (1985). A generalized hypoelastic constitutive law. *In: Proc. XI Int. Conf. Soil Mechanics and Foundation Engineering*, Vol. 5, pp. 2626.
- [5] Kolymbas, D. (1991). An outline of hypoplasticity. *Archive of Applied Mechanics*, Vol. 61, No. 3, pp. 143-151.
- [6] Niemunis, A. & Herle, I. (1997). Hypoplastic model for cohesionless soils with elastic strain range. *Mechanics of Cohesive - frictional Materials*, Vol. 2, No. 4, pp. 279-299.
- [7] Von Wolffersdorff, P. A. (1996). A hypoplastic relation for granular materials with a predefined limit state surface. *Mechanics of Cohesive - frictional Materials*, Vol. 1, No. 3, pp. 251-271.

LARGE DEFORMATION FINITE ELEMENT ANALYSIS OF SPUDCAN PENETRATION BEHAVIOUR ON UNEVEN SEABED CONDITION

H.D.V. Khoa¹, Y. Shin¹, H.J. Park², J.H. Kim², D.S. Kim², J. Han³ and S. Lee³

¹ Norwegian Geotechnical Institute, Oslo, Norway

² Korean Advanced Institute of Science and Technology, South Korea

³ Korean Institute of Civil Engineering and Building Technology, South Korea

1. Introduction and motivation

Jack-ups are self-elevating mobile units, which are extensively used in the offshore oil and gas industry. Each jack-up leg is generally supported by an individual spudcan foundation. The spudcan installation or reinstallation behaviour on a sloping surface is complex and strongly influenced by many parameters such as seabed geometry, soil heterogeneity and jack-up structural properties, etc. To support and facilitate the industrial design of spudcan foundation, a computer program named SPLAT (Spudcan Leg Analysis Tool) has been developed through a collaboration between the NGI (Norwegian Geotechnical Institute) and COFS (Centre for Offshore Foundation Systems). The SPLAT program covers the most relevant methods of spudcan penetration analysis recommended in industry guidelines (e.g. SNAME, ISO and INSAFE) and some newer and more advanced methods developed from recent research using both physical and numerical modelling.

The SPLAT program has been widely and successfully applied to calculate the spudcan penetration resistance (see [1]). However, the program may not be applicable for some following cases: complex spudcan geometry, complex interaction between different soil failure mechanisms (soil plugging, soil squeezing and soil back-flow) and uneven seabed condition. The last case, which could be either a sloping seabed or a footprint derived from previous jack-up installation, is the main focus of the study presented in this paper.

Finite element (FE) analysis using the Coupled Eulerian-Lagrangian (CEL) method has been widely used in solving offshore geotechnical problems involving large deformation. Many researchers have successfully applied the CEL FE-method to deep penetration analyses of the spudcan foundation and suction anchors [2]. This paper aims at applying the Abaqus CEL method to analyzing the spudcan penetration on uneven seabed condition. A series of centrifuge tests of spudcan penetrating next to an existing footprint conducted by Kong [3] as well as centrifuge tests of spudcan installation on different sloping seabed performed by KAIST [4] are back-analyzed. The calculated results provide insight into both the spudcan penetration resistance and the complex soil failure mechanism, which can help to further improve and develop the SPLAT program.

2. Discussion of calculated FE-results

In the Abaqus/Explicit CEL FE-model, the spudcan foundation is assumed to be rigid and discretized by using Lagrangian rigid elements whereas the soil is modelled with Eulerian elements. The spudcan-soil interaction is described by the general contact algorithm. During the deep penetration of the spudcan, the material points (soil) can freely deform through the fixed Eulerian mesh so that no numerical convergence problem caused by severely distorted elements occurs. The clay is modelled by the Tresca model while the Mohr-Coulomb model is considered for the sand.

Kong [3] conducted a comprehensive series of centrifuge tests of spudcan installation in clay next to both idealized and real footprints. Due to the high complexity of the spudcan-footprint interaction problem, effects of different parameters such as the offset distance between spudcan and footprint, the footprint geometry and the clay properties were experimentally investigated in isolation as well as in combination in order to better understand the testing results. These centrifuge

tests are back-analyzed. The calculated CEL FE-results of two typical cases: FS (flat surface, i.e. no footprint) and TB-2D-10D (with idealized footprint) are presented in Figure 1. It can be seen that the CEL FE-analyses can predict reasonably well the centrifuge testing measurements in terms of both the spudcan resistance and the complex failure mechanisms in the soil. The calculated results of the back-analyses of the centrifuge tests and a set of parametric studies using the CEL FE-model provide the good basis for developing a prediction method in the SPLAT program.

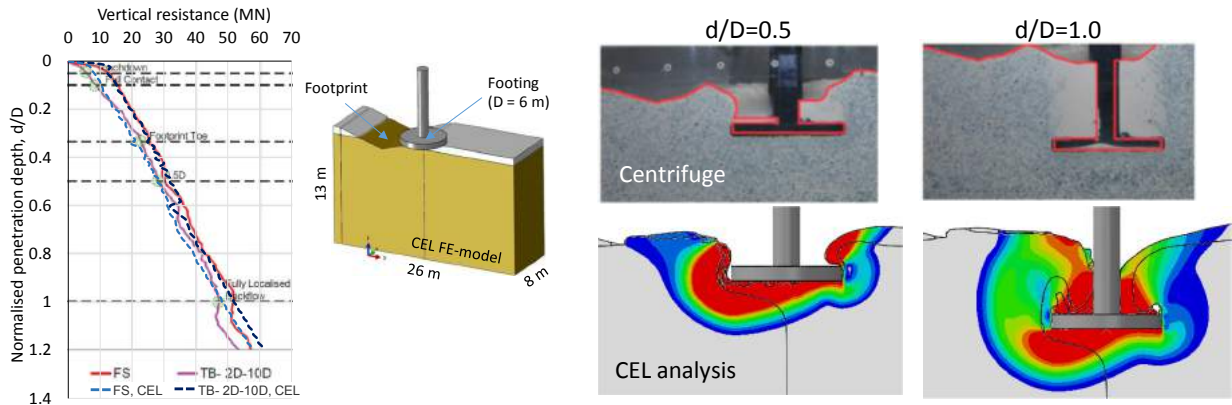


Figure 1. Spudcan resistances and CEL FE-model (left) and soil failure mechanisms (right).

The uneven seabed condition is related to not only existing footprints but also natural sloping seabed. A total of 3 centrifuge tests of spudcan penetrating through silty sand with 3 sloping surface angles of 0° , 5° and 10° were conducted by KAIST [4]. These centrifuge tests are also back-analyzed by using the CEL method. Figure 2 presents a front view of the physical modelling and comparison of the spudcan penetration resistances in the vertical and horizontal directions. It is observed that the FE-results match reasonably well the measurement data. Additional FE-analyses have been performed to support the development of a prediction method in the SPLAT program.

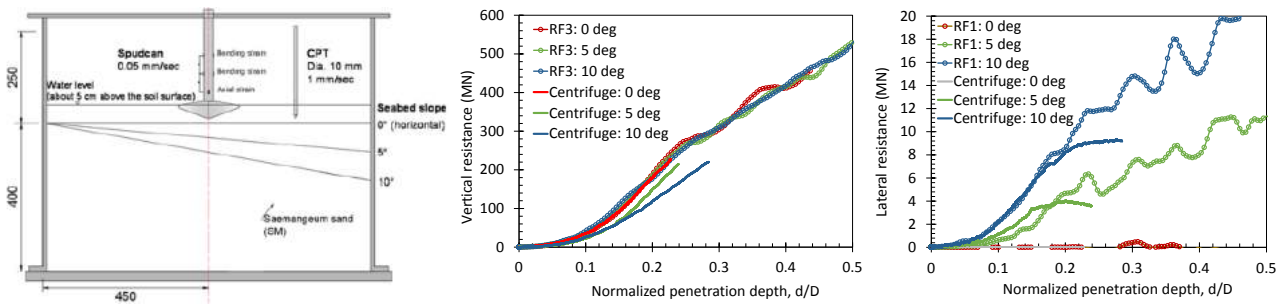


Figure 2. Physical modelling (left) and measured and calculated spudcan resistances (right).

3. References

- [1] Zhang, Y., Khoa, H.D.V., Meyer, V. & Cassidy, M.J. (2015). Jack-up spudcan penetration analysis: review of semi-analytical and numerical methods. *Proc. Int. Symp. Front. Offshore Geotech.*, Oslo, Norway, ISFOG, 1341–1346.
- [2] Khoa, H.D.V. & Jostad H.P. (2016). Application of Coupled Eulerian-Lagrangian Method to Large Deformation Analyses of Offshore Foundations and Suction Anchors. *International Journal of Offshore and Polar Engineering*, **26**(3), 304–314.
- [3] Kong, V.W. (2011). *Jack-up reinstallation near existing footprints*. Ph.D. thesis at University of Western Australia, Perth, Australia.
- [4] KAIST (2016). *Behavior of Spudcan-Soil Interaction in Sloped Seabed using Centrifuge Model Tests*. KOCED Geotechnical Centrifuge Testing Center at KAIST.

IMPLEMENTATION OF A HYPOPLASTIC MODEL WITH INTERGRANULAR STRAIN FOR THE MODELLING OF SPUDCAN CYCLIC RESPONSE IN SILTY CLAY

Ragni R.^{1*}, Bienen B.¹, Mašín D.², Jerman J.², Wang D.³, Cassidy M.J.¹

¹The University of Western Australia, Perth, Australia

² Charles University, Prague, Czech Republic

³ Ocean University of China, Qingdao, China

1. Introduction

Jack-up units are mobile self-elevating platforms extensively used in oil & gas and offshore wind energy sectors (LHS Figure 1). The super-structure relies on the bearing capacity offered by the circular foundations – known as spudcans – located at the end of each leg.

[1][2] demonstrated that when spudcans are installed in fine grained material, consolidation can play an important part in shaping the response of the foundation. In particular, the progressive dissipation of excess pore pressures was demonstrated to increase both vertical and combined multi-directional undrained bearing capacity.

However, jack-ups are constantly subjected to metocean actions, e.g. wind, waves and currents, so that an assessment of the spudcan response to such loading of cyclic nature is required.

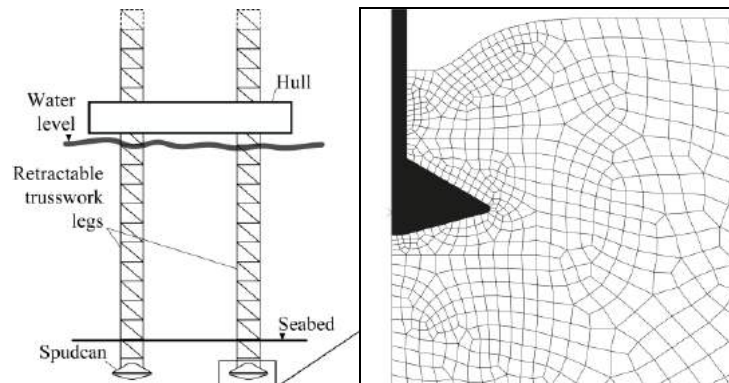


Figure 1. Schematic of jack-up (LHS) and numerical modelling of spudcan foundation (RHS) in finite element code Abaqus/Standard.

2. Methodology

A hypoplastic model for structured clays was adopted to accurately reproduce the behavior of a carbonate silty clay found in the north-west shelf of Australia. The model is a combination of [3] hypoplastic clay model with structured clay extension defined by [4]. The constitutive model is further enhanced with the intergranular strain concept [5], which allows the small strain stiffness to be modelled and the cyclic response to be correctly reproduced.

The Remeshing and Interpolation Technique with Small Strain [6] was used in the finite element code Abaqus/Standard to achieve the desired installation depth $w/D = 1$ ($D =$ spudcan diameter) and analyse further penetration following consolidation. A link between length of consolidation (achieved by holding the vertical load) and increase in undrained bearing capacity V_0^* was defined.

A case involving no consolidation and two other cases with a non-dimensional period of consolidation $T = c_v t / D^2 = 0.01; 0.05$ ($c_v =$ coefficient of vertical consolidation; $t =$ dimensional

time) following penetration to $w/D = 1$ were studied. For each T a parametric study analysed the effects of both mean (V_m) and cyclic (ΔV) component of the cyclic loading. The results obtained from the application of 100 cycles with $V_m = 0.75V_0^*$ and $\Delta V = 0.1V_0^*$ are presented here, being $V_0^* = f(T)$. A loading frequency of 0.1 Hz guaranteed undrained response within the single cycle.

3. Results

Figure 2 shows that a period of consolidation leads to a significantly smaller accumulation of normalised settlement $\Delta w/D$. The evolution of the normalised excess pore pressures $\Delta u/q$ (q = bearing pressure held in consolidation, Figure 2b) appears to play a decisive role, for the delay in dissipation for $T = 0$ leads to a settlement rate ~ 17 times higher than the value measured when $\Delta u/q < 0.1$.

A broader analysis of the parametric study revealed the importance of the small strain stiffness once most of the excess pore pressures have been dissipated. Lower ΔV values consistently led to smaller settlements, due to the intergranular strain direction more frequently aligning with the straining direction, which causes the model to offer a stiffer response.

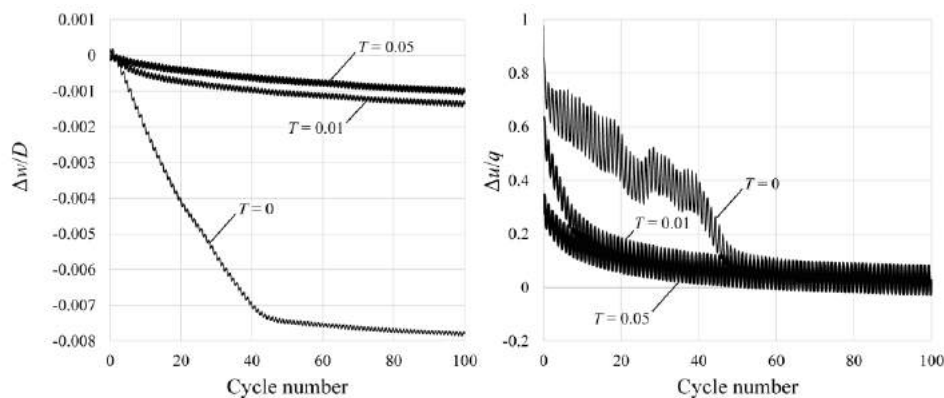


Figure 2. Normalised settlement $\Delta w/D$ (LHS) and excess pore pressure $\Delta u/q$ (RHS) evolution with number of cycles.

5. References

- [1] Ragni, R., Wang, D., Mašin, D., Bienen, B., Cassidy, M.J. & Stanier, S.A. (2016). Numerical modelling of the effects of consolidation on jack-up spudcan penetration. *Computers and Geotechnics*, **78**, 25-37.
- [2] Ragni, R., Bienen, B., Wang, D., Mašin, D. & Cassidy, M.J. (2017). Numerical modelling of the effects of consolidation on the undrained spudcan capacity under combined loading in silty clay. *Computers and Geotechnics*, **86**, 33-51.
- [3] Mašin, D. (2014). Clay hypoplasticity model including stiffness anisotropy. *Géotechnique* **64**, No. 3, 232-238.
- [4] Mašin, D. (2007). A hypoplastic constitutive model for clays with meta-stable structure. *Canadian Geotechnical Journal*, **44**, 3, 363-375.
- [5] Niemunis, A. and I. Herle (1997). Hypoplastic model for cohesionless soils with elastic strain range. *Mechanics of Cohesive-Frictional Materials* **2**, 279-299.
- [6] Hu, Y. & Randolph, M.F. (1998). A practical numerical approach for large deformation problems in soil. *International Journal of Numerical and Analytical Methods in Geomechanics*, **22**, 5, 327-350.

3D FEA OF ULTIMATE LIMIT STATES: FINITE ELEMENT LIMIT ANALYSES VS DISPLACEMENT BASED FINITE ELEMENT ANALYSES

F. Tschuchnigg, H.F. Schweiger

*Institute of Soil Mechanics, Foundation Engineering and Computational Geotechnics,
Graz University of Technology, Graz, Austria*

1. Introduction

Numerical techniques like the displacement based finite element method (FEA) and finite element limit analyses (FELA) are utilized with increased regularity to compute ultimate limit states and consequently factors of safety. Since FELA is limited to associated plasticity Davis [1] suggested to use reduced strength parameters in combination with an associated flow rule in order to model non-associated plasticity. When using strength reduction techniques this approach could lead to very conservative results compared to FEA with non-associated plasticity [2]. This issue may be overcome by modifications of the original Davis approach, where the reduced strength parameters are related to the actual degree of non-associativity. Previous studies of slope stability problems showed, that the modified Davis procedure seems to compute more realistic factors of safety [3]. However, the topics addressed in this paper are related to 3D analysis of ultimate limit states. Therefore the paper compares results of 2D and 3D FEA with 2D and full 3D finite element limit analysis, using a recently released Version of the software OptumG3 [4]. The boundary value problem considered for the numerical studies is the bearing capacity of shallow foundations. Additionally a real load test on a shallow foundation is back analyzed by means of FEA and FELA. This load test was conducted as part of the Ballina test field project in Ballina (New South Wales) [5], thus the calculated results are compared with measurements [6].

2. Numerical methods used for comparison

The finite-element code Plaxis [7] is used for all displacement finite-element analyses discussed in this paper. Ultimate limit state considerations employing FEA with non-associated plasticity may lead to numerical instabilities without any clear defined failure mechanism. This is particularly the case for purely frictional materials with high friction angles ϕ' . Finite element limit analyses were used on the other hand, where FELA provide rigorous upper and lower bounds on the failure load. Therefore, these results are used in the studies as reference solutions for comparison with those obtained from the displacement based finite element analyses.

3. Finite element limit analyses (FELA) vs Displacement based finite element analyses (FEA)

Preliminary studies on the bearing capacity of shallow foundations are based on 2D plane strain and 2D axisymmetric models. Both displacement based FE and FELA have been performed. The soil materials investigated include purely frictional materials (no cohesion), cohesive frictional materials and Tresca type materials. Thus, both drained and undrained conditions are considered. The results obtained with the 2D calculations are compared with full 3D analyses. Based on these studies the influence of the element type, the mesh discretization and the flow rule is discussed.

The paper presents also 3D FEA and 3D FELA of a large-scale shallow foundation load test on soft clay [6]. For FEA different constitutive models have been employed and both strength and stiffness properties used have been validated with in-situ tests and laboratory tests. The class A predictions obtained by means of 2D and 3D FEA are compared with the measurements presented in [6]. Figure 1 shows the 3D finite element model used for the class A predictions and the obtained

failure mechanism. Based on the published test data [6] and [8] the FE model was slightly adjusted and further numerical studies using FEA and FELA have been conducted.

The comparisons show that displacement based finite element analysis yield similar results as FELA as long as a fine mesh discretisation and an associated flow rule is used. When performing FEA in combination with non-associated plasticity the obtained failure load reduces and (in some cases) numerical instabilities occur. 3D FELA on the other hand requires also a reasonable fine mesh along the failure mechanism to decrease the distance between lower- and upper-bound solutions. Currently further research is ongoing to investigate the effect of non-associated plasticity and the performance of the Davis procedure [3] in more detail.

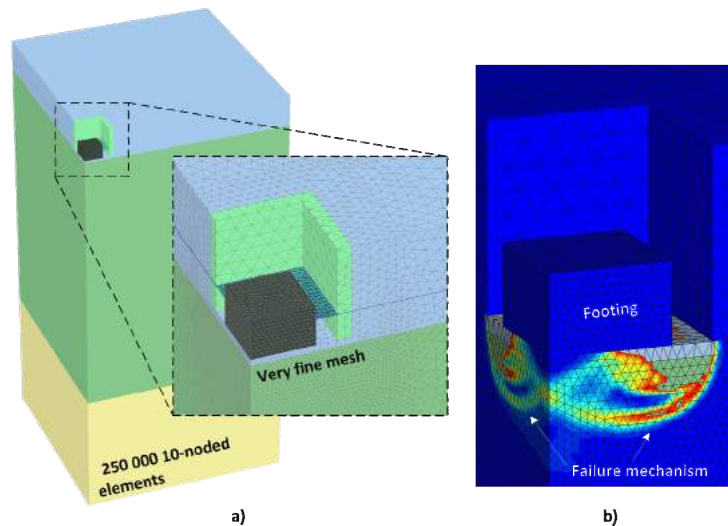


Figure 1: 3D FE model (a) and obtained failure mechanism (b)

4. References

- [1] Davis, E.H. (1968). Theories of plasticity and failure of soil masses. In *Soil mechanics: selected topics*. (ed. I. K. Lee), pp.341–354. New York, NY, USA: Elsevier.
- [2] Tschuchnigg F, Schweiger H.F., Sloan S.W., Lyamin A.V., Raissakis I. (2015). Comparison of finite element limit analysis and strength reduction techniques. *Geotechnique* 2015; **65**(4):249–57.
- [3] Tschuchnigg, F., Schweiger, H.F. and Sloan, S.W. (2015). Slope stability analysis by means of finite element limit analysis and finite element strength reduction techniques. Part I: Numerical studies considering non-associated plasticity. *Computers and Geotechnics* **70**: 169–177.
- [4] Krabbenhöft, K., Lyamin, A.V. and Krabbenhöft, J. (2016). *Optum G2 2016 - User Manual*. Newcastle, Australia: Optum Computational Engineering.
- [5] Kelly R.B., Sloan S.W., Pineda J.A., Kouretzis G., Huang J.. Outcomes of the Newcastle symposium for the prediction of embankment behaviour on soft soil. *Computers and Geotechnics* **93**: 9–41.
- [6] Gaone F.M., Gourvenec S., Doherty J.P. Large scale shallow foundation load tests on soft clay – at the National Field Testing Facility (NFTF), Ballina, NSW, Australia. *Computers and Geotechnics* **93**: 253–268.
- [7] Brinkgreve, R.B.J., Kumaraswamy, S. and Swolfs, W.M. (2016). *PLAXIS 2D 2016 - User Manual*. Delft: The Netherlands: Plaxis bv.
- [8] Doherty J.P., Gaone F.M., Gourvenec S. Insights from a shallow foundation load-settlement prediction exercise. *Computers and Geotechnics* **93**: 269–79

ESTIMATION OF PILE CAPACITIES USING CASE-BASED REASONING METHOD

H. K. Engin¹, F. Nadim¹, P. Carotenuto¹ and K. Bach²

¹ Norwegian Geotechnical Institute, Oslo, Norway

² Norwegian University of Science and Technology, Trondheim, Norway

1. Introduction

In current practice of offshore foundation design, the axial capacity of an offshore pile may be assessed using CPT-based methods, e.g. NGI-05, Fugro-05, ICP-05, and UWA-05. As expected, these methods perform well in the domain they have been calibrated, but their predictions exhibit more scatter when they are applied to other pile load tests. In fact, recent reliability analyses performed for pile foundation of actual platforms show that the model uncertainty associated with different prediction methods is the most important contributor to the uncertainty in foundation performance.

The idea of this work is to propose a 'method-free' CPT-based approach for estimating pile capacities directly from a database of pile load tests using Case-Based Reasoning (CBR). The method is applied on high quality database of pile tests in sand and clay sites. Case-Based Reasoning is an Artificial Intelligence method that captures previous experiences and provides them to solve new problems. A CBR system carries out a similarity-based retrieval in order to best match a new problem to the collection of past cases. Once a CBR system is implemented as learning system, new and adapted cases can be added to the case base, therewith increasing the competence of the system [1]. The method is superior to ANN (Artificial Neural Networks) since it allows the user (i.e. expert engineer) to follow the reasoning step on every level. The method gives possibility of expanding the case base without updating the established control parameters. CBR has been used in other disciplines, but its potential application to geotechnical problems has not been explored. The paper presents the application of the method to estimating pile capacities in layered soils, and compares its predictions with those of the established CPT-based methods in use today.

2. Case-Based (Method-free) Estimation of Pile Capacities

In this work, we implemented a CBR system that estimates pile capacities based on previous observed (measured) capacities from high-quality pile load tests. For the implementation and testing, we used the myCBR tool [2] that has been successfully applied in various domains [3]. Figure 1 summarizes the process schematically.

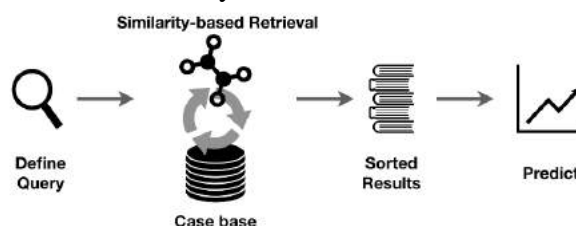


Figure 1. Process of defining a query for a given problem, comparing it to the case base, sorting the results according to their similarity and using the most similar case for making a prediction.

The case-based approach allows one to define customized similarity measures and weights for selecting and prioritizing cases from the case base and therewith provide predictions more suitable than in a pure database retrieval.

We created two different case bases, one for the pile tests in sand and one for the pile tests in clay, with cases following a homogeneous case structure. A case contains of 11 attributes with

individual similarity measures as well as a weighted function for the similarity-based retrieval. Defined attributes are pile ID, site name, testing info (compression or tension), pile material (concrete or steel), pile diameter (D), (segment) length to diameter ratio L/D , outer surface area of the pile shaft, average in-situ vertical stress (for sand cases only) and average cone resistance along pile length, average unit skin friction, average plasticity index (for clay cases), as input, and average unit base and skin resistances, as output. For the cases, in which only total pile capacity was measured, percentage of shaft and tip resistances were separated based on the average of the predictions of the CPT-based design methods, i.e. Fugro-96, Fugro-10, ICP-05, NGI-05, and UWA-05. The method is verified by testing the cases from the database, i.e. obtaining similarity of 1.0 (i.e. exact match). The retrieval query is initiated with 11 attributes, while the validation testing is performed excluding irrelevant (e.g. pile ID) or unavailable data (e.g. plasticity index).

3. Results

The Tokyo Bay pile test [4] was used for validation case. The results show quite successful prediction of the total capacity as well as the top 12 m skin friction capacity of the pile using the CBR method. However, the skin friction distribution and base resistances deviate from the measurements significantly. The tip resistance is quite significantly overestimated even compared to few CPT-based design methods, which overestimate the base resistance about ~50%. However, this is not surprising as identifying the relative contributions of tip capacity and skin friction of the lowest part of the pile (5 to 10 times the diameter) in pile load tests is very difficult. Nevertheless, the authors believe that the presented CBR tool can be improved by calibrating the number of attributes, their local similarity measures and global weights to obtain successful estimates of pile capacities (both skin and base capacities) in layered soils.

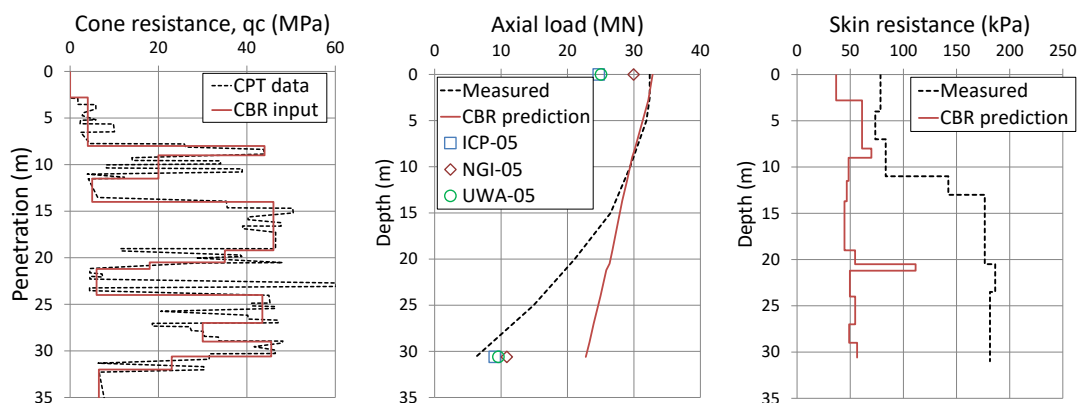


Figure 2. Tokyo Bay pile testing site a) actual and simplified CPT data, b) comparison of field measurements, CBR and CPT-based design method predictions, and c) comparison of measured and predicted skin friction distributions.

5. References

- [1] Aamodt, A. & Plaza, E. (1994). Case-based reasoning: Foundational issues, methodological variations, and system approaches. *Artificial Intelligence Communications*, 7(1), 39–59
- [2] <http://www.mycbr-project.net/index.html>
- [3] Bach, K. & Althoff, K.-D. (2012). Developing Case-Based Reasoning Applications Using myCBR 3. In: Watson, I., Agudo, B.D. (eds.) *Case-based Reasoning in Research and Development, Proceedings of the 20th International Conference on Case-Based Reasoning (ICCBR-12)*. pp. 17–31. LNAI 6880, Springer.
- [4] Shioi, Y., Yoshida, O., Meta, T. & Momma, M. (2012). Estimation of bearing capacity of steel pipe pile by static loading test and stress-wave theory. In *Proc. 4th Int. Conf. on the Application of Stress-Wave Theory to Piles*: 325–330. AA Balkema, Rotterdam.

3D SPATIAL VARIABILITY OF MECHANICAL PROPERTIES OF EMILIA ROMAGNA ALLUVIAL DEPOSITS AND ITS IMPLICATIONS IN GEOTECHNICAL DESIGNING OF FOUNDATIONS

G. Vessia¹, A. Castrignanò², D. Di Curzio¹ and W. Puła³

¹University “G. d’Annunzio” of Chieti-Pescara, Chieti, Italy

²Council of Agricultural Research and Economics (CREA), Bari, Italy

³Wroclaw University of Science and Technology, Wroclaw, Poland

1. Introduction

Mechanical characterization of urban or peri-urban territories is needed for both planning and building designing purposes. Nonetheless, in-field geotechnical investigations are commonly a point-based (e.g. Standard Penetrometer Tests SPT, Cone Penetration Tests CPT, Field Vane Test (FVT), Dilatometer Tests DTM and in hole Seismic Tests (SDMT, CH, DH...)) and performed up to tens of meters below the surface, at a few locations, in order to reconstruct a 1D model of the foundation volume. In addition, when seismic urban scale microzonation is undertaken at some locations, drilling tests must be executed for estimating some parameters, such as the liquefaction potential index IL and shear wave velocity V_s . This point information is commonly assumed to be representative of subsoil volumes although the following issues should be taken into account:

- 1) Assessment of spatial variability of natural soil litho-technical properties within a soil type depending on testing device;
- 2) Heterogeneity of soil and rock formations in space;
- 3) Different local conditions (water table depth; strata dipping; altitude and topography).

A large Database of Cone Penetration Test profiles (CPTs) was collected throughout the whole territory of Emilia-Romagna Region by the Regional Office for Territorial protection and development (<http://geoportale.regione.emilia-romagna.it/it>). From this large database 182 CPT readings of cone tip resistance Q_c and sleeve friction f_s , located within the Bologna province territory, were selected to describe the litho-technical unit variability up to 35-m depth using Geostatistical tools implemented in Geovariances ISATIS code (<https://www.geovariances.com/en/software-geovariances>). The aim of this study is to assess and model the spatial variability of the mixtures of clay, silts and sands, in order to produce 3-dimensional estimates of the mechanical variables and their uncertainties on the Bologna province.

In this study the application of ordinary kriging [1] to Q_c and f_s has been shown and the maps of the estimated values and their uncertainties have been illustrated.

2. Spatial variability assessment and modelling of CPTs profiles

Geostatistics is based on the Regionalized Variable Theory [2]. This theory states that spatial measurement values are spatially correlated so that the estimates of a variable can be expressed as the summation of its expected value, a random fluctuation spatially correlated and a residual error that is not spatially correlated (characterized by a null mean value and its variance σ^2). Kriging method, like all interpolation techniques, is built on the basic principle of geography that “things that are close to one another are more alike than those farther away from each other” (quantified here as spatial autocorrelation). The empirical semivariogram is a means to explore this relationship. To make spatial prediction, an authorized mathematical model has to be fitted to experimental variogram.

In this case study, the 3D anisotropic spatial model has been built from the 182 Q_c and f_s profiles performed within about 30 km area and approximately 1km apart. The vertical profiles

extended up to 20 to 35- m depth and data have been recorded each 2 cm. From the experimental measures the following nested semivariogram models have been drawn (Fig. 1).

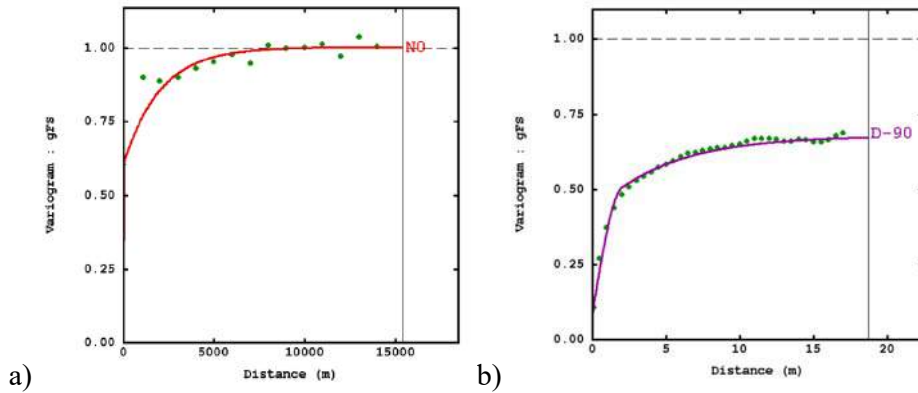


Figure 1. Experimental directional variograms (dots) and fitted nested anisotropic models (line) of f_s measures: a) surface and b) vertical direction.

The Kriging estimate can be calculated by solving the system of linear equations through inverting the coefficient matrix. From its solutions, estimation variance is also calculated, which is a measure of uncertainty (Fig. 2).

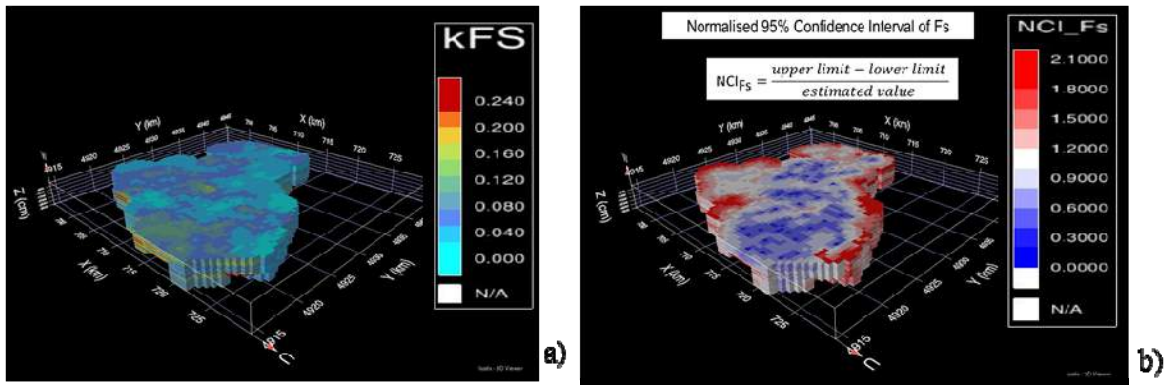


Figure 2. a) 3D estimates of f_s variable and b) uncertainty of f_s estimates expressed in relative terms as the ratio of 95% confidence interval of f_s estimation to its estimated value.

As a result, the 3D continuous model of the sleeve friction (Fig. 2a) shows an area of higher values at the southern border side which highlights the presence of coarser alluvial fans interdigitated within the finer soil mixtures. The reliability of this litho-technical model is evaluated by the uncertainty index NCI (Normalized 95% Confidence Interval) distribution (Fig. 2b).

3. References

[1] Castrignanò, A. (2011). *Introduction to spatial data processing*. Aracne, Rome.
 [2] Matheron G. (1973). The intrinsic random functions and their applications. *Advances in Appl. Prob.*, **5**, 439–468.

NUMERICAL IMPLEMENTATION OF A STRESS-SATURATION SOIL MODEL WITH HYDRAULIC HYSTERESIS EFFECTS

Yue Zhang¹, Annan Zhou¹, Majidreza Nazem¹ and John P Carter²

¹ *Royal Melbourne Institute of Technology (RMIT University), Melbourne, Australia*

² *University of Newcastle, Newcastle, Australia*

1. Introduction

Because of issues associated with climate change, such as extreme weather events, the analysis of geotechnical problems generally requires increasing attention being paid to the effect of the hydraulic characteristics on the behavior of unsaturated soils. This is especially important in problems such as landslides, the wetting collapse of soil induced by unpredictable heavy rainfall, and expansive soil problems due to cyclic climatic drying and wetting processes. In this study a stress-saturation constitutive model ([1], [2]) of unsaturated soil is implemented in the finite element (FE) framework by considering hydraulic hysteresis effects and fully coupled hydro-mechanical interaction. During nonlinear analysis by the FE method, the stresses are required to be updated by integrating the constitutive equations with a known strain increment, so stress integration is an essential task. In addition, the governing equations need to be consistent with the constitutive model, as this will affect individual terms in the global equations. When extending the capabilities of a numerical tool to incorporate advanced soil models for consolidation analysis of unsaturated soils, it is important to ensure that the governing equations are consistent with the applied constitutive model, including the stress variables and the hydraulic behaviour. This consistency is usually ignored in the literature for simplicity, but its inclusion and examination is the main goal of this study.

2. Stress integration

The general form of the constitutive equations required for stress integration is derived based on [3]. Although the constitutive model is developed in the space of Bishop's effective stress (σ') and the effective degree of saturation (S_e), the degree of saturation (S_r) and the net stress (σ) are updated at each stress point during the stress integration by solving the following system of partial differential equations:

$$\begin{Bmatrix} d\sigma \\ dS_r \end{Bmatrix} = \begin{bmatrix} \mathbf{D}_{ep} & \mathbf{W}_{ep} \\ \mathbf{R}_{ep} & Q_{ep} \end{bmatrix} \begin{Bmatrix} d\boldsymbol{\varepsilon} \\ du_w \end{Bmatrix} \quad (1)$$

where matrices \mathbf{D}_{ep} , \mathbf{W}_{ep} , \mathbf{R}_{ep} and Q_{ep} are developed based on the method proposed by Zhang and Zhou (2016), $\boldsymbol{\varepsilon}$ is the strain and u_w is the pore water pressure. In the general form, the suction is treated as a strain variable, but the degree of saturation used in this constitutive model is treated as a stress variable. An explicit integration scheme is adopted to solve Equation (1) in this research.

3. Governing equations

The simplest formulations which capture the key features of unsaturated soil behaviour are based on mass conservation of water and mechanical equilibrium of the total soil volume. The net stress (σ) is adopted instead of the effective stress in the mechanical equilibrium due to the requirement of the stress integration. For the mass conservation of water, considering the mass balance of pore fluids leads to the continuity equation of pore fluid flow. The volumetric water content, $\theta_w = n \cdot S_r$ in the mass conservation, and $\dot{\theta}_w = \dot{n} = \dot{\varepsilon}_v$ (where n is the porosity and ε_v is the volumetric strain) with S_r taking a value of 1 in fully saturated conditions. That means the

changes in net stress or pore water pressure causes a change of volumetric strain ($\dot{\epsilon}_v$), and also changes in the porosity (\dot{n}) with equal effect. Thus, the effective stress (σ') is used for fully saturated conditions to determine the volumetric strain. However, in unsaturated conditions, changes in θ_w result from both changes in the porosity (\dot{n}) and the degree of saturation (\dot{S}_r), where $\dot{n} = \dot{\epsilon}_v$. The change of degree of saturation (\dot{S}_r) involved in $\dot{\theta}_w$ is normally obtained from the soil-water characteristics as $S_r = f(s)$ [4]. However, the change of net stress may also cause the change of degree of saturation as some deforming voids can result in the water drainage. The change of the degree of saturation in this model is determined as ([1], [2]):

$$dS_r = \frac{\partial S_r}{\partial s} ds + \frac{\partial S_r}{\partial \epsilon_{v\sigma}} d\epsilon_{v\sigma} \quad (2)$$

where, $\epsilon_{v\sigma}$ is the volumetric strain caused by the change of net stress, $\partial S_r / \partial \epsilon_{v\sigma}$ is given by Zhou et al. [1], and $\partial S_r / \partial u_w$ is obtained from the hysteresis behaviour [2].

4. Flexible footing analyses

Two-dimensional problems of a flexible strip footing on an elastoplastic soil layer are considered in this section. Mechanical loading is applied to the soil after drying-wetting cycles. Figure 1(a) shows that suction path ABA and ADA are simulated without hysteresis behaviour, and path ABC and ADE consider the hysteresis effect. Figure 1(b) shows the hydraulic hysteresis behaviour has a significant effect on the mechanical behaviour of the footing. In conclusion, the stress-saturation model has been implemented into FE frame work with new proposed general constitutive equations and governing equations, and the FE code is advantageous for coupled analysis of geotechnical problems with hydraulic hysteresis effects.

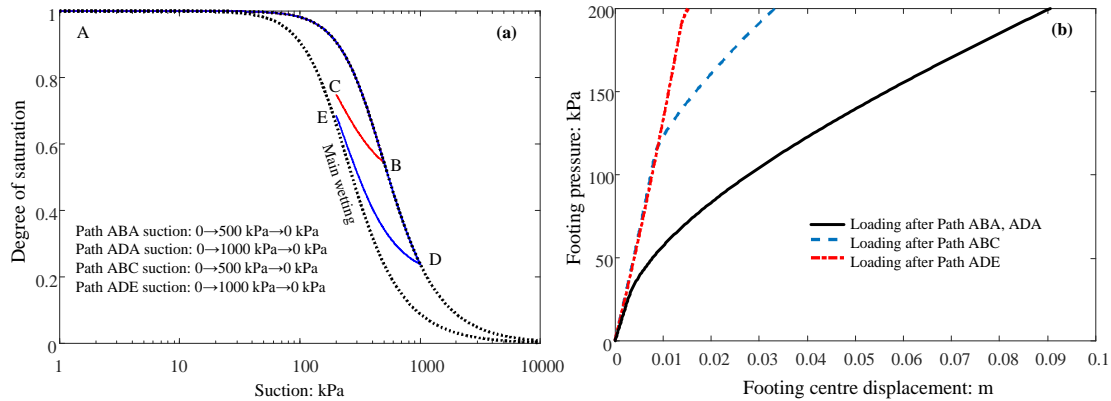


Figure 1 Hydraulic path and footing centre displacement during loading

5. References

- [1] Zhou, A.N., Sheng, D., Sloan, S.W. & Gens, A. (2012). 'Interpretation of unsaturated soil behaviour in the stress-saturation space: II: Constitutive relationships and validations', *Computers and Geotechnics*, **43**, 111-23.
- [2] Zhou, A.N., Sheng, D., Sloan, S.W., and Gens, A. (2012). Interpretation of unsaturated soil behaviour in the stress - Saturation space, I: Volume change and water retention behaviour. *Computers and Geotechnics* **43**, 178-187.
- [3] Zhang, Y & Zhou, A.N. (2016). Explicit integration of a porosity-dependent hydro-mechanical model for unsaturated soils', *International Journal for Numerical and Analytical Methods in Geomechanics*, **40**(17), 2353-82.
- [4] Sheng, D., Sloan, S.W., Gens, A., and Smith, D.W. (2003). Finite element formulation and algorithms for unsaturated soils. Part I: Theory. *International Journal for Numerical and Analytical Methods in Geomechanics* **27**(9), 745-765.

NUMERICAL STUDY OF PENETRATION PROBLEMS IN FINE GRAINED SOILS WITH THE PARTICLE FINITE ELEMENT METHOD

L. Monforte¹, M. Arroyo¹, A. Gens¹ and J. M. Carbonell²

¹ Universitat Politècnica de Catalunya – BarcelonaTech, Barcelona, Spain

² Centre Internacional de Mètodes Numèrics en Enginyeria (CIMNE), Barcelona, Spain

1. Introduction

The most commonly used sampling method is the tube sampling and constitutes a core activity in site investigation. During the process –that encompass boring, sampling, storage and extrusion- the sample may suffer significant disturbance and the soil may no longer be representative of the in situ state [1].

Traditionally, this problem has been studied by approximated analytical methods, such as the Strain Path Method [2] but very limited numerical work has been performed on the process [3]. Realistic numerical simulations of this problem are now becoming possible thanks to methods like the Particle Finite Element Method (PFEM) [4].

2. Simulation method

The PFEM is characterized by a particle discretization of the domain: every time step a finite element mesh –whose nodes are the particles– is constructed using a Delaunay’s tessellation and the solution is evaluated using this mesh with well-shaped, low order elements. The continuum is modeled using an Updated Lagrangian formulation.

Numerical simulations have been carried out by means of the numerical code G-PFEM [5], specifically developed for the analysis of large strain contact problems in geomechanics. The code is able to accurately simulate the interaction between fluid-saturated porous media and rigid structures.

The sampling process occurs at relatively high velocity compared with the hydraulic properties of clay; as such, it is modeled with a total stress approach. Then, the material is assumed to satisfy a Tresca yield criterion in conjunction with a linear elastic model. A Poisson’s ratio of 0.49 is used. Therefore, techniques to alleviate volumetric locking are required: in this work, a mixed stabilized formulation is adopted [5].

3. Representative numerical simulation

For the reference case, a rigidity index, $I_r = G/S_u$, equal to 100 is considered and the contact interface is smooth. The sampler is thick –the ratio between the outer diameter and the thickness is equal to 10- and its tip is rounded; Figure 1 shows the employed axisymmetric model.

Figure 1 depicts the Almansi vertical strain. All the material that enters the sampler suffers high vertical strains in compression whereas very low deformations are found in the rest of the soil mass. From this figure, the failure mechanism may be interpreted: just beneath the tube sampler a localization zone is formed and soil exhibits high plastic vertical strains and compression in the radial and circumferential directions; once the soil element is inside the tube sampler the soil remains in elastic regime. All deformation occurs in the area of the cutting shoe of the sampler.

The value of the vertical strain at the centerline has been frequently regarded as a magnitude of soil disturbance due to the sampling process. For instance, using the Strain Path Method [2], the values of the maximum and minimum vertical strain coincide (in absolute value) and are equal to 3.85% for this particular geometry. In contrast, in the numerical analysis reported here, the maximum vertical extension is in the order of 50% whereas the maximum compression is 0.4%.

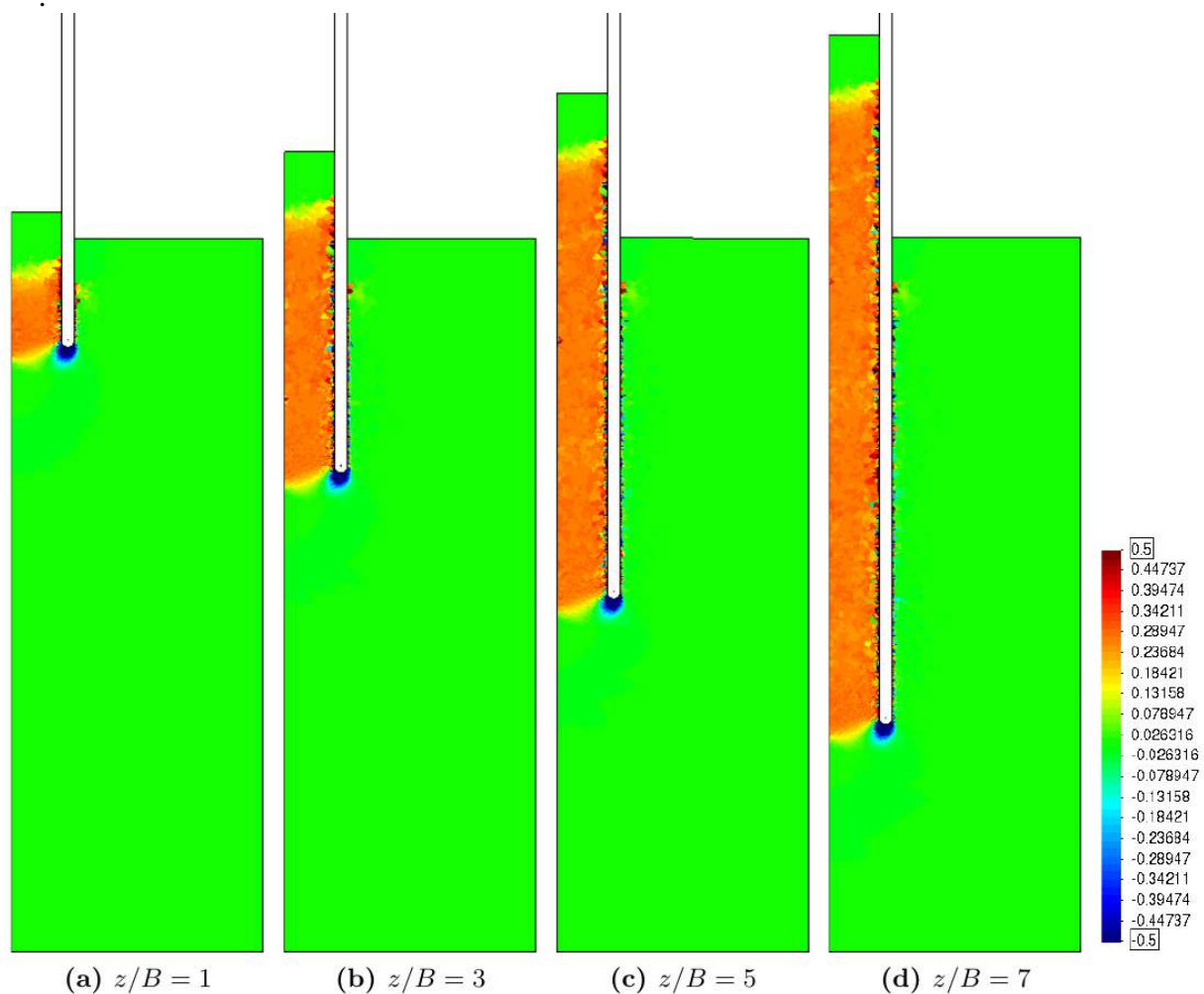


Figure 1. Vertical component of the Almansi strain tensor at several normalized penetrations.

4. References

- [1] Hvorslev, M. J. (1949) *Subsurface exploration and sampling of soils for civil engineering purposes*. Report on a Research project of the American Society of Civil Engineers
- [2] Baligh, M. M., Azzouz, A. S. & Chin, C. T. (1987) Disturbance due to “ideal” tube sampling. *Journal Geotechnical Engineering*, 113(7): 739-757.
- [3] Alonso, E.E, Oñate, E. & Casanovas, J.S. (1981) An investigation into sampling disturbance *Proc 10th Int. Conf. Soil. Mech. Found. Eng.*, Vol. 2. 423-426.
- [4] Oñate, E., Idelshon, S.R, Del Pin, F. & Aubry, R. (2004) The Particle Finite Element Method (PFEM). An overview. *International Journal of Computational Methods*, 1(2):267-304.
- [5] Monforte, L., Carbonell, J.M., Arroyo, M. & Gens, A. (2017) Performance of mixed formulations for the particle finite element method in soil mechanics problems. *Computational Particle Mechanics*, 4(3):269-284.

NUMERICAL SIMULATION AND VERIFICATION OF STATIC LIQUEFACTION USING THE MATERIAL POINT METHOD

E. D. Wobbes^{1}, J.R. Silva², V. Galavi³, J.T. Eggenhuisen², and C. Vuik¹*

¹ *Department of Applied Mathematics, Delft University of Technology, Van Mourik Broekmanweg 6, 2628 XE Delft, The Netherlands*

² *Department of Earth Sciences, Utrecht University, PO Box 80021, 3508 TA Utrecht, The Netherlands*

³ *Geo-Engineering section, Deltares, Boussinesqweg 1, 2629 HV Delft, The Netherlands*

Static liquefaction can be described as a significant increase of excess pore water pressure in loose saturated sand, which causes substantial loss of shear strength in a strain-softening manner. This complex phenomenon may induce excessive deformation, such as the failure of earthen embankments and submarine landslides. In this study, static liquefaction is numerically modelled with the double-point Material Point Method (MPM) [1, 2, 3]. The novel part of the research is that MPM is combined with an elasto-plastic UBC3D-PLM constitutive model [4] and the numerical results are validated experimentally.

MPM [5] is an effective tool to simulate problems that involve large deformations. It is a continuum-based method, where the material is represented by a set of Lagrangian particles that move through an Eulerian background mesh. In double-point MPM, solid and liquid phases are represented by distinct sets of particles allowing modelling of the accumulation and dissipation of excess pore pressure, the fluid-like behaviour of soil, and the transition from free water to groundwater. The motion of both phases is captured by momentum balance equations, which include the drag force as described in [6] and are solved in their weak form.

The effective stress is calculated by UBC3D-PLM model, a three-dimensional generalization of the well-known UBCSAND model [7]. In the UBC3D-PLM model, the elastic behaviour is described by a nonlinear Hooke's law, whereby the elastic shear modulus and the elastic bulk modulus are stress-dependent. The model uses two yield surfaces in order to distinguish between primary and secondary loading. Both yield surfaces are defined by the Mohr-Coulomb yield function, while the plastic potential function originates from the Drucker-Prager criterion.

The numerical results are compared with experimental tests describing static liquefaction of a submerged column of loose sand with a length and height of 0.40 m and width of 0.22 m. The sand (median diameter, $D_{50}=0.135$ mm) is deposited in a flume filled with water and constrained with a removable vertical plate on one side. The failure, monitored with a video camera, is triggered by removing the confining plate, which results in a sudden collapse of the sand. Furthermore, a set of triaxial tests were performed to calibrate the UBC3D-PLM parameters (Figure 1).

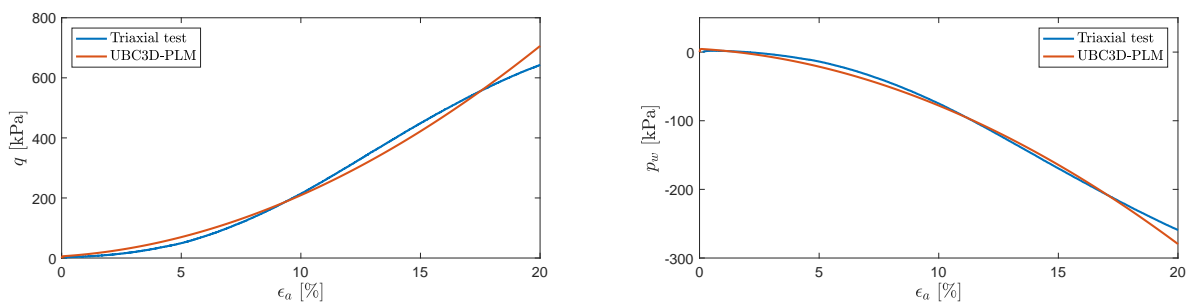


Figure 1. Curve fitting results for deviatoric stress q and pore water pressure p_w versus axial strain ϵ_a .

The comparison of numerical and experimental results is shown in Figure 2. The liquefaction started almost immediately in both cases, and the numerical simulation accurately captured its general evolution. However, the failure process progressed approximately 4 times faster during the MPM simulation than it was observed in the laboratory. In addition, the numerical prediction of the final displacement of the deposit was approximately 0.3 m larger than the experimental one. These inaccuracies can probably be eliminated by including the soil viscosity in the constitutive model.

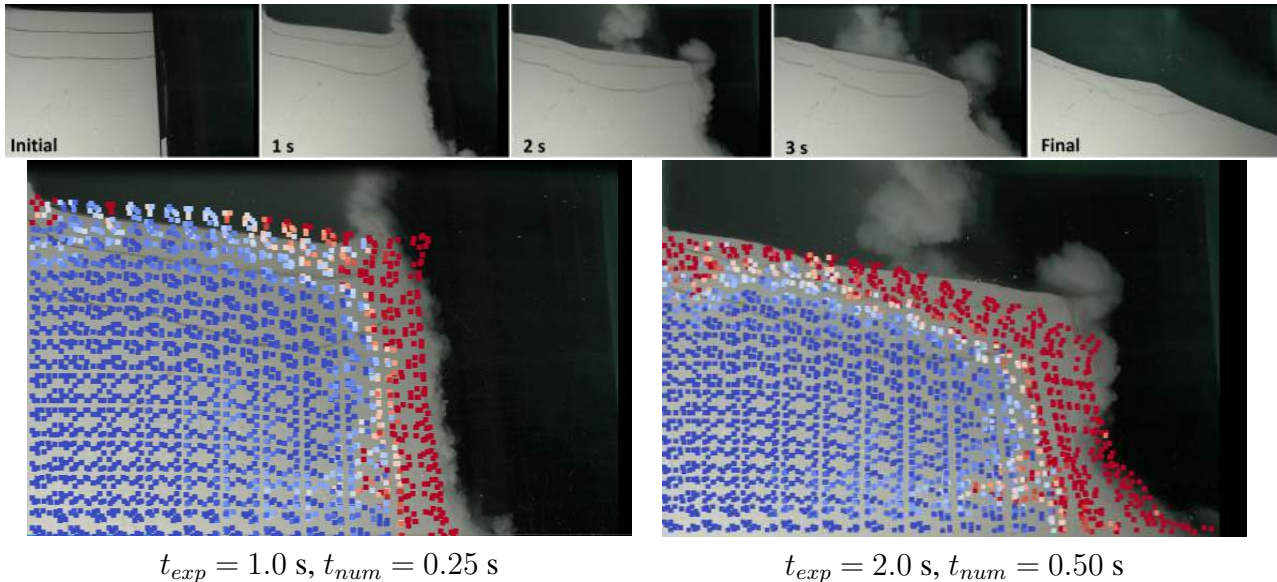


Figure 2. Experimental results and their comparison with the numerical simulation; t_{exp} denotes the experimental time, t_{num} denotes the numerical time. The colour of the material points identifies the porosity varying from 0.49 (dark blue) to 0.52 (red).

In this study, double-point MPM has been applied in conjunction with UBC3D-PLM model to numerically model static soil liquefaction. While the constitutive model can be further improved, it was demonstrated that the considered numerical approach captured the general evolution of the failure observed experimentally.

References

- [1] Bandara, S. (2013). *Material Point Method to simulate large deformation problems in fluid-saturated granular medium*. Ph.D. thesis, University of Cambridge.
- [2] Vermeer, P., Wieckowski, Z., Sittoni, L., and Beuth, L. (2013). Modelling soil-fluid and fluid-soil transitions with applications to tailings. *Tailings and Mine Waste*, Canada, pp. 305–315.
- [3] Martinelli, M. and Rohe, A. (2015). Modelling fluidisation and sedimentation using material point method. *1st Pan-American Congress on Computational Mechanics*.
- [4] Petalas, A., Galavi, V., and Brinkgreve, R. (2014). A 3d practical constitutive model for predicting seismic liquefaction in sands. *Installation Effects in Geotechnical Engineering*, pp. 65–71.
- [5] Sulsky, D., Chen, Z., and Schreyer, H. (1994). A particle method for history-dependent materials. *Computer Methods in Applied Mechanics and Engineering*, **118**, 179–196.
- [6] Ergun, S. (1952). Fluid flow through packed columns. *Chemical Engineering Progress*, **43**, 89–94.
- [7] Beaty, M. and Byrne, P. (2011). Ubsand constitutive model. version 904ar, documentation report: Ubsand constitutive model on itasca udm website. Tech. rep.

MODELLING SATURATED SOIL COLUMN COLLAPSE WITH 2-PHASE 2-POINT MATERIAL POINT METHOD

Veronica Girardi¹, Francesca Ceccato¹, Paolo Simonini¹

¹DICEA – University of Padua, via Ognissanti 39, 35129 Padua, Italy

1. Introduction

The collapse of soil columns is commonly employed in geotechnical modelling to study the rheology of complex natural mixtures, as well as to calibrate major parameters controlling free surface earthfall behavior and potentially correlated debris-flows.

Despite many experimental and computational works formerly carried out, the scientific literature still lacks experiences with 2-phase models. Capturing solid grains and pore fluid interactions and their evolution along time is challenging. This issue is investigated numerically in this study by means of the Material Point Method (MPM). The potentialities of a recently proposed 2-phase 2-point formulation [1], implemented in the software Anura3D (www.anura3d.eu), are investigated.

This formulation assumes that the saturated porous medium consists of a superposition of two independent continuum, and it is governed by the momentum balance and mass balance equations of the two phases, together with the constitutive laws. The drag force determines the interaction between the phases. The solid skeleton and the liquid phase are represented separately by two sets of Lagrangian MPs: solid material points (SMPs) and liquid material points (LMPs). While SMPs move attached to the solid skeleton, LMPs follow the liquid motion, both carrying properties of respective phases. The behaviour of the continuum can vary from dry porous media to pure fluid; moreover fluidization and sedimentation processes can be simulated. The latter lead to extreme changes in flow regime and high volumetric strain rates depending on concentration ratio gradients of the two phases.

2. Results

This groundbreaking formulation is tested in the present work, focusing on two main aspects: the drag force expression, and the phase transition from solid to liquid state.

The drag force vector, incorporates two terms (see Eq. 1): a first “viscous” term, linearly proportional to the relative velocity between the phases through the material permeability, and a second term depending on the squared of the relative velocity vector, introduced by [2], to correctly account for turbulent flow. The drag expression resembles the formulation proposed by Ergun, after studies on fluidized beds, including two empirical constants (A, B) from the same work [3].

$$\mathbf{f}^d = \frac{n_L^2 \mu_L}{\kappa_L} (\mathbf{v}_L - \mathbf{v}_S) + \beta n_L^3 \rho_L |\mathbf{v}_L - \mathbf{v}_S| (\mathbf{v}_L - \mathbf{v}_S) \quad (1)$$

Where n_L = porosity, μ_L = liquid dynamic viscosity, ρ_L = liquid density, \mathbf{v}_L = liquid velocity, \mathbf{v}_S = solid velocity, β = non-Darcy flow coefficient depending on κ_L = intrinsic permeability as follows

$$\beta = B / \sqrt{\kappa_L A n_L^3}, \quad \kappa_L = \frac{D^2}{A} n_L^3 / (1 - n_L)^2 \quad (2)$$

A=150 and B =1.75 are empirical constants, D = effective grain size diameter.

Since the influence of the soil intrinsic permeability, calculated and updated at every time step with a Kozeny-Karman formula, plays a fundamental role in the drag force computation, a parametrical study has been performed on columns with three different values of initial intrinsic permeability (Fig. 1), depending on grain effective diameter variations, since initial porosity is constant for all the cases.

Another series of tests was undertaken for each column, with drag force including or neglecting the non-linear term, to make comparisons in terms of viscous or kinetic forces predominance, during the run out (Fig. 1). Analyzing the propagation of the front, the formation of a granular front appears in coarse materials if both linear and quadratic terms of the drag force are included. In contrast, a liquid front is observed if only the linear term is used. Concurrently, particle recirculation seems to develop in a portion close to the front and at the contact with the column base.

As previously mentioned, a special attention was given to the liquefaction process, thanks to an assigned value of maximum porosity, separating solid and fluid states; it essentially corresponds to the moment of complete particles detachment, which fluctuates in the fluid, losing all the resistance and cohesion properties, with consequent effective stress state annulment.

In conclusion, this numerical work on saturated soil columns collapse, draws attention to the need of further research to correctly evaluate stress states in both phases, and to understand the correlation between fluid flow and solid stress transmission. A key issue to correctly describe these problems is the definition of the interaction term (drag force in eq. 1) between the two phases.

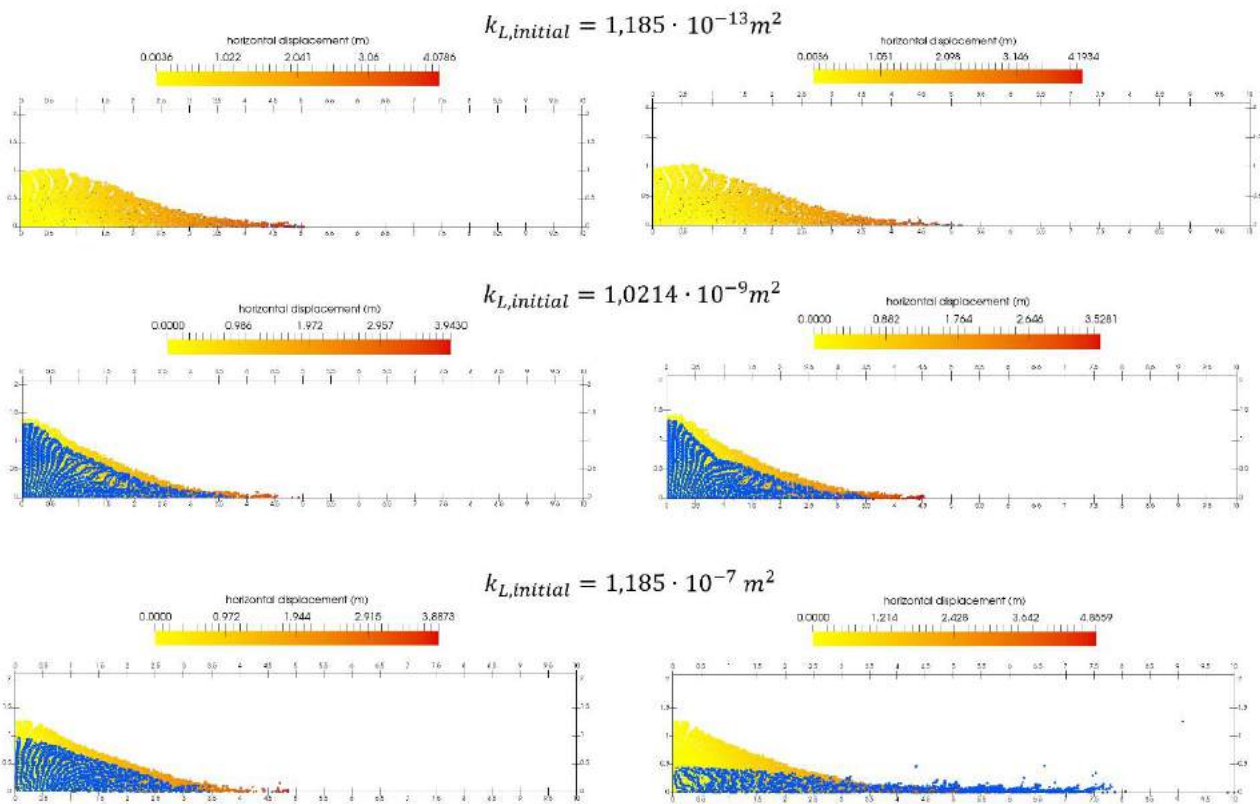


Figure 1. Location of LMPs (blue dots) and horizontal displacements for SMPs at time $t=2,5$ s for columns with 3 different initial intrinsic permeabilities. Left set performed with linear and quadratic terms of drag force, right set performed only with linear term.

3. References

- [1] Martinelli, M. (2015). 2 Layer Formulation: Joint MPM Software. Deltares, Delft, The Netherlands. Published and printed by: *MPM Research Community*.
- [2] Forchheimer, P. (1901). Wasserbewegung durch Boden. *Z Ver Deutsch Ing*, **45**, 1782-1788.
- [3] Ergun, S. & Orning, A.A. (1952). Fluid Flow Through Packed Columns, *C. E. P.*, **48**, 89-94.

SIMULATION OF FREE WATER-FULLY SATURATED SOIL INTERACTION USING THE MATERIAL POINT METHOD

F. Fatemizadeh¹, D. Stolle² and C. Moormann¹
¹ *University of Stuttgart, Stuttgart, Germany*
² *McMaster University, Hamilton, Ontario, Canada*

1. Introduction

Interaction between free water and fully saturated soil is observed frequently in geotechnical engineering; e.g. the phenomenon of hydraulic heave or dam-water interaction. Software packages based on the Finite Element Method (FEM) are normally used to simulate such cases with domain decomposition being used to represent free water and fully saturated soil separately along with appropriate boundary conditions. In applications including large deformations, the boundary is not defined clearly and FEM is not capable of simulating large deformations of the soil.

In this study the Material Point Method (MPM) is used to represent large deformations. The applicability of MPM for geotechnical engineering has been demonstrated by different researchers (e.g. [1] and [2]). Here water (free and pore water) is represented as one continuum, where a sudden jump from free water with a porosity of one to fully saturated soil with its porosity causes numerical difficulty specially when linear elements are used. Here the third order B-Spline functions are used in an in-house developed MPM program as the shape functions to represent the porosity field.

2. Methodology

MPM is a numerical procedure that is capable of representing large deformations and displacements of a continuum, and overcoming the mesh tangling problem of classical Lagrangian FEM [1]. Here the continuum is represented using material points or particles that move through a background fixed Eulerian mesh. The method has already been applied to biphasic applications in geotechnical engineering where single type particles [1] and double type particles [2] are used to represent the biphasic medium.

The governing equations are the momentum balance of the water and solid phases. The momentum balance of the water phase can be written as:

$$\mathbf{M}^w \mathbf{a}^w = \mathbf{F}_{trac}^w - \mathbf{F}_{int}^w - \mathbf{F}_{porosity} - \mathbf{F}_{drag} + \mathbf{F}_{grav}^w \quad (1)$$

where \mathbf{a}^w is the acceleration vector, \mathbf{M}^w is the lumped mass matrix, \mathbf{F}_{trac}^w is the traction force vector, \mathbf{F}_{int}^w is the internal force vector and \mathbf{F}_{grav}^w is the gravitational force vector of the water phase. The vector $\mathbf{F}_{porosity}$ is the force due to the change in the porosity field and \mathbf{F}_{drag} is the interaction force between the water and solid phases.

The momentum balance of the solid phase can be written as:

$$\mathbf{M}^s \mathbf{a}^s = \mathbf{F}_{trac}^s - \mathbf{F}_{int}^s + \mathbf{F}_{porosity} + \mathbf{F}_{drag} + \mathbf{F}_{grav}^s \quad (2)$$

where, \mathbf{a}^s is the acceleration vector, \mathbf{M}^s is the lumped mass matrix, \mathbf{F}_{trac}^s is the traction force vector, \mathbf{F}_{int}^s is the internal force vector and \mathbf{F}_{grav}^s is the gravitational force vector of the solid phase.

3. Results

Based on the above mentioned formulation a 2-D plane strain program is developed with linear elements using two different sets of particles to represent the water and solid phases separately. To calculate the gradient of the porosity field third order B-Spline functions are used as the shape functions as shown in Figure 1. To show the effectivity of using B-spline functions for the

porosity field an example is considered in which half a meter fully saturated soil is submerged under half a meter of water. The pressure of the water and effective stress in the soil for the hydrostatic condition is compared with analytical solution, first without considering $F_{porosity}$ and then considering this term using linear shape functions and finally using third order B-spline shape functions. This is done for three different cases, namely when the boundary between free water and porous medium is sharp (Figure 2), when one element is used as transition (Figure 3) and when two elements are used as transition at the boundary where the porosity is decreased from 1 in free water to 0.4 in soil. As can be seen in the figures the pressure in free water matches well with the analytical solution in all cases. The oscillation at the boundary decreases by using B-spline function as well as using a transition zone between the free water and biphasic medium. The method will be used to simulate the hydraulic heave phenomenon and the results will be compared to analytical solutions and experimental investigations which will be shown in the presentation at the conference.

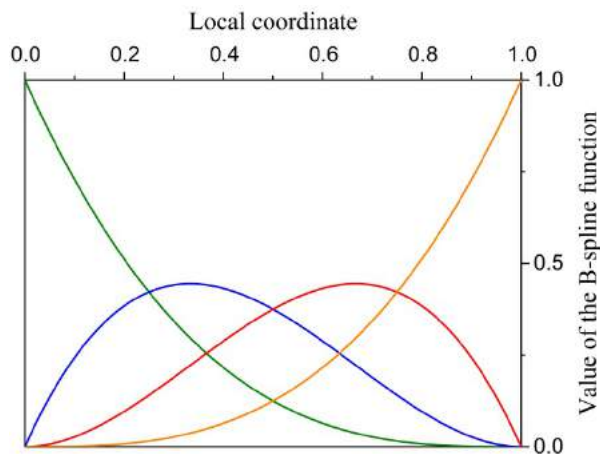


Figure 1: Third order B-spline functions

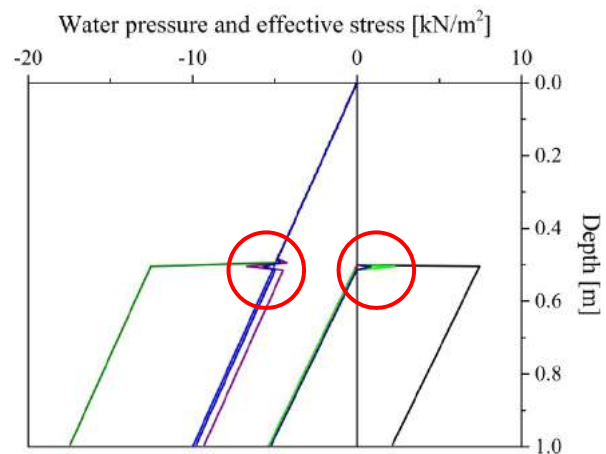


Figure 2: Sharp boundary

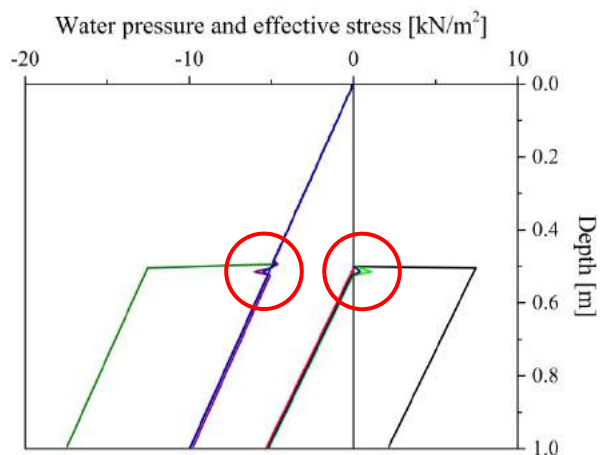


Figure 3: One element transition

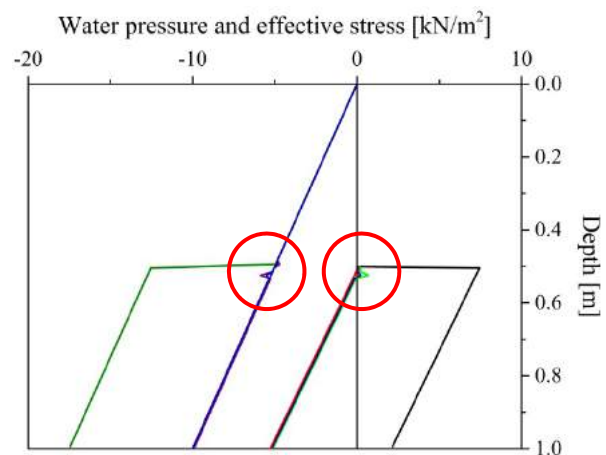
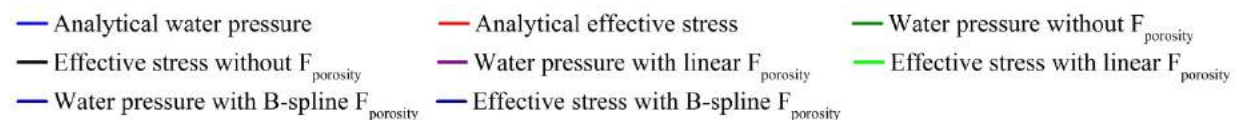


Figure 4: Two elements transition



5. References

- [1] Al-Kafaji, I.K.J. (2013). *Formulation of a dynamic Material Point Method (MPM) for geomechanical problems*. Institute of geotechnical engineering (IGS), University of Stuttgart.
- [2] Bandara, S.S. (2013). *Material Point Method to simulate Large Deformation Problems in Fluid-saturated Granular Medium*. University of Cambridge.

SIMULATION OF VIBRATORY DRIVEN PILES WITH THE AXISYMMETRIC MATERIAL POINT METHOD

V. Galavi¹, M. Martinelli¹, F.S. Tehrani¹, A. Elkadi¹ and D. Luger¹

¹ *Deltares, Geo-Engineering section, The Netherlands*

1. Introduction

The pile installation leads to significant changes in soil structure and soil state (void ratio and stress state) in the vicinity of piles which affects their lateral and axial bearing capacity. A good understanding of the effect of pile installation on the bearing capacity is expected to reduce costs in the construction of both off-shore and on-shore foundations. A proper numerical tool for simulating pile installations would allow assessing installation time, pile refusal probability and material fatigue which are important factors in the reduction of costs. The effect of pile installation cannot be considered using common numerical simulation methods (*e.g.* Finite Element Method) as it involves modeling of large deformations which is problematic. The Material Point Method (MPM) was introduced by Sulsky et al. [4] for solving problems in which large deformations are involved. The method can be considered as an extension of the Updated Lagrangian Finite Element Method (UL-FEM). In order to prevent mesh distortion, associated with the Lagrangian method, all computational data including stresses and state variables are stored in material points, which move through the Eulerian mesh at the end of each computational step. In this way, the method benefits from the advantages of both Lagrangian and Eulerian methods, while preventing the disadvantages of those methods, namely the mesh distortion in the Lagrangian method and the difficulty in tracking of state variables in history dependent materials in the Eulerian method. Extra calculation steps introduced in the MPM, compared to the UL-FEM, make the method computationally expensive. Furthermore, in order to properly describe the mechanical behaviour of soils, highly nonlinear material models are needed which makes the method more expensive. For axisymmetric large deformation problems, such as installation of piles with circular cross-sections, the 3-dimensional formulation of the method can be simplified to a less expensive 2-dimensional axisymmetric form. In this paper, a 2-dimensional axisymmetric formulation of the Material Point Method, which is implemented in an in-house MPM code [1], is used to simulate a series of pile installations under cyclic loading in centrifuge. The quality of the simulation is assessed by comparing the results of the numerical simulation to the results of the physical modelling.

2. Numerical and physical modelling

The experimental set-up is shown in Figure 1. The tests were carried out in a 0.6 m diameter and 0.79 m tall steel sand-filled container. The Baskarp sand was used for the tests. The basic soil parameters of the sand and the full description of the tests can be found in [2]. The hypoplastic model [3] is used to describe the mechanical behavior of the sand using MPM.

The cone penetrometer is initially wished in placed at the depth of $10D = 0.113$ m below the ground surface. The cone penetrator is then pushed into the sand using the following cyclic prescribed displacement with $v_0 = 1$ mm/s and $A = 0.25$ mm:

$$u = v_0 t - A \sin(2\pi t) \quad (1)$$

The comparison of the numerical and the experimental results is shown in Figure 2 for two samples, namely a loose sample ($R_D = 37.5\%$) and a dense sample ($R_D=65.5\%$).

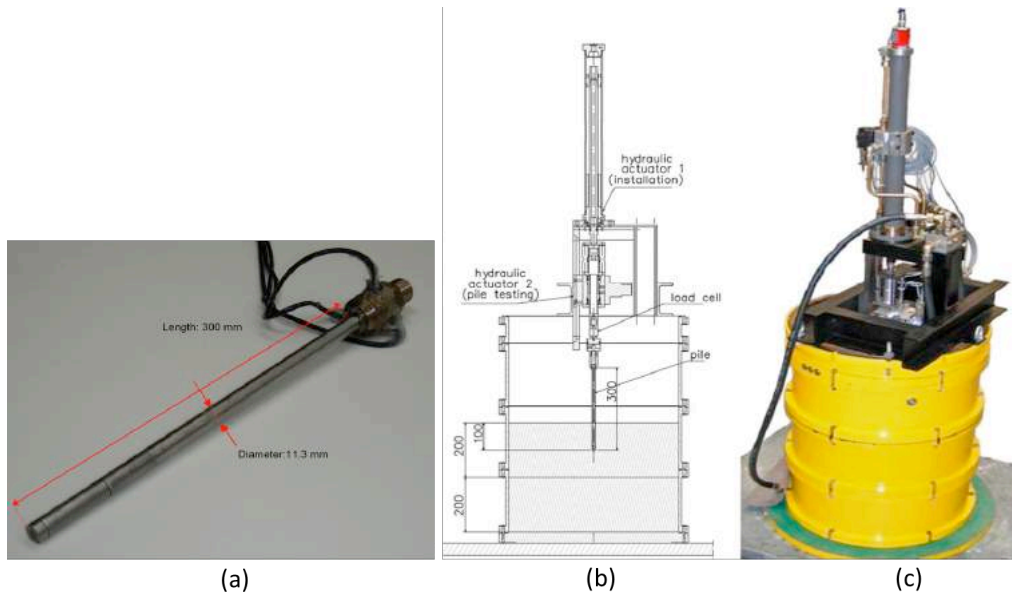


Figure 1. Test set-up; a) dimensions of cone penetrometer; b) dimensions of centrifuge test set-up; c) Photograph centrifuge test set-up

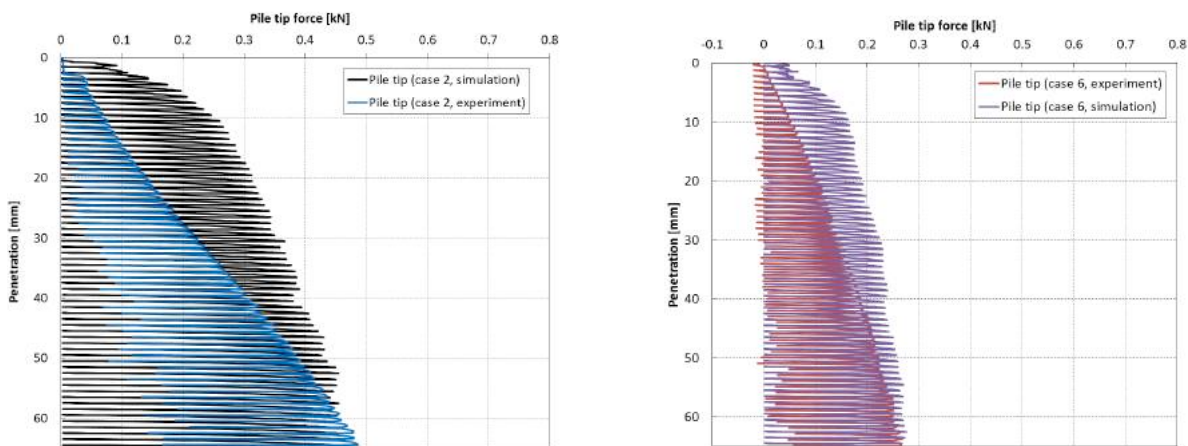


Figure 2. Comparisons of the numerical simulations to the experimental tests; Left: $R_D=65.3\%$; Right: $R_D=37.5\%$.

5. References

- [1] Galavi, V., Tehrani, F.S., Martinelli, M., Elkadi, A.S. & Luger, D. (2018). Axisymmetric formulation of the material point method for geotechnical engineering applications. 9th European Conference on Numerical Methods in Geotechnical Engineering (NUMGE18). Accepted.
- [2] Stoevelaar, R, Bezuijen, A., Lottum, H. van & Tol, A.F. van, (2011). Effects of crushing on point bearing capacity in sand tested in a geotechnical centrifuge. 15th European Conf. ISSMGE, Athens. Proceedings, vol. 2, pp. 939-944.
- [3] Von Wolffersdorf, P. A hypoplastic relation for granular materials with a predefined limit state surface. *Mechanics of cohesive-frictional materials*, 1 (1996), 251-271.
- [4] Sulsky D., Chen Z. & Schreyer H. L. (1994). A particle method for history-dependent materials. *Computer Methods in Applied Mechanics and Engineering*, 118(1-2) (1994), 179–196.

ISOGOMETRIC BOUNDARY ELEMENT ANALYSIS OF UNDERGROUND EXCAVATIONS CONSIDERING EFFECTS OF GEOLOGY

G. Beer¹ and Ch. Duenser¹

¹ *Institute for Structural Analysis, TU Graz, Austria*

1. General

The Boundary Element Method (BEM) is ideally suited for underground excavation problems because the infinite domain can be explicitly considered. Isogeometric concepts have been introduced into the Boundary Element Method (IGABEM) in recent years and this has resulted in a more accurate description of the geometry and more accurate simulations with fewer unknowns. This is because of the unique features of the NURBS patches, which allow smooth geometries to be defined with few parameters. The aim of the current paper is to show how geological features can be incorporated in the analysis without generating a mesh. Geological inclusions are defined by bounding NURBS patches and a linear interpolation between them. The inclusions can have material properties different to the infinite domain and can also exhibit nonlinear material behaviour.

2. IGABEM with inclusions

Details of the implementation of the IGABEM with inclusions have been presented elsewhere [1],[2]. The effect of inclusions is considered via body forces. These give rise to volume integrals, which are dealt with in an innovative way. The result is that a simulation can be carried out without mesh generation. For the approximation of the unknowns we use a geometry independent field approximation, meaning that the description of the geometry remains unchanged while the approximation is refined.

3. Results

Results of test examples, which prove the accuracy of the proposed method are being reported elsewhere [3]. Here we revisit a 3-D simulation, which was carried out some time ago with the coupled Finite Element/Boundary Element program BEFE reported in [4]. The example relates to the simulation of the Masjed cavern in southern Iran. A cross-section showing the final excavation geometry and the geology is shown in Figure 1. The properties of the mudstone layers, which were considered in the simulation, are shown in Table 1. The compressive virgin stresses were assumed to be $\sigma_{z0} = 0.027 \times \text{depth}$ MPa and $\sigma_{x0} = \sigma_{y0} = 0.5 \times \sigma_{z0}$, the depth on the top of the cavern being 310 m. Figure 1 on the right shows the definition of the geometry of the cavern and of the inclusions by finite and infinite NURBS patches. Only 9 control points were required to exactly specify the geometry of the cavern in one section. The simulation has only 192 degrees of freedom. The results

	Modulus	Poisson's ratio	Yield condition
Rock mass	10 GPa	0.2	elastic
Inclusions	6 GPa	0.25	Mohr-Coulomb ($\phi = 30^\circ$, $c=0.73$ MPa, $\psi = 0$)

Table 1. Properties

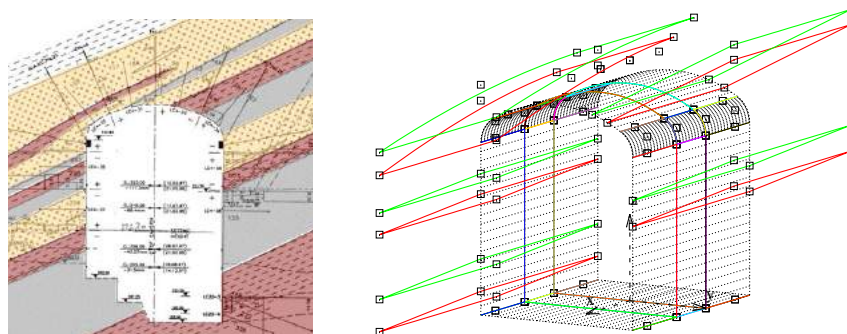


Figure 1. Masjed cavern: Geology (left) and Definition of geometry and inclusions with NURBS patches (right). Control points are depicted by hollow squares.

were compared with the BEFE simulation which has over 4000 degrees of freedom. Figure 2 shows a comparison of the displaced shape. The maximum downward displacement of the BEFE analysis was 0.0248 m and of the current analysis 0.0245 m.

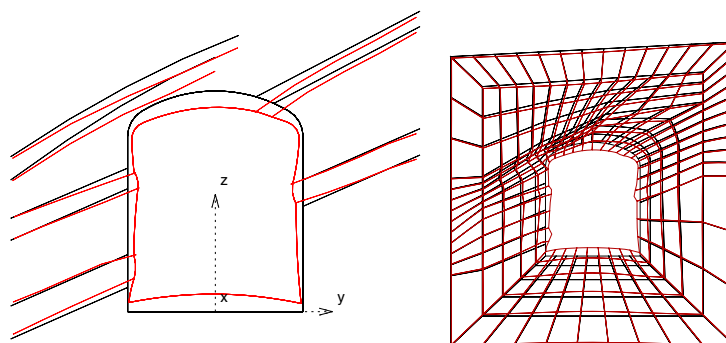


Figure 2. Masjed cavern: Comparison of displacements. Left IGABEM, right BEFE

4. Summary and Conclusions

A novel approach has been presented for the 3-D simulation of underground excavations without the requirement of mesh generation. Geometrical data can be taken directly from a CAD program and no refinement of the geometry is required. The approximation of the unknowns is achieved via the refinement options available for NURBS. Good agreement with a coupled analysis was found.

References

- [1] Beer, G., Marussig, B., Zechner, J., Duenser, C., and Fries, T.-P. (2016). Isogeometric Boundary Element Analysis with elasto-plastic inclusions. Part 1: plane problems. *Computer Methods in Applied Mechanics and Engineering*, **308**, 552–570.
- [2] Beer, G., Mallardo, V., Ruocco, E., Marussig, B., Zechner, J., Duenser, C., and Fries, T. P. (2017). Isogeometric Boundary Element Analysis with elasto-plastic inclusions. Part 2: 3-D problems. *Computer Methods in Applied Mechanics and Engineering*, **315**, 418–433.
- [3] Beer, G. and Duenser, C. (2018). Advanced 3-D Boundary Element analysis of underground excavations. *Computers and Geotechnics*, **submitted**.
- [4] Beer, G., Smith, I., and Duenser, C. (2008). *The Boundary Element Method with Programming*. Springer.

NUMERICAL ANISOTROPIC MODELLING OF A DEEP DRIFT AT THE MEUSE/Haute-Marne URL

E. D. Coarita-Tintaya^{1,2}, M. Souley¹, M. N. Vu³ and F. Golfier²

¹ INERIS, Ecole des Mines, Campus ARTEM, 54042 Nancy, France

² Université de Lorraine, CNRS, GeoRessources, F-54000 Nancy, France

³ Andra R&D, 92298 Châtenay - Malabry, France

Abstract

The development of nuclear energy raised the issue of radioactive waste disposal in deep geological formations. Clay formations in their natural state show very favorable confining conditions as repositories for radioactive waste due to their generally low values of hydraulic conductivity and significant retention capacity for radionuclides. Three clay formations in Europe are currently being studied in details as potential host rocks for high level radioactive waste disposal, i.e. the Boom Clay in Belgium, the Opalinus Clay in Switzerland and the Callovo-Oxfordian Claystone (COx) in France. Lastly, the French national radioactive waste management agency (Andra) started building the underground research laboratory (URL) at Bure in the Meuse district. Several specific in situ experiments were carried out with the main objectives in term of underground civil engineering to: (a) evaluate the geological environment of the future Deep Geological Repository (DGR), (b) collect data from the clay formation in order to assess the performances of the future DGR, (c) test and demonstrate the feasibility of the future DGR. The feedback of these experiments and in situ measurements as well as the numerous theoretical analyzes and numerical modeling works undertaken on the COx allowed to identify the key mechanisms (mainly in the framework of THM processes) governing the behavior of the COx [1]. In addition to the THM processes and the associated parameters, it appears necessary to consider the anisotropies (mechanical, hydraulic and thermal) of such rock, but also its time-dependent behavior. This paper deals with these issues.

Saturated hydromechanical coupling was investigated on a circular experimental gallery of radius 2.6 m (GCS drift) excavated following the principal major stress and without rigid lining at the URL. The plane strain assumption is considered. Then a cross section of the GCS drift with a drainage condition along its wall, was modeled with COMSOL Multiphysics software. The initial pore pressure and in situ stress fields at the main level (-490 m) are given in figure 1. The model geometry and the poromechanical properties are presented in figure 1 and table 1, respectively. For simplicity, the creep of COx is described by a power law ($A=1.26 \times 10^{-26} \text{ Pa}^{1/n} \text{ s}^{-1}$ and $n=1.98$).

The instantaneous ($t=0+$) response induced by excavation leads to overpressures with a maximum value of 1.3 MPa in the horizontal direction (i.e. direction of initial minor stress) and underpressures in the vertical direction (i.e. direction of initial major stress) with respect to the GCS section (figure 2). These pore pressure distributions are in good agreement with a poroelastic analysis presented by [2]. Moreover, with time and in the horizontal direction, the pressure peak, shift towards the interior of the rock mass and decreasing with time at a very small rate due to the low permeability of the COx. This remains in agreement with the in-situ observations [3].

It is observed that the evolution of the pore pressure around drift, is not influenced by creeping (figure 2), in accordance with the creep model used (not dependent on the mean stress). Conversely, the creep relaxes the von Mises stress until a distance of 2 diameters (depending on the used creep model and associated parameters) from the wall (figure 3 b) at 100 years. The radial displacement (figure 3 a) highlights a significant increase in magnitude from 10 years. These results will be compared with the in-situ measurements.

Parameter	Unit	Value
E_x / E_y	(GPa)	5.2 / 4
ν_{xz} / ν_{yx}	(-)	0.2 / 0.3
G_{xy}	(MPa)	1740
b	(-)	0.6
k_x / k_y	(m^2)	4/1.33 ($\times 10^{-20}$)
ϕ_0	(-)	0.18

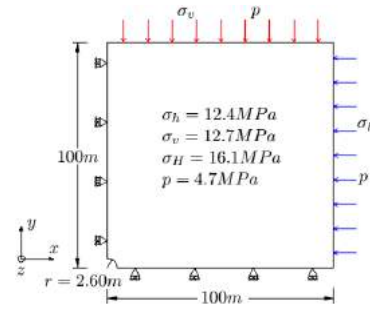


Table 1. Poromechanical properties.

Figure 1. Geometry and boundary conditions.

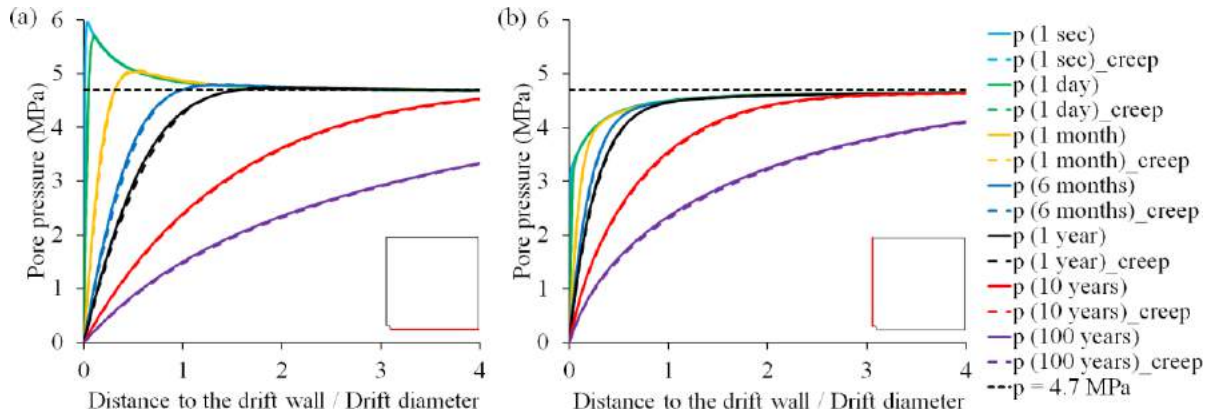


Figure 2. Pore pressure profiles (a) horizontal direction (b) vertical direction (continue = proelastic, dashed = poroviscoplastic).

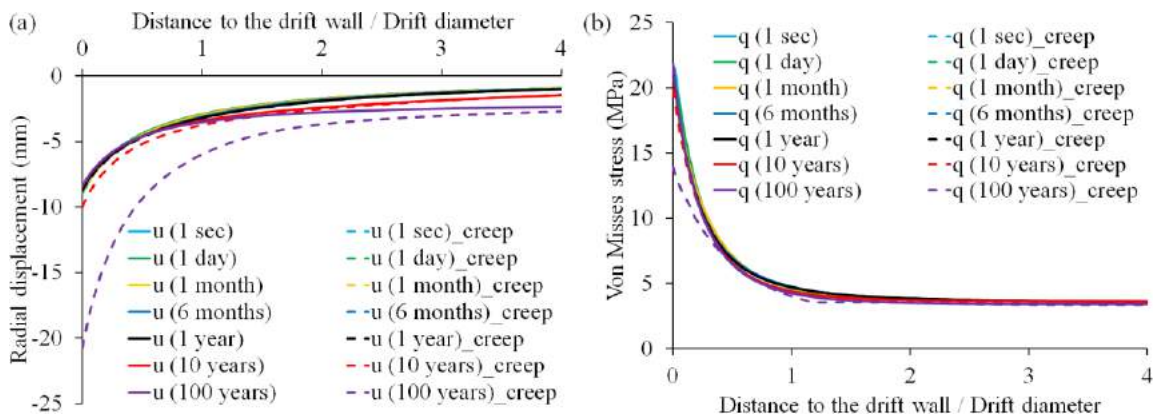


Figure 3. (a) Radial displacement and (b) von Mises stress in the horizontal direction (continue = proelastic, dashed = poroviscoplastic).

References

- [1] Armand, G., Conil, N., Talandier, J., and Seyedi, D.M. (2017). Fundamental aspects of the hydromechanical behavior of Callovo-Oxfordian claystone: From experimental studies to model calibration and validation. *Computers and Geotechnics*, **85**, 277–286.
- [2] Guayacán-Carrillo, L., Ghabezloo, S., Sulem, J., Seyedi, D.M., and Armand, G. (2017). Effect of anisotropy and hydro-mechanical couplings on pore pressure evolution during tunnel excavation in low-permeability ground. *Int. J. of Rock Mech. and Min. Sci.*, **97**, 1-14.
- [3] Seyedi, D.M., Armand, G., and Noiret, A. (2017). “Transverse Action” – A model benchmark exercise for numerical analysis of the Callovo-Oxfordian claystone hydromechanical response to excavation operations. *Computers and Geotechnics*, **85**, 287–305.

A MACROELEMENT FOR COUPLED ANALYSIS OF THE MECHANICAL RESPONSE OF DEEP TUNNEL FRONTS IN COHESIVE SOILS

C. di Prisco¹ and L. Flessati¹

¹ *Politecnico di Milano, Milano, Italy*

1. Introduction

The macroelement (ME) approach, commonly employed to study soil-structure interaction problems, stems from the aim of describing the global response of a complex system by means of a single upscaled constitutive relationship, relating generalized forces and displacements. In this work, a new generalized non-dimensional strain hardening elastic-plastic constitutive relationship aimed at simulating the mechanical response of deep tunnel fronts in cohesive soils is presented. As is well-known, this problem is governed by the consolidation process taking place in the soil domain: the system response is severely affected by the excavation rate and during front standstill the front displacements progressively increase with time. The authors employed the results of a series of non-linear 3D FEM numerical analyses ([1]) to conceive and to calibrate a new constitutive relationship. To take into account the consolidation process in the constitutive law, the authors defined a “generalized effective stress principle” and introduced in the constitutive relationship the dependence on a suitably defined non-dimensional time. The model is capable of reproducing satisfactorily both the influence of the excavation rate on the system response and the increment of the front displacements during front standstill.

2. Model definition

By following the approach proposed in [1] and [2], the excavation process is modelled as a reduction in the pressure applied on the tunnel front and the mechanical response of the front is summarized by employing the front characteristic curve, relating the average front displacements (u_f) and the average stress applied to the front (σ_f). According to [1] and [2], it is convenient to analyse the hydro/mechanical coupled response of the front by employing three non-dimensional variables: a non-dimensional generalized stress (Q_f), a non-dimensional generalized strain (q_f) and a non-dimensional time (T), defined as:

$$Q_f = \left(1 - \frac{\sigma_f}{\sigma_{f0}}\right) \frac{\sigma_{f0}}{S_u^*} \quad q_f = \frac{u_f}{u_{fr,elu}} \frac{\sigma_{f0}}{S_u^*} \quad T = \frac{kKt}{\gamma_w D^2}, \quad (1)$$

where σ_{f0} is the initial value of σ_f , S_u^* a suitably defined equivalent undrained strength for the system ([1]), $u_{fr,elu}$ the elastic residual (for $\sigma_f = 0$) displacement under undrained conditions ([2]), t is the time, k the soil permeability, K the soil elastic volumetric stiffness, γ_w the water unit weight and D the tunnel diameter, respectively.

The 1D constitutive relationship conceived by the authors is formulated by employing Q_f , q_f and T . For the sake of clarity, a rheological model schematizing the constitutive relationship is reported in Figure 1a. The model is divided in two main parts put in series: (i) the elastic spring and the plastic slider define the undrained response and (ii) the viscous damper in parallel with another elastic spring and another plastic slider define the increment in the front displacement induced by the dissipation of the excess pore water pressure.

Owing to the definition of Q_f and q_f , the stiffness of the undrained elastic spring is equal to 1. To describe the undrained plastic response, the yield function (f_u) and the hardening rule are respectively defined as:

$$f_u = Q_f - Q_{fu} \quad \dot{Q}_{fu} = \frac{\dot{q}_{fu}^{pl}}{e^{Q_f/a_u - 1} - 1} \quad (2)$$

where Q_{fu} is the hardening variable, a_u a constitutive parameter and dots represent the derivative with respect to T . a_u is calibrated on the undrained ($T = 0$) numerical results ([2]). The initial Q_{fu} value is assumed equal to a_u ([1]).

In the lower in parallel part of the rheological model, the (total) generalized stress Q_f is subdivided in two parts: Q' acts the spring and on the slider, whereas U acts on the damper. The stiffness of the drained elastic spring K_d^{el} is calculated from the drained numerical results of [1]. The yield function (f_d) and the hardening rule are respectively defined as:

$$f_d = Q'_f - Q_{fd} \quad \dot{Q}_{fd} = a_d \left(\frac{Q_L - Q_{fd}}{Q_L} \right) \dot{q}_{fd}^{pl} + b_d \dot{q}_{fu}^{pl} \quad (3)$$

where Q_{fd} is the hardening variable, Q_L , a_d and b_d are constitutive parameters: Q_L represent the limit load of the system under drained conditions ([1]), whereas a_d and b_d are calibrated on the drained ($T \rightarrow +\infty$) numerical results of [1]. The initial Q_{fd} value is obtained from the numerical results of [1]. The viscous damper constitutive relationship is defined:

$$U = \eta \dot{q}_{fd}^{pl} \quad (4)$$

where parameter η is calibrated on a numerical “partially drained” characteristic curve ([1]).

The model is capable of reproducing both (i) the front response for different unloading rates (in Figure 1b the FEM characteristic curves are compared with the ones obtained with the ME) and (ii) a stable ($Q_f < Q_L$) front standstill and an unstable ($Q_f > Q_L$) front standstill (Figure 1c).

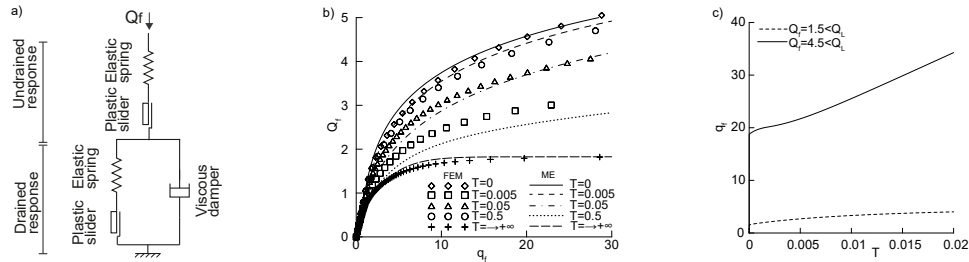


Figure 1. a) Rheological model, b) comparison between the numerical (FEM) and the macroelement (ME) front characteristic curve and c) stable and unstable front standstill

3. Concluding remarks

In this paper the authors present a new generalized strain hardening constitutive relationship to reproduce the hydro/mechanical coupled response of deep tunnel fronts in cohesive soils. The constitutive relationship parameters are calibrated on FEM numerical results and the agreement is very satisfactory.

References

- [1] di Prisco, C. and Flessati (2018). A numerical tool for estimating deep tunnel front displacements: the role of the excavation rate in cohesive soils. *Acta Geotechnica*, Submitted for publication.
- [2] di Prisco, C., Flessati, L., Frigerio, G., and Lunardi, P. (2017). A numerical exercise for the definition under undrained conditions of the deep tunnel front characteristic curve. *Acta Geotechnica*, pp. 1–15.

EULERIAN ANALYSIS OF TUNNEL EXCAVATION WITH AN EPB SHIELD

N. Losacco¹, G.M.B. Viggiani² and D. Branque³

¹ Università degli studi di Roma 'Tor Vergata', Rome, Italy

² University of Cambridge, Cambridge, UK

³ Université de Lyon, ENTPE, Lyon, France

1. Introduction

In this work the excavation of a tunnel with an EPB shield is simulated in an Eulerian framework: the tunnelling machine is fixed in space, while the soil flows around and through it. The excavation advance is simulated as a continuous process, with the face support pressure constantly applied at the machine head, as opposed to the commonly employed step-by-step approach in which a slice of elements ahead of the shield is removed at each analysis increment. The back of the pressure chamber is also an eulerian boundary, through which the soil can flow out of the FE domain. Different excavation regimes can be simulated by varying the mass outflow of soil through this boundary and the advance speed of the excavation, hence different face support pressures are obtained as an output of the analyses.

The analyses are carried out using the Arbitrary Lagrangian-Eulerian (ALE) method [1] implemented in the Abaqus FE program; this allows the material to move independently of the nodes, which in turn are moved in order to reduce mesh distortion and capture the highest solution gradients. The results obtained with the proposed method are compared qualitatively with the experimental data of a small-scale model of tunnel excavation in sand set up at the ENTPE in Lyon [2]. Given the high computational cost and the scarce scalability of the ALE implementation in Abaqus, parametric analyses were only carried out in plane strain, for a longitudinal section of the problem.

2. Numerical models and results

Figure 1 shows a scheme of the plane strain model used for parametric analyses. As stationary conditions are sought, excavation of in an infinite domain is simulated by allowing the soil to flow into and out of the sides of the mesh, located far from the excavation head. A constant velocity is prescribed at the right inflow boundary, to simulate the advancement of the shield, while constant pressure is applied at the opposite outflow boundary. Under-, over- or balanced excavation conditions are obtained by changing the outflow velocity inside the shield, corresponding to a mass flow 10% larger, 10% smaller or equal to the nominal excavation rate, respectively. The EPB shield is modelled as an analytical surface; a no-penetration, perfectly smooth contact is enforced with the surrounding soil. A simple linear elastic-perfectly plastic material law with a Mohr-Coulomb yield surface is used for the sand.

The 3D model aims at reproducing the experimental results obtained at the ENTPE. The initial configuration of the mesh is depicted in Figure 2. In this case the front and the rear sides of the mesh are lagrangian boundaries, i.e. they cannot be crossed by the soil, representing the walls of the steel box in which the excavation is carried out.

For the plane strain analyses, Figure 3 shows settlements of the soil surface, normalised with respect to the maximum settlement obtained in the balanced case. As expected, the settlements predicted for over-excavation are always larger than for balanced conditions. On the contrary, for under-excavation the settlement profile exhibits some uplift ahead of the tunnel face and smaller settlements up to 1D behind it. The same settlements as for the balanced excavation case are recovered at further distance; this is possibly due to large tensile strains developing at the soil surface behind the head of the EPB shield for large applied face pressure, as observed in [3].

The predicted longitudinal settlement trough in the 3D model is plotted in Figure 4 and compared with the measurements of the experiment. The numerical results agree fairly with the experimental data, especially in the early stages of the test. After approximately half of the maximum excavation advancement, the numerical longitudinal trough is shifted upwards as heave develops progressively ahead of the excavation face. Consequently, the settlements in the transverse monitoring sections are underpredicted by as much as 70%. This might be ascribed to the concurrent effect of the front boundary and of the simple linear elastic-perfectly plastic constitutive model used for the soil.

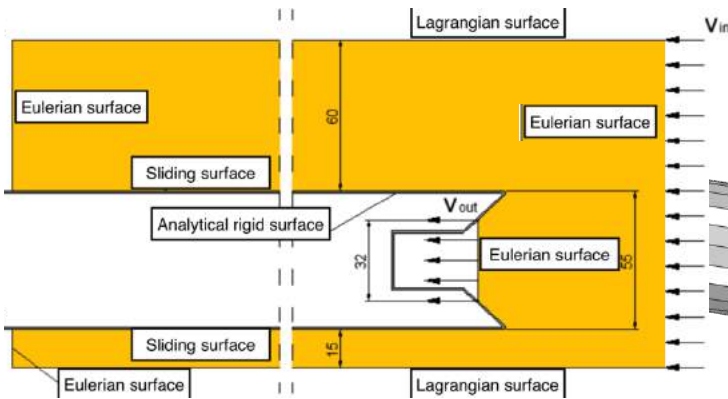


Figure 1. 2D model: scheme

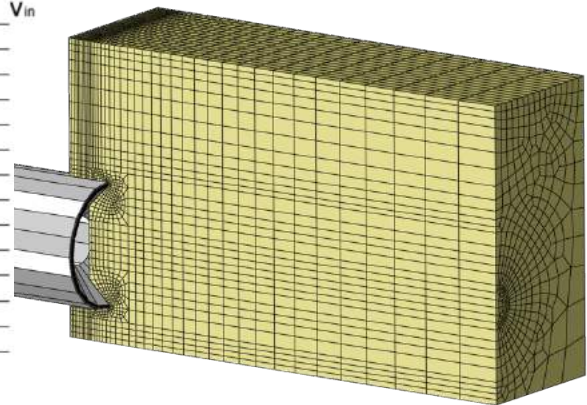


Figure 2. 3D model: initial mesh

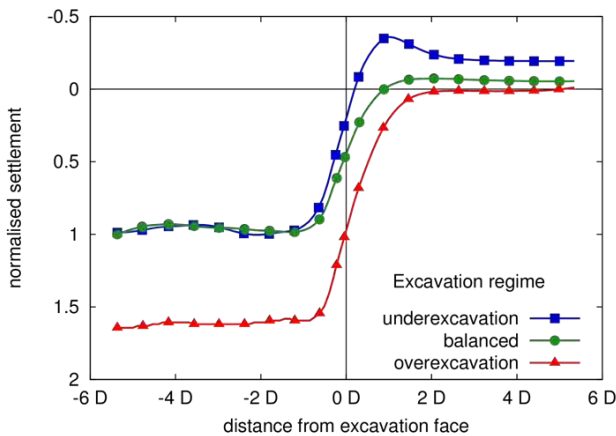


Figure 3. 2D model: effect of excavation regime.

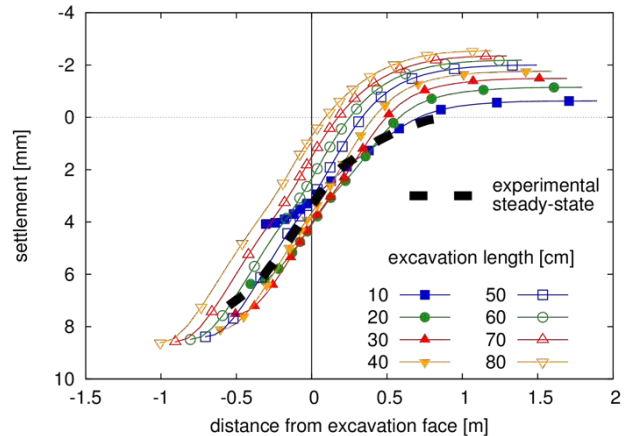


Figure 4. 3D model: evolution of settlement trough

3. References

- [1] Donea, J., Huerta, A., Ponthot, J.Ph. & Ferran, A.R., 2004, "Chapter 14: Arbitrary Lagrangian–Eulerian Methods", Encyclopedia of Computational Mechanics, Edited by Erwin Stein, René de Borst and Thomas JR Hughes. Volume 1: Fundamentals. John Wiley & Sons, Ltd.
- [2] Bel, J., Branque, D., Wong, H., Viggiani, G.M.B. & Losacco, N. (2015) Experimental study on a 1g reduced scale model of TBM: impact of tunnelling on piled structures. In: Geotechnical Engineering for Infrastructure and Development. pp 413–418.
- [3] Berthoz, N., Branque, D., Wong, H., Subrin, D. (2018) TBM soft ground interaction: Experimental study on a 1 g reduced-scale EPBS model. Tunnelling and Underground Space Technology 72:189–209 . doi: 10.1016/j.tust.2017.11.022

DEVELOPMENT OF A DEEP-LEARNING BASED AUTOMATIC TUNNEL INCIDENT DETECTION SYSTEM ON CCTVS

Kyu-Beom Lee¹, Hyu-Soung Shin² and Dong-Gyou Kim³

¹ Student Researcher, Geotechnical Engineering Research Institute, Korea Institute of Civil Engineering and Building Technology (KICT) & Integrated PhD student, Geospace Engineering Department, University of Science & Technology (UST)

² Head, Extreme Construction Research Center, Korea Institute of Civil Engineering and Building Technology (KICT), hyushin@kict.re.kr (corresponding author)

³ Research Fellow, Geotechnical Engineering Research Institute, Korea Institute of Civil Engineering and Building Technology (KICT)

Significance of an early detection for un-usual events or happenings in tunnels, which could lead to bigger secondary disasters, has been grown up to dates. Therefore, CCTVs have been installed in tunnels and automatic detection systems on the CCTVs have been operated in a part of the tunnel sites with the CCTVs. Despite of this, it is noticed that current algorithm-based incident detection systems under operation show very low detectable rates by less than 50%. The putative major reasons seem to be (1) very weak intensity of illumination (2) dust in tunnel (3) limited installation height of CCTV to about 3.5m, etc. Therefore, an attempt in this study is made to develop an **AI deep-learning based tunnel incident detection system**, which is relatively insensitive to very poor tunnel conditions. A **Faster R-CNN** as a deep-learning algorithm is adopted for a tunnel video incident detection system (Shin et. al., 2017).

According to the Korean hazard mitigation guideline (MOLIT, 2016), automatic tunnel incident detection system must detect 4 events taking place in tunnel as shown Fig 1. Its theoretical background is given and validation tests for object detection are undertaken on the 3 target object classes such as car, person and fire to be detected. The detected object ‘car’, which means we obtain the position and size of the ‘car’ object, is used for calculating a moving vector of the car with the position inferred on the previous image frame. Then the critical events on the car, collision or stop, and reverse driving are easily determined by the moving vector.

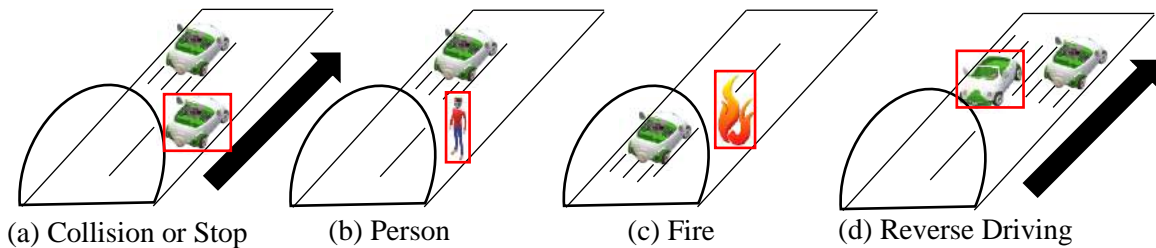


Fig 1. Incidents in tunnel to be detected officially due to the Korean hazard mitigation guideline

Faster R-CNN is not logic-based algorithm but an AI based trainable model (Ren et. al., 2016). In order to detect 3 target object classes such as car, person and fire, the Faster R-CNN must train a dataset composed of pairs of an image with object(s) and corresponding a label file in which there are text line(s) being defined by coordinates of bound box of the object(s) and event class(es) such as ‘car’, ‘person’, etc. shown in Fig 1. Then the trained model can be used for detecting object(s) and corresponding event class(es) on CCTV images in real time. Those processes are shown in Fig 2.

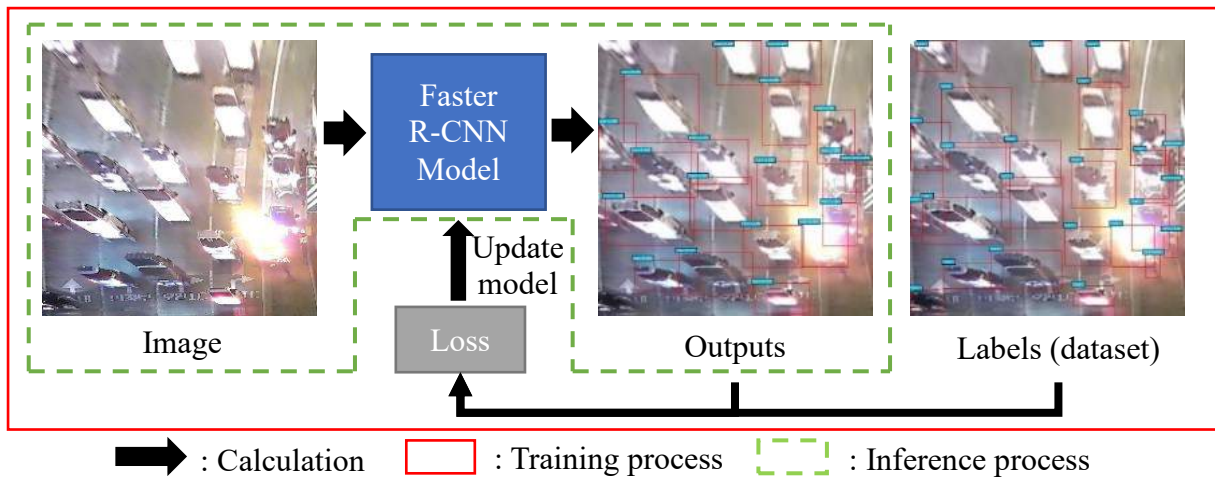


Fig 2. Faster R-CNN Object Detection Network's Training & Inference process

For validation of the suggested system with a set of real CCTV images, Two validation models for (1) 'car' and 'person' detection and (2) 'fire' detection, were separately set up because there were no video images available in containing of all the events on the same image. Also, 'fire' event shows an image feature similar to other vehicle head/tail lights and other electric lights in tunnels. But the both features, 'fire' and other vehicle/electric lights, should be clearly separated in automatic object detection.

In validation model for 'car' and 'person' detection, two scenarios are set up: (1) training and prediction in the same tunnel (2) training in a tunnel and prediction in the other tunnel. From the both cases, targeted object detection in prediction mode are well achieved to detectable rate to higher than 90% in case of similar time period between training and prediction but it shows a bit low detectable rate to 40%.

For validation on 'fire' detection, a dataset of 'fire' only images without any other electric light was used for training and validation of the trained model. The trained model with 'fire' objects showed almost perfect inference capacity to 100% accuracy even for untrained 'fire' images. However, when another image dataset consisting of 'fire' as well as other many vehicle/electric lights was used for training of 'fire' objects only and validation, many of electric lights were detected as 'fire' objects which are wrong detection. It means that the trained model with only 'fire' objects is hard to separate light objects similar to 'fire' in image. Therefore, a new attempt was taken for defining the 'lights' as a target object which have then been trained with 'fire' objects. The result show a great enhancement in detection of 'fire' to 85% accuracy in detection of un-trained 'fire' objects. This validation test indicates that extra definition of similar 'objects', which however should be separated, could greatly assist enhancement of detection for the target object. And also it is believed that the AI based system would enhance its predictability automatically as further training are followed with accumulated CCTV BigData without any revision or calibration of the incident detection system.

References

- [1] Ren, S., He, K., Girshick, R., & Sun, J. (2015). Faster R-CNN: Towards real-time object detection with region proposal networks. In *Advances in neural information processing systems*. 91-99.
- [2] Shin, H.S., Lee, K.B., Yim, M.J. & Kim, D.K. (2017). Development of a deep-learning based tunnel incident detection system on CCTVs. *Journal of Korean Tunnelling and Underground Space Association.*, **19**, 915–936.
- [3] Ministry of Land, Infrastructure and Transport (MOLIT) (2016). Guideline of installation and management of disaster prevention facilities on road tunnels.

NUMERICAL ANALYSIS OF SOIL PENETRATION WITH ADVANCED EFFECTIVE STRESS SOIL MODELS

Z.Y. Orazalin¹, A.J. Whittle²

¹ *Singapore-MIT Alliance for Research and Technology, Singapore*

² *Massachusetts Institute of Technology, Cambridge, MA, USA*

1. Introduction

The numerical simulations of piezocone soil penetration tests are generally challenging due to large deformations, the complex constitutive behavior of soils, various drainage conditions and soil-penetrometer contact interactions. Most prior research on cone penetration using large deformation finite element method has usually been limited to simplified assumptions on drainage conditions and constitutive behavior. This research focuses on the piezocone penetration tests in soft soils over a range of steady penetration velocities (considering the effects of partial drainage) and a methodology for performing realistic numerical simulations of large deformation, quasi-static soil penetration using advanced effective stress soil models.

2. Methodology

Following earlier work by Hu & Randolph (1998), we propose a finite element (FE) analysis procedure using automated remeshing and solution mapping through a Python scripting interface within a commercial FE solver (Abaqus/Standard) in order to simulate quasi-static piezocone penetration using advanced effective stress soil models. The numerical analysis consists of a series of conventional Lagrangian Finite Element analysis steps, followed by a complete remeshing of the domain and the interpolation of the solution variables (stresses, pore pressures, state variables, etc.) from the previous mesh. The accuracy of the analysis depends on the success of the interpolation employed to map the solution variables (Fig. 1). This is especially important for complex constitutive soil models with history-dependent state variables.

The main FE model represents a standard piezocone ($R = 1.78\text{cm}$) moving vertically at specified displacement rate, v , within a homogenous element of soil (0.5m high with radius 0.5m ; i.e., $z/R = 28 = r/R$). The model simulates a calibration chamber configuration (i.e., uniform initial stress state) with an initial vertical effective stress, $\sigma'_{v0} = 100\text{kPa}$ applied as a surcharge at the top surface and K_0 conditions (controlled by stress history). The far boundaries (lateral and base) are free draining (zero excess pore pressures), while the top surface is assumed to be impermeable. The current analyses assume smooth, frictionless contact between the penetrometer and the soil ($\delta = 0^\circ$). The penetrometer is specified as a rigid shell with a rounded tip geometry which approximates the simple pile geometry (Aubeny, 1992).

3. Main Results

The penetration resistance for a piezocone device is analyzed using two elasto-plastic soil models (MCC, MIT-E3) and the recent elasto-viscoplastic soil model capable of describing a rate dependent behavior. The predictions of piezocone penetration using the proposed FE analyses are evaluated through comparison (Fig. 2) with undrained steady state analytical solutions obtained from the Strain Path Method (Aubeny, 1992) and the field measurements from South Boston (Ladd, 1999).

Partial drainage effects are readily simulated in the proposed FE analyses by varying either the penetration rate, hydraulic conductivity or size of the cone. Results in Figure 3 show typical predictions of normalized penetration tip resistance (in the calibration chamber model) using the MCC soil model for normally consolidated BBC at penetration rates varying from $4 \times 10^{-6} - 200\text{cm/s}$.

Each simulation was conducted to a minimum penetration depth, $z/R = 5$ with at least 50 automated re-meshing steps.

The proposed large deformation effective stress penetration analyses provide a framework that can be used to investigate the effects of partial drainage that occurs in piezocone penetration tests for soils of intermediate permeability and the effects of strain rate and stress history in undrained penetration for low permeability clays.

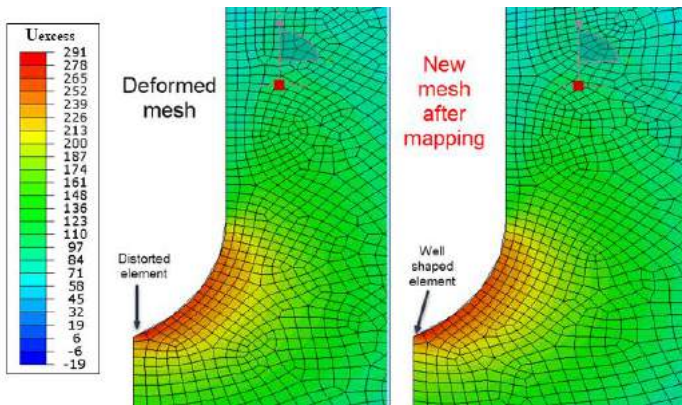


Figure 1: Proposed Procedure - Solution Mapping Example

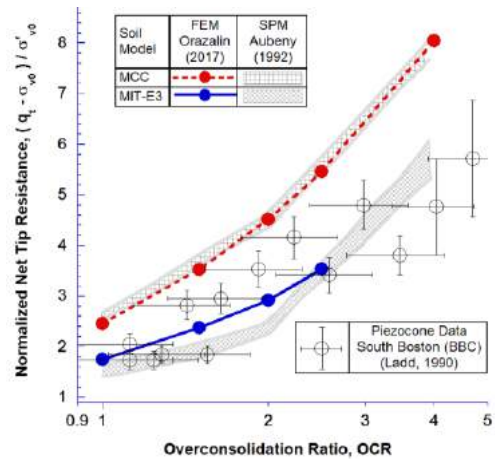


Figure 2. Evaluation of FE predictions of undrained penetration resistance in BBC

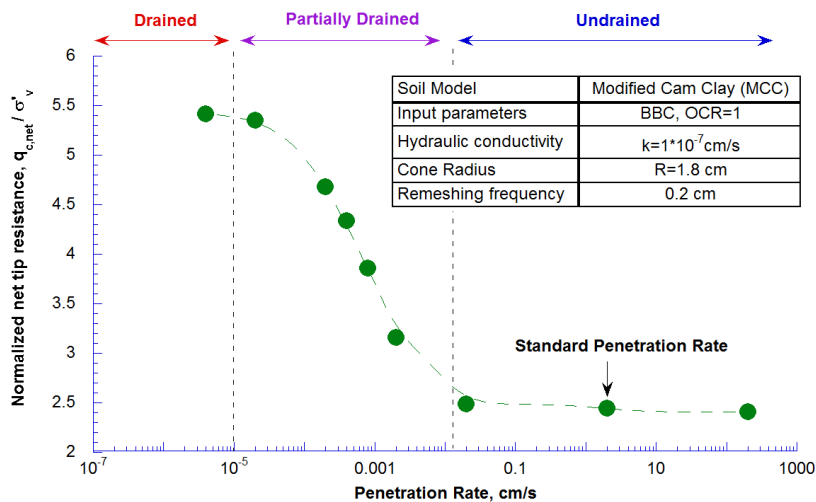


Figure 3. Effect of penetration rate on computed penetration resistance using MCC soil model

4. References

- [1] Aubeny, C.P. 1992. *Rational interpretation of in-situ tests in cohesive soils*. Ph.D. Thesis, Massachusetts Institute of Technology, 433p.
- [2] Hu, Y. & Randolph, M.F. (1998). A practical numerical approach for large deformation problems in soil. *International Journal for Numerical and Analytical Methods in Geomechanics* 22(5): 327-350.
- [3] Ladd, C., Young, G.A., Kraemer, S. & Burke, D. (1999). Engineering properties of Boston Blue Clay from Special Testing Program. In *Special Geotechnical testing: Central Artery/Tunnel Project in Boston, Massachusetts, ASCE GSP 91*, 1–24.
- [4] Orazalin, Z.Y. (2017). *Analysis of large deformation offshore geotechnical problems in soft clay*. Ph.D. Thesis, Massachusetts Institute of Technology, 303p.
- [5] Whittle, A. & Kavvas, M. (1994). Formulation of MIT-E3 constitutive model for overconsolidated clays. *ASCE Journal of Geotechnical Engineering* 120 (1), 173–198.

NUMERICAL MODEL OF FLAT DILATOMETER TEST IN COHESIONLESS SOILS

A. Truty¹ and K. Podles¹

¹ Cracow University of Technology, Cracow, Poland

1. Introduction

Flat dilatometer (DMT) and cone penetration (CPTU) tests are frequently used to assess certain geotechnical parameters of subsoil in the course of designing foundation systems for a wide class of engineering structures. However, parameters deduced from these tests are usually sufficient to calibrate simplest subsoil models ie. elastic ones or at best elasto-plastic in which, behaviour, within the strength envelope, remains linear elastic. In the modern designing of advanced engineering structures (deep excavations, high buildings etc.) it is usually impossible to neglect soil-structure interaction that can efficiently be analyzed with aid of FE software and advanced soil models implemented there. The Hardening Soil (HS) [1, 2] is one of the most efficient soil models in the aforementioned domain. Moreover, its parameters can fully be determined based on properly designed laboratory tests ie. tri-axial CD test (including measurement of shear wave velocity) and oedometer test. Using field test results (DMT and/or CPTU) and artificial neural networks (ANN) trained on the numerically generated DMT and/or CPTU tests to estimate certain HS model parameters (those describing the stiffness are of the major interest), is the main goal of our current research. The idea of using ANN's trained on numerical models of self boring pressuremeter and CPTU field tests, for class of normally consolidated or lightly overconsolidated cohesive soils, to predict Modified Cam-Clay model parameters has been successfully verified by Obrzud et al.[3, 4, 5]. The present study is the first step in this direction and we focus our attention on the initial stress disturbance during DMT blade insertion, and relation between p_o and p_1 readings and membrane deflection, in a normally consolidated sand, described with aid of the HS constitutive model.

2. 3D model of DMT test in sand

Problem of the DMT blade insertion into cohesionless subsoil and then membrane inflation to obtain numerical p_o and p_1 readings is solved with aid of the large strain Updated Lagrangian (UL) FE formulation (8 node F-bar elements are used), following the work by Rodriguez-Ferran et al. [6], and large deformation node-to-segment contact approach after Parisch et al.[7], implemented by the first author in the custom version of ZSoil software. The 3D model of the test is shown in the figure. It is pretty obvious that UL formulation in conjunction with finite elements is not optimal for solving this class of problems. However, with aid of a simple numerical trick, shown in the figure, problems with high mesh distortion can easily be canceled. To reduce size of the numerical model we assume that two symmetry planes exist and on external boundaries of the FE mesh infinite elements are added to simulate unbounded domain. In the analyzed domain body forces are neglected while the initial vertical stress is equal to 100 kPa and initial stress parameter $K_o = 0.5$. HS model parameters used in the simulation are: $E_{ur}^{ref} = 100000$ kPa, $m = 0.5$, $E_{50}^{ref} = 33000$ kPa, $E_{oed}^{ref} = 33000$ kPa, $\phi = 30^\circ$, $\psi = 5^\circ$, $\sigma^{ref} = 100$ kPa and OCR = 1. In this simulation stiffness stress dependency in the HS model is driven by the mean stress p rather than σ_3 . Hence the in situ unloading-reloading stiffness modulus $E_{ur} = E_{ur}^{ref} (p/\sigma^{ref})^m \approx 81650$ kPa. After inserting the blade at depth 25 cm (to cancel boundary effects and reach steady state) the membrane is incrementally loaded by the internal pressure to reach 1.1mm of deflection. The resulting $p_o = 300$ kPa while $p_1 = 2100$ kPa. Basing on these values one may compute DMT parameters $I_D \approx 6$, $K_D \approx 3$, $E_D \approx 62500$ kPa and $M_{DMT} \approx 90000$ kPa. In the course of inserting the blade strong preconsolidation effect is observed therefore basing on the M_{DMT}

modulus one may easily derive the current $E_{ur} \approx 0.9 * 90000 = 81000$ kPa. This shows an excellent agreement between assumed and interpreted values of the E_{ur} modulus.

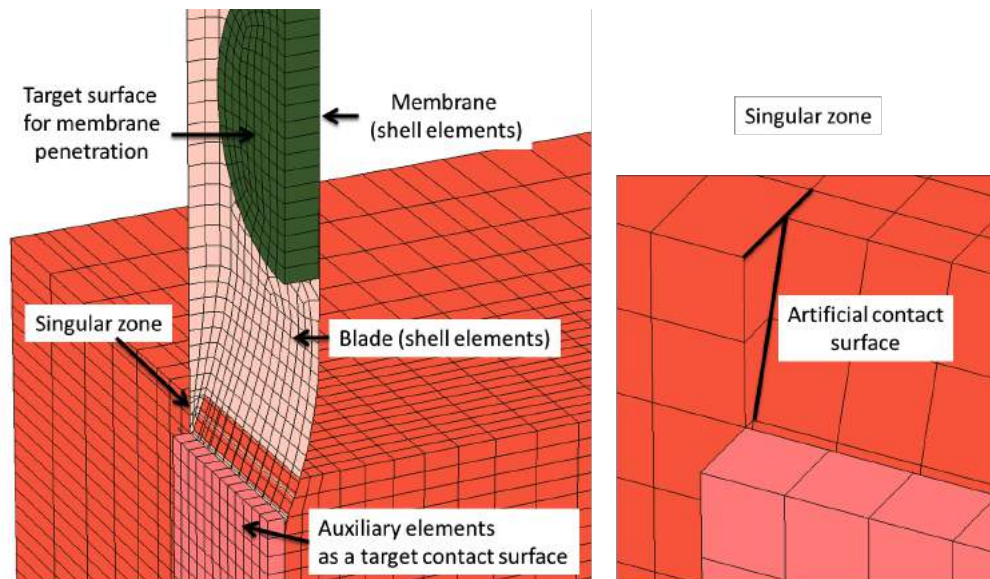


Figure 1. FE model with auxiliary contact zone (initial configuration)

3. Conclusions

Result of the DMT test simulation in the cohesionless soil shows a significant preconsolidation effect observed in the stage of blade insertion. In the context of the HS model parameter identification this is not a drawback, but rather a benefit, as the volumetric plastic mechanism becomes inactive and E_{ur} modulus can directly be determined. It has to be mentioned that in the in situ conditions $OCR=1$ hence shear and volumetric mechanisms are both active.

References

- [1] Benz, T. (2006). *Small-strain stiffness of soils and its numerical consequences*. Ph.d thesis, University of Stuttgart.
- [2] Schanz, T., Vermeer, P., and Bonier, P. (1999). Formulation and verification of the Hardening Soil Model. *Beyond 2000 in Computational Geotechnics*, Balkema, Rotterdam.
- [3] Obrzud, R. (2009). *Numerical Modeling and Neural Networks to Identify Constitutive Parameters from In Situ Tests*. Ph.D. thesis, Swiss Federal Institute of Technology.
- [4] R. Obrzud, L. V., A. Truty (2011). Numerical modeling and neural networks to identify model parameters from piezocone tests: I. FEM analysis of penetration in two-phase continuum . "*International Journal for Numerical and Analytical Methods in Geomechanics*", **35**, 1703–1730.
- [5] R. Obrzud, L. V., A. Truty (2012). Numerical modeling and neural networks to identify model parameters from piezocone tests: II. Multi-parameter identification from piezocone data. "*International Journal for Numerical and Analytical Methods in Geomechanics*", **36**, 743–779.
- [6] A. Rodriguez-Ferran, P. P. and Huerta, A. (1997). Two stress algorithms for large strains: Accuracy analysis and numerical implementation. *International Journal for Numerical Methods in Engineering*, **40**, 4363–4404.
- [7] Parisch, H. and Lübbing, C. (1997). A formulation of arbitrarily shaped surface elements for three-dimensional large deformation contact with friction. *International Journal for Numerical Methods in Engineering*, **40**, 3359–3383.

NUMERICAL MODELLING OF AN ANCHOR LOAD TEST - INFLUENCE OF THE GROUT

C. Fabris¹, B. Pulko² and H.F. Schweiger¹

¹ *Graz University of Technology, Computational Geotechnics Group, Austria*

² *University of Ljubljana, Faculty for Civil and Geodetic Engineering, Slovenia*

1. Introduction

Although the bearing capacity of ground anchors mainly depends on the mechanical behaviour of the surrounding soil, details of construction of the anchor may also play a significant role. In this respect, two aspects are investigated in this study: the influence of the pressure grouted body at the fixed length and the behaviour of the so-called free length. Numerical simulations of pressure and gravity grouting were performed as well as simulations with and without the introduction of the grout at the free length. The results are compared against field measurements performed during an anchor pull-out test.

2. Description of the pull-out test and numerical simulations

The pull-out test was performed by Keller Grundbau in St. Kanzian, Austria, in December 2017. The free length was 12 m long and the fixed length 8 m. The anchor was pressure grouted at the fixed length and 6 strands were employed. The displacements of the head of the tendon were monitored, allowing the assessment of the load-displacement behaviour of the structure. The anchor was vertically installed and post-grouted. The soil, locally known as “Seeton”, is a clayey silt of low plasticity. Laboratory and in-situ investigations, such as oedometer test, direct shear test and seismic dilatometer test, were performed in order to determine the soil properties. Due to the vertical anchor geometry, the model was axisymmetric. Three different numerical simulations were performed:

- With grout at the free length and fixed length pressure grouted (simulation 1 – S1);
- No grout at the free length and fixed length pressure grouted (simulation 2 – S2);
- With grout at the free length and fixed length gravity grouted (simulation 3 – S3).

The actual configuration employed in-situ was the first one. The other two enable the evaluation of the contribution from the pressuring procedure and from the grout application at the free length. The geometry is presented in Figure 1.

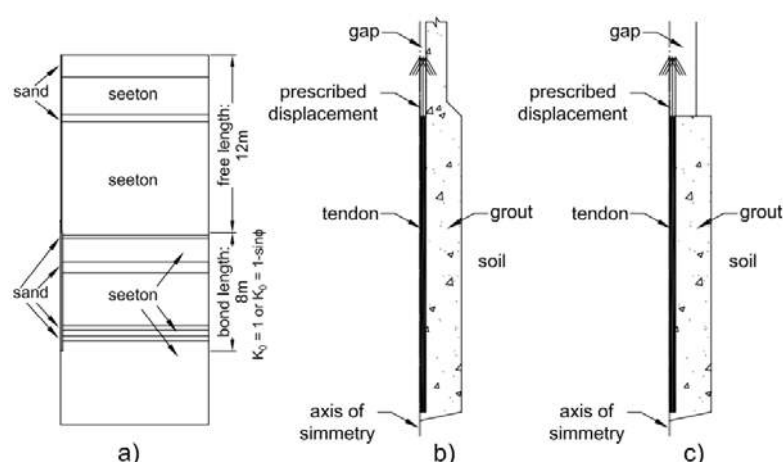


Figure 1. Model geometry: a) Full geometry; b) anchor detail (S1 and S3) and c) anchor detail (S2)

The pressure grouting effect was taken into account by an increase of the lateral stress in the ground, i.e. an increase of the coefficient of lateral earth pressure ($K_0 = 1$). The tendon was modelled only in the fixed length and a gap was introduced between the axis of symmetry and the grout in the free length. The tendon was simulated as a linear elastic material, the grout was modelled with a nonlinear constitutive model, originally developed for modelling the behaviour of shotcrete (Schädlich and Schweiger, 2014). This model allows post-peak softening in compression and tension and therefore the development of cracks in the grout can be captured. For the soil the Hardening Soil model with small strain stiffness as implemented in the finite element code Plaxis 2D (Brinkgreve et al., 2016) was employed.

3. Results and conclusions

The load-displacement curves obtained numerically and in-situ are shown in Figure 2. The displacements considered are on top of the tendon, at the fixed length.

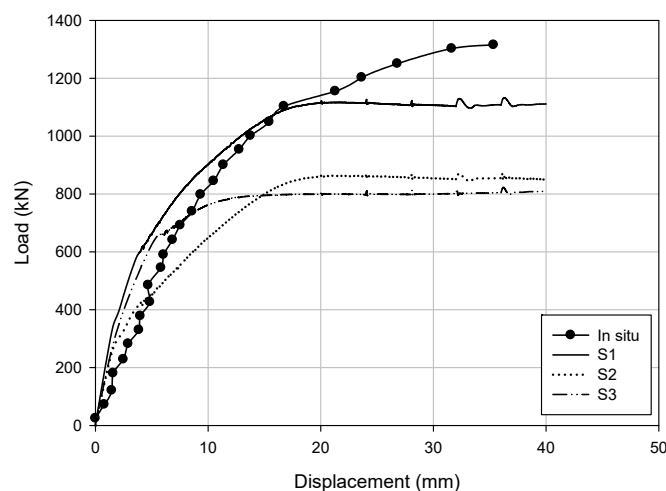


Figure 2. Load-displacement curves

As expected, the best agreement was achieved with simulation S1. Although the in-situ measurement showed higher load values at the end of the test, at about 1100 kN the “creep”, conventionally taken as a measure for ultimate capacity, was larger than 2 mm. If no grout was considered in the free length (S2), the ultimate load decreased substantially and the load-displacement behaviour was softer. This configuration reflects conventional design, where it is assumed that there is no load transfer into the soil in the free length although it is very often also grouted in order to provide protection against corrosion. However, the numerical results clearly showed that significant load may be transferred into the ground in the free length. If the anchor is gravity grouted in the fixed length (S3), i.e. no increase of K_0 is assumed in the numerical model, the behaviour at the beginning is similar to “S1” but the ultimate capacity is close to “S2”. For this reason, in this particular case the grout in the free length would compensate roughly for not pressure grouting the fixed length.

4. References

- [1] Brinkgreve, R.B.J., Kumarswamy, S. & Swolfs, W.M. (2016). *PLAXIS 2016. Finite element code for soil and rock analyses, User Manual*. Plaxis bv, Delft, The Netherlands.
- [2] Schädlich, B. & Schweiger, H.F. (2014). A new constitutive model for shotcrete. *Proc. Numerical Methods in Geotechnical Engineering (Hicks, Brinkgreve & Rohe, eds)*. Taylor & Francis Group, London, 103-108.

NUMERICAL ANALYSES AND MODEL TESTS ON COUNTERMEASURE AGAINST DAMAGE OF EXISTING STRUCTURE DUE TO TUNNELING

Suzuki, M.¹, Kashiyama, M.¹, Nakai, T.² and Shahin, H.M.³

¹ *Chiba Institute of Technology, Chiba, Japan*

² *Geo-Research Institute, Nagoya, Japan*

³ *Islamic University of Technology, Gazipur, Bangladesh*

Urban tunneling is increasing all over the world. However, tunnel excavations inevitably cause ground deformations and may affect existing structures. Numerical and experimental studies on the settlement of existing structure caused by tunneling have been done, and it is clarified that large settlement and rotation occur at the position of the structure [1][2]. In the present study, following the previous studies, effective method to prevent and/or reduce the settlement and rotation of the structure is discussed based on 2D finite element analyses and model tests. In the analyses the Subloading t_{ij} model [3] is used as the constitutive model of geomaterials. In the model tests aluminum rod mass is used as the ground material. Layout of these numerical simulations and model tests are the same as the previous ones. As the countermeasure, sheet pile is installed from the ground surface between the existing structure and the tunnel. Effective position, length, stiffness and skin friction are investigated.

The circular tunneling device with a diameter of $B=10\text{cm}$, which is moveable with the ground deformation, is used in the experiments (see Fig. 1). Pile foundation is set up near tunnel, and constant dead load, which is about $1/3$ of the ultimate bearing capacity, is applied at the center of the foundation before tunnel excavation. Since steel sheet pile is assumed as a countermeasure work in practice, aluminum plate with a thickness of 0.5mm is used in the model tests, considering the similarity ratio with prototype. Excavation is done with the shrinkage of the tunnel $d_r=4.0\text{ mm}$. The horizontal separation between the structure and the plate is denoted by S_p , and the penetration length of the plate is denoted by S_d . The depth of tunnel is $D=2.0B$ and the horizontal separation $S_t=0.5B$ between the structure and tunnel is constant in every case. The model tests are performed under different values of S_d . The corresponding analyses are carried out in the same condition as the tests.

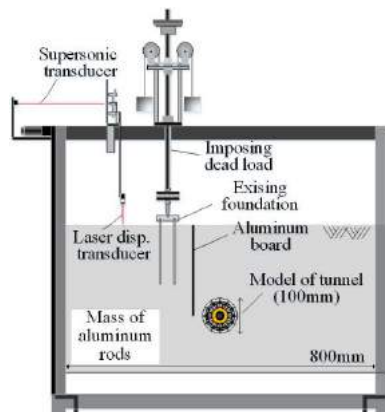


Figure 1 Schematic diagram of the experimental apparatus

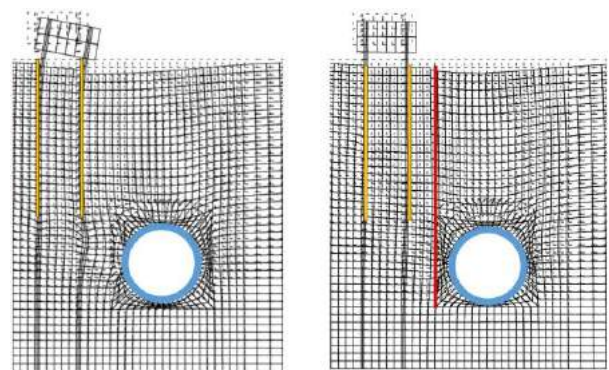


Figure 2 Deformations of analysis with and without countermeasure

Fig.2 shows the computed deformations of the ground with and without the plate ($S_p=0.2B$; pile length $L=200\text{ mm}$). Fig. 3 shows the observed and computed deviatoric strain distributions in the ground for the cases with and without the plate, when the tunnel shrinkage $d_r=4.0\text{mm}$ is applied. Deviatoric strains are generated from the vicinity of the invert to the pile tips in the case of no-countermeasure. However, in the case where the plate (penetration length $S_d=3.5B$) is used, large deviatoric strain occurs right side of the plate and does not reach the pile tips.

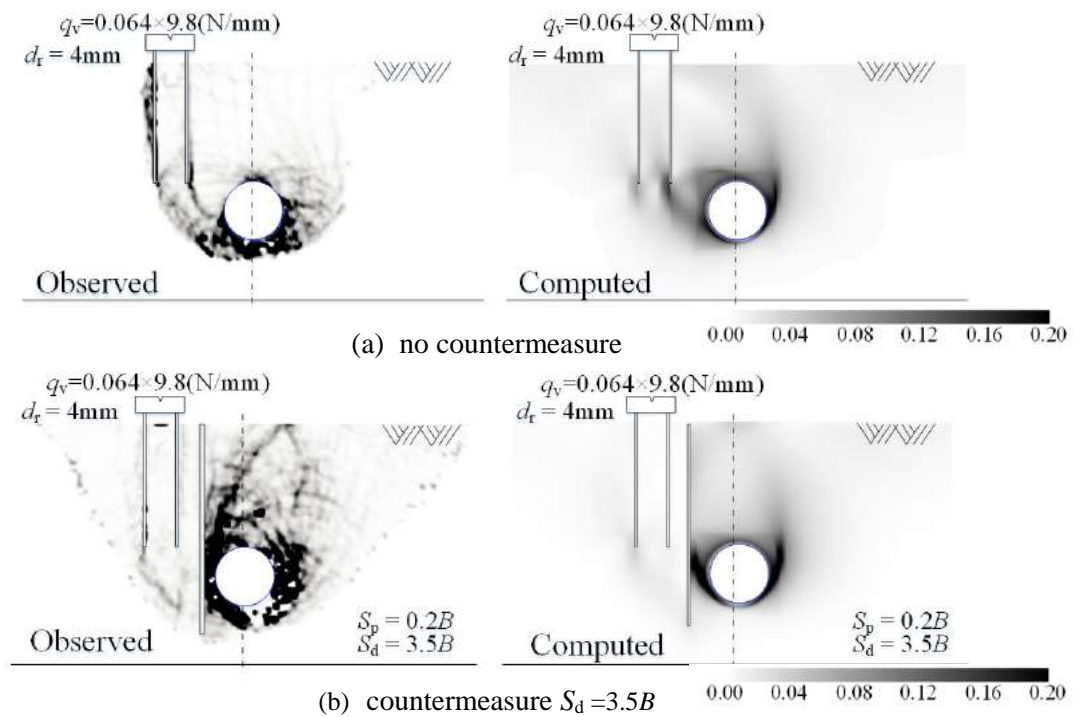


Figure 3 Deviatoric strain distribution

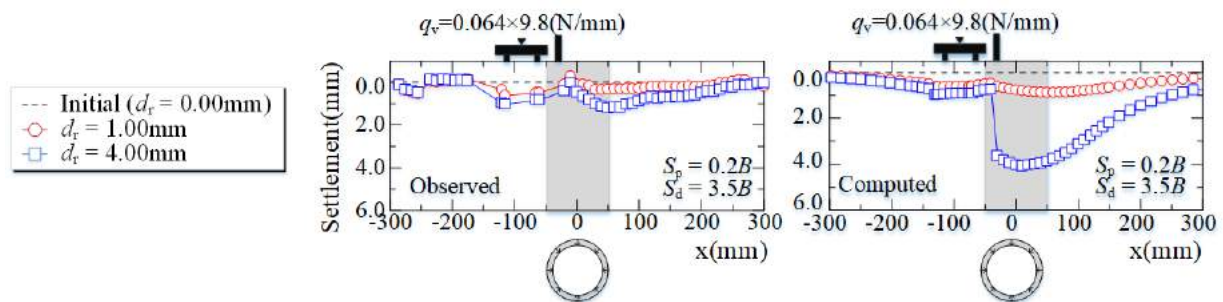


Figure 4 Settlement of the ground surface

Fig. 4 shows the computed and observed surface settlements for the case with countermeasure when $d_r=1.0\text{mm}$ and 4.0mm are applied. Although the computed results over predict the settlement of right side of the plate (above the tunnel) in $d_r=4.0\text{mm}$, the settlement of the foundation does not increase much with increase of tunnel shrinkage. Although figures are not shown here, the plate which length is not deeper than the tunnel invert is not effective.

The results of numerical simulations, in which mechanical behavior of geomaterials, stiffness of structure and sheet pile and skin friction of sheet pile are properly taken into account, have good agreements with those of model tests.

References

- [1] Shahin, H.M., Nakai, T., Zhang, F., Kikumoto, M. & Nakahara, E. (2011). Behavior of ground and response of existing foundation due to tunneling, *Soils & Foundation*, **51**(3), 395-409.
- [2] Shahin, H.M., Nakai, T., Ishii, K., Iwata, T. & Kuroi, S. (2016). Investigation of influence of tunneling on existing building and tunnel – model tests and numerical simulations, *Acta Geotechnica*, **11**(3), 679-692.
- [3] Nakai, T. and Hinokio, M. (2004). A simple elastoplastic model for normally and over consolidated soils with unified material parameters, *Soils and Foundations*, **44**(2), 53-70.